



TECHNISCHE
UNIVERSITÄT
WIEN
Vienna University of Technology

DISSERTATION

SURFACE SCIENCE STUDIES ON ZIRCONIA THIN-FILM MODEL SYSTEMS

Ausgeführt zum Zwecke der Erlangung des akademischen Grades eines
Doktors der technischen Wissenschaften unter der Leitung von

AO.UNIV.PROF. DIPL.-ING. DR. TECHN. MICHAEL SCHMID

und

UNIV.PROF. DIPL.-ING. DR. TECHN. ULRIKE DIEBOLD

INSTITUT FÜR ANGEWANDTE PHYSIK E134

eingereicht an der Technischen Universität Wien
Fakultät für Physik

von

DIPL.-ING. PETER LACKNER, BSc

Wien, April 2019

Acknowledgement

Eine Doktorarbeit wird normalerweise einer einzelnen Person zugeschrieben. Dem Autor bleiben dann diese Worte, um alle Helfer zu würdigen, die – indirekt oder direkt – daran mitgewirkt haben.

Zu allererst will ich meinem Dissertationsbetreuer Michael danken. Er hat mir den Freiraum gegeben, die Messungen durchzuführen, von denen ich der Meinung war, dass sie zum Ziel führen würden, doch seine Tür stand immer offen, falls Fragen aufkamen. Ich konnte meinen eigenen Ideen nachgehen, und auf seine Ratschläge zurückgreifen, wenn ich in einer Sackgasse gelandet bin. Man kann sich keinen besseren Doktorvater wünschen.

Großer Dank gilt auch Ulli. Dafür, dass die Gruppe, in der ich die letzten Jahre arbeiten durfte, so kollegial ist, wie sie ist, und natürlich für die Chance, meine Doktorarbeit hier machen zu dürfen. In diesem Sinne auch danke an Gareth: Dafür, dass er einem jungen Bachelorstudenten, der zufällig dem selben Zimmer zugeteilt war, so begeistert den ersten Einblick in die Oberflächenphysik gewährt hat. Eine Begeisterung, die von Margereta geteilt wurde, der ich sehr dankbar dafür bin, dass sie mir die Tricks beigebracht hat, die man für erfolgreiche Laborarbeit braucht. Zum Beispiel die richtige Menge an Soft Cakes pro Tag. Jedem und jeder in meiner Arbeitsgruppe, die mir geholfen haben: Danke. Und nicht zu vergessen, Sabrina und alle Bachelor- und Projektarbeitsstudenten, die mit mir gemessen haben, von denen ich zumindest genauso viel gelernt habe, als sie von mir.

An meine Familie und meine Freunde, die mich in harten Zeiten aufgemuntert haben: ein herzliches Dankeschön. Auch dafür, dass sie ehrliches Interesse daran hatten, welche Ergebnisse ich über die Jahre produziert habe, und für ihr Verständnis, wenn ich freitags wieder einmal zu spät kam, weil sich eine Vakuumkammer nicht von selbst repariert. Besonders gilt all das für Birgit. Danke für alles – und mehr. Du weißt ja wie weit.

Zuletzt danke ich dem österreichischen Fonds zur Förderung der wissenschaft-

lichen Forschung (FWF), Projekt F45-05 und F45-11 (FOXSI), für die finanzielle Unterstützung.

Abstract

Zirconia is an oxide material used in many industrial applications, ranging from dental implants and catalysis to solid oxide fuel cells. In all these fields, surface interactions play a major role for functionality. In this thesis, zirconia surfaces are studied using the surface science approach; zirconia model systems are prepared and studied in ultrahigh vacuum using films with a thickness of one layer (“ultrathin”) and several layers (“thin”). The small thickness is necessary to achieve electronic conductivity as zirconia is an insulator with a band gap of ≥ 5 eV. The films are studied with a multi-technique approach, combining scanning tunneling microscopy, x-ray photoelectron spectroscopy, temperature-programmed desorption, low-energy electron diffraction, and Auger electron spectroscopy.

Four methods for zirconia film growth are investigated in this thesis: Oxidation of zirconium alloys, growth on metallic substrates using ultrahigh-vacuum-compatible sputter deposition, chemical vapor deposition of Zirconium (IV) Tert-Butoxide (ZTB), and oxidation of Zr(0001) single crystals.

Gas adsorption and desorption studies of water, methanol, CO, CO₂, O₂, and Kr were conducted on previously well-examined ultrathin zirconia films on Pt₃Zr(0001). The main part focussing on water found primarily molecular adsorption; dissociative adsorption occurs at a limited number of sites. By comparison with near-ambient pressure measurements on powder samples, these results show the validity of ultrathin zirconia as a zirconia model system.

Sputter-deposited zirconia films of five monolayer thickness were studied mainly on Rh(111) substrates, but also on Pt(111) and Pt₃Zr(0001). These films could be stabilized in two phases: tetragonal and monoclinic zirconia. At low annealing temperatures (< 730 °C), tetragonal zirconia was stable due to $\approx 2\%$ oxygen vacancies present. These lead to a shift of the electronic levels of the material due to band bending induced by positively charged oxygen vacancies. Fully transformed monoclinic films were found above 850 °C. The transformation was accompanied by dewetting, which

led to holes down to the Rh(111) substrate. This allowed for oxygen dissociation and full oxidation of the film. The films could also be fully oxidized by depositing a catalyst on top of the film. In both cases, the shift of the electron levels was reverted.

The third part of the thesis investigates the behaviour of zirconia in terms of the strong metal-support interaction (SMSI). This process is known from catalysis for reducible oxides, but the existence for the hardly reducible zirconia was unclear. It is shown that upon annealing zirconia films under reducing conditions, an ultrathin film covered the metal support – the typical SMSI behaviour.

Finally, a proof of principle for the growth of zirconia via chemical vapor deposition on Pt(111) is discussed, and the reason why the oxidation of Zr(0001) single crystals does not lead to stable zirconia films.

Zusammenfassung

Das Material Zirconiumdioxid (Zirconia) kommt in verschiedensten Industriesparten zum Einsatz. Die Anwendungsbereiche reichen von Zahnimplantaten über Katalyse bis hin zu Festoxidbrennstoffzellen (solid oxide fuel cells, SOFCs), wobei Wechselwirkungen an Oberflächen in jedem dieser Gebiete eine wichtige Rolle für die Funktionalität spielen. In dieser Dissertation werden Zirconiaoberflächen mittels oberflächenphysikalischer Untersuchungsmethoden studiert. Dabei werden einlagige ("ultradünne") oder mehrlagige ("dünne") Zirconia-Modellsysteme in Ultrahochvakuum präpariert und mittels mehrerer Messmethoden untersucht: Rastertunnelmikroskopie (STM), Röntgen-Photoelektronenspektroskopie (XPS), thermische Desorptionsspektroskopie (TPD), Beugung niederenergetischer Elektronen (LEED) sowie Augerelektronenspektroskopie. Solch dünne Schichten sind notwendig, weil Zirconia eine Bandlücke von ≥ 5 eV aufweist und damit zu den Nichtleitern zählt.

In dieser Dissertation werden vier Methoden zum Wachstum dünner Schichten untersucht: Oxidation von Zirconiumlegierungen, Wachstum auf metallischen Substraten via ultrahochvakuumkompatibler Sputterdeposition, chemische Gasphasenabscheidung (CVD) aus Zirconium (IV) Tert-Butoxid (ZTB) sowie Oxidation von Zr(0001)-Einkristallen.

Gasadsorptions- und Desorptionsstudien von Wasser, Methanol, CO, CO₂, O₂ und Krypton wurden auf wohldefinierten ultradünnen Zirkoniaschichten auf Pt₃Zr(0001) durchgeführt. Wasser adsorbiert hauptsächlich molekular, dissoziative Adsorption tritt nur auf speziellen Adsorptionsplätzen auf. Die Gültigkeit dieses Systems als Modellsystem für reale Zirconiaanwendungen wurde durch den Vergleich mit Messungen nahe an Atmosphärendruck an Zirconiapulver überprüft.

Aufgesputterte Zirconiaschichten mit einer Dicke von fünf Monolagen wurden hauptsächlich mit Rh(111)-Einkristallen als Substrate durchgeführt. Messungen auf Pt(111) und Pt₃Zr(0001) werden ebenfalls präsentiert. Solche Schichten konnten in zwei ZrO₂-Phasen stabilisiert werden, tetragonal und monoklin. Bei niedrigen Heiz-

temperaturen ($< 730\text{ }^{\circ}\text{C}$) ist tetragonales Zirconia durch $\approx 2\%$ Sauerstofffehlstellen stabilisiert. Diese führen zu einer Verschiebung der elektronischen Zustände, die von positiv geladenen Sauerstofffehlstellen erzeugt wird. Oberhalb von $850\text{ }^{\circ}\text{C}$ konnte monoklines Zirconia stabilisiert werden. Die Phasentransformation fand zur selben Zeit wie ein Aufbrechen der Oxidschicht statt, welches Sauerstoffdissoziation auf dem Rhodiumsubstrat und damit die vollständige Oxidation der Schicht ermöglicht. Es wurde eine weitere Möglichkeit für die vollständige Oxidation der Oxidschicht gefunden: Das Aufbringen eines Katalysators direkt auf dem Zirconiafilm. In beiden Fällen wurde die Verschiebung der elektronischen Zustände aufgehoben.

Im dritten Teil dieser Dissertation wird das Verhalten von Zirconia im Sinne der sogenannten "strong metal-support interaction" (SMSI) untersucht. Dieser aus der Katalysatorforschung bekannte Prozess ist für reduzierbare Oxide verstanden, doch das Verhalten von kaum reduzierbarem Zirconia war nicht eindeutig bekannt. Es wird gezeigt, dass unter reduzierenden Bedingungen ein ultradünner Film über dem Metallsubstrat wächst, was dem typischen SMSI-Verhalten entspricht.

Zuletzt wird das grundlegende Wachstum von Zirconia via chemischer Gasphasenabscheidung gezeigt, sowie die Gründe diskutiert, warum die Oxidation von Zr (0001)-Einkristallen nicht zu stabilen Zirconiaschichten führt.

Contents

Acknowledgement	iii
Abstract	v
Zusammenfassung	vii
Acronyms	xiii
1 Introduction	1
1.1 Properties and Application	1
1.2 The Many Forms of Zirconia	2
1.3 Previous Experimental Studies	5
1.4 Overview	6
2 Experimental Setup and Methods	9
2.1 Ultrahigh-vacuum Chambers	9
2.1.1 Room-Temperature STM Chamber - "RT-STM"	9
2.1.2 Low-Temperature STM Chamber - "LT-STM"	10
2.1.3 TPD Chamber	11
2.2 UHV-compatible Zirconium Sputter Deposition Source	11
2.2.1 Motivation	12
2.2.2 Description of the Source	14
2.2.3 Evaluation of the Source	19
2.2.4 Parameters for ZrO ₂ Thin Film Growth	25
2.2.5 Conclusions	26
2.3 Experimental Techniques	26
2.3.1 Scanning Tunneling Microscopy	26
2.3.2 X-ray Photoelectron Spectroscopy	28

2.3.3	Auger Electron Spectroscopy	31
2.3.4	Temperature-Programmed Desorption	31
2.3.5	Low-Energy Electron Diffraction	32
3	Gas Adsorption Behaviour on Ultrathin ZrO₂/Pt₃Zr	35
3.1	Sample Preparation	35
3.2	Bare Ultrathin Zirconia Grown on Pt ₃ Zr	36
3.3	Dislocation Lines	37
3.4	Water	38
3.4.1	Previous Studies	38
3.4.2	Water Adsorption and Desorption on Zirconia/Pt ₃ Zr	41
3.4.3	Stoichiometry of the Ultrathin Zirconia Film	48
3.4.4	Water-Induced Surface Changes	48
3.4.5	DFT and FTIR Studies by Collaborators	52
3.4.6	Discussion	55
3.4.7	Conclusion	60
3.5	Methanol	61
3.5.1	TPD	61
3.5.2	XPS	61
3.5.3	Discussion	63
3.6	Other Gases	64
3.6.1	Carbon Monoxide	64
3.6.2	Carbon Dioxide	65
3.6.3	Krypton	66
3.6.4	Oxygen	68
4	Thin ZrO₂ Films	71
4.1	Sample Preparation	71
4.2	Surface Structures on Rh(111)	72
4.2.1	Zirconia Layers of Increasing Thickness	72
4.2.2	Tetragonal Zirconia films	75
4.2.3	Monoclinic Zirconia films	79
4.2.4	Discussion	81
4.3	Conclusion	84

4.4	Energy Levels of Thin ZrO ₂ Films	85
4.4.1	XPS of Tetragonal and Monoclinic Films	85
4.4.2	Possible Reasons for Differences in Binding Energy	90
4.4.3	Test Experiment: Full Oxidation of Tetragonal ZrO ₂ by Rh Deposition	93
4.4.4	Band Bending Model	94
4.4.5	Discussion	97
4.4.6	Conclusion	100
4.5	Thin ZrO ₂ Films on Pt(111) and Pt ₃ Zr(0001)	100
4.5.1	Pt(111)	100
4.5.2	Pt ₃ Zr(0001)	105
4.5.3	Discussion	106
5	SMSI of Zirconia on Rh(111) and Pt(111)	109
5.1	Introduction	109
5.2	Results	110
5.2.1	Zirconia on Rh(111)	110
5.2.2	Zirconia on Pt(111)	114
5.2.3	Photoelectron Spectroscopy	116
5.2.4	Stoichiometry of Ultrathin Zirconia	117
5.2.5	Diffusion of Alloyed Zr in Rh and Pt	121
5.2.6	Transfer through Air	123
5.3	Discussion	123
5.4	Summary	126
6	Chemical Vapor Deposition of Zirconia	127
6.1	Sample Preparation	127
6.2	Results and Discussion	128
7	Oxidation of Zr(0001)	131
7.1	Previous Results	131
7.2	Sample Preparation	133
7.3	Results	134
7.3.1	Initial Reproducibility	134
7.3.2	Oxygen Dosing on Clean Surface	135

7.3.3 Cleanliness	137
7.4 Discussion	139
8 Conclusion and Outlook	143
Appendix	145
A Thermocouple Temperatures	145
B Raw Data Locations	147
Bibliography	149

Acronyms

Methods:

CVD – chemical vapor deposition

DFT – density functional theory

FFT – fast Fourier transformation

FTIR – Fourier-transform infrared spectroscopy

STM – scanning tunneling microscopy

TPD – temperature programmed desorption

UHV – ultrahigh vacuum

XPS – x-ray photoelectron spectroscopy

UHV systems:

RT-STM – room-temperature STM, see chapter [2.1.1](#)

LT-STM – low-temperature STM, see chapter [2.1.2](#)

TPD chamber – see chapter [2.1.3](#)

Materials:

c-ZrO₂ – cubic zirconia

m-ZrO₂ – monoclinic zirconia

t-ZrO₂ – tetragonal zirconia

YSZ – yttria-stabilized zirconia

ZTB – zirconium (IV) tert-butoxide

Other abbreviations:

E_B – binding energy

FWHM – full width at half maximum

GB – grain boundary

IMFP – inelastic mean free path

LHe – liquid helium

LN₂ – liquid nitrogen

SMSI – strong metal-support interaction

V_O – oxygen vacancy

Chapter 1

Introduction

1.1 Properties and Application

Zirconia (ZrO_2 , zirconium dioxide) is a ceramic material with a band gap of > 5 eV [1] and is therefore considered a perfect insulator. By doping zirconia with various materials (e.g., MgO , La_2O_3 , and most importantly, Y_2O_3), a large range of interesting properties emerges [2]. Zirconia has a high resistance to acids and alkaline solutions [3], and a high thermal stability with a melting point of 2710°C [4,5] combined with low thermal conductivity [6]. Furthermore, zirconia is known for its high toughness in the form of partially stabilized zirconia (PSZ) [7], see below. The number of interesting technical properties offered by zirconia make it versatile enough to be of interest in a broad set of industrial fields; zirconia is used as catalyst support [8] and catalyst [9], as a refractory ceramic [6, 10, 11], and as a dental implant material due to its good biocompatibility [12, 13]. A large amount of zirconia, 300 t/year, was used for diamond substitutes already before the turn of the millenium [14]; an optical distinction between diamond and zirconia is difficult because of the high band gap of zirconia, as well as similar dispersion and refractive index. (Jewelers rely on thermal conductivity measurements.) Zirconia was also discussed as a gate dielectric in semiconductors due to its high dielectric constant κ ; nowadays, HfO_2 (which is very similar to ZrO_2) is favored [15]. Chemically doped zirconia (mostly yttrium-doped, then known as yttria-stabilized zirconia, YSZ) is heavily used as solid-state electrolyte in solid oxide fuel cells (SOFCs) [16] and gas sensors [17]. While the material is an electronic insulator up to high temperatures, it can conduct oxygen (and, thereby, electric charge) via vacancy diffusion, which forms the basis for using zir-

conia as an electrolyte. As the intrinsic concentration of oxygen vacancies (V_{O}) in ZrO_2 is very low even at high temperatures and reducing atmosphere, additional V_{O} are introduced by chemical doping with trivalent elements such as yttrium.

Natural deposits of ZrO_2 (in the form of baddeleyite, see section 1.2), are not very common. The most abundant source for Zr is zircon (ZrSiO_4), which can be found alongside other heavy minerals such as TiO_2 . In nature, such heavy minerals are split from lighter materials by sand deposition following erosion, and are therefore found in river deltas and at beaches. Zircon is mostly mined as a side product during Ti ore production [3]. Zirconia mining is mainly conducted in Australia and South Africa, with an estimated yearly production of 600 t and 400 t, respectively, in the year 2017 [18]. Worldwide production rose from about 900 t in 1997 [19] to 1600 t in 2017 [18].

1.2 The Many Forms of Zirconia

Excerpts of this chapter have been published in Ref. 24, which includes a detailed introduction into zirconia and zirconia surface studies.

Depending on temperature or dopant concentration, zirconia exhibits three stable bulk structures at atmospheric pressure: For pure, stoichiometric ZrO_2 , the cubic structure (c- ZrO_2 , fluorite lattice) can be found above 2377 °C. At lower temperatures the tetragonal phase (t- ZrO_2) is stable above 1205 °C, and finally monoclinic ZrO_2 (m- ZrO_2 , also known as baddeleyite) is found at room temperature [4]. These phases are shown in Figure 1.1a. While all these phases are related to the cubic fluorite structure, pure c- ZrO_2 does not exist at room temperature due to the small O–O distance imposed by the short (strong) Zr–O bonds ($d_{\text{O–O}} \approx 256$ pm for hypothetical room-temperature c- ZrO_2 [20]). The average O–O distance can be increased by shifting the O atoms alternately up or down in [001] direction, leading to the tetragonal phase ($d_{\text{O–O}} \approx 260$ pm), which, however, is still unstable for pure, stoichiometric ZrO_2 at room temperature. Upon transformation to m- ZrO_2 , Zr–O bonds are broken, the coordination of Zr changes from 8 to 7, and for half of the O atoms the coordination is reduced from fourfold (tetrahedral) to threefold (planar); the volume increases by $\approx 5\%$. These changes substantially increase the average O–O distance, while the Zr–O bonds remain short. The Zr–Zr distances are large for all phases and therefore do not hinder any transformations.

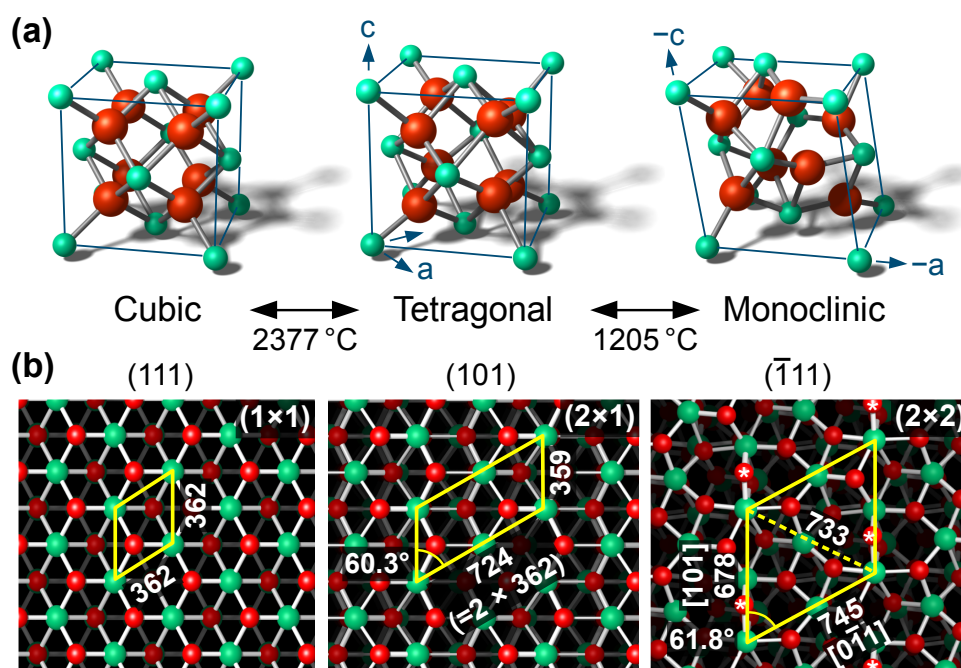


Figure 1.1: The three stable ambient-pressure bulk phases of zirconia. (a) Bulk unit cells and (b) bulk-terminated surfaces equivalent to the (111) surface of cubic ZrO_2 , with the surface unit cells marked in yellow. Oxygen (2-) ions are depicted in red, zirconium (4+) ions in green. Room-temperature cell sizes in (b) are given in pm and based on Refs. 20 and 21 for cubic (extrapolated from doped to undoped ZrO_2), Ref. 22 for tetragonal, and Ref. 23 for monoclinic ZrO_2 . The surface cell of t- ZrO_2 deviates only slightly from two unit cells of c- ZrO_2 .

The tetragonal and cubic phases can be stabilized at room temperature by introducing V_{O} s, which can be achieved by doping with e.g. yttria [4, 25–27]. Additional V_{O} s increase the average $d_{\text{O-O}}$, thereby stabilizing otherwise instable phases. Y_2O_3 concentrations above ≈ 8 mol% (corresponding to $\text{Zr}_{0.85}\text{Y}_{0.15}\text{O}_{1.93}$) stabilize the cubic phase (yttria-stabilized zirconia, YSZ). At lower dopant concentrations one finds mixtures of cubic and tetragonal, or cubic and monoclinic zirconia, known as partially stabilized zirconia (PSZ) [7]. The lower doping limit is 1.5–2 mol% Y_2O_3 , where the monoclinic phase remains stable [28]. The tetragonal phase is also found in pure nanoscale ZrO_2 at room temperature; while this was initially attributed to its favorable surface energy [10], newer works rather point towards a stabilization by V_{O} s instead [26, 27].

Figure 1.1b shows the surface termination of $c\text{-ZrO}_2(111)$ and the corresponding lowest-energy terminations of the other phases. Despite the distortions with respect to $c\text{-ZrO}_2$, all these surfaces are non-polar. The cubic phase exhibits a hexagonal (1×1) structure. The shifted O columns in the tetragonal phase lead to a (2×1) unit cell w.r.t. the cubic phase. As a result of the different unit cell, the (111) face of cubic ZrO_2 becomes (101) in the tetragonal phase. The monoclinic phase features a distorted (2×2) surface unit cell (again, w.r.t. $c\text{-ZrO}_2$). For this latter phase, density functional theory (DFT) calculations predict that the $(\bar{1}11)$ surface has the lowest surface energy [29]; in contrast to (111), it has only one (instead of two) surface O with twofold coordination per unit cell (marked by an asterisk in Figure 1.1b).

Apart from the above-mentioned structures, several orthorhombic high-pressure phases of zirconia exist; some of these are metastable at ambient conditions [30]. Recently, the orthorhombic phases of ZrO_2 and mixed $\text{ZrO}_2/\text{HfO}_2$ have received increased attention as candidate materials for ferroelectric memory devices [31]. Similar to monoclinic ZrO_2 , these orthorhombic phases are based on distortions of the cubic fluorite structure, again having 7-fold coordinated Zr and O with 3-fold and 4-fold coordination [32, 33]. When cut along a direction equivalent to $c\text{-ZrO}_2(111)$, the most common orthorhombic I and II phases would exhibit a (2×2) or (2×4) surface unit cell with respect to the cubic phase, respectively.

1.3 Previous Experimental Studies

In spite of its technological importance, zirconia has received surprisingly little attention from the surface-science community. This is partly due to its insulating nature, as most surface-science methods rely on electronic conductance, e.g., scanning tunneling microscopy (STM), low-energy electron diffraction (LEED), or x-ray photoelectron spectroscopy (XPS). Furthermore, the phase transitions make it impossible to grow a ZrO_2 single crystal from the melt. This second limitation does not exist for cubic YSZ, where single crystals are readily available and inexpensive. Morrow *et al.* [34] used a YSZ single crystal for high-temperature STM studies; this work was conducted at $\approx 300^\circ\text{C}$ to ensure sufficient conductivity. While atomic resolution was achieved, this approach is limited to high temperatures, and due to Y segregation the surfaces had a rather high Y concentration [35]. In our group, measurements on YSZ single crystals at room temperature were tried to no avail; even after extreme reduction treatment, after which XPS showed metallic Zr and the crystal turned black, tip approaches for STM measurements failed.

Several groups have followed a different approach and used monolayer- and few-monolayer-thick films of pure zirconia as model systems. Meinel *et al.* [36–38] performed STM studies on up to 10 ML-thick zirconia films that were deposited onto Pt(111) via physical vapor deposition (PVD) of Zr in an O_2 atmosphere. Their work had been built on a previous LEED study by Maurice *et al.* [39], but involved annealing at higher temperatures. Depending on film thickness and annealing temperature, Meinel *et al.* found a large number of superstructures in LEED and STM. It must be noted that films as thick as 10 ML broke up upon annealing and eventually dissolved in the Pt substrate, so it is not straightforward to decide which structures should be assigned to the multilayer films and which ones to Pt-Zr or Pt-Zr-O structures. Nevertheless, it is clear that the initial structures were based on $\text{ZrO}_2(111)$, with a $\text{ZrO}_2(111)-(2 \times 2)$ LEED pattern w.r.t. cubic ZrO_2 . (In LEED, a (2×2) pattern can also originate from three domains of a (2×1) pattern.) Also, spots interpreted as $\text{ZrO}_2(111)-(1 \times 1)$ rotated by $\pm 6.6^\circ$ w.r.t. Pt(111) after 3 min of annealing at 680°C can be attributed to the ZrO_2 films. Submonolayer films exhibited (5×5) and $(\sqrt{19} \times \sqrt{19})R36.6^\circ$ superstructures with respect to Pt(111) [40]; the latter structure also appeared when thicker films were annealed at high temperatures. Possibly those formed at areas where the thicker ZrO_2 film had disappeared. STM indicates

the presence of a band gap at least for films ≥ 2 ML and density functional theory (DFT) indicates that bulk-like band gaps are reached at 5 ML [37].

A further approach to zirconia model systems is the growth of ultrathin zirconia films by oxidation of alloy single crystals as first shown by Antlanger *et al.* [41]. Two substrates were used: Pt₃Zr(0001) [41, 42] and Pd₃Zr(0001) [43]. By annealing these crystals at 400 °C in O₂, disordered zirconia formed, which consumed Zr from the top layers of the alloy. In the case of Pt₃Zr, Zr diffusion is slow, so the interface was essentially pure Pt(111). For Pd₃Zr, Zr diffuses from the bulk to the surface layers and a Pd:Zr ratio of close to 3:1 is found in XPS [43]. By annealing at 900 °C in UHV, the disordered zirconia transformed to an ordered monolayer corresponding to one O–Zr–O trilayer repeat unit of ZrO₂(111). For ZrO₂/Pt₃Zr, the film exhibited the same ($\sqrt{19} \times \sqrt{19}$)R23.4° superstructure (this rotation angle is equivalent to 36.6°) as found in previous studies of zirconia on Pt(111) by Meinel *et al.* [38, 40], confirming that this structure on Pt(111) likely corresponded to an ultrathin film. ZrO₂/Pd₃Zr formed an O–Zr–O trilayer with an almost identical in-plane lattice constant (both 0.35 nm) and a large ($\sqrt{217} \times \sqrt{217}$)R10.16° superstructure cell. Both, STM measurements and DFT calculations indicated a substantial buckling of the films. These alloy-based, ultrathin zirconia films were successfully used as model systems for surfaces of bulk ZrO₂ in metal growth [44] and water adsorption [45] studies.

Thin zirconia films can also be grown by atomic layer deposition (ALD) using the precursor zirconium (IV) tert-butoxide (ZTB). While this technique is typically used in industry [46] and not in UHV studies, it was successfully applied to deposit sub-monolayer coverages of ZrO₂ on Pd(111) [47, 48] and Cu(111) [49]. However, it remains to be seen whether this method can be used to grow atomically flat zirconia films with a thickness of several monolayers.

1.4 Overview

In this thesis, all three of the above-mentioned model system approaches are investigated, plus a new attempt with Zr(0001) single crystals:

- ultrathin zirconia trilayers grown by oxidation of Zr-alloy single crystals (chapter 3),
- several-ML-thick films grown on metallic substrates using an ultrahigh va-

cuum (UHV)-compatible sputter source (chapter 4 and 5),

- ultrathin trilayers deposited on Pd(111) via chemical vapor deposition (CVD) of zirconium(IV)-tert-butoxide (ZTB), and
- zirconia films grown by oxidation of a Zr(0001) single crystal (a non-fruitful attempt)

In chapter 2 the UHV systems used in the investigations are presented, as well as the Zr sputter source used for deposition of several-monolayer-thick ZrO_2 films. Additionally, the experimental methods used in this thesis are discussed. In chapter 3, details on adsorption on ZrO_2 -trilayers on Pt_3Zr are discussed. The main focus lies on TPD and XPS measurements of adsorbed water, but additional measurements on methanol, CO, CO_2 , O_2 , and Kr are presented. Chapter 4 presents a detailed study of several-monolayer-thick zirconia films on (mainly) Rh(111), but also Pt(111) and $\text{Pt}_3\text{Zr}(0001)$. Both, the surface structure and electronic states are investigated in detail. In chapter 5, the existence of the strong metal-support interaction (SMSI) is shown for $\text{ZrO}_2/\text{Rh}(111)$ and Pt(111): ultrathin ZrO_{1-x} films grow between zirconia islands upon annealing in UHV and are stabilized by alloyed Zr in the substrate. Chemical vapor deposition of zirconia on Pd(111) is explored in chapter 6. Chapter 7 documents the failed attempt of using Zr(0001) as a zirconia growth substrate. Previously found structures are attributed to impurities. In chapter 8, a conclusion and outlook are given.

Chapter 2

Experimental Setup and Methods

2.1 Ultrahigh-vacuum Chambers

The experiments presented in this work were conducted in three different experimental setups in the labs at TU Wien, which are presented below. The sample preparation is explained in each chapter separately.

2.1.1 Room-Temperature STM Chamber - "RT-STM"

The UHV system comprises two chambers, one for sample preparation and one for analysis. The preparation chamber (base pressure below 1×10^{-10} mbar) contains an ion source for Ar^+ sputtering and an electron-beam heater for cleaning of the single crystals, as well as a home-built, UHV-compatible sputter source for deposition of Zr [50], see chapter 2.2. (We have used 99.999% Ar for all sputtering purposes (CAN-gas, www.messergroup.com)). The thermocouple for temperature measurement is attached to the fixed part of the sample holder – the measured temperature can therefore differ from the sample surface temperature by more than 100°C at $T > 800^\circ\text{C}$. This large difference stems from the sample heating setup, where the electron beam used for heating is directed through a hole in the sample plate at the back of the sample. The temperature difference for samples without a hole in the sample plate is much lower. At temperatures above 700°C , radiation in the visible spectrum is strong enough for temperature calibration using a disappearing-filament pyrometer. Lower temperatures are derived from the high-temperature values by linear extrapolation. We estimate the temperatures given in this thesis to be accurate within $\pm 30^\circ\text{C}$. Table A.1 in the appendix lists the thermocouple temperatures T_{TC} and the

respective estimated, real temperatures T_{real} for all crystals used in the RT-STM chamber. The analysis chamber ($p_{\text{base}} < 7 \times 10^{-11}$ mbar) houses an Omicron micro STM for room-temperature tunneling microscopy (thus the name of the chamber), LEED optics (VSI Er-LEED), and spectroscopy capabilities: A hemispherical electron energy analyzer (Specs Phoibos 100, five channels, with iris) for XPS and ISS measurements, as well as an AES cylindrical analyzer with built-in electron gun (Perkin Elmer 10-155). For XPS, a non-monochromatized x-ray source is available. In this work, a Mg $K\alpha$ ($h\nu = 1253.6$ eV) anode is used (with the exception of chapter 3, see section 2.1.3). XPS data were recorded with an angle of emission 15° off-normal, in medium magnification mode with an iris diameter of 15 mm, $E_{\text{pass}} = 16$ eV or 30 eV for detail and overview spectra, respectively. A few spectra in this thesis were acquired with a pass energy of 30 eV using an older hemispherical analyzer (Specs EA10 plus) previously mounted to the same chamber. (These spectra are marked in the figure caption.) The whole system is suspended on springs for vibration damping.

For all STM measurements in the RT- and the LT-STM chamber, etched W tips were used, cleaned by Ar^+ sputtering and conditioned by voltage pulses on a Au(110) crystal. All STM images showing atomic lattices or well-ordered superlattices were corrected for piezo drift as described in Ref. 43.

2.1.2 Low-Temperature STM Chamber - "LT-STM"

This UHV system consists, similar to the system described above, of two UHV chambers that are connected via a gate valve. One chamber is meant solely for low-temperature STM and houses an Omicron LT-STM cooled by a bath cryostat for LN_2 or LHe cooling; the base pressure is below 1.5×10^{-11} mbar. During the measurement the sample was cooled to 78 K (LN_2 temperature) unless otherwise stated. The second chamber, a combined preparation and analysis chamber, contains a sputter gun and an electron-beam heating stage for cleaning samples, LEED optics (Specs ErLEED), as well as a hemispherical electron analyzer (Specs Phoibos 100, 5 channel setup, no iris) for XPS measurements. In this thesis, only the STM is used. The base pressure of the second chamber is 4×10^{-11} mbar.

2.1.3 TPD Chamber

Temperature-programmed desorption (TPD) and x-ray photoelectron spectroscopy (XPS) measurements were performed in a μ -metal UHV chamber described in all details elsewhere. [51] This system features a LHe flow cryostat (Janis ST-400), which can cool the sample to ≈ 20 K. The base pressure in the chamber was below 10^{-10} mbar. Typically, samples are mounted on special sample plates that are then connected to the cryostat. For the measurements presented in chapter 3, a Pt₃Zr(0001) single crystal (6 mm diameter) was wrapped with Ta ribbons at the circumference; these were spot-welded to thicker Ta wires leading directly to the cryostat to ensure good thermal contact. A K-type thermocouple was spot-welded directly to the backside of the crystal for accurate temperature measurements, and no sample plate was used. The chamber includes a molecular-beam setup for precise gas dosing with a sharp top-hat profile in a circular area with a diameter of 3.2 mm [51]. This allows us to perform TPD and XPS measurements with water sticking exclusively to the center of the crystal surface; there is no influence from water on the Ta ribbons or from the edges of the crystal. Furthermore, the molecular beam provides accurate gas doses. Since the sticking coefficient equals unity at low temperatures, the coverage can be given in monolayers defined as molecules per Zr atom in the oxide film. For XPS, a monochromatised Al K α (1486.7 eV) x-ray source was used in combination with a SPECS Phoibos 150 hemispherical analyzer (nine channels). All XPS measurements were done at 100 K and in normal emission, medium area mode and $E_{\text{pass}} = 20$ eV. TPD measurements were conducted using a HIDEN HAL 3F PIC quadrupole mass spectrometer. Samples were cleaned by Ne⁺ sputtering and annealing.

2.2 UHV-compatible Zirconium Sputter Deposition Source

This chapter is based on a published article, Ref. 50. The chapter, however, contains additional data and information.

2.2.1 Motivation

Growth of (ultra-)thin films for surface-science experiments in an ultrahigh-vacuum (UHV) environment is usually performed by evaporation, using resistive heating for low to medium temperatures and electron-beam evaporation for materials that require high temperatures for evaporation. For materials that reach a sufficiently high vapor pressure below or at the melting point, electron-beam evaporation from a rod is the method of choice, having the advantage that the material is not in contact with anything that could be a source of contaminations. Other materials require temperatures well above the melting point for sufficient vapor pressures. When the end of a rod gets heated to such a high temperature, a droplet would form and detach from the rod. Thus, such materials (e.g., Al, Au, Sn, Pb) are usually evaporated from crucibles. This requires that the material must not react with the crucible at high temperatures. The crucibles of large electron-beam evaporators (kilowatt range) can be cooled while the melt is at higher temperatures, but this is not the case for the small evaporators typically used in surface science, where the electrons impinge on the crucible, not the melt. Zirconium is a particularly notorious material for evaporation; it has a vapor pressure of only $\approx 4 \times 10^{-5}$ mbar at the melting point (≈ 1850 °C), corresponding to evaporation of about two monolayers (ML) per second; the deposition rate at the substrate is typically lower by four orders of magnitude. Thus, evaporation from rods is very slow. Zr forms eutectic alloys with the refractory metals Mo, Ru, Ta, W, Re, and Ir, which precludes the use of metal crucibles. Zr also reacts with graphite crucibles. Fortunately, these problems are not relevant for sputter deposition.

In many cases, a further advantage of sputter deposition, compared to evaporation, is better layer-by-layer growth of the films. One reason for improved growth is the higher kinetic energy of the sputtered atoms (few eV compared to sub-eV for evaporated atoms) and also the presence of other energetic particles during sputter deposition [52]. Compared to evaporation, additional advantages of sputter deposition are the possibility to grow compounds with the film composition being close to that of the sputter target, and better stability and reproducibility of the deposition rate compared to most UHV evaporators.

Conventional magnetron sputter sources using a gas discharge typically operate at pressures between 10^{-3} and 10^{-2} mbar and deposition rates of nanometers per second, which is hard to reconcile with UHV surface-science experiments. A way out

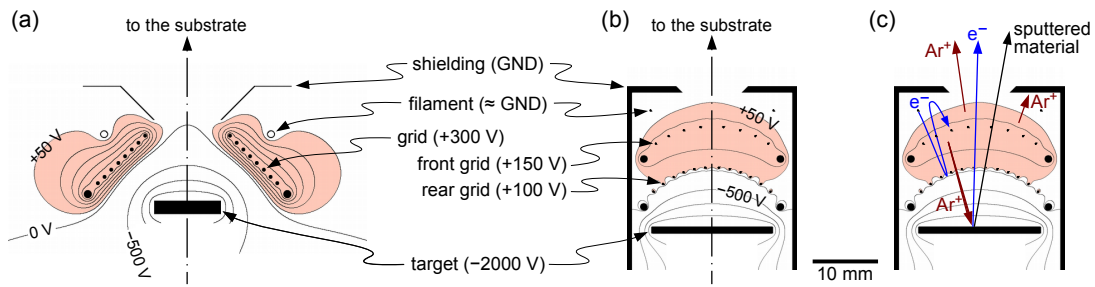


Figure 2.1: Cross sections and equipotential lines (ignoring space-charge effects) of (a) the original sputter source design by Mayr *et al.* [53, 54] and (b) the design presented in this work. Schematic particle trajectories are shown in (c). The light-red shading shows the region where the electron energy exceeds 50 eV; this is roughly the volume where efficient ionization of Ar is possible. Equipotential lines are drawn in 50 V intervals for positive and 500 V intervals for negative voltages.

is using a standard UHV-type ion source for sputtering and collecting the sputtered material at the substrate [52, 55, 56]. This technique is sometimes referred to as ion-beam sputter deposition (IBSD) and requires a special setup of the vacuum chamber. To circumvent the rather low deposition rates achieved with standard (electron-impact ionization) UHV ion sources, high-current ion sources such as duoplasmatron or Kaufman sources can be used [55, 56]. A much simpler approach is a dedicated UHV-compatible sputter deposition source, as recently designed by Mayr *et al.* for deposition of Zr [53, 54]. This source was also found to be useful for oxides, e.g. ZrO_2 or YSZ (yttria-stabilized zirconia). As there is no gas discharge involved, this type of deposition source can be operated at much lower Ar pressures than magnetrons.

The design by Mayr *et al.* [53] comprises a filament at ground potential emitting electrons with a current of ≈ 150 mA and a grid at +300 V collecting the electrons. When the vacuum chamber is backfilled with Ar, Ar^+ ions created by electron-impact ionization are accelerated onto the sputter target biased at -2 keV. At an Ar pressure of 10^{-4} mbar, an ion current of 50–100 μA at the target was obtained [53]. A closer analysis of the design reveals, however, that the electron cloud ionizing the Ar gas [light red in Figure 2.1a] is mainly at the front side of the grid, where the filament is placed, and at the periphery. The Ar^+ ions generated there bombard the shield at the top side of the sputter source and the surrounding vacuum chamber, which may cause deposition of unwanted material onto the substrate and target as well as desorption of molecules into the residual gas. The maximum kinetic energy of the Ar^+ ions, when impinging on grounded surfaces, is given by the grid voltage

(300 eV). At the other side of the grid, facing the target, the electrons are repelled by the negative high voltage of the target, so ionization is possible only in a rather small volume close to the grid. Ar^+ ions created at this side of the grid near the axis are accelerated to the target for sputtering (the desired effect). It should be noted that the number of ions impinging near the target center could be optimized by placing the target somewhat further away from the grid than shown in Figure 2.1a; the design in Figure 2.1a is a compromise between optimum sputtering and sufficient heating of the target by thermal radiation from the filament (which is required for sputtering of materials that are insulating at room temperature, such as YSZ) [57].

2.2.2 Description of the Source

Two-Grid Design

The problem of only a small fraction of the ionized Ar impinging onto the target can be avoided by using our new design, which features two grids instead of one. The design is shown in Figure 2.1b; grids are thin dots in the cross section, only the grid holder rings appear as thick dots. In the region between the two grids, the electric field directs Ar^+ ions in the direction towards the target, and the concentric shape of the grids ensures good focusing onto the central area of the target. Nevertheless, some Ar^+ ions are also created at the other side of the front grid; these ions bombard either the housing of the source or the substrate, yet only at a maximum energy set by the front grid voltage, see Figure 2.1c. Compared to the original one-grid design [53], the efficiency of the two-grid source is significantly better: With grid voltages of +300 and +200 V for the front and rear (target-side) grid, respectively, a target current of $66 \mu\text{A}$ can be achieved with an emission current of $22 + 12 \text{ mA}$ (values at the front and rear grid, respectively). This is roughly a quarter of the emission current needed for the same ion current in the one-grid design, at a much lower Ar gas pressure in the UHV system. We used a pressure of $9 \times 10^{-6} \text{ mbar}$ Ar in the vacuum chamber. As the Ar leak valve is connected to the inside of the source housing, the pressure in the source is 27 times higher, about a factor of 2–3 above the pressure used by Mayr *et al.* ($\approx 10^{-4} \text{ mbar}$ in the UHV chamber, equal to the pressure in the source [53]). The ratio of source and chamber pressures can be determined either from the ratio between the pumping speed and conductance of the orifice or from comparing the target current with Ar supplied to the source and that obtained by backfilling the

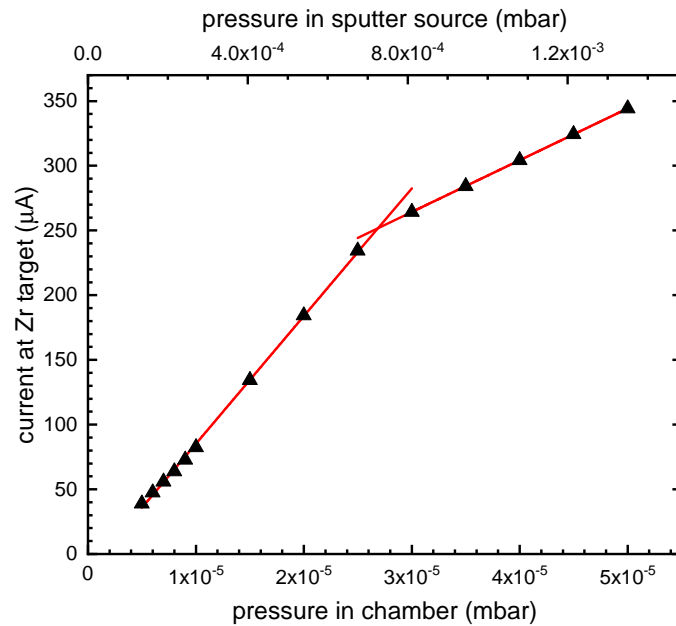


Figure 2.2: Dependence of the sputter current at the Zr target on the Ar pressure. Above 2.5×10^{-5} mbar, the efficiency decreases, see fitted lines.

chamber with Ar from a leak valve not connected to the source. These two values agree very well ($< 3\%$ difference).

We can also use lower grid voltages of +150 and 100 V, as shown in Figure 2.1b. This requires a higher filament current (2.4 A through a 0.15 mm diameter W wire) and yields a target current of $66 \mu\text{A}$ at 27 mA emission current (thereof 18 mA into the front grid and 9 mA into the back grid). At these conditions, the total power dissipated by electron impact on the grids is only 3.6 W, compared to 45 W in the original one-grid design. We have also tried higher gas pressures and found that the ion current is proportional to the Ar pressure up to $\approx 2.5 \times 10^{-5}$ mbar (corresponding to $\approx 7 \times 10^{-4}$ mbar in the source), see Figure 2.2; at higher pressures, the efficiency (ion current at the target per emitted electron and gas pressure) decreases. We could not determine the exact reason for this behavior; possibly it is related to the space charge of the ions, i.e. the charge of the ionized gas starts having a significant influence on the potential landscape.

Design Details

The source region is enclosed by a housing cooled with liquid nitrogen (LN_2). With deposition of reactive metals (such as Zr) on the inner walls, there is also some pumping of reactive residual-gas molecules (similar to a titanium sublimation pump), which helps to ensure optimum purity of the films deposited. For less stringent purity requirements, the source could also be cooled by water. The housing has the shape of a tube with 24 mm inner and 36 mm outer diameter, made of a CuCrZr alloy (CW106C) with good thermal conductivity (Figure 2.3). At the outside, this housing has a groove tightly fitting a stainless steel tube with 8 mm outer diameter (OD) for cooling [Figure 2.3a]; a concentric inner tube (3 mm OD) transports the LN_2 to the closed end of the 8 mm tube. The source housing is pressed against the LN_2 -cooled tube; this tube also serves as support rod to fix the source on the base flange. Tests of a similar design revealed however that the heat conduction between steel tube and housing is not sufficient to cool the housing if a filament is run at even higher power. A possible solution would be to add a thin Sn foil between tube and housing, and melt it by running the source without cooling until $\approx 200^\circ\text{C}$. It would be desirable to add an additional thermocouple to the sputter source design to determine the temperature of the housing. The end plate of the source at the front side has a 9 mm hole (orifice for the sputtered material). The back plate contains a high-voltage feedthrough for the target voltage and the Ar gas inlet, connected by hydraulically formed bellows to the weld in the base flange where the tube from the leak valve enters.

The filament is a loop of 0.15 mm W wire, spot welded to the supply wires (0.8 mm Ta); the negative terminal of the filament supply is at ground potential. The grids have the shape of spherical caps, with the center of curvature roughly in the center of the target, to focus the Ar^+ ions to the target center [see the bright erosion spot in the center of the target in Figure 2.3a]. This yields a uniform deposition rate on the substrate, without vignetting. The grids are made from 0.175 mm W wire spot-welded onto rings (≈ 20 mm outer diameter) made from 0.8 mm Ta wire. A previous attempt to make the rings from stainless steel was unsuccessful; at high power (+300 V at the front grid), the steel ring got hot enough to soften and deform, finally touching the housing of the source. The rings of the grids are held by fork-like arms (three per grid); these protrude through the source housing and are held by ceramic insulators

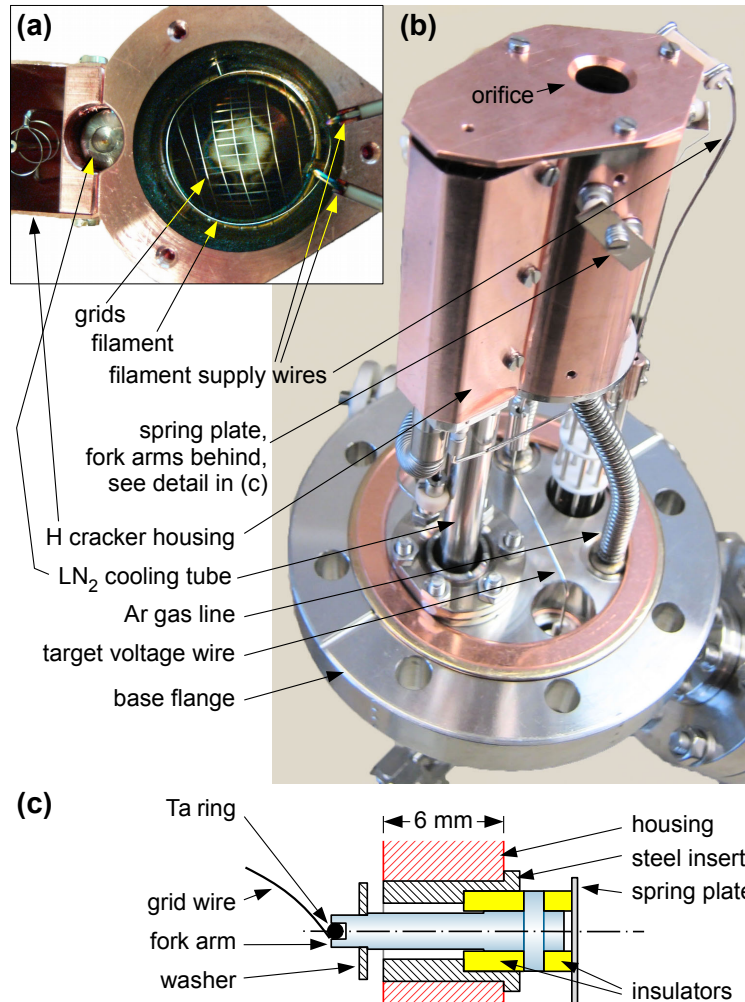


Figure 2.3: (a, b) Photos of the sputter source (the hydrogen cracker also seen is unrelated to the function of the sputter source). (a) Front view with the top cover removed; note the bright eroded spot in the middle of the otherwise dark target, where the Ar⁺ ions are focused to (visible behind the grids). (c) Cross section through the housing at the position of one of the insulated fork arms holding a grid.

[Figure 2.3c]. Washers protect the insulators from sputtered material scattered by the Ar gas. For mounting the grids inside the housing, the grids have to be temporarily held in position from the open end of the source housing, then the forks are inserted radially from the outside. Spring plates (one of them marked in Figure 2.3) prevent the forks from sliding back. For Zr deposition, the target is a disk of Zr metal (diameter 18 mm, thickness 1 mm) with 99.9% purity (HMW Hauner, Germany). The target was spot welded to a support rod at its back side; the rod is held by the high-voltage feedthrough in the back plate of the source housing.

While the sputter source is typically maintenance-free for long periods of time, usually many months, a few problems are known to occur. Apart from breaking filaments, the two grids can get shorted – to ground, typically. The reason for this are flakes of sputter-deposited Zr detaching from the housing. These flakes can often be removed without breaking vacuum by repeatedly applying high voltages to the grids. If this is not successful, the source has to be removed from the chamber. As assembly and disassembly is tiresome, one can first try removing the flakes by mechanical force: A wire can be carefully inserted between grids and housing to remove flakes. Applying high voltages in air can also help by burning away Zr flakes. It is furthermore suggested to scratch deposited Zr off the housing walls every time the source is accessible to prevent said problems; the resulting flakes can then be removed by gently knocking the sputter source against a hard object while turned upside down.

The source is placed on a DN63CF base flange (4.5” outer diameter). The base flange has DN16CF (1.25” outer diameter) ports for the electrical feedthroughs, the LN₂ tube and the Ar gas. As the source is rather compact (yet too spacious for a DN40CF flange), there is enough space for further components on the same base flange. We have added a hydrogen cracker similar to Refs. 58, 59; the housing of the H cracker is cooled together with the sputter source. In addition, for future extensions, there is some space for mounting further sources, e.g. tiny crucibles for evaporation, at the sides of the sputter source (to make space, two sides of the source housing are milled flat, as visible in Figure 2.3a).

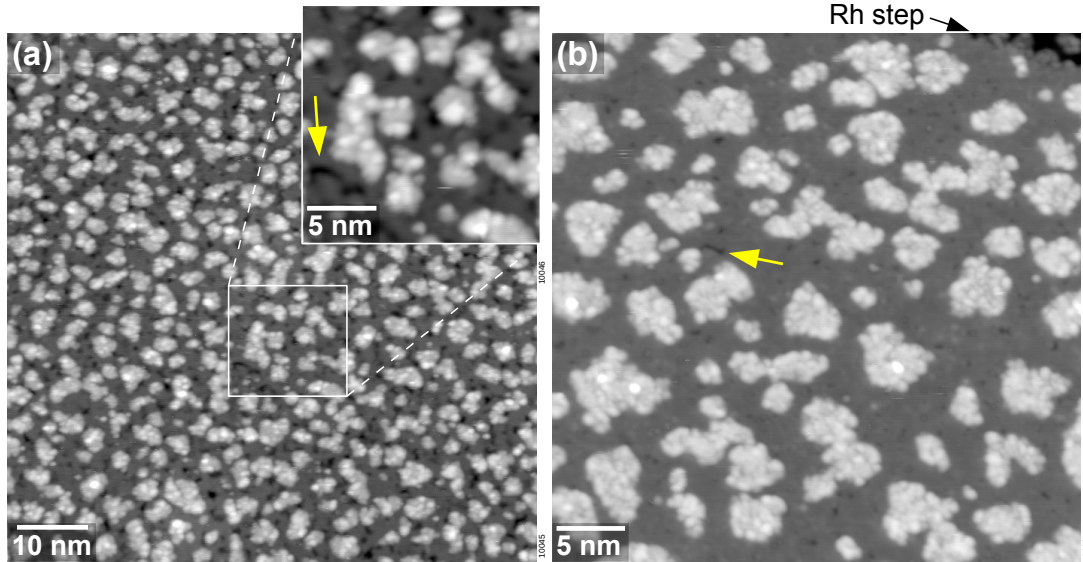


Figure 2.4: STM images of a Rh(111) surface after deposition of 0.35 ML of Zr with front/rear grid voltages of (a) 300 V/200 V and (b) 150 V/100 V. Vacancy islands appear as small black patches in the images, examples are pointed out by yellow arrows. The sputter damage can be reduced drastically by reducing the grid voltages.

2.2.3 Evaluation of the Source

Deposition Rate

We can calculate the deposition rate F from the source by assuming a cosine (Lambertian) angular distribution of the sputtered atoms. Assuming an incident ion current I_{sp} , a sputter yield Y , and r being the distance between the target and the substrate, we obtain

$$F(r) = \frac{I_{sp}Y}{r^2\pi|e|} = \frac{I_tY}{r^2\pi|e|(1+\gamma)} \quad (2.1)$$

for emission perpendicular to the target, which is the direction to the substrate (Figure 2.1). The charge of the ions is $|e|$, and the factor $(1 + \gamma)$ in the denominator of the last term accounts for the fact that the measured target current I_t is higher than that of the incident ions (I_{sp}) due to ion-induced electron emission, with γ being the electron yield upon ion impact. Equation (2.1) neglects the effects of resonant neutralization of fast Ar^+ ions by collisions with neutral Ar. This is justified when considering the short path of the Ar^+ ions (1–2 cm). With a target current of $66 \mu\text{A}$, $r = 50 \text{ mm}$, $Y = 1.15$ (for $2 \text{ keV Ar}^+ \rightarrow \text{Zr}$, Ref. 60), and γ in the range of 0.1–0.2 (consistent with the measured electron current at the substrate, see below), Eq. (2.1) yields a deposited flux F between 5 and 5.5×10^{12} atoms per cm^2 and second.

Since the deposition rate determined with a quartz crystal microbalance (QCM) is not very accurate in this case (see below), we have determined the deposition rate by submonolayer growth of Zr on a well-defined single-crystal substrate, Rh(111), and determined the area covered by Zr islands by scanning tunneling microscopy (STM). For an example of such a depositon, see Figure 2.4. (The choice of Rh(111) is arbitrary – any well defined single crystal on which Zr grows two-dimensionally can be used.) To determine the deposition rate from the Zr-covered area A_{Zr} , we assume that the density of Zr atoms σ_{Zr} in the islands is equal to that in the basal plane of Zr, $1.11 \times 10^{15} \text{ cm}^{-2}$. A simple calculation of the deposition rate

$$F(\text{substrate}) = \frac{A_{Zr}/A_{STM} \times \sigma_{Zr}}{t_{\text{dep,Zr}}}, \quad (2.2)$$

with the deposition time $t_{\text{dep,Zr}}$ then yields $4.5 \times 10^{12} \text{ cm}^{-2}\text{s}^{-1}$. Considering the uncertainty of the sputter yield and the angular distribution, the agreement with the value of $5.5 \times 10^{12} \text{ cm}^{-2}\text{s}^{-1}$ (calculated from Eq. 2.1) must be considered excellent. As the quantities in Eq. 2.1 are not expected to change with time, this also indicates that the sputter source should have excellent stability of the deposition rate, which perfectly agrees with our experience (provided that the sputter target is sufficiently clean, which is usually the case after several minutes of operation). The deposition rate was found to also remain unchanged when the source is operated at an additional oxygen partial pressure of 10^{-6} mbar for growing ZrO_2 films (we monitored the reproducibility of the deposition rate by checking for completion of the 5th ZrO_2 layer with STM; this should be accurate within a few percent).

To calculate the deposition time for a certain amount of (cubic) ZrO_2 -monolayers, one simply has to take the number of Zr-atoms per zirconia monolayer $\sigma_{Zr(\text{ZrO}_2)}$ and cm^2 and divide by the deposition rate:

$$t_{\text{dep,ZrO}_2} = \frac{\sigma_{Zr(\text{ZrO}_2)}}{F(\text{substrate})}, \quad (2.3)$$

with $\sigma_{Zr(\text{ZrO}_2)} = 8.91 \times 10^{14} \text{ cm}^{-2}$ per zirconia layer, assuming a Zr-Zr distance of 360 pm. The typical deposition time for a 5 ML-thick zirconia film is ≈ 17 min.

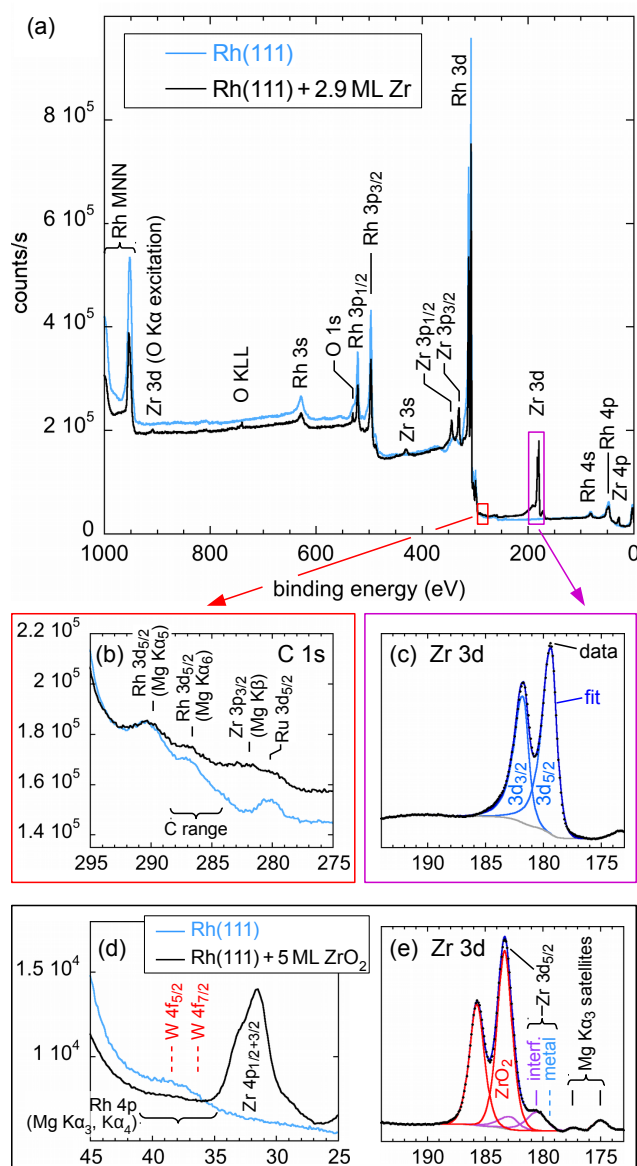


Figure 2.5: (a–c) XPS of a clean Rh(111) surface and after deposition of 2.9 ML (0.74 nm) Zr. (a) Overview spectrum. The C 1s region (b) was measured with high sensitivity; the range of typical carbon impurities (adventitious carbon and species with C–O bonds) is indicated. The detailed spectrum of the Zr 3d range (c) shows only metallic Zr (Zr 3d_{5/2} at 179.4 eV) as indicated by the fit; a slight shoulder to the left, if any, has very low intensity. Spectra obtained after Zr deposition in 10^{−6} mbar O₂ [1.0 nm Zr corresponding to 5 ML ZrO₂(111)] show (d) the absence of (oxidized) tungsten and (e) only oxidic Zr peaks. Analyzer pass energy (a) 20 eV (b) 50 eV (for increased count rate); in all other spectra 16 eV.

Purity of the Films

Figure 2.5a–c shows x-ray photoelectron spectra (XPS) of a clean Rh(111) surface and immediately after deposition of 2.9 ML Zr with the sputter source taken in the RT chamber, see section 2.1.1. We define 1 ML as the areal density of Zr in the basal plane ($1.11 \times 10^{15} \text{ cm}^{-2}$). The Rh(111) substrate was at room temperature during deposition, as is the case for all depositions discussed in this thesis. The only impurity detectable is a small amount of oxygen, probably from oxygen implanted into the Zr target or dissolved there during many previous experiments at 10^{-6} mbar O_2 for growing ZrO_2 films. The C 1s region does not show any indication of carbon-containing impurities; the small peaks found in this range after Zr deposition are due to excitation of stronger lines by satellite lines of the x-ray source, as well as Ru, which is an impurity in our Rh substrate [Figure 2.5b]. Zooming in onto the Zr 3d lines shows only metallic Zr peaks [Figure 2.5c]. The Zr $3d_{5/2}$ binding energy of 179.4 eV is slightly higher than usually reported for pure Zr bulk (178.7–178.9 eV). We attribute this peak shift partly to the surface core level shift, which is about half an eV to higher BE for close-packed surfaces of the early 4d transition metals. [61,62] A further contribution will come from interaction of Zr with Rh at the interface, as Zr $3d_{5/2}$ energies of ≈ 179.6 eV are found for Zr alloys with Pt (Pt_3Zr [42]). To some degree, the shift may be also related to interaction with oxygen impurities. In addition, curve fitting cannot exclude an extremely weak shoulder to the left (Zr $3d_{3/2}$ at 184–184.5 eV, corresponding to $3d_{5/2}$ at ≈ 182 eV), possibly also related to oxygen: Ultrathin and bulk-like ZrO_2 would have the Zr $3d_{5/2}$ peaks at 180.7, see chapter 5.2.3 and [42], and between 181.6 and 183.4 eV, respectively, see chapter 4.4.

Figure 2.5d,e shows spectra obtained after Zr deposition on Rh(111) at an additional oxygen partial pressure of 10^{-6} mbar. At these conditions, a ZrO_2 film grows, but without post-annealing the oxide is poorly ordered. The main peak at 183.3 eV is from ZrO_2 (typical for slightly reduced tetragonal zirconia, see chapter 4.4). There is also a minor peak at 180.4 eV, which decreases with increasing film thickness, thus it must come from Zr at the interface. As this peak does not disappear upon annealing under oxidizing conditions, we attribute it to ZrO_2 , not to a lower oxidation state of Zr, in agreement with DFT calculations that predict a lower Zr 3d binding energy at the ZrO_2 -metal interface [42]. This assignment is confirmed in chapter 4.4. The spectrum shows no metallic Zr. Mayr *et al.* have reported that their source, when operated

with O_2 in the background gas, can lead to tungsten and tantalum impurities in the films, presumably from formation of volatile oxides on the filament and grid materials (W and Ta, respectively; due to the high power these grids get very hot) [53]. We also checked for tungsten impurities coming from the filament or grid wires (in our source, both are W). Figure 2.5d shows no indication of any W signal at the positions where it was observed by Mayr *et al.* (dashed lines in the figure). W would show a sharp doublet there, superimposed on the broad Rh 4p Mg $K\alpha_3 + K\alpha_4$ satellite, thus we can exclude such a problem for our source.

Ar⁺ Ion and Electron Emission

Apart from sputtered target material, two types of particles are emitted from the source [Figure 2.1c]: Ar⁺ ions and electrons. As mentioned above, Ar gas ionized in the region above the front grid will not be accelerated towards the target but rather to the end plate with the orifice or through the orifice, towards the substrate. These ions can sputter material from the inside of the source housing onto the target. Fortunately, after short operation of the source, all the inside of the housing is covered with target material, so there is no contamination of the target by wall material. Some Ar⁺ ions (with energies in eV up to the voltage of the front grid) also reach the substrate; these Ar⁺ ions will lead to mild sputtering of the target. Indeed, in our calibration experiments with sputter deposition of Zr onto well-prepared Rh(111) single crystals, we have observed the formation of vacancy islands in the Rh surface. The scanning tunneling microscopy (STM) images in Figure 2.4a show the vacancy islands as small black patches. These vacancy islands can be explained only by sputtering of the sample, which happens in addition to the deposition of sputtered target material (Zr). In some cases, this effect can be desired (ion-beam assisted deposition, IBAD) [52, 63]. Impingement of particles with energies above ≈ 150 eV leads to an increased density of nuclei, which can promote layer-by-layer growth in some cases [64]. A disadvantage of mild sputtering is reduced accuracy of the deposition rate due to mass removal. When growing oxides or compound materials, preferential sputtering will also alter the composition of the film. For the experiment shown in Figure 2.4a, the grid voltages were 300 and 200 V for the front and rear grid, respectively (Ar⁺ energies up to 300 eV). We usually choose grid voltages of 150 and 100 V. In this case, the sputter yield Y at the maximum ion energy (150 eV) is sufficiently

low to avoid these problems (e.g., $Y \approx 0.34$ for $150 \text{ eV Ar}^+ \rightarrow \text{Rh}$, Ref. 60). This is also seen in Figure 2.4b, where only very few and small vacancy islands are found.

The sputter deposition source also emits electrons, which are liberated by ion impact at the target, see Figure 2.1c. These electrons are accelerated to 2 keV by the target voltage. Quantification of the electron current on the substrate is not easy, because only the sum of the electron and Ar^+ ion current can be measured; the emission of secondary electrons upon 2 keV-electron impact at the substrate further complicates the problem. The substrate current is given by

$$I_{\text{substr}} = I_{\text{ion}} + I_{\text{el}}(1 - \delta) \quad (2.4)$$

where δ is the secondary electron yield for electron impact at the substrate (due to the low ion energies, ion-induced electron emission from the substrate can be neglected). We have studied this effect with a Pt(111) single crystal serving as substrate. In the initial phase of the deposition, while the substrate was essentially uncovered, we have measured a substrate current of $I_{\text{Pt}} = 2.2 \mu\text{A}$; with increasing Zr coverage it was found to decrease to $I_{\text{Zr}} = -1.2 \mu\text{A}$. With these two values, and $\delta = 1.22$ (0.51) for Pt (Zr) at 2 keV [65], we obtain an electron current of

$$I_{\text{el}} = -\frac{I_{\text{Pt}} - I_{\text{Zr}}}{\delta_{\text{Pt}} - \delta_{\text{Zr}}} \approx -4.8 \mu\text{A} \quad (2.5)$$

and an ion current of $\approx 1.1 \mu\text{A}$. Eq. (2.5) contains the difference between two secondary electron yield values δ , which are not known with high accuracy; the exact value of δ may also depend on the crystallographic properties of the material and electron scattering in the layers below (Pt single crystal and Zr thin film in our experiment vs. δ values of polycrystalline material in the literature). Thus, some uncertainty of the electron current is to be expected. This uncertainty has a significant impact on the ion current, which is calculated as the difference of two larger quantities according to Eq. (2.4). We have also tried to determine the secondary electron yields with a 2 keV electron source from the difference between the sample current with and without a positive 30 V sample bias, yielding $\delta_{\text{Pt}} = 1.82$ and $\delta_{\text{Zr}} = 0.68$. These values would result in $I_{\text{el}} = -3.0 \mu\text{A}$, but an (non-physical) negative ion current ($-0.2 \mu\text{A}$). Thus, the ion current cannot be determined with reasonable accuracy by this method. Based on the sputter damage observed by STM, we estimate that the ion current is actually

in between these two values; i.e. a few tenths of a μA .

Due to the high kinetic energy of the electrons, they dissipate a power of ≈ 10 mW at the substrate. This is not an issue for most substrates, but it affects the reading of a quartz crystal microbalance used to determine the deposition rate. In our experience, with standard AT-cut 6 MHz quartz crystals used for thin-film deposition monitors [66] and a water-cooled crystal holder, the time for equilibration (until a stable deposition rate is displayed) is about 10–20 min for thermal evaporation, but about an hour with the sputter deposition source (SC-cut quartz crystals, which are also used for sputter yield measurements [67], are less sensitive to thermal stress and would perform better). In our experience, even after equilibration the QCM readings scatter by more than 10%. We rather rely on the deposition rate determined once (months ago) from the coverage determined by STM, see above. To ensure best reproducibility each time, we adjust the Ar gas pressure to get the same target current. In other words, the reproducibility of the deposition rate of the sputter source (estimated to be better than a few percent over several months, including several bakeout cycles of the UHV system) is better than that of the QCM readings.

In case that electron or ion emission cause a substantial problem, it would be possible to add an extra electrode at the orifice to repel or deflect these charged species. If the position of the front end of the source is constrained by having to avoid collisions with the sample holder, this would slightly increase the target-to-substrate distance and thereby reduce the deposition rate. If the substrate can be biased, this would provide another possibility to repel either electrons or ions (at the cost of increased kinetic energy of the other species).

2.2.4 Parameters for ZrO_2 Thin Film Growth

For ZrO_2 deposition, zirconium was sputter-deposited on the clean substrate at RT in a mixed Ar/ O_2 atmosphere ($p_{\text{Ar}} = 8 \times 10^{-6}$ mbar, $p_{\text{O}_2} = 1 \times 10^{-6}$ mbar). We chose rather gentle operating conditions with Ar^+ energies below 150 eV (grid voltages of 150 V and 100 V for the front and rear grid, respectively, unless noted otherwise). The amount of deposited material was calibrated by deposition of metallic Zr and measuring island areas with STM, see section 2.2.3; the coverage was reproducible within 0.1 ML, see above. We give the thickness in ZrO_2 monolayers (ML), with one O–Zr–O repeat unit of c- $\text{ZrO}_2(111)$ defined as one monolayer, which corresponds to

$\approx 9 \times 10^{18}$ Zr atoms/m² or ≈ 0.3 nm thickness.

The as-deposited films were not fully oxidized and were therefore post-annealed for 10 min in O₂ ($p_{\text{O}_2} = 5 \times 10^{-7}$ mbar) at temperatures of at least 550 °C. In most experiments the post-annealing temperatures were such that a continuous but well-ordered film was obtained at the given film thickness; at higher temperatures and low film thickness (≤ 3 ML), holes down to the Rh substrate appeared, see chapter 4.2.

2.2.5 Conclusions

We have presented a sputter deposition source optimized for growth of clean films in ultrahigh vacuum. Compared with the design by Mayr *et al.* [53], the source operates at more benign values of filament and emission current and lower Ar gas pressures in the UHV chamber for comparable target current and deposition rate. If desired, higher deposition rates could be achieved by increasing the gas pressure or emission current. The source also features excellent long-time reproducibility and the films grown show very high purity. During deposition, the substrate is subject to a flux of both electrons and low-energy Ar⁺ ions. The energy of the latter can be controlled by the grid voltages, so the source provides the possibility of either ion-beam-assisted deposition or negligible sputtering of the substrate and films by Ar⁺ ions. Apart from materials that are difficult to evaporate in UHV (such as Zr), due to the high purity of the films grown we consider our source a good choice also for many other materials, especially when considering the advantages of sputter deposition mentioned in section 2.2.1.

2.3 Experimental Techniques

2.3.1 Scanning Tunneling Microscopy

STM was developed by Binnig and Rohrer [68] as a surface imaging technique with atomic resolution. It has since revolutionized the basic understanding of surfaces and all connected phenomena, including material growth, chemical reactions, catalysis, and others. STM is based in its principles on the quantum tunneling effect. A sharp metal tip, typically electrochemically etched from W, is mounted on a scanner for

x-, y-, and z-movement with piezo elements. (In some setups, the sample is moved.) The STM setup is completed by electronics which control movement and record the tunneling current. The whole setup is shown in Figure 2.6. For tunneling, the tip is approached to few Å above a conductive surface. For the beginning, let us imagine a one-dimensional case. The electron wave function in the vacuum between tip and surface is given by the solution of Schrödinger's equation

$$\Phi(z) = \Phi(0) \cdot e^{-z \cdot \overbrace{\sqrt{2m(V-E)/\hbar}}^{\kappa}}, \quad (2.6)$$

with z being the distance from the surface, V the vacuum potential, and E the electron energy (which is assumed to be smaller than V). The STM current is then proportional to the tunneling probability P :

$$I_t \propto P \propto |\Phi(d)|^2 \propto e^{-2\kappa d} \quad (2.7)$$

The tunneling current therefore depends exponentially on the tip-sample distance d , which gives STM a pm resolution in z -direction. To measure a current, a voltage is applied between tip and sample, and electrons tunnel between electronic states of the tip to the sample or vice-versa, depending on the sign of the applied voltage. The tunneling probability, and therefore the tunneling current, thus depends on the availability of states to tunnel into. As a result, STM probes both the tip-sample distance (topology) and the local density of states (LDOS) at the same time. Heights measured by STM are always “apparent” heights, combining the influence from both sources. If at a certain bias no states are available for electrons to tunnel into, no current can flow.

For a 2D image of the surface, the tip is moved line by line over an area, typically $10 \times 10 - 400 \times 400 \text{ nm}^2$. When moving the tip over the surface, both the tip-sample distance and the local density of states (LDOS) below the tip can change. There are two measurement modes: Constant height and constant current. In the first case, the height of the tip is held constant and the changes in the tunneling current are recorded, giving an image. In the second case, the current is kept constant by adjusting the height of the tip via a feedback loop. The image is then created by plotting the tip movements in z -direction, which give the apparent height. All STM images in

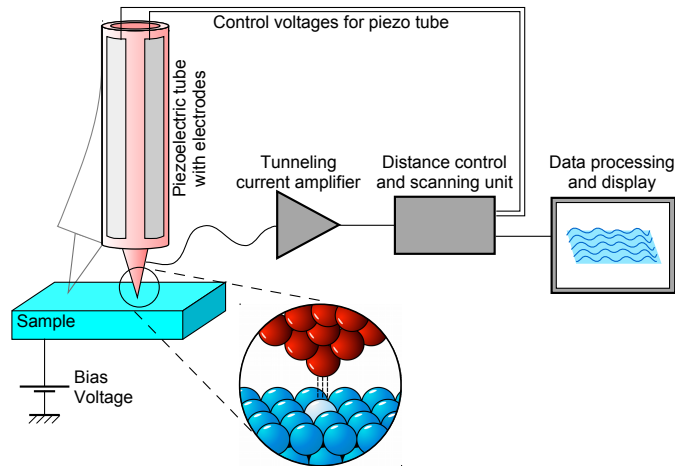


Figure 2.6: Setup of a Scanning Tunneling Microscope [69]

this thesis were recorded in constant current mode. Sample voltages are given with STM images, thus positive voltages refer to tunneling into the unoccupied states of the surface.

2.3.2 X-ray Photoelectron Spectroscopy

In XPS, the sample is irradiated by — ideally monochromatized — x-rays. These lead to ionization of the core level states; the resulting photoelectrons and Auger electrons (see section 2.3.3) are then measured with an electron energy analyzer. Simply speaking, the kinetic energy of the photoelectrons E_{kin} measured at the analyzer is a function of the binding energy E_{B} , photon energy $h\nu$, and the work function of the analyzer Φ :

$$E_{\text{kin}} = h\nu - E_{\text{B}} - \Phi \quad (2.8)$$

In the case of a measurement, the Fermi energies of analyzer and sample are aligned and used as a reference for E_{kin} . Φ is calibrated when setting up the analyzer. Therefore, the binding energy can be extracted directly. As E_{B} is element-specific, XPS is used for elemental analysis. The binding energy is influenced by the chemical surrounding of the element, e.g. chemical bonds to other atoms (a so-called chemical shift) or atoms located in the top-most surface layer (surface core level shifts). Further possible shifts are discussed in detail in chapter 4.4.

In reality, not the true binding energy of the core level is measured, as the ionization influences the energy levels. This can not only shift the main line in the recorded spectra, but can also lead to additional, separated lines above and below the main line, so-called shake-up and shake-down lines. Additionally, electrons ionized from other than the main x-ray line can be encountered when measuring with non-monochromatized radiation. For Mg $K\alpha$, these are Mg $K\alpha_{III}$ ($E_B - 8.4$ eV), $K\alpha_{IV}$ ($E_B - 10.1$ eV), $K\alpha_V$ ($E_B - 17.6$ eV), $K\alpha_{VI}$ ($E_B - 20.6$ eV), and $K\beta$ ($E_B - 48.7$ eV) [70]. In our RT-STM setup, an impurity line from O $K\alpha$ ($E_B + 728.7$ eV) is also encountered.

A freed electron must travel through the material to the surface; the longer the travelled distance, the higher the probability of an inelastic scattering event. All electrons that lost kinetic energy before arriving at the analyzer do not contribute to the line originating from electrons that only scattered inelastically – they only raise the background. The typical path that an electron can travel before it loses energy is the inelastic mean free path (IMFP). The IMFP is – nearly independent of the material – around 5–15 Å, so roughly 5 layers of material, depending on E_{kin} . At normal emission, the intensity from energy loss-free electrons originating from a depth equal to the IMFP is reduced by 1/e. Spectroscopic methods relying on electrons are therefore inherently surface-sensitive.

Measured lines are not infinitely sharp, but appear as peaks of certain width (measured as the full width at half of the maximum intensity, FWHM) and shape. The peak shape and width are influenced by the analyzer, the ionizing radiation, and the electronic structure of the sample. When fitting spectra, not all of these factors are known, but are estimated by using a combination of Gaussian and Lorentzian curves. Metallic systems often show asymmetric peak shapes due to many-electron interactions between conduction band electrons and the core level hole, which can be taken into account by exponential tails or special functions, e.g. the Doniach-Sunjic line shape [71].

Peak Fitting

The program CasaXPS was used for peak deconvolution and background subtraction. Typically, for Zr 3d a Shirley-type background, and for O 1s a linear background was used. The following parameters were used for the Zr 3d doublets: $\Delta E = 2.4$ eV, ratio of areas 1:0.69 [72] (tested over several ZrO_2 systems). The binding energies for Zr

given in this thesis are the Zr $3d_{5/2}$ peak positions unless otherwise mentioned. The line shape was set to the Gauss-Lorentzian product function “GL(60)” (60% Lorentzian) for all peaks except for the Zr 3d interface peaks, which behave very similar to ultrathin films [42] and thus appear metallic; they are therefore fitted additionally with an exponentially tailed function “GL(60)T(1.8)”. For Zr^0 , a more pronounced tail is needed, so “GL(60)T(1.1)” is used. For spectra that are dominated by the ultrathin film peak (e.g. the preparation for the stoichiometry determination of ultrathin zirconia on Rh(111), see section 5.2.4), the high- E_B background is not described well by an exponential tail; in this case, a Doniach-Sunjic [71] term is added instead by using the line shape “F(0.01,60,0)GL(60)”.

XPS Simulation

The program SESSA [73], version 2.1, was used for the simulation of XPS spectra. In SESSA, any material can be set up in e.g. thin film or bulk configuration. A large database is provided for all necessary material parameters, which are, among others, inelastic mean free paths, scattering cross sections, ionization cross sections, and line shapes. SESSA calculates inelastic scattering events with an analytic theory, while elastic scattering is tackled with a numerical Monte Carlo approach. As output, SESSA gives XPS peak areas as well as a simulated spectrum including theoretical line shapes. In this thesis, only peak areas are used for comparison with experimental data. The following settings were typically used in this thesis:

- Source: Mg $K\alpha$
- Morphology: Planar
- For thin zirconia films:
 - Band gap: 5 eV
 - Thickness: 3 Å per layer
 - Density: 9.1×10^{22} atoms per cm^3
- Convergence factor: 10^{-4}
- Number of collisions: 70+
- Number of trajectories: ≈ 10.000
- Both approximations off

2.3.3 Auger Electron Spectroscopy

AES is based on the Auger effect, which describes a three-electron ionization process: At first, an electron of a core shell is emitted when an atom is ionized by an x-ray or electron. The resulting hole is filled with an electron from an upper shell. The energy gained is transferred to an electron of the same upper shell, which is in turn also emitted. The resulting kinetic energy of this third electron is independent of the energy of the incoming particle. For example, the energy of an Auger electron KL_1L_{II} transition is given by:

$$E_{\text{kin}} = E_K - E_{L_I} - E_{L_{II}} - \Phi \quad (2.9)$$

with the work function Φ . All energies are element specific; when detecting these Auger electrons, elements can be identified. However, measured Auger energies can deviate from the above equation, since the probed atom is in an ionized state when the Auger process happens.

In contrast to XPS, incoming particles in AES are not photons but electrons emitted from an electron gun (typically 2 – 10 keV, in this thesis: 3 keV). This has the advantages of higher count rates and a far smaller irradiated area; in our setup, a diameter < 100 μm can be reached. (In some Auger systems, the electron beam can be focussed to less than 100 nm diameter.) Disadvantages of an electron beam are a higher destructive influence on the sample due to electron-stimulated desorption (e.g. oxygen desorbs over time (also oxygen bound in oxides); fluorine is hardly measurable) and cleanliness; CO, which is a background gas in all vacuum chambers, dissociates under the electron beam, which leads to an increase of the C signal over time during AES measurements.

The high number of inelastically scattered electrons in this method leads to a large background signal, thus, typically differentiated spectra are shown.

2.3.4 Temperature-Programmed Desorption

TPD measurements are done in two steps: Adsorption of a (defined) coverage of molecules is followed by a controlled desorption. The sample temperature during desorption is increased in a controlled fashion, typically following a linear ramp. While the temperatures changes, the mass and amount of desorbing molecules is measured by a (quadrupole) mass spectrometer. By plotting the intensity per mass/charge ratio

(m/e) vs. the temperature, TPD shows at which temperatures how many molecules desorb. Desorption peaks follow the law

$$\frac{d\theta}{dt} = -\nu(\theta) \theta^n \exp\left(\frac{-E_{\text{des}}(\theta)}{k_{\text{B}}T}\right) \quad (2.10)$$

with the coverage Θ , “prefactor” ν (attempt frequency for first-order desorption), desorption energy E_{des} , Boltzmann constant k_{B} and temperature T . By analyzing spectra of varying coverage, the exponent n can be extracted. For $n = 1$ (1st order), the desorption peak maximum is independent of the coverage, while for $n = 2$ (2nd order) the maximum shifts towards lower temperatures with increasing coverage. Zero-order peaks are typical multilayer peaks, where the peak maximum shifts to higher temperature with increasing coverage.

The basic principle of TPD is simple, and gaining qualitative information about the desorption behaviour of molecules is straightforward, as long as the preparation is controlled. With a suitable setup [51], the total adsorbed coverage is known. For this, the sample has to be cooled to low T , below the desorption peak of multilayers. While dosing, the mass spectrometer is used to check whether the sticking coefficient is unity, i.e. whether all dosed molecules adsorb at the surface. Together with a molecular beam (as in the TPD chamber, see section 2.1.3), the exact dose of molecules on the surface is known, making TPD a very powerful method.

To extract the desorption energy from TPD data, extra analysis is necessary. In Eqn. 2.10, all variables are given by TPD data except for the prefactor ν . To extract the prefactor, an inversion analysis can be used. The details are explained in chapter 3.4.2.

2.3.5 Low-Energy Electron Diffraction

As an electron diffraction method, LEED is based on the wave character of electrons. Following the De Broglie wavelength

$$\lambda = h/\sqrt{2m_e E} \approx \sqrt{\frac{150 \text{ eV}}{E}} [\text{\AA}], \quad (2.11)$$

electrons between an energy E of 20 and 500 eV have a wavelength of 0.23 and 0.05 nm, which is in the range of the typical inter-atomic distance ($\approx 0.2 - 0.3$ nm) or

below.

Electrons impinging on a regular grid of atoms — a solid surface — are therefore scattered and show a diffraction pattern. By placing a spherical luminescent screen above the surface, diffraction maxima are measured as bright spots. In case of vertical impingement of electrons, a projection of the screen on a horizontal plane corresponds to a k -space image of the surface structure. As explained in chapter 2.3.2, elastically scattered electrons originate only from the top layers of the sample. LEED surface sensitivity is achieved by suppressing inelastically scattered electrons (by suppression grids between sample and screen). As a result, LEED measurements give a direct view of the surface structure and can be used to identify surface structures and moiré patterns.

Chapter 3

Gas Adsorption Behaviour on Ultrathin $\text{ZrO}_2/\text{Pt}_3\text{Zr}$

In this chapter, the adsorption and desorption behaviour of gases on ultrathin zirconia films grown by oxidation of $\text{Pt}_3\text{Zr}(0001)$ single crystals is investigated using a combination of temperature programmed desorption (TPD), x-ray photoelectron spectroscopy (XPS), and scanning tunneling microscopy (STM). The main focus lies on an extensive study of water and water-induced changes of the surface layer; these two topics are based on an article, Ref. 45, but are presented with additional data and information. Furthermore, the water results are compared to density functional theory (DFT) calculations and Fourier-transform infrared spectroscopy (FTIR) absorption measurements on monoclinic ZrO_2 powder to test the validity of the ultrathin oxide as a model system for technological zirconia surfaces.

3.1 Sample Preparation

The $\text{Pt}_3\text{Zr}(0001)$ single crystals used for UHV studies were grown, cut and polished by MaTeck (Germany). The cleaning procedure was based on the recipe from Ref. 41, with slight changes: Cycles of sputtering (2 keV Ne^+ ions in the XPS/TPD chamber, or Ar^+ in the STM chambers; 20 min, current density $\approx 4 \mu\text{A cm}^{-2}$) and annealing (1175 K, 10 min). The last sputter cycle was applied during a linear temperature ramp from 680 K to 380 K in 20 min to reduce the density of steps and eliminate half-steps [41]. The cleanliness of the sample was checked with XPS. An ultrathin zirconia trilayer (O-Zr-O) was prepared by first annealing in oxygen ($p = 1 \times 10^{-7}$ mbar,

680 K, 10 min) and then in UHV (1205 K, 30 min). The first annealing step causes Zr diffusion to the surface and oxidation, but results in poorly ordered structures. In the second step, the oxide forms a well-ordered ultrathin O-Zr-O trilayer; three-dimensional (3D) ZrO_2 clusters disappear by spreading out and/or dissolving into the bulk. In the present study, the final annealing temperature was set higher than in Refs. 41 and 42 to reduce the number of ZrO_2 clusters. Although both, the annealing temperature and the annealing time were increased compared to the recipe from Antlanger *et al.* [41], the film did not break up, as verified by CO TPD, which did not show any indications of a CO signal from adsorption on the substrate [42]. The resulting sample is a zirconia trilayer on a Zr-depleted $\text{Pt}_3\text{Zr}(0001)$ surface. In the following this is shortened to “zirconia/ Pt_3Zr ”.

The TPD and XPS measurements reported in this chapter were performed in the TPD chamber, see section 2.1.3. STM measurements at room temperature and LN_2 temperature were conducted in the RT-STM chamber and the LT-STM chamber, respectively. For the LT-STM measurements, the sample could be annealed to only 1160 K; nevertheless, STM showed large areas free of ZrO_2 clusters (Figure 3.1a).

D_2O (TPD and XPS measurements), H_2O (STM measurements), and methanol were purified via several freeze-pump-thaw cycles. All gases were checked for cleanliness with mass spectrometers. For TPD and XPS measurements, gases were dosed using the molecular-beam doser (see chapter 2.1.3); for STM measurements, gases were dosed by back-filling of the chamber, making the given doses less accurate. In this chapter, we define one monolayer (ML) as one molecule per surface Zr atom (9.5 nm^{-2} , corresponding to 12 molecules per $(\sqrt{19} \times \sqrt{19})\text{R}23.4^\circ$ zirconia trilayer unit cell).

3.2 Bare Ultrathin Zirconia Grown on Pt_3Zr

Ultrathin zirconia films are prepared by oxidation of a $\text{Pt}_3\text{Zr}(0001)$ crystal [41, 44]. Compared to sputter-deposited films, this approach has the advantage of a faster preparation and a more uniform thickness. According to previous studies, which applied a combination of STM, Auger and photoelectron spectroscopy, as well as DFT, the films grown by alloy oxidation consist of one trilayer (O-Zr-O), structurally equivalent to a trilayer of cubic $\text{ZrO}_2(111)$, but with additional distortions [41–43]. (The actual stoichiometry of such films is under debate, see section 3.4.3 and chapter 5.2.4.)

The oxide film is created by Zr diffusion to the surface when annealing in oxygen. On a large scale, the ultrathin film covers the Pt₃Zr substrate completely. Typically, STM finds large areas free from clusters, see Figure 3.1a. However, clusters can be found, as seen in Figure 3.1b. The cluster density can be estimated using XPS, see section 3.4.2. The atoms in the ultrathin zirconia trilayer are well ordered, with an average in-plane distance of 350 pm, and exhibit strong vertical buckling. These height differences are related to the $(\sqrt{19} \times \sqrt{19})R23.4^\circ$ superstructure (1.2 nm periodicity), resulting from the different lattice constants of the oxide and the underlying Pt layer (see section 3.3). The unit cell of the superstructure includes 12 Zr atoms, which are easily accessible to adsorbates due to the large distance between the O atoms in the layer above, and the low interlayer distance between the O and Zr layers [41]. A model of the superstructure as calculated by density functional theory (DFT), taken from [45] can be seen in Figure 3.9 (page 53).

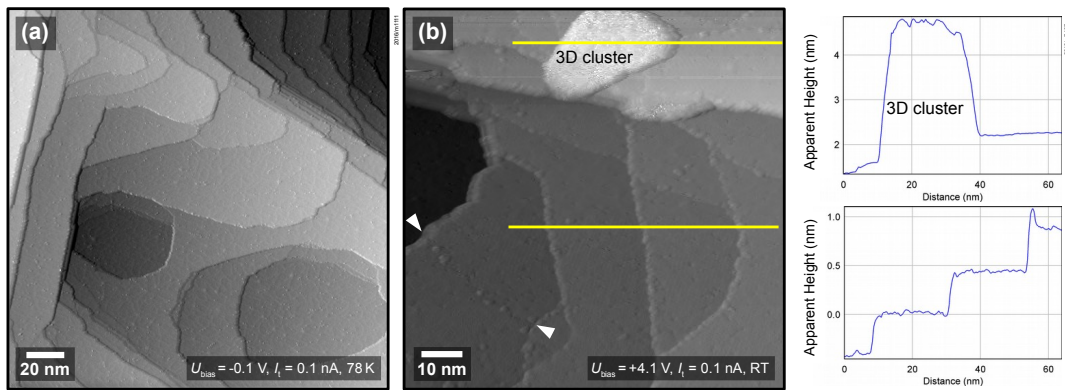


Figure 3.1: Overview STM images of the zirconia/Pt₃Zr surface **(a)** prepared in the LT-STM system, and **(b)** annealed at 1200 K with a 3D oxide cluster. Line scans along the yellow lines are shown at the right; the bottom one shows the 0.4 nm steps of the substrate between equivalent terminations (a few steps of 0.2 nm height are seen with weaker contrast in other parts of the image). Two white arrows indicate the ends of an orientational domain boundary of the trilayer oxide. The noisy appearance of the cluster surface and the tip changes (horizontal streaks) when imaging the 3D cluster are due to its insulating nature. Both images are displayed as if illuminated from the left for improved contrast.

3.3 Dislocation Lines

In the case of Pt₃Zr, diffusion of Zr in the alloy is slow. Thus, after oxidation, a Zr-depleted Pt region remains below the oxide [41]. The surface layer of Pt(111) is known

to be close to forming a reconstruction [74]; the slightly smaller interatomic distance of Pt (0.2775 nm) in comparison with Pt_3Zr (0.281 nm) therefore leads to a contraction of the Pt layer below the oxide film [41]. As a consequence, misfit dislocations form between the Pt layer and the alloy below. These subsurface dislocations are visible as bright ridges in STM, see Figure 3.2a. To investigate the formation of the dislocation lines, Pt was evaporated onto a clean Pt_3Zr substrate. For submonolayer coverages, the Pt layer continues the Pt_3Zr periodicity (not shown). After depositing 1.8 ML (calibrated by STM), and annealing at $\approx 800^\circ\text{C}$, dislocation lines appear as expected, see Figure 3.2b. In contrast to dislocation lines after the oxidation of Pt_3Zr , these show long-range order. This difference can originate from the higher purity of deposited Pt layers w.r.t. the Zr-depleted Pt layers below the zirconia trilayer; this may imply that small amounts of Zr are present in the top substrate layers after formation of an ultrathin oxide film.

The unit cell distance of the top Pt layer can be extracted from the FFT of STM images with atomic resolution, see Figure 3.2c and d; with a unit cell distance of 0.261 nm, it is strongly contracted by 6% (vs. 0.2775 nm on Pt(111)). A small rotation of $\approx 2^\circ$ is found. The nodes forming the regular array of bright features have an apparent height of just 20 pm. Therefore, in contrast to similar features with a height of 200 pm found for the oxidized surface [41] (white, large features in Figure 3.2a), they are not formed by an additional Pt layer. For the Pt layer below the zirconia film, the contraction is less, as shown by the larger spacing of the dislocation lines. Considering that in this case, the lattice originates from Pt_3Zr with a lattice constant (0.281 nm) larger than Pt(111), the lattice constant of the contracted Pt layer can be estimated to be only slightly below that of Pt(111).

3.4 Water

3.4.1 Previous Studies

Many technological applications of zirconia (pure or yttrium-doped) involve interaction with water. Examples are internal steam reforming in solid oxide fuel cells [75], catalysis [9], gas sensors [17], or applications as biocompatible material [13]. However, little is known about the interaction of water with ZrO_2 surfaces on a fundamental level, which is mostly due to a lack of suitable samples. This is quite differ-

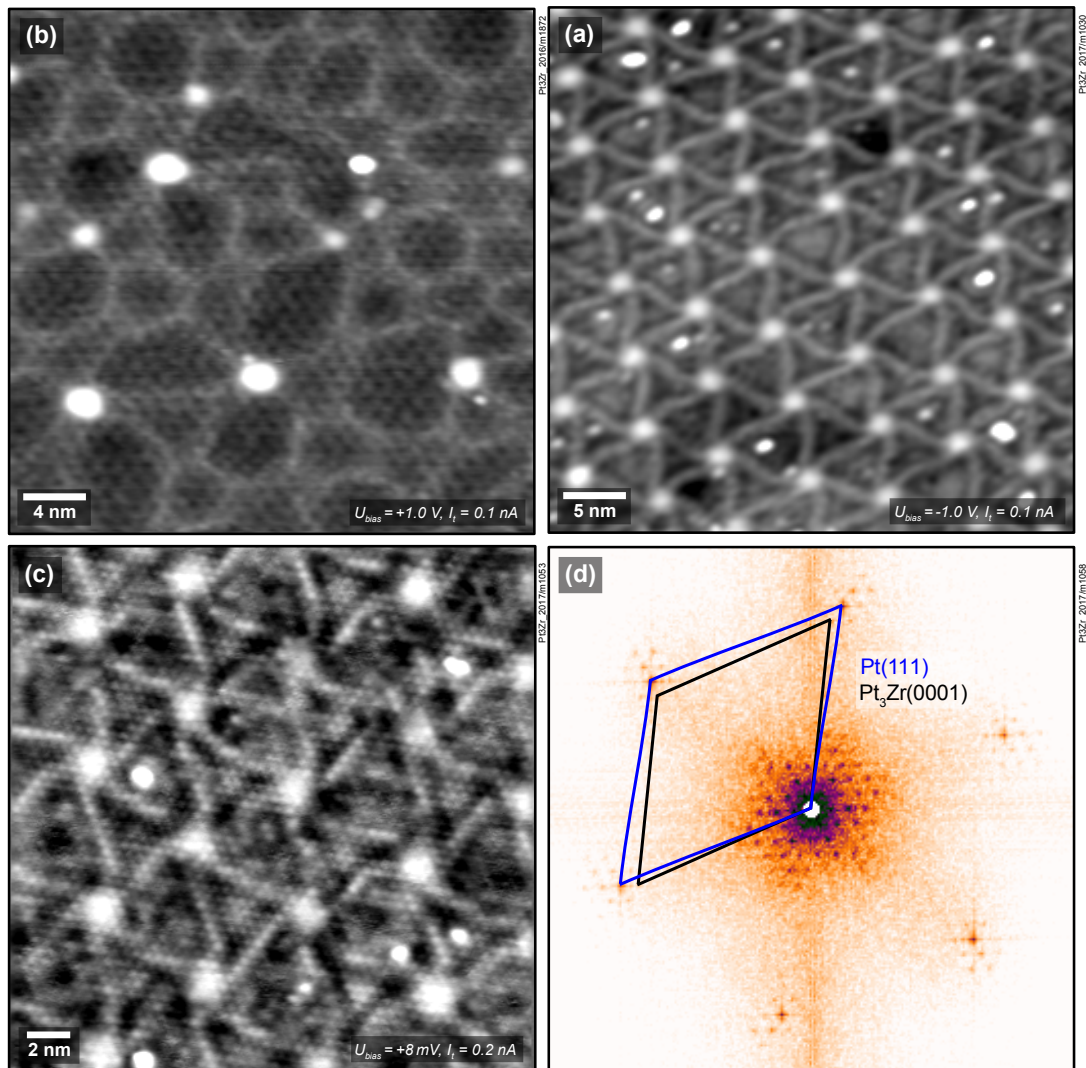


Figure 3.2: (a) STM image of an ultrathin zirconia film grown by oxidation of Pt₃Zr, leading to a depletion of the top substrate layers from Zr. The resulting Pt layers contract and form dislocation lines, yet no long-range moiré pattern. (b) Overview image of 1.8 ML Pt deposited on a clean Pt₃Zr(0001) surface, showing the long-range order of the resulting moiré pattern. (c) Atomically resolved image of the preparation of (a). (d) FFT of a larger STM image with the same resolution as (c), where the contracted Pt(111) grid and the Pt₃Zr grid are marked. The resulting moiré spots can be seen around the (0,0) spot and each of the Pt(111) spots. All STM images were taken at LN₂ temperature.

ent for other oxides [76–78]. Water adsorbs only weakly on many defect-free oxide surfaces; in ultrahigh vacuum (UHV) it then desorbs below room temperature (RT), typically at 160–250 K [79–81]. H_2O can bind more strongly to surfaces with defects, as shown for the prototypical example of rutile $\text{TiO}_2(110)$ [82, 83]. In these cases, H_2O dissociates into an OH group, which fills an oxygen vacancy, and into a hydrogen atom, which binds to surface oxygen and forms a second OH group. On TiO_2 , these OH groups are stable up to ≈ 490 K [84]. On defect-free oxide surfaces, water can bind strongly if the surface termination includes highly reactive cations. It can then readily dissociate, e.g. on $\alpha\text{-Cr}_2\text{O}_3(001)$ [85], $\alpha\text{-Fe}_2\text{O}_3(012)$ [86], and on oxides of the alkaline earths [87], including CaO-terminated $\text{Ca}_3\text{Ru}_2\text{O}_7(001)$ [88]. On $\text{RuO}_2(110)$ [89], $\text{PdO}(101)$ [90], and $\text{Fe}_3\text{O}_4(001)$ [91], water binds to coordinatively unsaturated cations and forms partially dissociated structures stabilized by hydrogen bonds.

Such detailed studies are not yet available for water on ZrO_2 ; only few reports on H_2O adsorption can be found in the literature. On powder materials, very high adsorption enthalpies were reported for low H_2O coverages ($\gtrsim 2$ eV on monoclinic and ≈ 1.5 eV on tetragonal ZrO_2), decreasing to liquid-water like binding (0.45 eV) at coverages around 2–4 $\text{H}_2\text{O}/\text{nm}^2$ [92, 93]. Moderate values (≈ 0.6 eV, derived from a TPD peak at 240–250 K) were reported for H_2O on oxidized, polycrystalline Zr, i.e., a hydroxylated and, possibly, substoichiometric film [94]. To the best of our knowledge, there are no studies of H_2O adsorption on well-defined single-crystalline ZrO_2 surfaces so far. This is related to the fact that single crystals of pure ZrO_2 grown from the melt exhibit phase transformations upon cooling, thus only crystals of doped zirconia (e.g., YSZ) are available; these retain the high-temperature cubic phase. The surface chemistry of YSZ is much more complex than that of pure ZrO_2 , however, as shown for adsorption of H_2O [95], hydrogen [96], or CO and CO_2 [97]. Therefore, the investigation of pure ZrO_2 , which is needed as a starting point of a well-grounded fundamental understanding, has to rely on thin films.

Temperature programmed desorption (TPD) studies on 7 ML-thick ZrO_2 films on Pt(111) show three desorption peaks (190 K, 275 K, and 370 K with adsorption energies 0.46, 0.68, and 0.92 eV, respectively) [98, 99]. The authors suggested that water in the low-temperature peak binds molecularly while the rest does so in dissociated form. The two desorption peaks at higher temperatures were assigned to defect sites.

3.4.2 Water Adsorption and Desorption on Zirconia/Pt₃Zr

Temperature Programmed Desorption

TPD measurements form the backbone of our analysis of the behavior of water on zirconia/Pt₃Zr. To reduce the influence of the residual gas on the TPD data, TPD experiments were done with D₂O. Figure 3.3a shows three distinct regions in the TPD spectrum for D₂O: two desorption peaks with maxima at 150 and 180 K, and a tail extending towards high temperatures. We also checked for simultaneous desorption of other species ($m/e = 3, 4, 18, 19,$ and 28) and found no peaks apart from the D₂O cracking products. The desorption temperature of 150 K is typical for multilayer water [80]. When plotting this peak in a $\log(I)$ vs. $1/T$ plot, see Figure 3.3b, the ascending slope (dotted line) yields a desorption energy of 0.47 eV [100, 101], which is slightly lower than expected for multilayer D₂O ice (0.53 ± 0.02 eV [102]). This may be due the second-layer ice not having fully developed its crystalline order.

The TPD peak with the maximum at 180 K exhibits first-order desorption behavior and reaches saturation at a coverage of approximately 1 ML (one D₂O molecule per Zr atom in the oxide); it is therefore the monolayer peak. The area of the monolayer peak does not stay perfectly constant during repeated TPD measurements, see the section on water-induced changes, below. On the high-temperature side of the monolayer peak, starting at approximately 190 K, the desorption rate decreases more slowly than expected for a first-order peak. The signal forms a long tail and vanishes below the detection limit at ≈ 540 K, see inset of Figure 3.3a. (Comparison with D₂O TPD of other surfaces shows that the tail is not an instrumental artifact.) The tail may consist of a multitude of peaks that cannot be discerned from each other. The coverage in the tail corresponds to approximately 0.15 ML, while the rest of the monolayer makes up the peak at 180 K. When plotting the desorbed amount of water, taken from TPD, vs. the dosed amount, the intercept of a linear fit yields a dose of 0.01 ML, see Figure 3.3d. This shows, within the error of such an analysis, that no water was present on the surface before dosing and no substantial amount of water remains at the surface after the TPD ramp ($T_{\max} = 550$ K).

The differential desorption energy E_{des} of water bound in the monolayer peak can be calculated using the inversion analysis method [103, 104]: The Polanyi-Wigner formula (3.1), which describes the desorption rate $-d\theta/dt$ in dependence of coverage

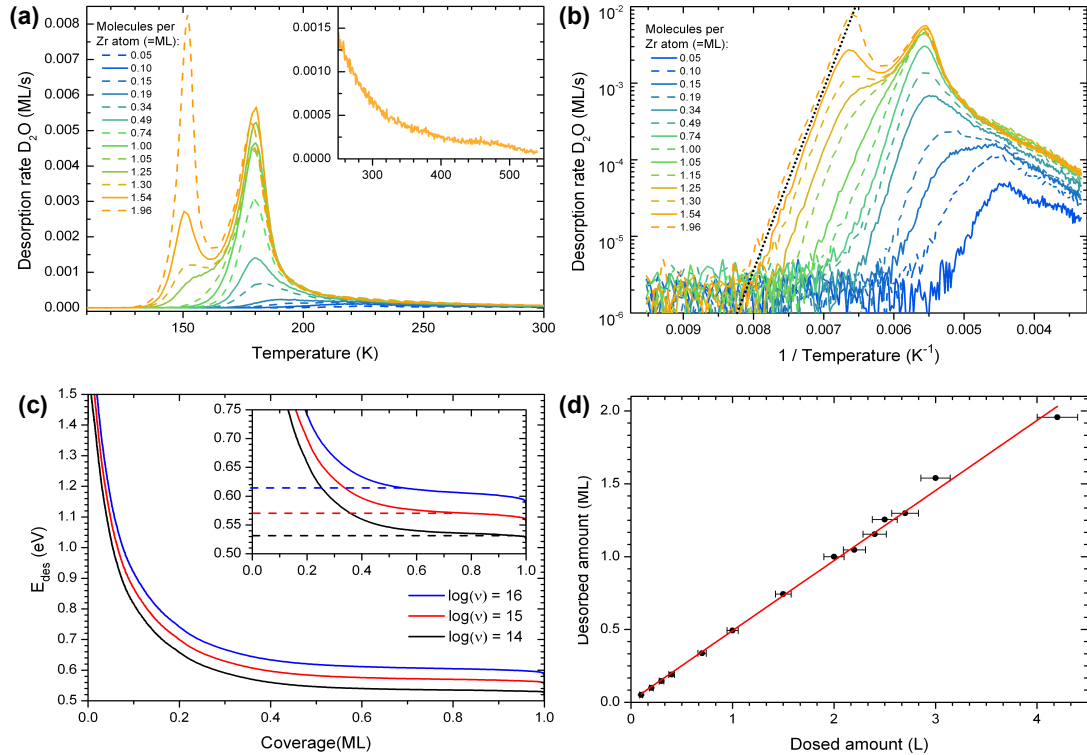


Figure 3.3: TPD of D_2O on zirconia/ Pt_3Zr (heating rate 1 K/s; no fresh sample preparation between spectra with different coverage). **(a)** The TPD spectra consist of three regions: The multilayer peak (150 K), the monolayer peak (180 K) and a high-temperature tail up to ≈ 540 K, see inset. **(b)** Logarithmic plot of the spectra in (a) vs. $1/T$. The linear onset of the multilayer peak gives $E_{\text{des}} = 0.47$ eV. **(c)** Inversion analysis showing the desorption barrier E_{des} vs. coverage using $\nu = 10^{15 \pm 1} \text{ s}^{-1}$. In the 0.5–0.95 ML range, E_{des} is 0.57 ± 0.04 eV. **(d)** Amount of desorbed D_2O (calculated from the integrated TPD signal) as a function of gas dose. The TPD intensities were calibrated assuming a sticking coefficient of one, thus 1 Langmuir (L) = 10^{-6} torr s corresponds to 0.48 ML. The red line is a linear fit.

θ , temperature T , and time t ,

$$\frac{d\theta}{dt} = -\nu(\theta) \theta^n \exp\left(\frac{-E_{\text{des}}(\theta)}{k_{\text{B}}T}\right) \quad (3.1)$$

is inverted under the assumptions of first-order desorption ($n = 1$), the prefactor ν being independent of θ , and a constant heating rate $\beta = dT/dt$:

$$E_{\text{des}}(\theta) = -k_{\text{B}}T \ln\left(-\frac{\beta}{\nu\theta} \frac{d\theta}{dT}\right). \quad (3.2)$$

Equation (3.2) is fully defined by the measured TPD data except for ν . To determine ν and E_{des} , we follow Ref. 105 in using equation (3.1) to simulate TPD spectra that consist mainly of the monolayer peak. In our case of D_2O on zirconia/ Pt_3Zr , the best overlap between experimental and simulated curves is achieved at $\nu = 10^{15 \pm 1} \text{s}^{-1}$. This is a typical value for water desorption [79]. Figure 3.3c shows E_{des} as a function of θ , derived for an initial coverage of 1 ML. The desorption energy stays almost constant between 0.55 and 0.95 ML and amounts to 0.57 ± 0.04 eV, taking the error bars of ν into account.

At lower coverages (well inside the high-temperature tail), the results of the inversion analysis in Figure 3.3c give adsorption energies of up to ≈ 1.5 eV. These energies should be treated with caution; here, ν might vary considerably from the value determined for the monolayer peak (e.g. due to recombinative desorption or surface restructuring during desorption).

X-ray Photoelectron Spectroscopy

To determine whether (or to what extent) water adsorbs in molecular or dissociated form on the zirconia/ Pt_3Zr surface, we have analyzed XPS O 1s data. When dosing 2 ML D_2O at 100 K, four different peaks are distinguished as originating from D_2O , OD, 3D ZrO_2 clusters, and the zirconia trilayer, see Figure 3.4a. Figure 3.4 b and c show the peak areas of these four different O 1s components after various flash-annealing steps. The peak at 530.1 eV originates from oxygen bound in the zirconia trilayer and is very close to the reported value of 529.9 eV [42]. This peak does not change significantly with coverage or temperature, except for a slight decrease when the intensity is dampened by 2 ML D_2O . Within the accuracy of the fits, the peak attributed to 3D clusters also remains constant. The trilayer and 3D ZrO_2 clusters have

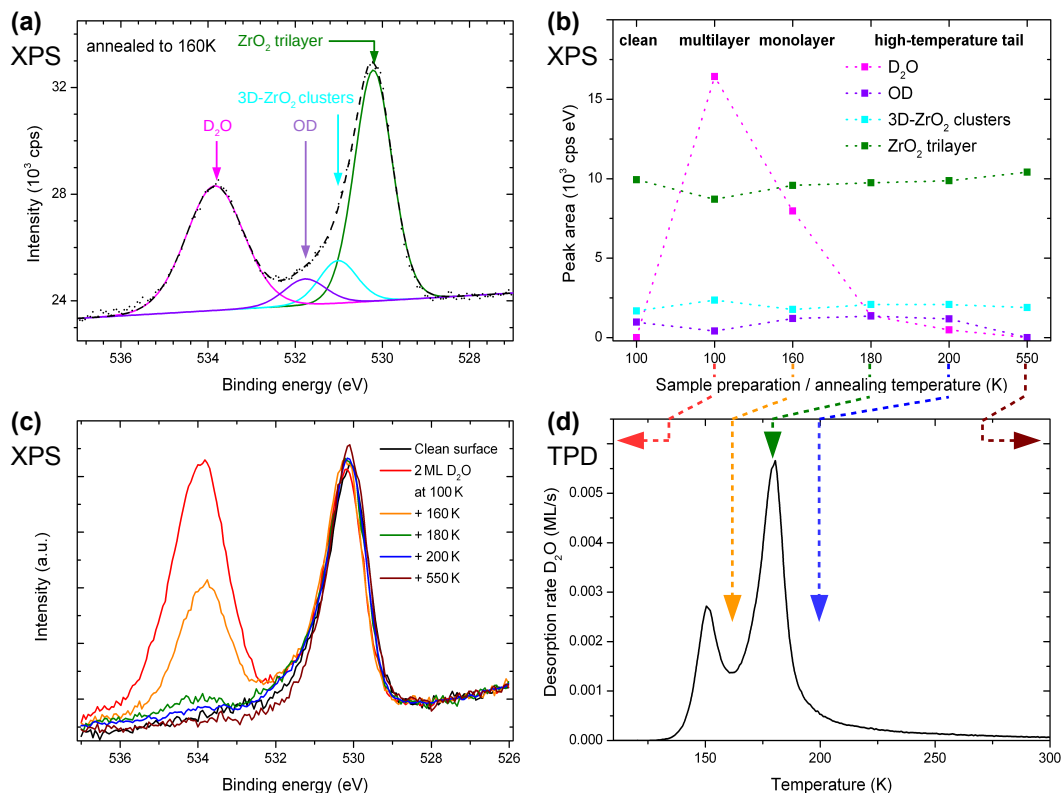


Figure 3.4: XPS of D_2O on zirconia/ Pt_3Zr . **(a)** O 1s region with 2 ML D_2O deposited at 100 K, then annealed to 160 K to remove the multilayer. **(b)** Comparison of spectra before and after D_2O adsorption, and after additional annealing steps. All XPS spectra were taken with monochromatized Al $K\alpha$ radiation at 100 K. **(c)** Intensities of the spectra in (b) for the peaks assigned to D_2O , OD, 3D ZrO_2 clusters, and the zirconia trilayer. **(d)** TPD measurement (1.54 ML) for comparison with the XPS results in (b,c).

distinct O 1s and Zr 3d spectra [42]; the 3D cluster/trilayer ratio is consistent for O 1s and Zr 3d, which confirms the correctness of our peak fitting. An STM image of a 3D ZrO_2 cluster can be found in the Figure 3.1b. The O 1s peak at 533.8 eV originates from non-dissociated D_2O . [77,106,107] When flash-annealing to 160 K, which is above the desorption temperature of the multilayer peak, yet below the desorption temperature of the monolayer peak, this peak decreases by roughly 50%, in agreement with only 1 ML remaining on the surface, see Figure 3.4c. When annealing to 180 K (maximum of the monolayer peak), the molecular D_2O peak decreases further and nearly vanishes at 200 K (beyond the monolayer peak). When annealing to 550 K, the spectrum decreases in the region 531-532 eV, i.e., between the two main peaks. This region contains signals from oxygen in zirconia clusters ($E_B = 531.0$ eV, similar to [42]) and from hydroxy groups¹ ($E_B = 531.8$ eV); a shift of 1.7 eV between the trilayer oxide peak and the hydroxy peak lies within the expected range [77, 106, 108, 109]. Since zirconia clusters do not change when annealed at 550 K, the decrease stems solely from hydroxy groups. The TPD high-temperature tail is therefore due to dissociated water, which recombines before desorption. When comparing the O 1s signal from OD groups and from the ultrathin film to XPS simulations using the SESSA program [73], the amount of water present as hydroxy groups is estimated as 0.12 ML. A small hydroxy component appears also on the as-prepared oxide (labelled “clean” in Figure 3.4b,c), possibly due to adsorption from the residual gas.

D_2O dissociation induced by x-ray beam damage was excluded by dosing 2 ML of D_2O at 100 K and annealing the sample directly to 200 K. This yielded exactly the same result as shown for 200 K in Figure 3.4b,c, showing that there is no dissociation while taking several x-ray photoelectron spectra.

Scanning Tunneling Microscopy

Figure 3.5a shows 0.12 ± 0.04 ML of H_2O dosed at 100 K (via back-filling of the chamber) on a freshly-prepared zirconia/ Pt_3Zr surface. This coverage corresponds to the high-temperature TPD tail. During STM measurements, the sample was held at 78 K. Both temperatures lie well below all desorption peaks of water, see above. Three different regions are present in the STM image: ordered, apparently uncovered and clustered areas. The water species in the ordered areas are stable during imaging;

¹In contrast to “hydroxyl”, the term used for an OH radical.

they typically appear as 80–100 pm high protrusions. The ordered areas mostly show the same periodicity as the zirconia trilayer, i.e. $(\sqrt{19} \times \sqrt{19})R23.4^\circ$ with respect to the Pt layer below [41]. The clustered areas, presumably with a higher local coverage, appear fuzzy, indicating that the water molecules are moving under the influence of the tip. This suggests that one or two adsorption sites per unit cell are more stable than the others. Following the XPS measurements shown above, which show that the most stable adsorption sites are occupied by hydroxy groups, we attribute the ordered features to OH; this assignment is confirmed below. Dissociation of H_2O leads to two hydroxy groups, one (O_wH , also known as terminal OH) containing the oxygen atom of the water, and the other formed by a surface oxygen atom and the split-off proton (O_sH). These two OH groups should appear differently in STM. As we see only one type of distinct protrusion, we have to assume that STM shows the terminal OH, which is geometrically higher, while an adjacent O_sH is invisible due to its smaller apparent height. (This is in agreement with DFT, presented in [45] and summarized in section 3.4.5.) The coverage of one dissociated H_2O , i.e., two OH groups, per $(\sqrt{19} \times \sqrt{19})R23.4^\circ$ unit cell was used as the input for an XPS simulation using SESSA [73]. The result shows that this coverage accounts for $\approx 2/3$ of the hydroxy groups seen in XPS.

When measuring H_2O on the zirconia film at room temperature (well inside the high-temperature tail), only a low coverage of H_2O -related protrusions is found even after supplying large gas doses, see Figure 3.5b. This is in agreement with the TPD results. Again, the protrusions appear about 80–100 pm high. The $(\sqrt{19} \times \sqrt{19})R23.4^\circ$ ordering can still be made out locally. Water adsorbs preferentially above the sub-surface dislocation lines. As mentioned in section 3.3, these stem from the misfit between the Zr-depleted Pt layer between the zirconia trilayer and the Pt_3Zr substrate [41]. Furthermore, water adsorbs on top of rotational domain boundaries [44] of the oxide film (these are rather sparse; there is none in Figure 3.5). Figures 3.5c and d show single water species (hydroxy groups) adsorbed on a zirconia trilayer, imaged with a special tip that lets these species appear as dark depressions. Assuming that the bright protrusions in the STM image correspond to Zr as suggested for “normal” tips in Ref. 41, the red lines indicate that the adsorption site of the water species is above a Zr atom. This is consistent with the site expected for the terminal O_wH .

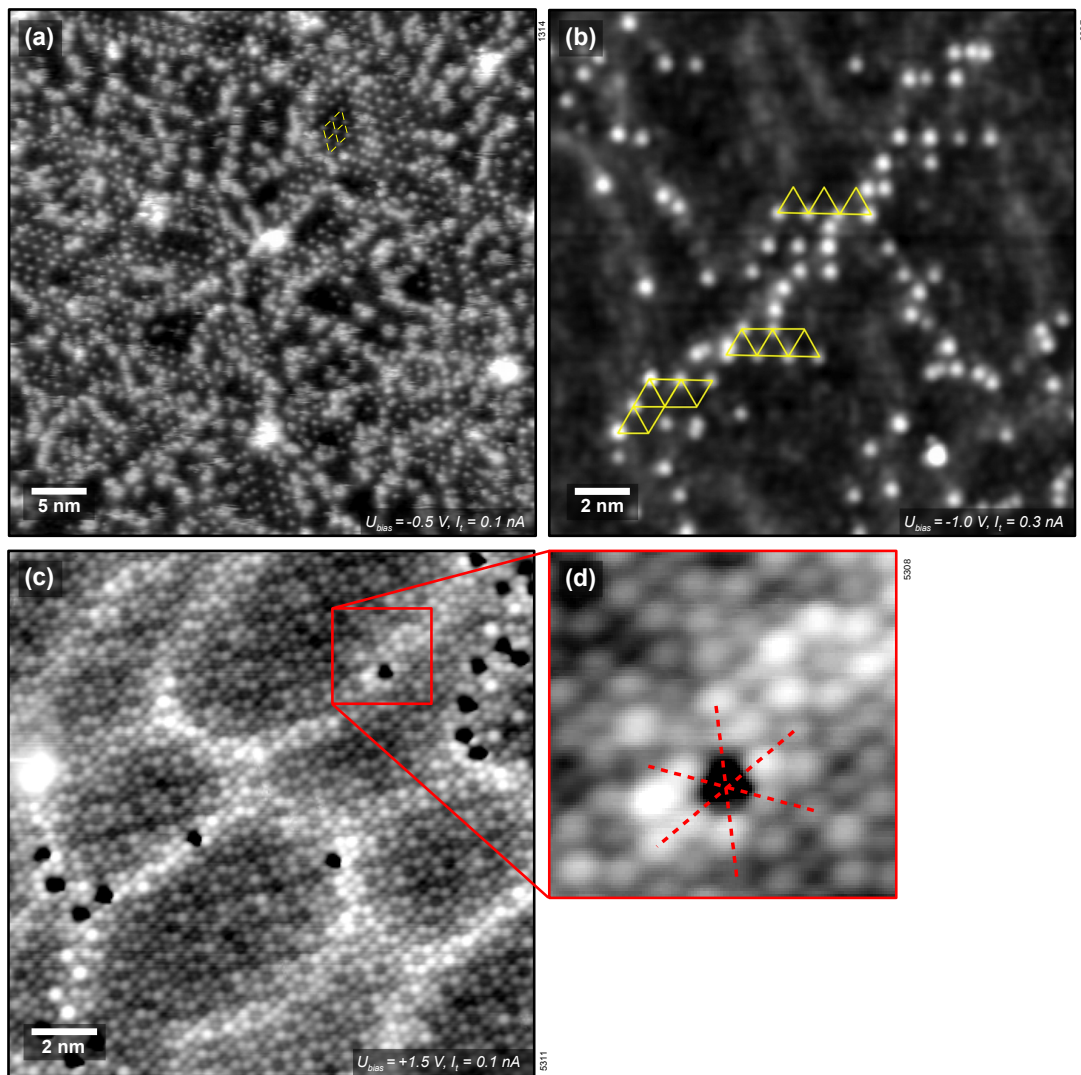


Figure 3.5: STM of small H_2O coverages on zirconia/ Pt_3Zr . **(a)** 0.12 ± 0.04 ML H_2O , dosed at 100 K, measured at 78 K. The surface consists of stable regions with water species arranged in the $(\sqrt{19} \times \sqrt{19})R23.4^\circ$ structure (yellow dashes), regions with higher coverages and unstable imaging (fuzzy gray patches), and apparently uncovered regions of the zirconia trilayer. **(b)** After dosing 15 L of H_2O at RT. Water-related species, namely O_wH , are found preferentially above subsurface dislocation lines (grey areas in the image). They locally show the $(\sqrt{19} \times \sqrt{19})R23.4^\circ$ order (yellow). **(c)** The surface after dosing 30 L of H_2O at RT and storage in UHV for 8 hours. The image was obtained with a special tip that shows OH as depressions (black). Apart from the few hydroxy groups, the clean oxide surface can be seen with atomic resolution. The red lines in the zoom-in **(d)** indicate that the OH are on top of Zr atoms (protrusions in the image). (b–d) adapted from [110].

3.4.3 Stoichiometry of the Ultrathin Zirconia Film

Using the TPD chamber (see chapter 2.1.3), the water dose is calibrated [51], so the coverage in monolayers is well defined. A coverage of one monolayer can be used as a reference for the stoichiometry of the zirconia trilayer, which can be calculated using the O 1s peak areas given in Figure 3.4a. As each ML contains one water molecule per unit cell, and each zirconia unit cell contains two oxygens, one expects the peak areas I to follow

$$\frac{I_{O\ 1s, \text{trilayer}} + \frac{1}{2}I_{O\ 1s, OD}}{I_{O\ 1s, D_2O} + \frac{1}{2}I_{O\ 1s, OD}} \cdot \frac{1}{(1 - \Theta_{\text{ZrO}_2 \text{ cluster}})(1 - \eta)} \stackrel{!}{=} 2. \quad (3.3)$$

One deuterium per dissociated D_2O is bound to a surface oxygen, so half of $I_{O\ 1s, OD}$ must be added to the trilayer signal. Taking into consideration that some water is bound to clusters (the cluster area fraction, $\Theta_{\text{ZrO}_2 \text{ cluster}}$, is estimated to be $\lesssim 7\%$) and that the trilayer signal is slightly attenuated by the water layer on top (by $\eta = 8.6\%$, taken from SESSA simulations [73]), one finds a stoichiometry of the ultrathin film of only $\approx \text{ZrO}_{1.40}$. This is clearly different from values found in previous works [41, 42], which had led to the assumption of a ZrO_2 film. The new value is close to the estimation for films grown on Rh(111) using the SMSI effect [111]: $\text{ZrO}_{1.5}$, see chapter 5.2.4.

3.4.4 Water-Induced Surface Changes

While repeating D_2O TPD measurements on zirconia/ Pt_3Zr , the ML peak changed over the course of several cycles, see Figure 3.6a. There, 18 successive TPD measurements were carried out, each starting with 2 ML D_2O dosed at 100 K and then ramped to 550 K (with one exception for the dose as noted below). The monolayer peak area decreases by 8% from the first to the 18th run, with the biggest decrease during the first cycles. At the same time, the amount of water desorbing above 185 K increases, such that the total amount of desorbed water remains constant (note that also the area of the multilayer peak stays constant within the experimental accuracy). Thus, the decreasing monolayer peak height is not due to an increasing amount of water remaining on the surface between TPD runs. Rather, these results show that, under the influence of repeated water adsorption/desorption cycles, adsorption sites with

low E_{des} ($T_{\text{des}} = 180$ K) change to adsorption sites with higher E_{des} . Between the 8th and the 18th run, eight TPD cycles with 2 ML and one with 15 ML were interposed (not shown); dosing 15 ML affects the surface in the same way as 2 ML. The changing height of the 180 K peak is also visible in Figure 3.3a. (Note that the measurements in Figure 3.3 were not done in the sequence of increasing or decreasing coverage, thus the 180 K peak heights at coverages above 1 ML seem to scatter randomly.) Such changes did not appear in multiple TPD cycles with CO_2 , so they must be caused by the interaction of the surface with water, not by the heating/cooling cycles alone.

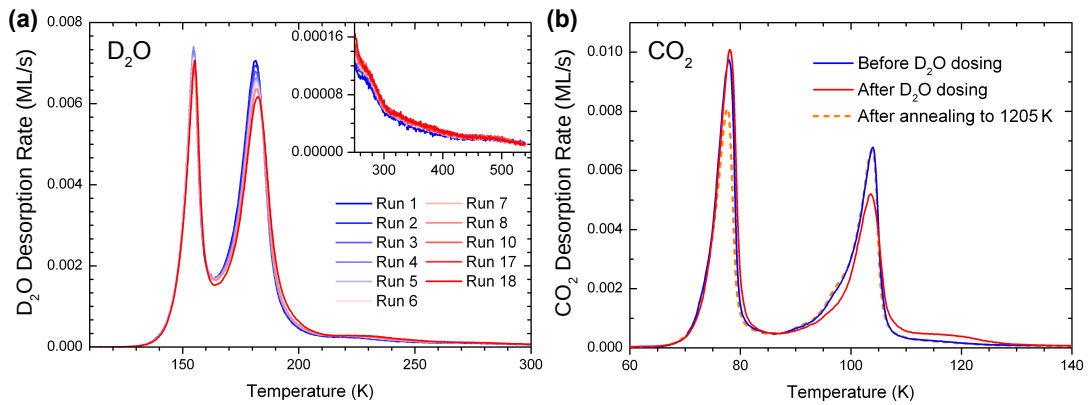


Figure 3.6: Water-induced modification of the zirconia/ Pt_3Zr trilayer. **(a)** Repeated D_2O TPD runs (heating rate 2 K/s) with a starting coverage of 2 ML each. The monolayer peak decreases while the high-temperature tail increases. **(b)** CO_2 TPD (initial dose ≈ 1 ML, heating rate 1 K/s) before (blue curve) and after (red) 18 D_2O TPD cycles. The increasing intensity in the 110–125 K range indicates an attractive interaction of CO_2 with the water-induced defect sites. Annealing to 1205 K restores the original state of the surface (orange, dotted).

We have also used STM to search for water-induced surface modifications. After one cycle of dosing 1.5 ± 0.3 ML water and annealing to 550 K, the surface appears as shown in Figure 3.7a (STM at $T = 78$ K). The $(\sqrt{19} \times \sqrt{19})R23.4^\circ$ superstructure of the zirconia trilayer and the dislocation lines appear unchanged. A small number of water-induced features (OH groups, see section 3.4.2) with an apparent height of 120–150 pm survives the 550 K annealing; their number increases with more adsorption/desorption cycles, and amounts to $\lesssim 0.01$ ML per adsorption cycle. These water species must originate from sites from where water would desorb above 550 K; the desorption rate measured for water in the high- T tail above 500 K is low, but not zero. Summing such a low coverage over several 100 K can originate in 1% of a ML. (This

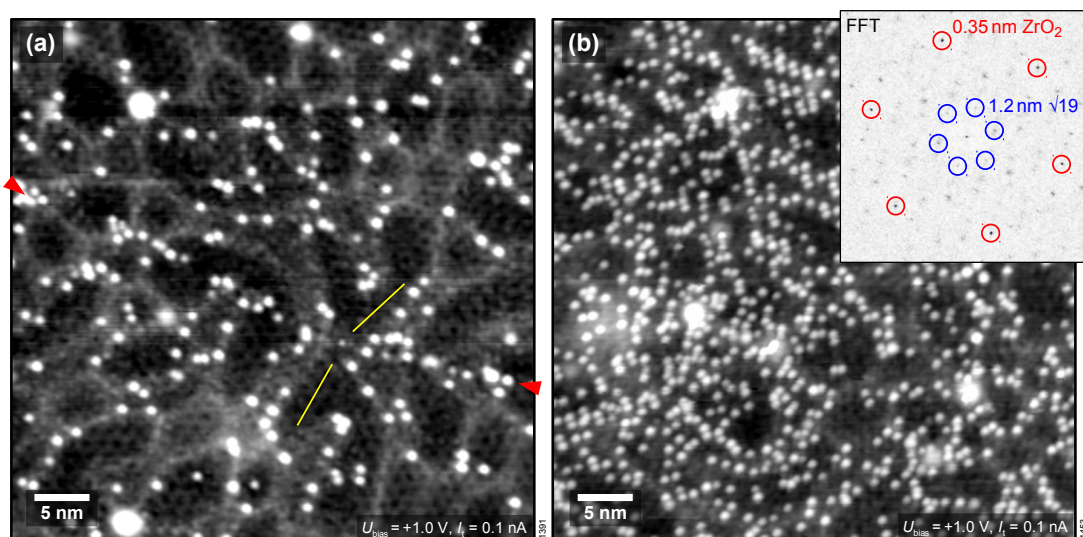


Figure 3.7: Effect of H_2O adsorption/desorption cycles on the zirconia/ Pt_3Zr trilayer seen by STM ($T_{\text{STM}} = 78\text{ K}$). **(a)** After one adsorption/desorption cycle. The water-induced, bright species form preferentially on top of dislocation lines (gray bands) as well as at a rotational domain boundary [between the red arrows in the margins; the orientation of the $(\sqrt{19} \times \sqrt{19})R23.4^\circ$ unit cell on both sides of the DB is indicated by yellow lines]. **(b)** After five adsorption/desorption cycles, the coverage of the bright spots (O_wH) has increased by almost a factor of five. An FFT of the bright features (inset) indicates equivalent positions on the 0.35 nm zirconia lattice and some influence by the $(\sqrt{19} \times \sqrt{19})R23.4^\circ$ superstructure.

coverage is too low to be noticed in the coverage analysis in Figure 3.3d.) Similar to the OH formed at room-temperature adsorption, these features preferentially bind to sites above the subsurface dislocation lines. After 5 cycles, see Figure 3.7b, some ordering of these water-induced features can be made out: In the Fourier transform of the positions of these species (inset of Figure 3.7b), the strong outer spots (marked by red circles) indicate equivalent positions with respect to the 0.35 nm zirconia lattice. There are also weaker spots corresponding to the $(\sqrt{19} \times \sqrt{19})R23.4^\circ$ superstructure of the zirconia trilayer on the oxide (blue circles), indicating that some sites in the superstructure are preferred over others. Based on the real-space images, there must be at least two such preferred positions. This behavior is similar to H_2O dosed at RT, see above. This observation can not be explained by H_2O or OH simply remaining on the surface bound to very stable adsorption sites without any surface change, as the density of water species (and therefore the density of sites) increases with the number of cycles. Likely, there is some modification (deformation) of the oxide film,

leading to stronger bonding to OH. Nevertheless, the oxide lattice remains largely intact as demonstrated by the sharp FFT spots.

It was found that CO₂ TPD is a good indicator for the water-induced surface change, see Figure 3.6b. Before the first and after the 18th D₂O TPD run, 1 ML of CO₂, corresponding to 1 CO₂ per surface Zr atom, was dosed (at 50 K) and desorbed by ramping the temperature to 300 K. CO₂ TPD measurements with varying coverages are shown in section 3.6.2. The CO₂ multilayer peak is at 78 K [51], and the low-temperature (90–100 K) shoulder of the monolayer peak is attributed to compression of the CO₂ layer [112, 113]. The monolayer peak (104 K) and the multilayer peak have roughly the same area, thus approximately one CO₂ molecule per two Zr atoms forms the monolayer. After the water adsorption/desorption cycles, the CO₂ monolayer peak area decreases and the high-temperature tail (105–130 K) increases by approximately 0.05 ML ($\approx 10\%$ of a CO₂ monolayer). When repeating the CO₂ TPD, there is no further change. The TPD behavior indicates that CO₂ binds more strongly to the newly-created sites. (The same measurements were done with krypton, but showed only a weak reaction to water-induced surface changes, see section 3.6.3.) The moderate increase of the CO₂ adsorption energy points to electrostatic interaction between OH and the quadrupole moment of CO₂, rather than chemical bonding of CO₂, e.g. as bicarbonate. (On TiO₂(110), the CO₂ TPD peak attributed to bicarbonate is at ≈ 213 K, Ref. 114.) The combined coverage of the CO₂ monolayer (including the low-T shoulder) and tail slightly decreases after the D₂O cycles (by $\approx 5\%$). This reduction of the total amount of CO₂ bound in the first layer seems to be mainly related to less compression (weaker low-T shoulder). It is likely the newly created sites with higher CO₂ and D₂O desorption energy pin the CO₂ layer, preventing the formation of a well-ordered compressed CO₂ layer. A study by Li *et al.* [115] confirms the interplay of H₂O and CO₂ of zirconia/Pt₃Zr: the interaction between water and CO₂ on ultrathin zirconia films was studied with FTIR and near-ambient pressure XPS. No reaction was found for CO₂ up to a pressure of 3×10^{-2} mbar at room temperature. However, when co-dosing H₂O and CO₂ at 70 °C, adsorption of species containing carbon was already found at 1×10^{-6} mbar; different carbonaceous species were detected and identified as dioxymethylene, formaldehyde, and carbon.

The interaction with CO₂ was also investigated using STM by dosing CO₂ after water dosing and annealing cycles. At LN₂ temperature, 0.1 L CO₂ were dosed after 5 cycles. Figure 3.8a shows water species induced by the cycles; additionally, stripes

originating from the interaction between the STM tip and species on the surface are found. These species might be weakly bound CO_2 . It is not surprising that CO_2 is not clearly visible at 78 K, as the onset of the TPD desorption peak of CO_2 is at about 90 K, only ≈ 12 K above the measurement temperature. When measuring at LHe temperature (after one cycle of H_2O adsorption and annealing, 0.05 L CO_2), two types of species are found, with apparent heights of 50 pm and 100 pm, see line profile in Figure 3.8b. OH appeared ≈ 100 pm high in previous measurements. As the 50 pm species appear mobile under the influence of the tip, they are assigned to CO_2 , while water-induced species are stable and do not hop under tip influence. However, no correlation between CO_2 and OH adsorption positions was found in this preliminary study. The possibility cannot be excluded that part of the CO_2 molecules are located too close to OH to be measured.

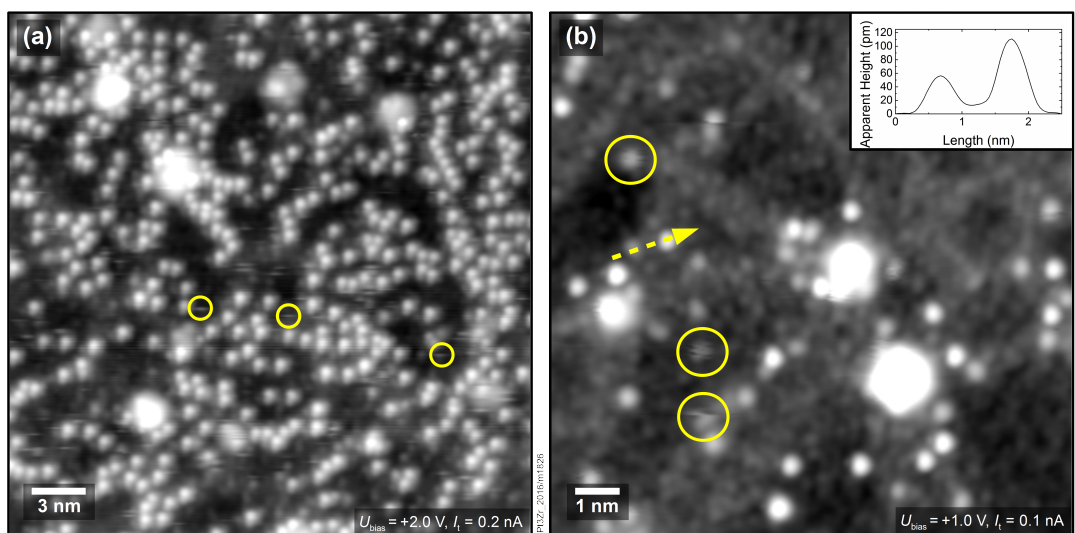


Figure 3.8: STM images of CO_2 dosed on zirconia/ Pt_3Zr with water-induced changes. **(a)** 0.1 L CO_2 . At LN_2 temperature, water-induced species are stable. The tip interacts with CO_2 , leading to stripes (marked in yellow). **(b)** 0.05 L CO_2 . At LHe temperature, CO_2 features (darker, examples marked in yellow) interact with the tip, while water features (brighter) appear stable.

3.4.5 DFT and FTIR Studies by Collaborators

In addition to the UHV studies presented above, our collaborators did DFT calculations and FTIR measurements. They are recapitulated shortly in this chapter; further details can be found in Ref. 45.

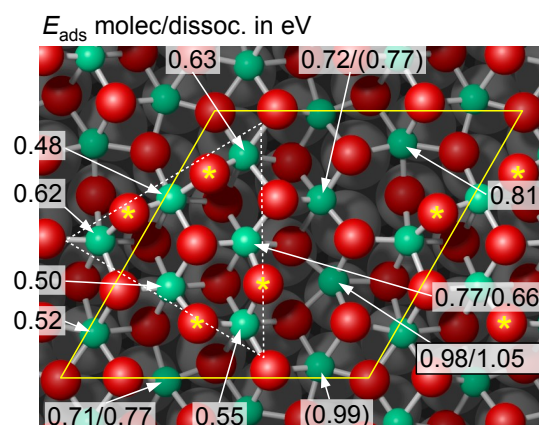


Figure 3.9: H₂O adsorption on a trilayer ZrO₂ film in DFT [45]: Top view of the fully-relaxed ($\sqrt{19} \times \sqrt{19}$)R23.4° ZrO₂/Pt(111) model cell including adsorption energies (in eV) at water adsorption sites. For selected sites, energies of dissociative adsorption are given after the slash. Values in parentheses indicate that the ZrO₂ film had moved and changed upon adsorption, resulting in a site of different character. The yellow rhombus indicates the unit cell, and the dashed triangle shows the group of six Zr atoms that are located higher than the others. Twofold-coordinated oxygen atoms are marked by yellow asterisks.

In DFT, a fully stoichiometric ZrO₂ trilayer was assumed. Accounting for the Pt₃Zr alloy as the substrate would require a very large unit cell (> 500 atoms). Therefore, a pure 5-layer Pt(111) slab served as the supporting structure of the ZrO₂ film ($d_{\text{Pt-Pt}} = 277.8$ pm; bottom two Pt layers fixed). As the layers below the ZrO₂ film are Zr-depleted in experiment, this assumption is reasonable. Such a model was also used by Meinel *et al.* [38] and for modeling the adsorption of metal [44]. Structural optimization using a simulated-annealing approach led to a heavily distorted, i.e. strongly buckled ZrO₂ film, shown in Figure 3.9. With the occurrence of twofold coordinated O atoms at the surface, this structure is similar to the one found by Puigdollers *et al.* [116]. Probably due to the flat potential-energy landscape with a large number of local minima, as well as the different stoichiometry, the present structure does not perfectly represent the experimental one in all details. For example, STM images as in Figure 3.5c suggest a higher symmetry than the DFT model. The main structural elements should therefore be represented well enough to capture the key features for the interaction with the water molecules. Furthermore, oxygen vacancies are preferentially located in the oxygen layer closer to the substrate [116]; thus, their influence on the adsorption behaviour of water should not be strong. The group of six high-

lying Zr atoms, marked with a dashed, white triangle in Figure 3.9, have contracted Zr–Zr distances of 323 to 347 pm. They are separated by low-lying Zr (“valleys”) with Zr–Zr distances up to 389 pm. In the high Zr triangles, interaction between the ultrathin oxide film and the Pt(111) substrate is dominated by the lower oxygen atoms of the trilayer, while in the valleys the Zr atoms bind strongly to the Pt surface atoms. This distortion breaks four Zr–O bonds at the surface, leading to a twofold coordination of some of the oxygen atoms at the borders of the high triangles.

H_2O molecules were found to adsorb near each of the twelve Zr atoms. The adsorbed H_2O molecules did not dissociate spontaneously in any of these twelve sites. Due to the distortions of the ZrO_2 film, these H_2O adsorption sites had substantially different local geometries, which led to a wide range of calculated adsorption energies, from 0.48 to 0.99 eV, see Figure 3.9. For isolated H_2O molecules, adsorption at the laterally compressed “high” Zr atoms is mostly on the weaker side, 0.48–0.77 eV. Adsorption is stronger at valley sites (0.62–0.99 eV), where the ultrathin ZrO_2 film is stretched, making the Zr atoms more reactive and accessible. The strongest adsorption was found where the H_2O molecule can form a hydrogen bond to an undercoordinated (twofold) oxygen atom at the border of a “high” Zr group (marked with energy “0.98” in Figure 3.9; the site “(0.99)” is equivalent, after shifting of the film). Due to the short H bond, dissociation via proton hopping is easy (67 meV barrier in DFT). At this site and one other (marked “0.71/0.77”; not counting sites where the oxide film gets substantially shifted), dissociation is slightly more favored than molecular adsorption. Upon adsorption of a full monolayer, the mean adsorption energy decreased to a value of 0.68 eV.

Furthermore, the core level binding energies of the O 1s states were calculated to confirm the identification of the different species by XPS. In the final-state approximation, taking the average binding energy of the O 1s states of the ZrO_2 film as a reference, the core levels shifted towards higher binding energies by 1.1 eV and 3.55 eV for the dissociated and molecular adsorbates, respectively. This agrees well with the respective experimental values of 1.7 eV and 3.7 eV. Only small differences of the core level shifts of about 0.1 eV are predicted for the different adsorption sites.

FTIR data taken on pre-sintered monoclinic powder samples showed broad bands without discernable sharp peaks, see Figure 3.10a. To circumvent the influence from water in the gas phase, which became noticeable at pressures above 10^{-2} mbar, the absorption was determined at wavenumbers of 3160 cm^{-1} [117]. From isothermal

(at room temperature) and isobaric experiments, the adsorption energy vs. relative coverage was extracted using thermodynamic considerations — making use of the fact that measurements were done in equilibrium of the gas phase and adsorbed water. Therefore, the chemical potentials of water in these two phases must be equal, $\mu_{\text{g}} = \mu_{\text{ad}} = -E_{\text{ad}} - TS_{\text{ad}}$. For calculating the adsorption energy E_{ad} , which can be directly compared to the DFT and TPD results above, S_{ad} — the entropy per molecule in the adsorbed state — has to be estimated. Figure 3.10b shows the results of this calculation, with two limits for S_{ad} : As a lower limit, an entropy of 0 is chosen; the upper limit is estimated from the entropy of ice. Again, the details can be found in Ref. 45. Taking all considerations into account, the analysis led to an estimate for E_{ad} of ≈ 0.65 eV for lower coverages, decreasing close to E_{ad} of ice at high coverages. This stands in remarkable agreement with 0.57 eV from TPD measurements obtained in UHV for the ultrathin zirconia film, which was used as a model system for ZrO_2 surfaces.

3.4.6 Discussion

Combining the data from literature and the results presented here, a simple picture emerges for H_2O at all pure zirconia surfaces: At low coverages, H_2O is strongly bound at a few sites, with adsorption energies up to 1.5 eV or more. When these sites are saturated, experimental adsorption energies are around 0.6 eV. The TPD value of 0.45 eV for 7 ML films on Pt(111) [98] is an exception, probably due to the simplistic assumption of the prefactor being 10^{13} s^{-1} : The TPD peak in Ref. 98 is 20 K above the multilayer peak, comparable to ours. Strongly bound water seems to be mostly dissociated; the weakly bound H_2O is in molecular form at least at low temperatures on our ultrathin films. Both, DFT results for the ultrathin films and DFT calculations for H_2O on monoclinic ZrO_2 from the literature [118, 119] predict dissociative adsorption at (some or all) twofold-oxygen sites, otherwise mostly molecular adsorption, in many cases forming H-bonded structures already at low coverage. This also nicely fits our XPS data as well as FTIR, where the absence of sharp peaks in FTIR spectroscopy (except for the negative peak from the initial coverage) can be explained only by ensembles of H-bonded species on the monoclinic powder sample. With the H_2O molecules on top of the Zr atoms, and in-plane Zr–Zr distances of $\approx 330\text{--}400$ pm, the $\text{H}_2\text{O}\text{--}\text{H}_2\text{O}$ spacing is too large for a two-dimensional ice-like network of H-bonded

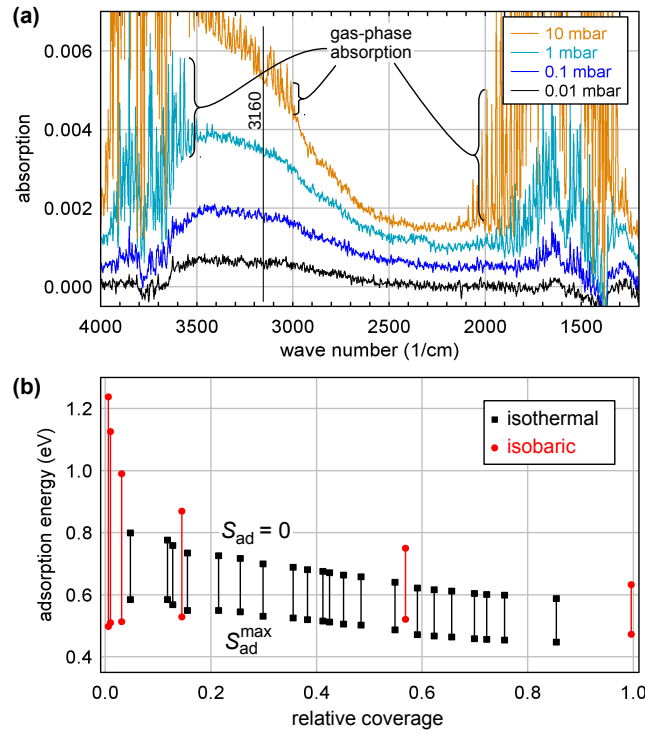


Figure 3.10: Infrared absorption of H_2O on sintered monoclinic ZrO_2 powder [45]. **(a)** Spectra at 298 K for selected partial pressures of H_2O . Spectra are shifted vertically for clarity, and a few regions of dense gas-phase absorption peaks are indicated. **(b)** Differential adsorption energies from the isobaric and isothermal measurements. The vertical lines span the results for the two extreme cases of zero (top) and maximum (ice-like, bottom) adsorbate entropy. Coverage values are normalized with respect to the value at $p_{\text{H}_2\text{O}} = 25$ mbar, which corresponds to 2–3 H_2O per surface Zr atom [95].

species (O–O spacings in ice are 275 pm). Thus, at low coverages, we should not expect extended areas of a 2D water film but only ensembles of very few of H-bonded species.

The DFT energies for water on the ultrathin film, see Figure 3.9, agree reasonably well with experiment, especially when considering the overestimation of H bonding with the functional used (optB86b [120, 121]); the calculated formation energy of hexagonal bulk ice Ih of 0.74 eV [45] is higher than the experimental value of 0.58 eV [122]. For bulk monoclinic ZrO_2 (m- ZrO_2), the experimental adsorption energies at low coverage are very high (≥ 2 eV [92, 93]). These values are even above DFT-calculated values for flat surfaces [118, 119]; probably they are related to defects. However, at high coverages, all experiments (including FTIR presented in section 3.4.5) indicate values of ≈ 0.6 eV, while DFT predicts strong H_2O adsorption on bulk m- ZrO_2 , with typical adsorption energies in the 0.8–1.2 eV range [118, 119]. Test calculations performed by our collaborators for a few $\text{H}_2\text{O}/\text{m-ZrO}_2$ configurations show similar results. To some degree, the problem may be blamed on overestimation of the strength of H bonds (as mentioned previously); this mainly affects the energies at high coverages.

The density of sites with high adsorption energy (“defect sites”) depends strongly on the type of samples used. Astonishingly, it is rather high for 7 ML $\text{ZrO}_2/\text{Pt}(111)$ films [98], when compared with the $\approx 15\%$ TPD tail (12% in XPS) in our ultrathin films. For the powder samples used in FTIR (Figure 3.10), it may come as a surprise that almost no strongly-bound H_2O is detected. To some degree, this may be an experimental artifact: As the reference spectrum was acquired after high-temperature annealing, very strongly bound hydroxy groups or H_2O readsorbed while cooling in vacuum would be included in the reference spectrum, and would go undetected. The density of these species should be small, however, as indicated by the small negative peak occurring when the preadsorbed H_2O joins the H-bonded adsorbates. The low density of defect sites in the powder samples used in the FTIR study may be due to the extensive high-temperature annealing (1 h at 1273 K in pure O_2), which is also responsible for the low specific surface area ($2 \text{ m}^2/\text{g}$) of the samples.

So what are these “defects” with high adsorption energy? Let us start this discussion with the substoichiometry of the ultrathin zirconia films, and therefore with the most common defect [123] of oxide surface science: oxygen vacancies. For the tetragonal $\text{ZrO}_2(101)$ surface (equivalent to $\{111\}$ -type surfaces of cubic or monoclinic

ZrO_2), the formation energy of oxygen vacancies at the surface is nearly as high as in the bulk, 6.0 eV [116]. Also for $m\text{-ZrO}_2(\bar{1}11)$, our calculations yield a high oxygen vacancy formation energy of 7.1 eV. This means that the concentration of oxygen vacancies at these surfaces will be negligible. However, calculations for the ultrathin ZrO_2 trilayer suggest much lower oxygen formation energies (2.23 eV) [116], and the stoichiometry is estimated as $\text{ZrO}_{1.40}$ by experiments. Oxygen vacancies, if present on the surface, should be easily filled by H_2O , and the desorption barrier at these sites should be high. Our TPD+XPS experiments exclude a significant amount of such species, however. Only $\approx 0.12\text{--}0.15$ ML of the adsorbed water is strongly bound, corresponding to 1.4 molecules/unit cell, in contrast to the expected 7.2 V_{O} s per unit cell. Since parts of the strongly bound species originate from other “defects”, only a minority of the V_{O} s seem to play a role in water adsorption. According to DFT, the formation energy of oxygen vacancies in ultrathin zirconia films is lower in the O-layer close to the substrate than at the surface [116]. Therefore, the assumption of a negligible oxygen vacancy concentration at the surface of the trilayer zirconia film is reasonable. Thus, most V_{O} s are not easily accessible, and are not expected to interact directly with adsorbates.

DFT indicates that ultrathin films are strongly distorted. This result has been obtained under the assumption of a stoichiometry of ZrO_2 , but it should be also expected for a zirconia layer with $\approx 60\%$ V_{O} s at the interface. Considering the sharp TPD peak (Figure 3.3) and the large variation of the DFT adsorption energies (Figure 3.9), we nevertheless believe that DFT overestimates the heterogeneity of the surface (and, related, the distortions). DFT tells us that the ZrO_2 film structure is rather unstable, prone to distortions, and breaking of Zr–O bonds that lead to twofold-oxygen sites. It has to be seen whether this would be also true for a substoichiometric film. If so, we consider it likely that this kind of instability is responsible for the changes induced by multiple adsorption/desorption cycles, which create additional defect sites. DFT reveals a complex potential-energy landscape of the uncovered ultrathin ZrO_2 film, but also the variety of ZrO_2 bulk structures of similar energy [124] can be seen as the root of this instability. The STM results indicate stronger water bonding at one or two of the 12 Zr sites per $(\sqrt{19} \times \sqrt{19})R23.4^\circ$ unit cell, in agreement with the $\approx 12\%$ defect sites. At room temperature, water is stable at such sites only above subsurface dislocations of the substrate, again showing that a minor disturbance (slight distortions of the substrate) significantly influences the ultrathin oxide. The DFT-calculated

$E_{ads} = 1.05$ eV for the most stable site in the supercell indicates that dissociated water should be barely stable for extended times at room temperature, which nicely fits these STM results, so these defect sites may be similar to the most stable site in DFT.

Furthermore, DFT suggests that twofold oxygen is the site of H_2O dissociation and provides an anchor [118, 119] for further H_2O by H bonding. Given that the most stable surfaces [29] of monoclinic ZrO_2 exhibit at least $1/4$ twofold oxygen atoms in the surface, and FTIR of well-annealed m- ZrO_2 suggests a low defect concentration, it is unlikely that a twofold oxygen is sufficient to qualify as a defect site. DFT (Figure 3.9) shows substantially different adsorption energies adjacent to twofold-oxygen sites, suggesting that the details of the geometry at a twofold oxygen and the Zr atom where H_2O adsorbs (and dissociates) strongly influences the bonding strength. This implies that not all twofold oxygens provide strong bonding to H_2O . On the other hand, DFT predicts much stronger H_2O adsorption on m- ZrO_2 than found in many experiments (including those presented here), which would indicate that the twofold oxygen atoms on m- ZrO_2 are not present or somehow blocked in reality.

Concerning minority sites, we should also consider that our ultrathin-film model system contains 3D ZrO_2 clusters [42]. The XPS signal from the clusters (Figure 3.4a) is about 18% of that from the ultrathin film. Our STM images indicate that the average cluster height is at least four trilayers. With these values, an XPS simulation [73] indicates that clusters account for less than 7% of the surface area. This area is not enough to have a large impact on our XPS and TPD results; e.g., a picture where all strongly bound or dissociated water is adsorbed on the 3D clusters would be inconsistent with the area fraction of the clusters.

Let us now compare H_2O adsorption on zirconia to structurally similar oxygen-terminated surfaces. The TPD peak temperature of H_2O on the ultrathin zirconia on $Pt_3Zr(0001)$ at 180 K is higher than on other oxygen-terminated oxides such as ultrathin alumina (164–168 K) [125, 126] or a 2 ML-thick FeO film (H_2O : 166 K, D_2O : 169 K) [127]. At least for the case of alumina, the top O–Al interlayer spacing (40 pm) [128] is less than in the present case, so the stronger bonding of H_2O on zirconia must be explained by the large in-plane O–O spacing (≈ 350 pm) on zirconia. This makes the metal cations more accessible than on most other oxygen-terminated oxides, where O–O distances are around 300 pm. Strong H_2O or OH adsorption requires that the metal cations are easily accessible; for O-terminated surfaces this means large O–O distances. Examples of structures with O–O distances similar to

zirconia are $\text{CeO}_2(111)$ [129] with the main TPD peak at 200 K and $\text{In}_2\text{O}_3(111)$ with H_2O adsorption energies of 1.2 eV (TPD peak well above room temperature) [108].

Finally, how good a model system is the ultrathin zirconia film for “real-world” ZrO_2 surfaces? The ultrathin film is based on a trilayer of cubic $\text{ZrO}_2(111)$ with many oxygen vacancies (at the interface), distortions, and probably some twofold-coordinated O atoms at the surface. Apart from the V_{Os} , geometrically it is similar to the two energetically most favorable monoclinic ZrO_2 surfaces, $(\bar{1}11)$ and (111) [29]. When comparing with ZrO_2 powder, nanocrystalline material will also exhibit a substantial number of edge and corner sites (more than the step sites in our model system), but for the high-temperature annealed material used for the FTIR study in Figure 3.10 we do not expect enough of these sites to play an important role. As is generally true for ultrathin oxide films on metal substrates, the main restriction as a model system applies if adsorption involves charge transfer. In such a case, one should expect stronger bonding on the ultrathin film than on thick films or bulk materials, where charge transfer is difficult or impossible [44, 130, 131]. For adsorption of H_2O , in molecular or dissociated form, there is no net charge transfer, so the fidelity of the film as a model system is probably limited by differences in geometry between the film and bulk structures. Unfortunately, the current DFT models, which are only based on stoichiometric ZrO_2 , do not agree well enough with experimental data for an exact comparison. Nevertheless, the good agreement of experimental H_2O adsorption energies for the ultrathin film and the powder material is encouraging.

3.4.7 Conclusion

We have investigated the adsorption and desorption of water on a trilayer of zirconia grown by oxidation of a $\text{Pt}_3\text{Zr}(0001)$ single crystal. With a combined TPD, XPS, and STM approach we could show that $\approx 88\%$ of the water molecules in the first monolayer adsorb molecularly, with an adsorption energy of $E_{\text{des}} = 0.57 \pm 0.04$ eV over a large range of coverages. This agrees well with DFT, which finds dissociative adsorption in only a few sites, with the proton accepted by twofold coordinated oxygen. Experiments also showed that the adsorption energies of dissociated water vary over a wide range, depending on local details of the structure (e.g. substrate dislocations below) and pretreatment (increasing number of “defect” sites after multiple adsorption-desorption cycles). FTIR measurements on ZrO_2 powder showed similar

adsorption energies as our the UHV TPD study, indicating that the ultrathin (tri-layer) zirconia film is a valid model system for water adsorption on well-annealed, real-world ZrO_2 surfaces.

3.5 Methanol

3.5.1 TPD

For a study of simple organic molecules, methanol (CH_3OH) was chosen. After dosing at 80 K, the strongest TPD signal was measured for a mass/charge ratio (m/e) of 31 u/e as expected, as it is the strongest dissociation fragment of methanol in e-beam based mass spectrometry. (One hydrogen is split off.) m/e of 32, 30, 29, 28, and 18 show the same behaviour, but at lower intensity. TPD shows a multilayer peak with the onset at ≈ 120 K, see inset of Figure 3.11. The highest coverage (1.56 ML) shows a high- T shoulder above the multilayer peak. As the peak without the shoulder incorporates approximately 1.1 ML, this strong peak might originate from a weakly bound disordered layer, and the shoulder is the onset of the true multilayer peak, similar to $\text{CO}/\text{Fe}_3\text{O}_4(111)$ [51]. A typical sharp monolayer peak was not found; instead, a broad region from 160 K to 260 K containing ≈ 0.2 ML was found; it is made up by at least two peaks with maxima at 195 K and 225 K. Furthermore, a shoulder to higher temperatures with a maximum at 280 K was found. Two minor peaks can be seen at 460 K and 560 K. Methanol TPD does not lead to changes of the surface as water TPD does, see section 3.4.4; this was tested with CO_2 TPD measurements before and after the methanol measurements (not shown), which showed no change.

During methanol TPD, other masses of possible products were checked; ethanol ($m/e = 46$) showed no signal at all, while hydrogen showed a small peak at 330 K, which might originate from H desorbing from wires holding the crystal in place.

3.5.2 XPS

For XPS measurements, 0.19 ML of methanol (1.5 L) were dosed at 80 K onto the surface and then flash-annealed to various temperatures; data were always taken at 80 K. Figure 3.12 reveals a complicated desorption behaviour. The O 1s region after dosing 0.19 ML shows two peaks, see Figure 3.12a: One at 530.1 eV originating from O in the

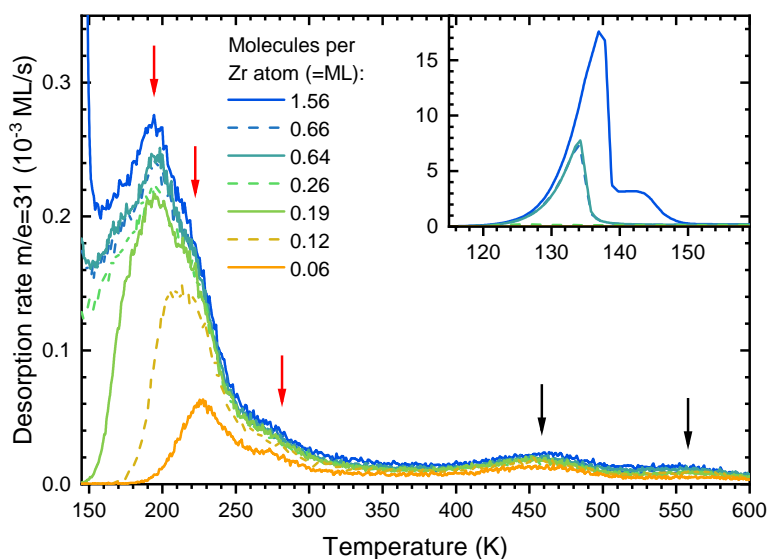


Figure 3.11: Methanol TPD (varying dose, heating rate 1 K/s) on ultrathin zirconia/ Pt_3Zr showing an area consisting of three peaks (marked with red arrows) and two further high- T peaks (marked with black arrows). The inset shows the multilayer region, which consists of two peaks.

zirconia trilayer [42], and another peak at $E_B = 533.7$ eV. When annealing at 200 K, this peak area is reduced by $\frac{2}{3}$. After flash-annealing to 215 K, the peak area is reduced further and the peak is fully removed after flash-annealing to 300 K. Adsorbed molecular water leads to an O 1s peak at 533.8 eV but would desorb fully at 200 K, see section 3.4.2; we can therefore exclude molecular water.

Additionally, the O 1s zirconia peak exhibits a high- E_B shoulder. As is known from the water studies (section 3.4.2) and Ref. 42, the XPS signals of bulk zirconia and OH groups are found in this region. When fitting the spectra using CasaXPS, see Figures 3.12c and d, the region contains two peaks at 531.0 eV (identified as ZrO_2 clusters [42]) and 531.6 eV, respectively. The peak at higher E_B has a E_B similar to OD groups (from D_2O dosing), although E_B of OD groups was found to be at slightly higher binding energy, 531.8 eV, see section 3.4.2. Upon flash-annealing to 200 K, the peak at 531.6 eV grows from 12.4% w.r.t. the zirconia O 1s peak to 23.1%, returns to 12% at 300 K and then gradually decreases until nearly vanishing at 500 K. This behaviour is similar to the behaviour of OD groups from D_2O dosing, which recombine to desorb as D_2O in a broad TPD tail up to 550 K, see Figure 3.3. However, in the case of methanol, the

adsorbed species again recombine to methanol, see below.

The C 1s region of the same experiment shows a single peak at 287.3 eV after dosing, see Figure 3.12b. It continuously weakens until being nearly gone at 500 K. E_B shifts to 286.8 eV (-0.5 eV) at 200 K, 286.7 eV (-0.6 eV) at 215 K, and 286.5 eV (-0.8 eV) at 300 K and higher temperatures.

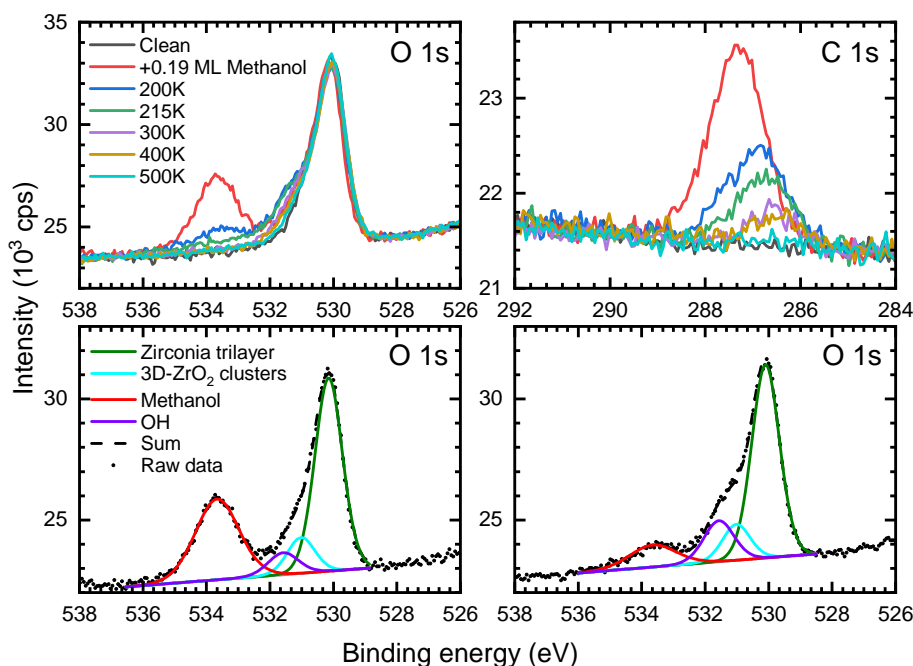


Figure 3.12: XPS measurements of 0.19 ML of methanol on ultrathin zirconia/Pt₃Zr, measured at 80 K. (a) O 1s region and (b) C 1s region flash-annealed at the temperatures given in the legend. Fitted O 1s spectra (c) after deposition and (d) after annealing at 200 K. $\frac{2}{3}$ of the molecular methanol desorbs, and the OH signal increases.

3.5.3 Discussion

It might not come as a surprise to the reader that the adsorption and desorption behaviour of an organic molecule cannot be fully understood by this preliminary TPD and XPS study. Nevertheless, typical behaviours can be confirmed also for CH₃OH on the ultrathin zirconia film: Methanol adsorbs only weakly (physisorbs) above a coverage of ≈ 0.2 ML, i.e. for most of the adsorption sites. This is also found for other oxide surfaces, where chemisorption is only found on step edges and defects [132,

133]. 0.2 ML are close to the coverage of water found to bind strongly to various defect sites (0.12-0.15 ML). It is therefore possible to conclude that also methanol-related species bind to the same sites. However, STM studies would be needed to proof this point.

XPS data suggest that also below 0.2 ML, most methanol adsorbs molecularly at 80 K, with a typical C 1s E_B of ≈ 287 eV [134]. After additional annealing, XPS shows shifted binding energies in the O 1s (similar to OH) and C 1s region; the binding energy of C 1s at ≈ 286.5 eV is assigned to chemisorbed methanol (on a (2×1) surface oxide on Cu [134]), and to methoxy species (on $\text{CeO}_2(111)$ [135]). Ref. 134 does not include O 1s data, yet in Ref. 135 a clear shoulder at 531.5 eV assigned to CH_3O , CH_2O , or OH is reported. The behaviour on CeO_2 fits to E_B found for zirconia thin films, suggesting that methanol does dissociate into methoxy species and possible terminal $\text{O}_{\text{surf}}\text{H}$ hydroxy groups on ultrathin zirconia films. Other C-containing species can be excluded from C 1s, where peaks originating from CH_2O and CH_x would be found at 288.4 eV and around 284 eV, respectively [134].

As the C 1s and the O 1s signals are reduced by the same amount at the same temperature above 300 K, recombinative desorption occurs. This also fits to the TPD spectra of all cracking products of methanol showing the same ratio, independent of the desorption temperature. Since the O 1s signal at 531.6 eV ($\text{CH}_3\text{O} + \text{OH}$) increases after annealing at 200 K, the dissociation process is enhanced by increasing temperatures.

3.6 Other Gases

The sensitivity of the thermocouple used in the TPD measurements quickly approaches zero at low T , below ≈ 30 K. Therefore, such low temperatures are measured only with large errors. As a further result, the actual minimal temperature that could be reached by our setup is unclear; krypton multilayers could not be adsorbed (see below), so a minimal temperature of ≈ 30 K can be estimated.

3.6.1 Carbon Monoxide

CO TPD measurements ($m/e = 28$) on zirconia on Pt_3Zr with varying dosages can be found in Figure 3.13. Apart from the multilayer peak below 30 K (no stable measure-

ment possible, see above), the spectrum consists of three overlapping peaks at 45 K, ≈ 70 K, and ≈ 105 K. Additionally, a defect peak is found at 200 K, see inset. The multilayer peak starts appearing at coverages ≥ 0.8 ML, so not each Zr atom can host a CO molecule. For $m/e = 18, 32, 44$, no desorption was detected.

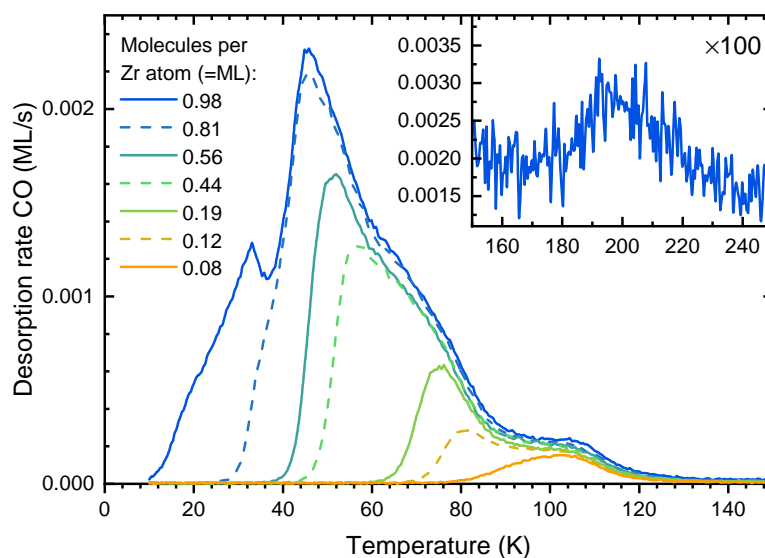


Figure 3.13: CO TPD (varying dose, heating rate 1 K/s) on ultrathin $\text{ZrO}_2/\text{Pt}_3\text{Zr}$, showing three overlapping peaks forming a ML peak which contains ≈ 0.8 ML CO. The inset shows a defect peak at 200 K.

3.6.2 Carbon Dioxide

CO_2 was used as a probe molecule for water-induced surface changes, see chapter 3.4.4. Here, the interaction with the pristine surface is discussed. CO_2 TPD was conducted on $\text{ZrO}_2/\text{Pt}_3\text{Zr}$ with varying coverages dosed at 50 K, see Figure 3.14 for the measurement (mass/e 44 u/e). It shows two main peaks, the monolayer peak at 101 K (slightly different than in Figure 3.6 due to different temperature calibration) and the multilayer peak with an onset around 70 K. This assignment is confirmed by a measurement of 4.45 ML CO_2 , see inset. The desorption energy of multilayers can be determined via the slope of a $\log(I)$ vs. $1/T$ plot, see Figure 3.15, as for water in section 3.4.2, giving $\approx 0.18 - 0.20$ eV. At temperatures above the monolayer peak, a small tail is visible; it originates from binding to defects and increases after water-induced

surface changes, see section 3.4.4; CO_2 was found to be the best probe molecule for this effect. The monolayer peak contains ≈ 0.5 ML of CO_2 , i.e. one molecule per two unit cells. At coverages slightly above half a monolayer (e.g. 0.58 ML, dashed dark blue curve), a small maximum is observed at ≈ 62 K – just below the multilayer peak. This peak vanishes at higher coverages. A similar behaviour was again found on magnetite, yet much more pronounced [51]; there, a separate peak for the second layer was found below the multilayer peak. On our sample, only a very small peak containing 1.5% of a ML can be observed. In fact, this amount is so small that this presumed 2nd layer peak could be forming only on top of 3D ZrO_2 clusters or other “defects”. Apart from the CO_2 signal, no significant signals were found in masses 18 and 32; desorption of CO (mass 28) followed the signature from CO_2 with about 10% of the intensity, as expected for this cracking product.

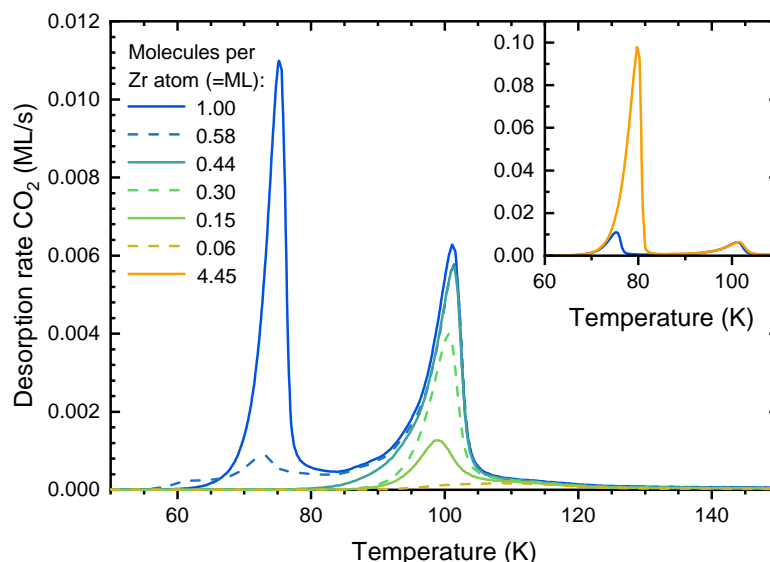


Figure 3.14: CO_2 TPD (varying dose, heating rate 1 K/s) on ultrathin $\text{ZrO}_2/\text{Pt}_3\text{Zr}$ showing a multilayer peak with an onset at 70 K and a monolayer peak at 101 K. The inset shows a coverage of 4.45 ML.

3.6.3 Krypton

Measuring the adsorption and desorption properties of noble gases is difficult, as they do not interact strongly with the substrate. As a result, all desorption peaks

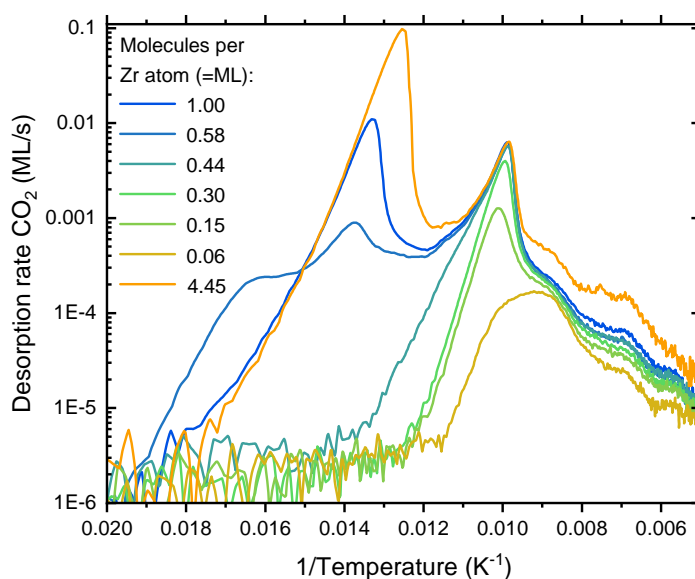


Figure 3.15: Logarithmic plot of the CO_2 TPD on ultrathin $\text{ZrO}_2/\text{Pt}_3\text{Zr}$ in Figure 3.14. From the slope of the 1 ML and 4.45 ML curves, a multilayer desorption energy of $\approx 0.18 - 0.20$ eV can be extracted.

are found at very low temperatures [136]. Argon, for example, was found to desorb from ultrathin zirconia at ≈ 30 K, a temperature which could not be easily stabilized in our setup, see above. Krypton, on the other hand, has slightly higher desorption temperatures and could therefore be measured, see Figure 3.16. The spectrum consists of a single peak at 51 K after dosing 4 L. The multilayer peak onset would be expected at ≈ 33 K [136]. Krypton was used as a probe molecule for water-induced surface changes, similar to CO_2 , see chapter 3.4.4. As one can see in Figure 3.16, the peak becomes slightly wider after 18 cycles of D_2O -TPD and the resulting changes in the surface, see section 3.4.4. In contrast to CO_2 , these changes are minor and no pronounced high- T shoulder can be detected. After annealing at 1205 K, the original state is recovered; the shifted temperature is most likely an experimental artefact. The desorbed amount of molecules falls by $\approx 5\%$ after the 18 D_2O cycles; this change possibly originates from a unintentional, slightly different dosage.

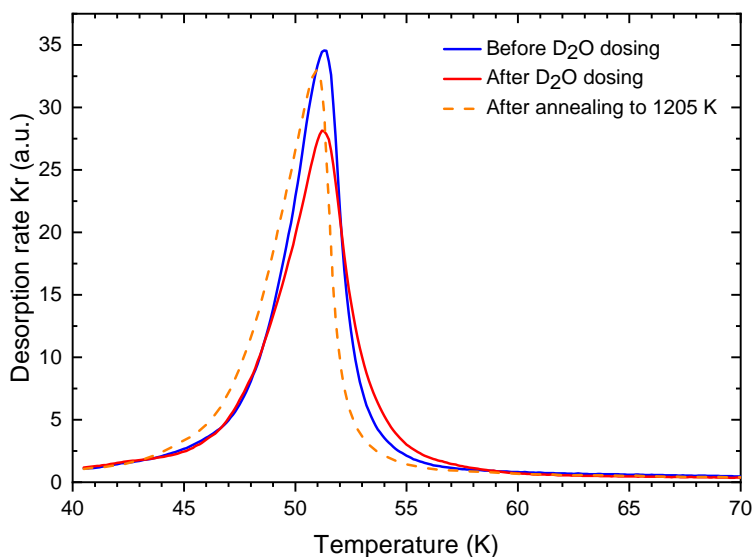


Figure 3.16: Kr TPD (initial dose ≈ 4 L, heating rate 1 K/s) before (blue curve) and after (red) 18 D_2O TPD cycles. The peak is then broadened, but shows no strong reaction to the changed surface. Annealing to 1205 K restores the original state of the surface (orange, dotted); the peak shift is attributed to an experimental artefact.

3.6.4 Oxygen

As a last test molecule, O_2 was dosed onto the ZrO_2 surface. TPD measurements of varying dosages show that O_2 only binds weakly to ZrO_2 with a monolayer peak at 34 K, see Figure 3.17. At such low temperatures, the temperature calibration is not reliable anymore, see above. This might explain why the multilayer O_2 peak is measured at < 10 K while it should be – according to literature [136] – at ≈ 30 K. The temperature scale in this measurement range is therefore inaccurate. The monolayer peak can nevertheless be identified as such; its growth is limited and stops slightly above 1 ML, with a shoulder at low and high temperatures. The high temperature shoulder is assigned to defects as for other gases. The low temperature shoulder is attributed to compression of the O_2 layer; the same phenomenon is found for CO_2 , see section 3.4.4 as well as Refs. 112, 113. Furthermore, the monolayer peak shifts to lower T with increasing dose, which indicates a repulsive force between O_2 molecules bound to the surface. A similar peak shift could, in principle, also occur for second-order desorption due to dissociation and recombination upon desorption, but this

behaviour can be excluded based on the low desorption temperatures.

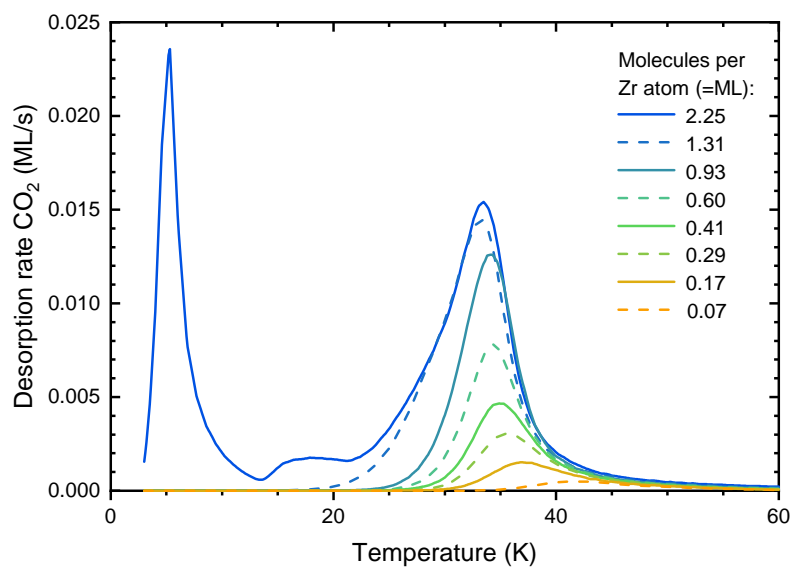


Figure 3.17: O₂ TPD (varying dose, heating rate 1 K/s) with a monolayer peak at 34 K. The temperature scale is inaccurate; the multilayer peak is expected to be around 30 K.

Chapter 4

Thin ZrO₂ Films

This chapter presents results obtained in the RT-STM UHV chamber (see chapter 2.1.1) from zirconia films deposited with a UHV-compatible sputter source [50] (see chapter 2.2). In this way, the film thickness can be controlled and is not limited to one monolayer as in systems based on alloy oxidation [41, 43], see chapter 3. Only thicker model films can be used to gain insights into oxygen vacancies (V_{O} s) and their diffusion, and, in general, in all processes in which charge transfer is involved. It will be shown that for thicknesses below 5 ML, the films are strongly influenced by the underlying Rh(111) substrate; we found varying structures with increasing film thickness. For thicknesses ≥ 5 ML, bulk-terminated, tetragonal or monoclinic zirconia can be obtained, depending on the annealing temperature.

This chapter is based on two forthcoming articles, Refs. 24 and 137. This chapter combines the publications and contains additional data and information.

4.1 Sample Preparation

For the main part of our research, we used Rh(111) as a substrate. Compared with Pt(111), it has the advantage of lower solubility of Zr in the bulk, and the 4:3 ratio of lattice constants between ZrO₂(111) and Rh favors the growth of unrotated zirconia films. Rh(111)¹ and Pt(111) were cleaned by cycles of sputtering (2 keV Ar⁺, 3.6 $\mu\text{A}/\text{cm}^2$, 10 min) and annealing ($T = 920$ °C, 10 min). If Zr or ZrO₂ was deposited before, the first annealing cycle is done in oxygen ($T = 670$ °C, $p_{\text{O}_2} = 1 \times 10^{-6}$ mbar, 10 min) to trap dissolved Zr at the surface. This is of high importance for Pt(111),

¹diameter 9 mm, height 2 mm, from MaTeck, Germany

where Zr easily dissolves in the bulk. The cleaning procedure for Pt₃Zr(0001) is described in chapter 3.1. On the clean substrate, zirconia films were deposited using the UHV-compatible sputter source [50]; the details are given in chapter 2.2.4.

4.2 Surface Structures on Rh(111)

4.2.1 Zirconia Layers of Increasing Thickness

When employing ZrO₂ (zirconia) films as a model system for the surface of bulk ZrO₂, a compromise between bulk-like properties (requiring thick films) and easy imaging by STM (requiring thin films due to their insulating nature) must be sought. Therefore, we have studied the structure of the films as a function of their thickness, starting from 1.5 ML. After annealing 1.5 ML of zirconia at 550 °C in O₂ ($p_{\text{O}_2} = 5 \times 10^{-8}$ mbar), the film partially de-wetted the surface and a 2 ML-thick film formed with holes to the Rh(111) substrate, see Figure 4.1a. A single monolayer was found to be unstable under these annealing conditions. At first glance, the LEED pattern suggests a structure with (3×3) oxide units per (4×4) Rh cells (marked by red lines in Figure 4.1a, which would require an oxide lattice of 358 pm. This would be an expected structure, as three *c*-ZrO₂ unit cells (3×0.36 nm = 1.08 nm) nearly coincide with 4 Rh unit cells (4×0.269 nm = 1.076 nm). However, when using the Rh spots as a gauge to measure the true value of the oxide lattice constant, we find a value of approximately 0.34 nm – far shorter than the 358 pm required for a true $(3 \times 3)/(4 \times 4)$ structure. The oxide structure can therefore not be explained by this superstructure. STM shows that the film is not perfectly ordered, as can be seen from the variations in the surface structure. In ordered areas, the most common feature resembles a rosette. The rosettes are hexagonally ordered with a periodicity of 1.2 nm, marked in the inset of Figure 4.1a. Usually, the domains of well-ordered rosettes are much smaller than in the inset of Figure 4.1a, however. From comparison with atomically resolved images of the Rh(111) surface (not shown), we find that the rosette lattice corresponds to a $(\sqrt{21} \times \sqrt{21})R10.9^\circ$ superstructure with respect to Rh(111). We can explain the ideal rosette lattice using the lattice constant from LEED if it is a $(\sqrt{13} \times \sqrt{13})R13.9^\circ$ superstructure w.r.t. a cubic ZrO₂(111) lattice. This results in an oxide lattice constant of 341 pm and a small 3° rotation of the oxide w.r.t. the Rh lattice. The in-plane lattice constant of 341 pm for ZrO₂ is surprisingly

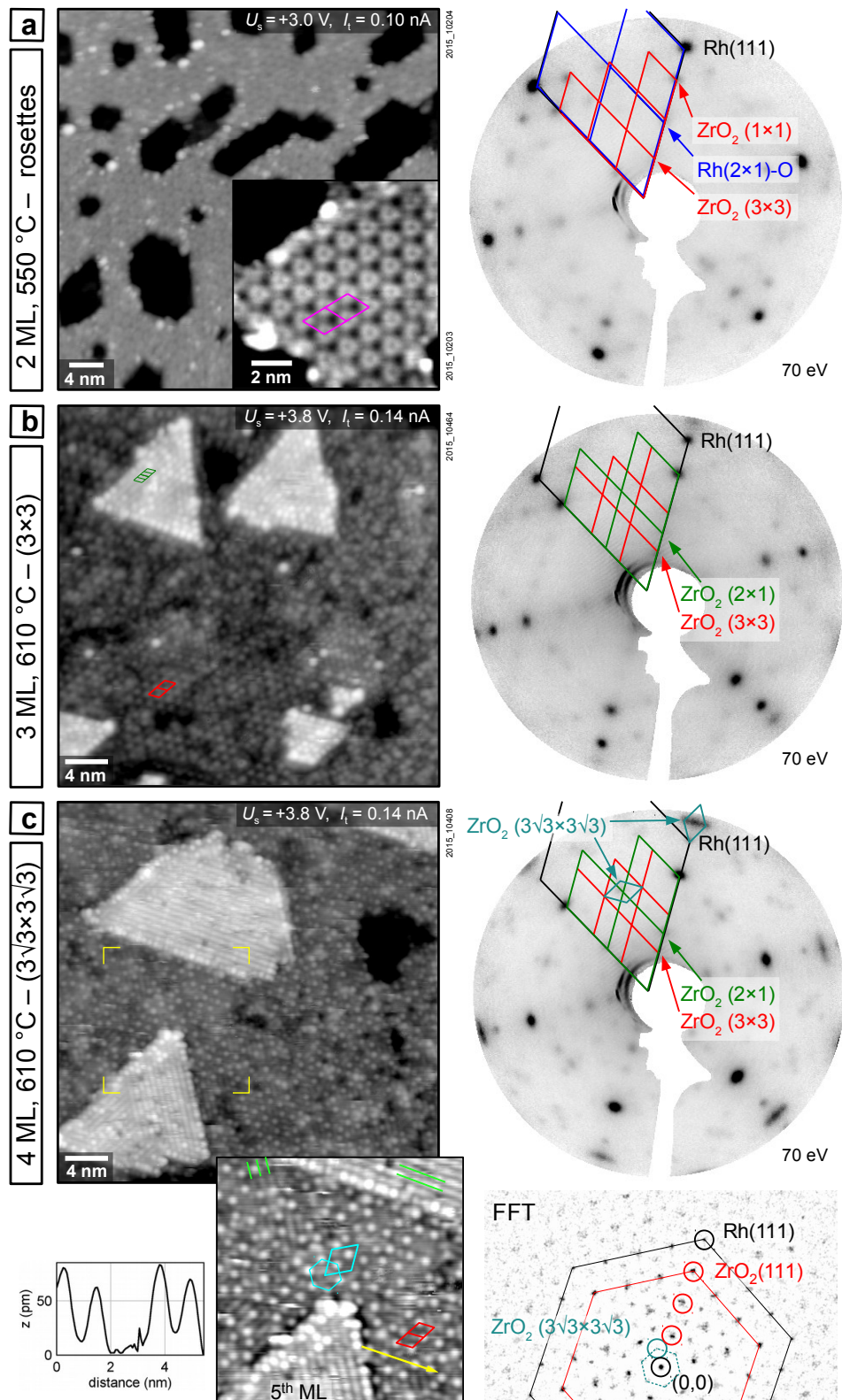


Figure 4.1: Surface structures of zirconia films with 2–4 ML thickness, as seen with STM (left) and LEED (right). Each thickness has its own surface reconstruction: (a) Rosettes at 2 ML, unit cell marked in pink, (b) (3×3) at 3 ML, (c) and a $(3\sqrt{3} \times 3\sqrt{3})$ superstructure of small protrusions at 4 ML. For 4 ML, the line scan shows the height of the protrusions, and an FFT of the protrusions shows weak spots of their superstructure. Superstructures are given with respect to $c\text{-ZrO}_2(111)$.

short: For metastable tetragonal or cubic ZrO₂, the corresponding value would be about 359–362 pm [22], and even 1 ML (single-trilayer) zirconia films have a larger in-plane lattice constant of ≈ 350 pm [41, 43]. As decreasing the lattice constant is constrained by O–O repulsion (see chapter 1.2), we consider it likely that these films are substantially oxygen-deficient. Based on the LEED image, however, the rotation of the oxide is less than 1° in most areas of the surface and therefore smaller than the 3° expected from the epitaxial relationship. This deviation can be explained, as we observe only small patches of well-ordered rosettes by STM, so the superstructure measured above is only an approximation. Thus, also the in-plane lattice constant may be slightly different from the one calculated assuming a perfectly commensurate superstructure.

We also observe LEED spots from a (2×1) -O structure on Rh(111) in the holes of the film. This structure is common when annealing Rh(111) in oxygen [138]; the corresponding periodicity can be also detected by STM in the holes (not shown).

A 3 ML-thick film annealed at 610 °C appears quite different in STM, see Figure 4.1b. Apart from some disordered regions in the upper half of the image, the predominant structure shows a (4×4) cell with respect to the substrate, which now nicely corresponds to (3×3) cells of the oxide (see the LEED pattern). This corresponds to an in-plane lattice constant of 358 pm, which is already close to the value for cubic zirconia (≈ 362 pm, see Figure 1.1). There is no sign of the rosette structure that was found at 2 ML. It would be tempting to anneal to a higher temperature in order to improve the ordering and eliminate the disordered patches. Unfortunately, these thin films break up easily, forming thicker films with holes. These then have the structures of the respective thicker films. The 3 ML-thick film shown here already has a small number of holes down to the Rh substrate, which explains the bright Rh spots in LEED. In addition to the ZrO₂ (3×3) superstructure, LEED shows a ZrO₂ (2×1) structure that originates from 4 ML-high terraces (according to STM). This structure is discussed below.

In Figure 4.1c, a 4 ML-thick film is shown, with a few terraces having a total height of 5 ML. The LEED image again indicates a (3×3) oxide lattice per (4×4) Rh units. The 4 ML-thick areas are covered by isolated protrusions with a typical height of 60 pm, see the contrast-enhanced inset and the line profile next to the inset. These protrusions can form a honeycomb-type short-range order with a $(3\sqrt{3} \times 3\sqrt{3})R30^\circ$ superstructure with respect to the oxide or $(4\sqrt{3} \times 4\sqrt{3})R30^\circ$ with respect to Rh (hexagon

in inset). We consider it likely that these protrusions are adatoms or molecules, but not impurities, as these features are solely present on the 4 ML films. The protrusions nicely mark the lattice periodicity: A fast Fourier transform (FFT) of their positions extracted from the STM image (bottom right of Figure 4.1c) shows the Rh and ZrO₂ periodicities, as well as weaker spots for the $(3\sqrt{3} \times 3\sqrt{3})R30^\circ$ lattice. Note that the circles in the FFT are exactly equidistant, marking the exact positions for a (4×4) superstructure. The oxide lattice is rotated by $\approx 0.5^\circ$ with respect to the Rh lattice, which causes slight deviations of the maxima in the FFT from the center of the circles.

Between the protrusions, rows can be made out in the STM image in Figure 4.1c (marked by green lines in the top left of the inset). These rows have the same periodicity as the rows on the 5 ML-thick structure, see Figure 4.2a and the islands in Figure 4.1c. The distance between the rows is ≈ 0.6 nm, which corresponds to a (2×1) structure with respect to the oxide, the expected unit cell of tetragonal zirconia (Figure 1.1). The 4 ML-high islands on the 3 ML film also show these rows (Figure 4.1b), thus the (2×1) already weakly appears in LEED at this coverage. This row structure persists also for thicker films, see below.

4.2.2 Tetragonal Zirconia films

Zirconia films with a thickness of 5 ML and annealed at temperatures of up to 730 °C in 5×10^{-7} mbar of O₂ are dominated by the row structure mentioned above. This structure has a (2×1) periodicity with respect to a ≈ 360 pm c-ZrO₂(111) lattice, see Figure 4.2a. This is the structure expected for a tetragonal ZrO₂ film. As expected for the ABC stacking of t-ZrO₂(101), the rows of adjacent layers are laterally shifted by $\frac{1}{3}$ of their spacing. This can be seen in panel a1 of Figure 4.2 (green lines). Domain sizes of ≈ 30 nm can be reached upon annealing at 730 °C in O₂ (Figure 4.2a). The apparent corrugation of the tetragonal rows is surprisingly high (typically 30 pm; up to 100 pm at 2.4 V sample bias). This cannot be explained by the geometric heights of the surface atoms in the tetragonal structure ($\Delta z = 35$ pm for the O atoms in a bulk-terminated structure, less for a relaxed surface [29]; the Zr atoms have roughly equal heights). Thus, the high corrugation stems from either a surface reconstruction or an electronic effect. As neighboring domains of the tetragonal surface appear to blend into each other in some places, then appearing like a (2×2) structure (yellow circle in Figure 4.2), we consider the latter explanation more likely.

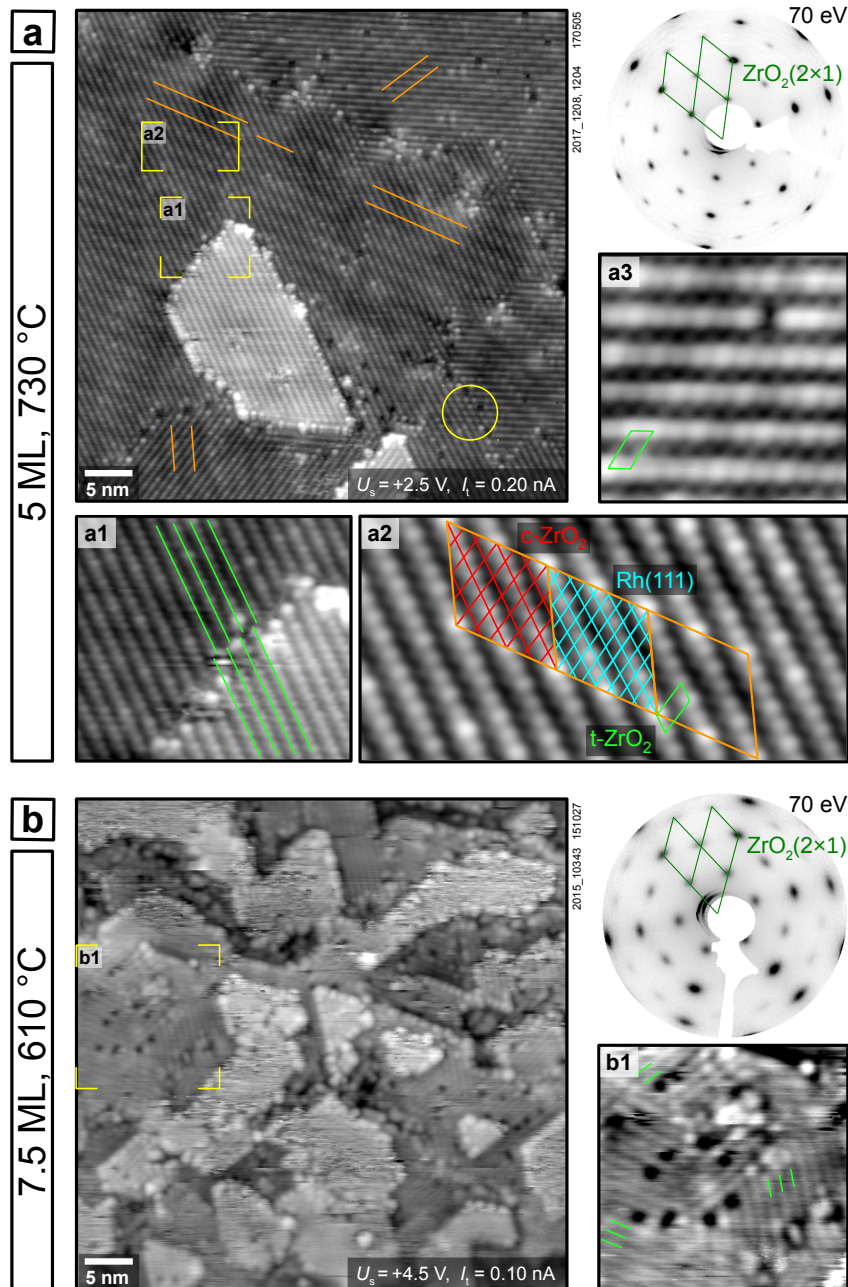


Figure 4.2: Tetragonal zirconia films with (a) 5 ML and (b) 7.5 ML, as seen with STM (large and zoom-in frames) and LEED (top right). Green lines mark the (2×1) surface structure with respect to cubic $\text{ZrO}_2(111)$. When going from the 5th to the 6th ML, the rows shift by $\frac{1}{3}$ of a unit cell as is expected for t- ZrO_2 , see frame (a1). Orange lines indicate the moiré structure visible in 5 ML films and some of its domain boundaries. The moiré superstructure cells are shown superimposed on the Fourier-filtered STM image in frame (a2), and a point defect is visible in frame (a3). The STM images have been processed to increase the contrast on the terraces.

At a thickness of 5 ML, the surface structure can be atomically resolved with STM. With increasing film thickness, the bias voltage has to be increased for stable imaging due to the higher thickness of the insulating material between the tip and the (conductive) substrate. The resolution of the images decreases accordingly (see the image of the 7.5 ML film in Figure 4.2b). It is difficult to obtain stable tunneling at a thickness of 10 ML; a minimum bias of 7.2 V is required. Nevertheless, the row structure of t-ZrO₂ remains visible at 7.5 ML (frame b1 of Figure 4.2) and at 10 ML (not shown), and the LEED pattern always shows a (2 × 1) pattern w.r.t. c-ZrO₂(111).

The structural order of thicker films can be tracked best by the sharpness of LEED spots, see Figure 4.3. LEED measurements are possible at thicknesses where STM does not give reasonable results anymore. The tetragonal structure stays stable at higher thicknesses (tested up to 50 ML ZrO₂), yet the spots become broader when the thickness is increased from 5 to 20 ML. An additional increase to 50 ML does not have a measurable effect. Annealing a 50 ML film for additional 90 min increases the spot sharpness again. Without the possibility of STM measurements, it is difficult to determine the reason for this decrease of overall structural order; a possibility would be roughening of the surface, i.e. an increase in island number and height.

Although an almost perfect 4:3 lattice match between tetragonal ZrO₂ and Rh(111) would be possible, the oxide is not exactly commensurate with the underlying Rh substrate. Upon careful inspection of the STM images, we find more than the three directions of the rows (in 120° increments) expected from the rotational symmetry of the substrate: The rows do not run exactly along the Rh⟨11̄0⟩ directions, but deviate from the close-packed directions of the substrate by up to ≈ 3°. This is accompanied by a moiré pattern, which is clearly visible in the STM images of the a 5 ML-thick film (orange lines in Figure 4.2a). The moiré pattern becomes almost invisible in regions with 6 ML thickness and cannot be discerned in STM images of thicker films. There are several similar moiré patterns, however, and each type of moiré has six possible orientations of the oxide (three rotational domains, plus mirror symmetry). The different rotations of the zirconia film in different domains, which lead to the different moirés, cannot be resolved in LEED; rather than split into separate spots, the diffraction maxima of the hexagonal pattern in Figure 4.2 are only slightly elongated in the azimuthal direction. For one of the domains with a nearly commensurate lattice, we could determine the moiré structure with respect to the substrate below (Figure 4.2, frame a2). This moiré cell corresponds to a (7 × 7)R21.8° superstructure with

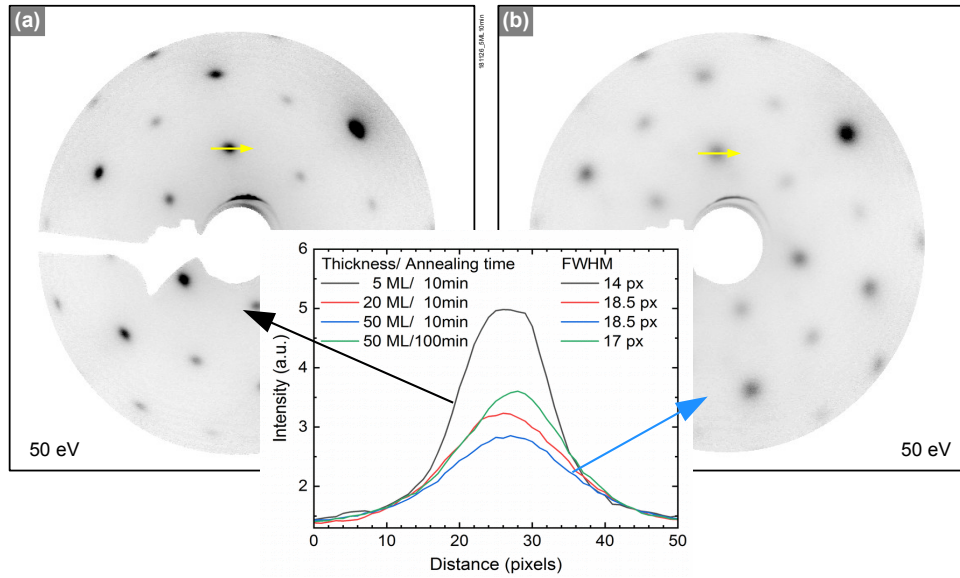


Figure 4.3: LEED of tetragonal ZrO₂ films of different thicknesses, annealed for 10 min at 670 °C in $p_{\text{O}_2} = 5 \times 10^{-7}$ mbar. **(a)** 5 ML-thick and **(b)** 50 ML-thick film. Line profiles of these two preparations plus a 20 ML-thick film and the 50 ML-thick film annealed for an extra 90 min. The FWHM-values are given in the plot: Spots broaden with increasing thickness, and the additional annealing time decreases the spot width again.

respect to Rh(111), which corresponds to $(2\sqrt{7} \times 2\sqrt{7})R19.1^\circ$ cells of cubic ZrO₂(111), or half that number of tetragonal cells. This yields a rotation of 2.7° between the oxide lattice and the Rh(111) substrate; the average in-plane nearest-neighbor distance in the zirconia lattice is calculated as 355 pm and the in-plane angles between the nearest-neighbor directions would be multiples of exactly 60° . This moiré cell is only approximate, however. The moiré changes phase on a length scale of 10 nm; this can be seen at the orange lines in Figure 4.2a. The phase change probably happens because the interatomic distance of 355 pm would be too short for t-ZrO₂. In addition, this deviation from a perfectly commensurate cell also leads to a deviation from angles of exactly 60° (as expected for t-ZrO₂, see Figure 1b). In other parts of the surface, we find roughly a 4:3 lattice match with the substrate in one direction, but nevertheless a moiré structure indicating a different (shorter) lattice constant in the other directions and deviations from 60° angles. Our best estimate for the average in-plane interatomic distances in the t-ZrO₂ films is around 357 pm, about 0.5% smaller than the room-temperature values from the literature [22], see Figure 1b.

4.2.3 Monoclinic Zirconia films

Upon annealing a 5 ML-thick ZrO_2 film at 850°C in 5×10^{-7} mbar O_2 , a phase transformation from t- ZrO_2 to m- ZrO_2 occurs. (Between 730°C and 850°C , the film is partially transformed with some domains showing the monoclinic and others the tetragonal structure.) Figure 4.4a shows a high-resolution STM image of the surface; the surface lattice appears hexagonal at first glance and no signs of the tetragonal row structure are visible. However, the monoclinic phase of zirconia is distorted with respect to the cubic and tetragonal phases, see Figure 1.1. Due to this distortion, in order to compare the unit cell of our film with the cell size of bulk m- ZrO_2 , we have to compare three different in-plane distances (or two distances plus one angle); approximate values for these three distances are shown in the inset of Figure 4.4a. In contrast to t- ZrO_2 , the monoclinic lattice does not have an approximate 6-fold symmetry, which would help us correct for distortions of the STM images and thereby make an accurate determination of the lattice constants possible. As a way out, we took three sets of images with the fast scanning direction aligned with each of the $\text{ZrO}_2\langle 110 \rangle$ directions. We then measured the distances along the fast scanning direction, which is almost unaffected by thermal drift or piezo creep. For calibration, we used atomically resolved images of the Rh(111) lattice recorded with the same scanning angle and scan speed (after removal of the oxide by sputtering). In our experience, this procedure should be accurate within $\approx 1\text{-}2\%$. The side lengths of the unit cell measured by this procedure are 727, 708, and 664 pm, which compares reasonably well with the values for m- $\text{ZrO}_2(\bar{1}11)$: 745, 733, and 678 pm [23]. The deviations from the expected values may hint at monoclinic distortions in the thin films being slightly different from the bulk. For comparison, the cell side lengths for the energetically less-favorable termination m- $\text{ZrO}_2(111)$ [29] would be 797, 745, and 733 pm [23]. Thus, we can rule out the (111) orientation, which would be the only other symmetry-inequivalent type of m- $\text{ZrO}_2\{111\}$ surfaces. The measured distances are also far from those expected for the orthorhombic structures, see chapter 1.2; their unit cells have much less distortion with respect to c- ZrO_2 . Thus, these films can be safely identified as m- $\text{ZrO}_2(\bar{1}11)$.

In the FFT of an STM image with four different domains (Figure 4.4d), spots from the different domains can be seen in each direction. In LEED, these spots are smeared out, indicating slight variations in azimuthal orientation (Figure 4.4b). Nevertheless,

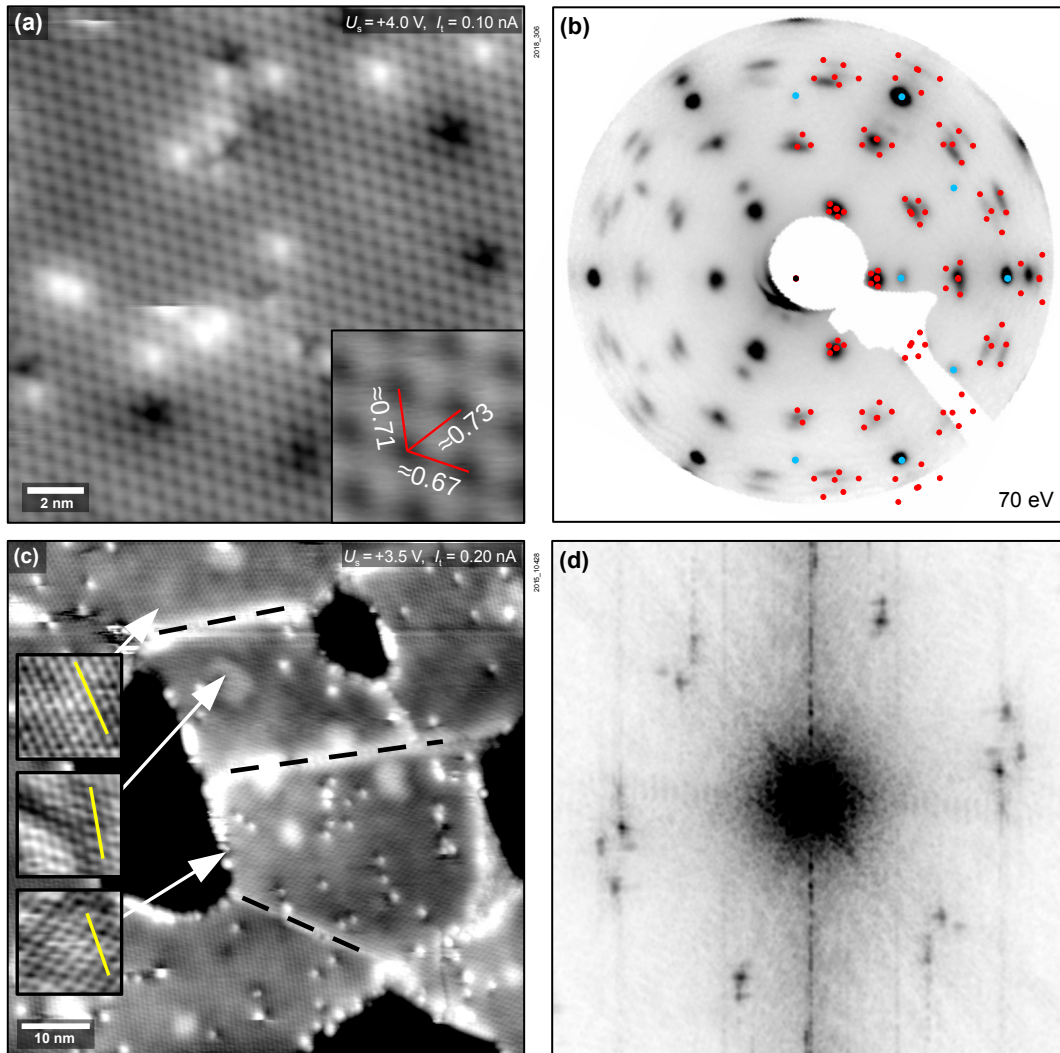


Figure 4.4: Monoclinic zirconia films: Upon annealing a 5 ML-thick film at 850°C in 5×10^{-7} mbar O_2 , the film breaks up and transforms into the thermodynamically stable monoclinic structure. **(a)** High-resolution STM image of the structure. The inset shows a zoom to one unit cell, with approximate lattice parameters given in nm. **(b)** LEED image. The calculated LEED pattern of the $(\bar{1}11)$ surface of monoclinic zirconia is shown by red dots: spots originating from $\text{Rh}(111)$ or $\text{Rh}(111) (2 \times 1)\text{-O}$ are blue. **(c)** STM overview image showing the holes down to $\text{Rh}(111)$ and different domains (a few grain boundaries are marked by black broken lines): In the Fourier transform, these domains result in a splitting of the spots. **(d)**

the splitting of the monoclinic spots makes it easy to distinguish monoclinic and tetragonal films by LEED. Figure 4.4b also shows the expected diffraction pattern from six domains of m-ZrO₂($\bar{1}11$); these show a good agreement with experiment except for the right edge of the LEED screen, where the experimental image is distorted. Apart from the ZrO₂ spots, only Rh(111)-(1 × 1) and (2 × 1) spots are visible; the Rh(111)-(2 × 1) again stems from the (2 × 1)-O overlayer that is formed on bare Rh in the holes upon annealing in O₂ [138].

Together with the tetragonal-to-monoclinic transformation, the film usually breaks up, which leads to holes down to the Rh(111) substrate, see Figure 4.4c. The material from the holes spreads over the remaining zirconia areas, and locally increases the thickness (e.g., from 5 to 6 ML), see Figure 5.1 on page 111. The formation of holes and the phase transformation do not always go hand in hand, however: By changing the deposition parameters, we can prepare a tetragonal film that breaks up at temperatures below the phase transition point. In this case, we have lowered the front grid voltage of the sputter source from 150 V to 60 V, which reduced the energy of the Ar⁺ ions that are hitting the surface during deposition [50]. Thus, the growth conditions become more comparable to thermal deposition. Such a weakly-sputtered film breaks up already at an annealing temperature of 670 °C, while it remains mostly in the tetragonal structure; smaller monoclinic domains can be seen in STM images. The onset temperature of the tetragonal-monoclinic transition is therefore lowered. The phase transformation from a tetragonal to a monoclinic film can be reversed by annealing at very high temperatures of 920 °C in UHV ($p_{\text{base}} < 1 \times 10^{-10}$ mbar), checked by the XPS E_{B} position, see section 4.4. (When annealing at such high temperatures in UHV, an ultrathin film forms in the holes and covers the Rh substrate, see chapter 5.) This preparation leads to a tetragonal film with holes down to Rh(111). Partial reversal of the transformation can be reached with UHV-annealing at lower temperatures; with higher temperatures, larger parts of the structure are transformed back towards tetragonal zirconia.

4.2.4 Discussion

Thin-film zirconia model systems have been studied since 1990 [39], yet the relation of these films to the ZrO₂ bulk structures could not be determined unambiguously. In hindsight, the LEED patterns originally interpreted as (2 × 2) with respect to c-

ZrO₂(111) by Maurice *et al.* and Meinel *et al.* [38,39] most likely correspond to three domains of the tetragonal structure, i.e. the three (2 × 1) domains in Figure 4.2. On Pt(111), these structures were not stable when annealing for more than one minute at 680 °C in O₂ and transformed into ($\sqrt{19} \times \sqrt{19}$) R36.6° w.r.t. Pt(111) [38]; this is the same structure as the ultrathin zirconia films on Pt₃Zr(0001) [41]. It is possible that this low stability is due to easy dissolution of Zr in the Pt bulk (the dissolution enthalpy of Zr in Pt is exceptionally high [139, 140], which was tested in chapter 5.2.3, Figure 5.5). On the other hand, the lower stability compared to our films might also be a consequence of thermal deposition in Refs. 36–38 vs. sputter deposition with additional ion bombardment in our case (remember that our films grown with softer ion bombardment than usual are less stable). The gentle Ar⁺ ion bombardment by the sputter deposition source may help stabilizing the films by creating defects or slight intermixing; especially reactive Zr atoms embedded in Rh at the interface may help stabilizing the films by providing strong Zr–O bonds with O in the bottom-most oxide layer (cf. the stabilization of zirconia films on Pd₃Zr(0001) [43]). The transformation of the films to monoclinic zirconia was not reported in literature previously. It occurs at temperatures of 850 °C, so the higher thermal stability of our sputter-deposited films on Rh(111) compared to films created by thermal deposition on Pt(111) is certainly beneficial.

Let us now consider the stability of the bulk phases (Figure 1a), where m-ZrO₂ is stable at room temperature and t-ZrO₂ is the high-temperature phase. It is then surprising that the tetragonal phase in the thin films is stable at lower annealing temperatures ($T \leq 730$ °C) and transforms to the monoclinic phase when annealed at 850 °C. Assuming a lower surface energy for t-ZrO₂ than m-ZrO₂, it has been suggested that the monoclinic-to-tetragonal transition temperature decreases with decreasing film thickness (below 1 μm) and should reach room temperature in the range of 20 nm [141]. As mentioned in the introduction, see chapter 1.2, the role of the surface energy stabilizing the tetragonal phase has to be questioned [10,26,27]. In any case, this is not the behavior encountered in our case, as the 5 ML (1.5 nm) tetragonal films can still be transformed to the monoclinic phase, which then remains stable upon cooling to RT. The tetragonal film is therefore in a metastable state, stabilized by the interface to the Rh substrate and oxygen deficiency (see chapter 4.4). Considering that Zr–O bonds get broken and the lattice gets distorted upon the tetragonal-to-monoclinic transformation (see chapter 1.2), it is clear that a substantial activation

energy is required to transform the films. The area density changes from 8.74 to 8.99×10^{18} Zr atoms/m² per layer (based on room-temperature bulk lattice constants [22, 23]), and the transformation also involves in-plane shear. In contrast to the expansion of the interlayer spacing (295 to 317 pm), changing the area density and in-plane shear clearly require thermal activation.

When comparing the tetragonal and the monoclinic films on Rh(111), the tetragonal films appear rather flat, while the monoclinic films show long-distance modulations in their apparent height, with bright halos around both point defects and grain boundaries (Figure 4.4c). At positive STM sample bias, such an increase of the apparent height (increased tunneling current at constant height) is typical for downwards band bending [142]. These observations are important for the use of (chemically doped) zirconia as a solid-state electrolyte: Grain boundaries (GBs) in YSZ impede oxygen ion transport ("grain boundary blocking"); this is attributed to the positive charge at GBs [143], probably caused by oxygen vacancies at GBs. (Oxygen vacancies in YSZ carry 2+ charge with respect to the undisturbed lattice with O²⁻ at the respective site – V_O^{••} in Kröger-Vink notation [144].) Our STM images are consistent with this model. The flat appearance of the tetragonal films points at a fixed position of the bands. Downwards band bending cannot occur if the conduction band minimum is already close to the Fermi level. In chapter 4.4, XPS measurements of tetragonal thin films are presented that show that, indeed, oxygen vacancies are present in tetragonal zirconia thin films; electrons from V_Os are transferred to the Rh(111) substrate, thereby inducing band bending. The existence of V_Os in tetragonal zirconia nicely fits the notion that V_Os are responsible for the stabilization of the tetragonal phase in nanoscale ZrO₂, and also in our thin films.

Let us finally discuss the films of lower thickness. While LEED indicates that all of these films are based on c-ZrO₂(111), the influence of the substrate does not allow these films to develop the surface structures expected for bulk ZrO₂. The in-plane lattice constants of the 2 ML film are clearly below those of the thicker films and the bulk phases. Again, this indicates sub-stoichiometric (oxygen-deficient) films; for example, it is possible that the rosette structure is related to ordering of oxygen vacancies. Starting from 3 ML, the in-plane lattice constants are already close to the bulk values ($\approx 3:4$ lattice match with Rh). For 4 ML films, the row structure of the tetragonal films is already locally visible by STM. It is unclear whether the bright features in Figure 4.1c are topographic (e.g. adatoms, small molecules, or clusters

on top of the t-ZrO₂ surface) or electronic features. The high corrugation of these features (line scan in Figure 4.1c) points to a topographic feature. It is unlikely that these features are due to impurities, as they were not observed on thicker films, and no impurities were found when investigating the cleanliness of the sputter source, see chapter 2.2.

4.3 Conclusion

Few-layer zirconia films can be reliably prepared by UHV-compatible sputter deposition. They show layer-by-layer growth and good homogeneity. Up to a thickness of 4 ML, the surface structure of the zirconia films is influenced by the underlying Rh(111) substrate. For each thickness below 5 ML, a different superstructure is found; apart from the 2 ML films, all structures are close to a commensurate lattice with (3×3) c-ZrO₂(111) cells on (4×4) Rh(111) unit cells. Zirconia films of 5 ML or larger thickness show the surface structures of either tetragonal or monoclinic zirconia, depending on the annealing temperature. Both structures can be prepared with large, atomically flat terraces; their surface lattices were resolved by STM, confirming their crystallographic structure. Preparation of a completely monoclinic film needs annealing at temperatures of at least 850 °C; at these temperatures, the film breaks up and holes reaching down to the substrate appear. Thus, the films show some instability towards dewetting. Due to the insulating nature of ZrO₂, imaging the surface with STM becomes increasingly difficult with increasing film thickness. Therefore, the thinnest films showing the structures of the ZrO₂ bulk phases (5 ML) are the best choice for an STM-accessible ZrO₂ model system. In comparison with the previous ZrO₂/Pt(111) model system, we believe that there are three reasons for the superior film homogeneity and stability on Rh(111): Firstly, the lower solubility of Zr in Rh than in Pt. Secondly, the 3:4 lattice matching, which leads to low rotation angles between different domains, and thirdly the use of a UHV-compatible sputter source providing additional slight ion bombardment.

4.4 Energy Levels of Thin ZrO₂ Films

Building on the results from the previous section, a thorough XPS study of these structurally well-defined 5 ML-thick zirconia films is presented in this section. It is based on an upcoming publication, Ref. 137.

4.4.1 XPS of Tetragonal and Monoclinic Films

XPS measurements of both, tetragonal and monoclinic 5 ML-thick films are shown in Figure 4.5. The films were annealed in O₂ at 670 and 810 °C, respectively. The Zr 3d_{5/2} binding energies of tetragonal (182.9 eV) and monoclinic films (181.6 eV) differ by 1.3 eV. In the O 1s region, this difference is 1.1 eV (530.6 eV and 529.5 eV, respectively). A closer look at the Zr 3d signal of the tetragonal film, see Figure 4.5a, reveals that the spectrum consists of a doublet with a shoulder to the low-binding-energy side. The spectrum can be fitted with two doublets – the larger one at 182.9 eV, the smaller at 180.9 eV. As the smaller signal decreases with increasing thickness, see the inset of Figure 4.5a, we assign it to the interface layer bonded to the Rh substrate. This low-binding-energy feature appears in the same energy range as the Zr signal of ultrathin zirconia films on Pt₃Zr(0001) (180.7 eV) [42]. It was already predicted by DFT that the interface layer of few-monolayer ZrO₂ films would have a distinctively different binding energy from the rest of the film, close to the value of ultrathin ZrO₂ [42]. The area of the interface doublet is between 8% and 10% of the main peak, depending on the exact preparation; this is somewhat less than the expected 14% from an attenuation simulation with the SESSA code [73]. The Zr 3d peak of the monoclinic films shows no shoulder, and can be fitted with only one doublet. It cannot be excluded that an interface peak also exists in this case. As the peaks would overlap, we cannot resolve it experimentally. For the O 1s region, where the differences between interface and main signal are even smaller [42], one peak was sufficient for a good fit in both cases, tetragonal and monoclinic.

The Zr 3d and O 1s binding energies depend on the exact preparation parameters, i.e. oxygen partial pressures during deposition and annealing, annealing temperature, and film thickness. For monoclinic films, a small spread of 181.8–181.6 eV was encountered. Tetragonal films show binding energies in a larger range, between 182.6 eV and 183.4 eV. The interface peak shifts in the opposite direction than the main

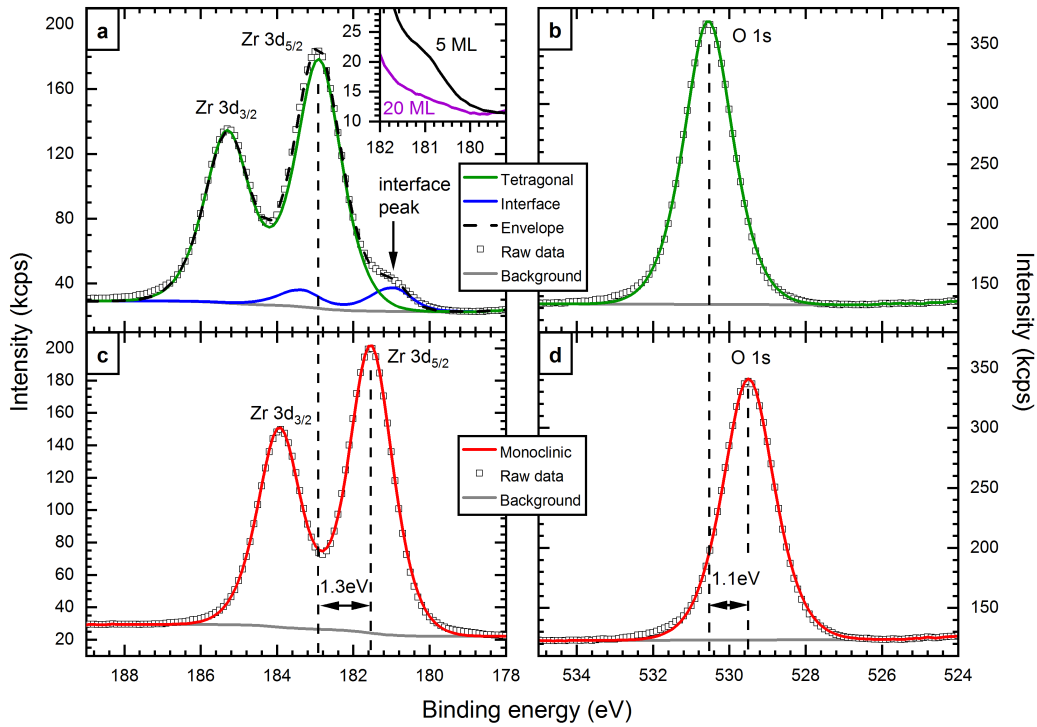


Figure 4.5: Fitted XPS spectra of (a,b) tetragonal and (c,d) monoclinic ZrO_2 films: All spectra can be fitted with one component, except for $\text{Zr } 3d_{\text{tetragonal}}$, which features a shoulder resulting from the interface layer of the film. The main signal shows a ΔE_B between monoclinic and tetragonal of 1.3 eV in Zr 3d and 1.1 eV in O 1s. The inset of (a) shows the interface peak area for a 5 ML (black) and a 20 ML-thick (violet) film. The interface peak is strongly attenuated at 20 ML thickness.

peak; at high E_B (>183 eV) of the main peak, it is a distinct peak with E_B between 181.7 eV–182.0 eV. At lower E_B , it is a less distinct shoulder as in Figure 4.5a, and becomes invisible when the main peak reaches ≈ 182.6 eV. For the main peak, higher annealing temperatures lead to higher binding energies (Figure 4.6), as does lower p_{O_2} during annealing (not shown). The pressure dependence could however not be studied in detail over a large range of p_{O_2} (many orders of magnitude) due to experimental limitations. Figure 4.7a shows the dependence of the binding energy on film thickness; for tetragonal zirconia, a shift of +0.1 eV occurs from 4 to 5 ML thickness (both annealed at 670 °C). When increasing the thickness to 7.5 ML (annealed at 550 °C), a further shift of +0.1 eV occurs. These values fit previous measurements of 8.3 ML compared with 4.5 ML ZrO₂ films on Pt; a shift of 0.3 eV was reported (corrected for the Pt 4f shift) and explained by charging [40]. This can be excluded in our case, see below. For monoclinic zirconia, the binding energies are almost independent of film thickness, see Figure 4.7b. For a deposited amount of 4, 5, and 7 ML, E_B shifts less than 0.1 eV. It should be noted that different film thicknesses need different annealing temperatures to reach full transformation to the monoclinic structure. These temperatures were 770 °C for 4 ML, 810 °C for 5 ML, and 870 °C for 7 ML. Above these temperatures, no further E_B shifts occur for monoclinic zirconia, as was tested for 5 ML. E.g., a 5 ML film annealed at 850 °C exhibits the same E_B of 181.6 eV as after annealing at 810 °C. The same behaviour can be expected for other thicknesses.

As discussed in detail in section 4.2.3, typical monoclinic films contain holes reaching down to the substrate, in contrast to tetragonal films created with the standard preparation parameters. Using different sputter deposition parameters however [24], we can also create tetragonal films that break up and form holes (exposing the Rh(111) substrate) when annealing to 670 °C. These films show a lower E_B than usual – 182.1 eV; the binding energy difference with respect to monoclinic ZrO₂ is only 0.5 eV for Zr 3d and 0.3 eV for O 1s ($E_B = 529.9$ eV). Another preparation method for tetragonal films with holes starts with a monoclinic film (containing holes). By annealing at 920 °C in UHV, the film can be transformed back to the tetragonal structure (also this film does not fully cover the substrate). We attribute this transformation to reduction of the ZrO₂ film, i.e. the formation of oxygen vacancies, which stabilize the tetragonal phase [26]. After annealing this film at 610 °C in O₂, the Zr 3d level again exhibits a binding energy of 182.1 eV. In both preparations, the Rh surface in the holes is covered by a (2 × 1)-O superstructure as usual for Rh annealed in oxygen at these

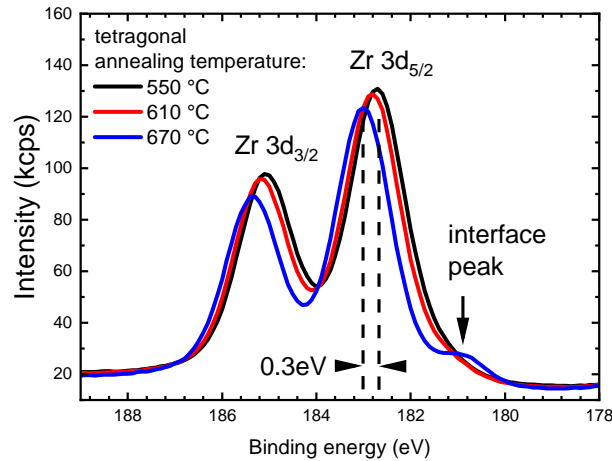


Figure 4.6: Dependence of the Zr 3d peak position of 5 ML-thick tetragonal films on the annealing temperature (annealing in 3×10^{-6} mbar O₂). The binding energy shifts from 182.7 eV at 550 °C (black) to 182.8 eV at 610 °C (red) and 183.0 eV at 670 °C (blue).

conditions [138, 145].

Apart from the peak positions, the peak width (FWHM, full width at half maximum) varies with preparation. In general, the main doublet of 5 ML-thick tetragonal films exhibits a peak width in the range of 1.35 eV – 1.5 eV, where low FWHM values are encountered for preparations with high binding energies. This behaviour is reversed for 5 ML-thick monoclinic films, where the range is 1.33 eV ($E_B \approx 181.6$ eV) – 1.41 eV (higher $E_B \approx 181.8$ eV).

Additionally, elemental ratios can be extracted from XPS measurements. One has to act with caution here however, as truly quantitative XPS results are difficult to achieve. The main reason for this is that the transmission function (sensitivity over kinetic energy) of typical XPS analysers are not known in detail. Therefore, analysing peak areas several 100 eV apart (as in the case of Zr 3d and O 1s) is only possible if a trustworthy reference is available. This is not the case for zirconia; pure bulk single crystals are not available, and the surface stoichiometry and composition of thick films or powders are not known. We therefore only compare tetragonal and monoclinic films. To compensate for changing film thickness (monoclinic films dewet the substrate and become thicker as a result) and the signal of O adsorbed on the uncovered Rh substrate (if any), we resort to XPS simulations with the program SESSA [73] (based on the morphology determined by STM). Then, the different pre-

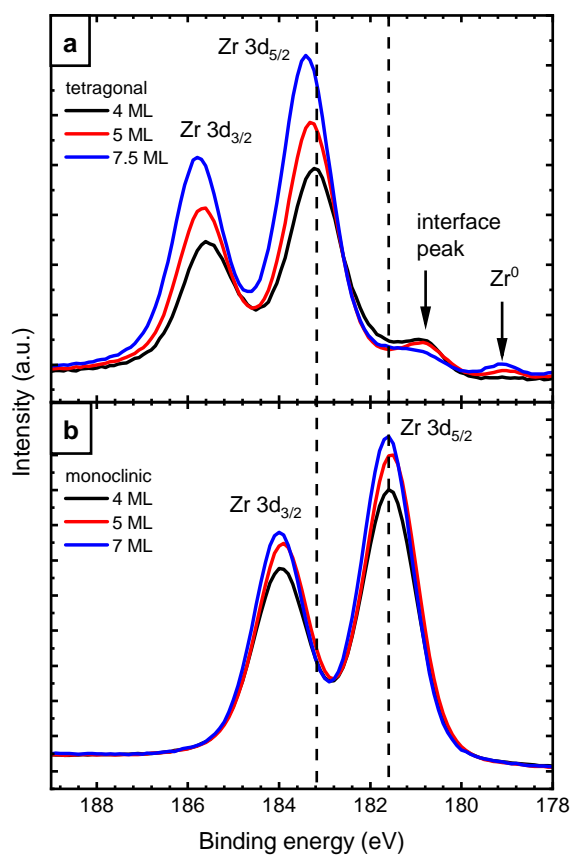


Figure 4.7: Changes of the Zr 3d peak position with film thickness. **(a)** Tetragonal ZrO_2 films show a shift towards higher binding energy, which increases with increasing film thickness. The interface peak decreases with increasing thickness. Additionally, a small signal from metallic Zr remaining from sputter-deposition is found. **(b)** Monoclinic ZrO_2 of different thicknesses shows no substantial shift. The spectra in (a) have been acquired with a different analyzer (see chapter 2.1.1).

parations can be compared with each other. All films show similar Zr:O ratios; the variations lie within $\pm 2\%$. These variations are within the error bars of our analysis.

Due to the influence of the Rh substrate, which is dominating the spectrum at the Fermi edge, the band gap region of 5 ML-thick films cannot be measured directly. For a 50 ML-thick film (annealed at 670 °C in $p_{\text{O}_2} = 5 \times 10^{-7}$ mbar for 100 min; no difference to $t_{\text{anneal}} = 10$ min), however, no signal from the Rh substrate is detected anymore. XPS data of this film, and the 5 ML-thick monoclinic film from Figure 4.5 for comparison, are shown in Figure 4.8. The valence band edges of both preparations were fitted, giving valence band onsets of 4.9 eV for the thicker film, and 0.0 eV for the thinner film, as expected for a signal dominated by metallic Rh. With a total band gap of $\approx 5\text{--}6$ eV [1], it is clear that the Fermi energy of the thicker film is close to the conduction band edge. Figure 4.8b shows the Zr 3d region of both films, with the Zr 3d_{5/2} peaks at 183.7 eV and 181.6 eV, respectively. The inset shows the O 1s region, where the difference is only 1.9 eV ($E_{\text{B}} = 531.4$ eV and 529.5 eV, respectively), 0.2 eV less than for Zr 3d, as usual for a comparison between tetragonal and monoclinic zirconia. The high E_{B} of the 50 ML-thick film follows the same trend as in Figure 4.7. ΔE_{B} can be used to estimate the position of the bands with respect to E_{F} for the monoclinic film. The whole electronic structure – including conduction and valence band – is shifted to lower E_{B} by 2.1 eV. This puts the valence band onset 2.8 eV below the Fermi level; with a band gap of $\approx 5.5\text{--}6$ eV, the Fermi energy is very close to the mid-gap position. A comparison with a fully oxidized (see below) 5 ML-thick film gives a stoichiometry ZrO_{1.83} for the 50 ML-thick film.

4.4.2 Possible Reasons for Differences in Binding Energy

Let us focus on the large difference of ≈ 1.3 eV between the Zr 3d levels of the tetragonal and monoclinic films. This chapter presents explanations that are commonly encountered in XPS studies, but can be excluded for this work. Then, oxygen vacancies in the tetragonal film are presented as the favoured explanation. At a first glimpse, the large ΔE_{B} is surprising, as tetragonal and monoclinic zirconia are not vastly different. In both, Zr is solely in the 4+ state. The same can be assumed for the majority of the Zr atoms in thin films, as the Zr:O ratio is nearly identical in both films. Thus, different Zr oxidation states can be excluded as a reason for differences of the films. However, tetragonal zirconia features eightfold-coordinated (8c) and

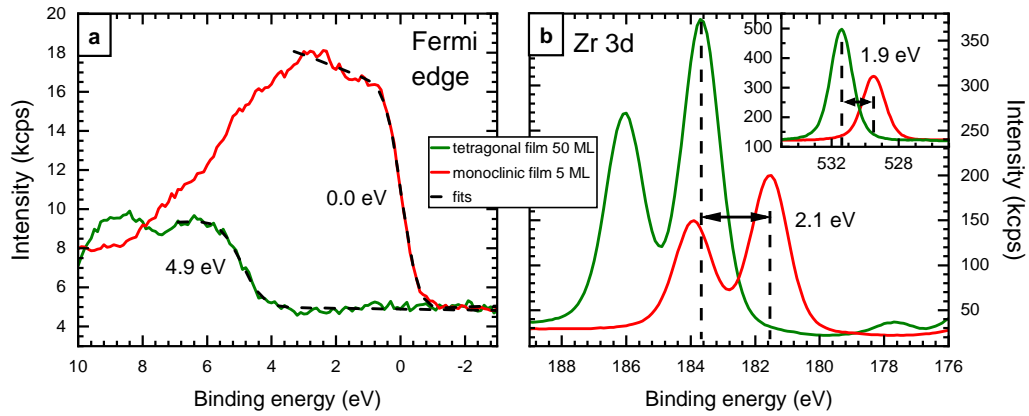


Figure 4.8: XPS measurement of a 50 ML-thick tetragonal zirconia film, and a 5 ML-thick monoclinic zirconia film for comparison. **(a)** Fermi edge of both films, with fits. The valence band edge of the 50 ML film is at a E_B of 4.9 eV, while the Fermi edge of the 5 ML film is at 0.0 eV, as expected, as the signal originates from the Rh support. **(b)** Zr 3d region of the two films, which show a binding energy difference of 2.1 eV to each other. **(inset)** The O 1s region shows a slightly smaller difference, 1.9 eV. The 50 ML data were normalized to a matching intensity at low E_B values.

fourfold-coordinated (4c) O [4], while in the monoclinic structure, Zr is 7c and O is half 4c and half 3c, but from such a coordination difference no large impact on the binding energy is expected.

A further possible difference is the band gap: The band gap of tetragonal ZrO_2 is expected to be larger than the band gap of monoclinic ZrO_2 by 0.5–1.0 eV according to ab-initio calculations, with the more recent works favouring values at the lower end of this range [1, 146]. However, in an experimental comparison of monoclinic and Y-stabilized tetragonal zirconia, the monoclinic band gap was found to be larger by 0.05–0.5 eV [147]. This disagreement makes a prediction for the band gap of the thin films difficult, but an upper limit of 1 eV can be used for an estimate of the influence of the band gap change. Assuming the Fermi energy is in the middle of the band gap, half of the band gap difference – up to 0.5 eV – could be measured as an increase of the binding energy of XPS, see Figure 4.9b. For the Fermi level at the conduction band edge (n-doped material), core level shifts equal to the band-gap differences would be conceivable. Only the largest values of the theoretically predicted band-gap differences (which we do not consider very realistic) would explain significant parts of the E_B difference.

In a previous XPS study, charging was suggested as an explanation for XPS shifts

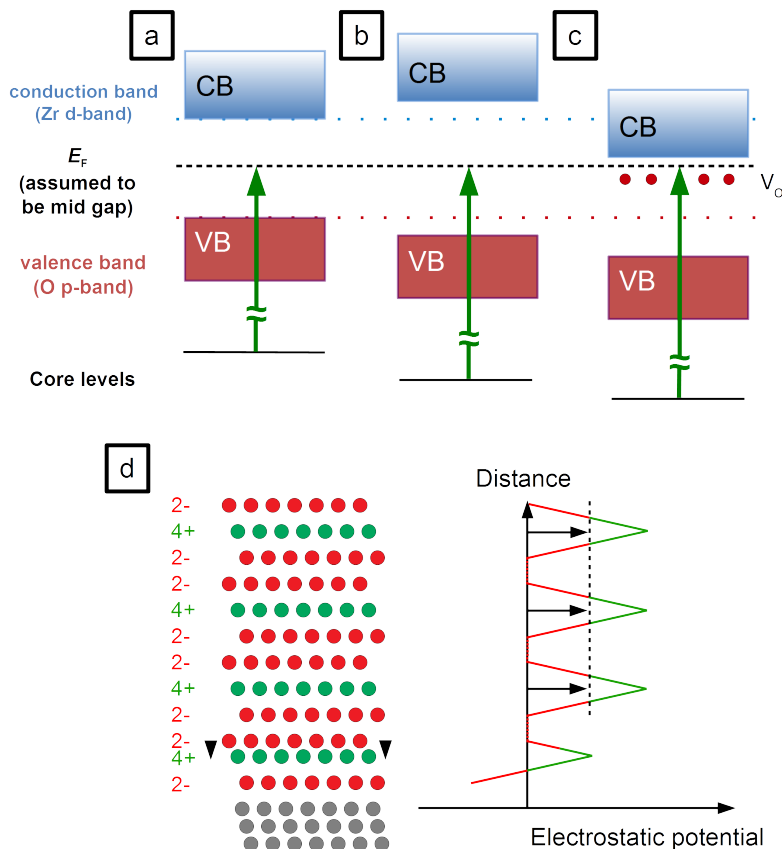


Figure 4.9: Sketch of the different possibilities for changes of the core level binding energy. (a) reference (no change), (b) larger band gap, (c) n-doping by oxygen vacancies, and (d) change of an interlayer distance.

[40]. Although zirconia is an insulating material, the possibility of STM measurements on up to 10 ML-thick films (see section 4.2.2 and [24]) exclude charging during XPS measurements: If any charging would occur, it would be stronger by orders of magnitude in an STM measurement due to the much higher current density (STM: nA/nm^2 , XPS: nA/mm^2), thus rendering STM impossible.

Further explanations for the E_B difference may be based on a different structure at the interface. Measurements presented in section 4.2 and Ref. 24 indicate that the tetragonal film is stabilized by slight ion bombardment during deposition. This could lead to intermixing between Rh and ZrO_2 . Assuming that this induces a structural change with a decreased distance between the lowest Zr layer and the O layer directly above, i.e. the second closest O layer to the interface, the resulting electrostatic potential would shift all states of the film in the higher layers to higher binding energies,

see Figure 4.9d. This effect would however depend on the intensity of ion bombardment during the deposition. Such a dependence could not be found. Furthermore, intermixing at the interface would not explain the increased binding energy measured when annealing tetragonal films at higher temperatures in O_2 . The opposite behaviour would then be expected, as Rh and ZrO_2 would phase separate due to the higher oxygen affinity of Zr.

The large band gap of zirconia leads to large shifts of the levels when the Fermi level gets pinned by gap states, or in the presence of electric fields caused e.g. by electronic doping, see Figure 4.9c. A careful study of the cleanliness of the films grown by our sputter source revealed no contaminations that could act as dopants [50]. The films can however be n-doped by oxygen vacancies (V_{O}). Strong reduction with stoichiometry changes above $\approx 2\%$ in the near-surface region can be excluded from XPS measurements showing roughly the same Zr:O ratio for both monoclinic and tetragonal ZrO_2 . However, a slight reduction would be enough to induce a shift of 1–2 eV range due to the lack of shielding charges in an insulator like zirconia. A slightly reduced tetragonal film compared with a fully oxidized monoclinic film can therefore explain the differences in XPS. The suggestion of V_{O} in tetragonal ZrO_2 is in agreement with the literature; V_{O} are the main candidate for explaining the stability of the tetragonal phase in powders [26], and in a previous work we have also suggested that V_{O} could explain the observation of band bending effects in STM images of monoclinic ZrO_2 films, and the lack thereof for tetragonal zirconia films, see section 4.2.4 and [24].

If the core level shift is mainly due to reduction, tetragonal films with a binding energy around 182 eV – less than usual 182.6–183.4 eV – are less reduced or not reduced at all. Both preparations with such a low E_{B} share one similarity: They are not continuous, but have holes reaching down to the Rh(111) substrate, which is a good catalyst for oxygen dissociation [148]. When annealing in oxygen, the accessibility of the catalyst will lead to oxidation of the film.

4.4.3 Test Experiment: Full Oxidation of Tetragonal ZrO_2 by Rh Deposition

A test experiment was designed to confirm that slight reduction of the tetragonal films is the reason for the large E_{B} difference between tetragonal and monoclinic

core levels. The experiment is sketched in the inset of Figure 4.10b. A standard 5 ML tetragonal film was prepared ($T_{\text{anneal}} = 630\text{ }^{\circ}\text{C}$, $p_{\text{O}_2} = 5 \times 10^{-7}\text{ mbar}$). Using STM and LEED, we confirmed that it had no holes reaching the substrate. XPS showed the Zr 3d_{5/2} level at 183.4 eV, see Figure 4.10a. (Here, E_{B} is somewhat higher than usual for tetragonal films, which most likely originates from a lower p_{O_2} during deposition, $5 \times 10^{-7}\text{ mbar}$.) Then, 1.6% of a monolayer of Rh ($1.4 \times 10^{13}\text{ cm}^{-2}$) were deposited on top of the zirconia film. This yielded a small E_{B} shift of -0.1 eV. After another annealing step at a lower temperature ($T = 610\text{ }^{\circ}\text{C}$, $p_{\text{O}_2} = 5 \times 10^{-7}\text{ mbar}$), the Zr 3d core levels shifted by 1.1 eV to 182.3 eV. The Zr:O ratio remained constant within the error bars of $\pm 2\%$. The structure was checked by STM and LEED and a tetragonal film with only few areas transformed to the monoclinic structure was found. This is however a minority (according to STM, less than 7% of the surface) and therefore cannot explain the substantial shift of the XPS peak. Thus, oxidation by O₂ spill-over from Rh reduces the E_{B} difference between the tetragonal film and typical values for the monoclinic film from 1.8 eV to 0.7 eV. This remaining difference most likely originates from remaining non-stoichiometry, and, to a lesser degree, from the different band gap and different structure, as discussed in the previous section. O 1s shifts by the same energy as Zr 3d, confirming our model of a shift of all bands with respect to the Fermi level. When comparing tetragonal (reduced or not) and monoclinic films, we consistently find a difference of 0.2 eV between changes of O 1s and Zr 3d. In other words, the difference between the O 1s and Zr 3d core levels depends on whether we have the monoclinic or tetragonal phase and must be due to the different structure and/or different band gaps of these phases.

4.4.4 Band Bending Model

Up to now, the analysis followed the assumption that the n-doping of the tetragonal ZrO₂ films leads to a rigid shift of the electronic levels. While this would be true for very thick films, for 5 ML-thick films the interface to the metallic substrate has to be taken into account. Assuming that the interface structure is essentially the same for monoclinic and tetragonal films, the band alignment between ZrO₂ and the substrate will be the same for the n-doped tetragonal ZrO₂ and the monoclinic films. For the oxide layers above, we can determine the electrostatic potential by solving Poisson's equation, assuming a homogeneous charge density given by the density of oxygen

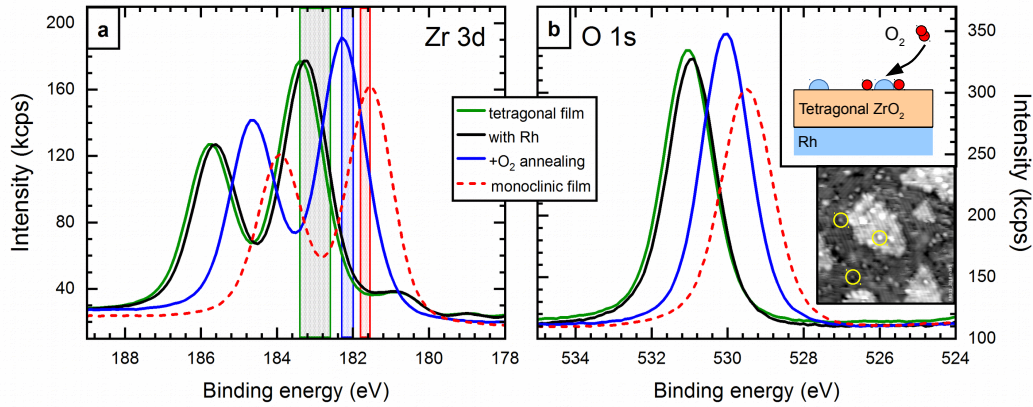


Figure 4.10: XPS measurements of the experiment to test oxidation of tetragonal films. **(a)** Zr 3d and **(b)** O 1s levels of a closed, tetragonal film before (green) and after (black) deposition of 1.6% of a ML Rh, and after annealing in O_2 at 610°C (blue). By annealing in the presence of Rh, the main peaks shift by 1.1 eV to 182.3 eV. The signal of a monoclinic film is shown as reference (red, dashed). The colored areas in (a) show the energy range of different preparations. The oxidized, tetragonal range (blue) includes broken tetragonal films, see section 4.4.1. (Top inset) Sketch of the setup of the test experiment. (Bottom inset) STM image of deposited Rh (yellow circles) on tetragonal ZrO_2 , $27 \times 27 \text{ nm}^2$, $U_{\text{bias}} = +3.7 \text{ V}$, $I = 70 \text{ pA}$.

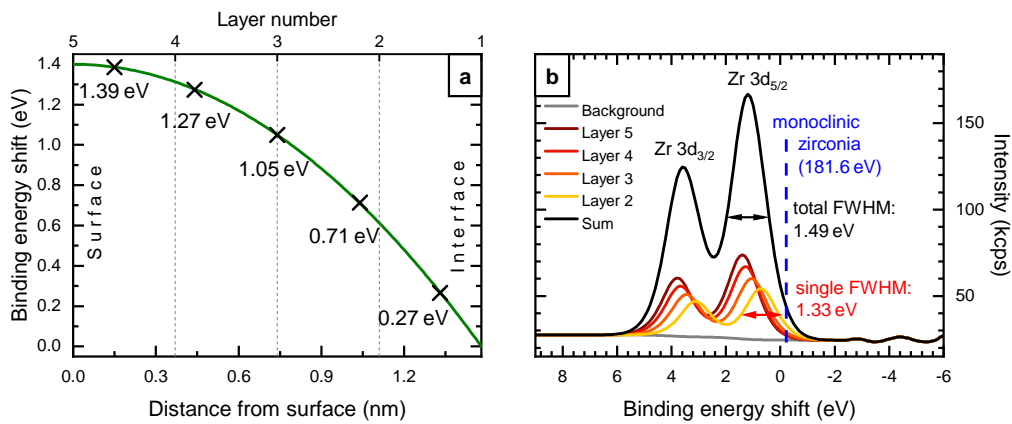


Figure 4.11: Band bending model: **(a)** Electrostatic potential (reflected in the binding energy shift) resulting from the solution of Poisson's equation assuming a homogeneous charge density. **(b)** Synthetic spectrum of a tetragonal zirconia film with the binding energy shifts from (a), excluding the interface layer. Monoclinic zirconia would be at -0.2 eV due to the intrinsic difference between the tetragonal and monoclinic structure, see text. The spectrum appears only slightly broadened (FWHM 1.49 eV, compared to 1.33 eV for the individual layers).

vacancies (charge +2e per oxygen vacancy) and a relative permittivity of $\epsilon_r = 22$ [149]. This leads to a parabolic potential (Figure 4.11a). The potential difference can be roughly estimated from XPS as the difference between a usual value for a tetragonal film (183.0 eV) minus the lowest (i.e. most oxidized) E_B encountered for monoclinic films (181.6 eV). The intrinsic difference between tetragonal and monoclinic zirconia can be estimated with 0.2 eV, see above, giving a total potential difference of 1.2 eV. As the value measured in XPS (weighted averaged over all layers, see below) will be lower than the total potential difference, we choose a slightly higher value, 1.4 eV. This results in an XPS shift of 1.2 eV w.r.t. a stoichiometric, tetragonal ZrO₂ film, see Figure 4.11b. For a 5 ML film we then get a charge density of 1.55×10^{21} e/cm³, which corresponds to 1.3% oxygen vacancies, i.e. ZrO_{1.974}, taking the unit cell volume of tetragonal zirconia as 66.6 Å³ [22], i.e. 33.3 Å³ per formula unit. The shape of the potential curve depends on the charge distribution; e.g. when having the same number of vacancies, but more concentrated near the interface, there would be less variation of the potential in the uppermost layers. Also, the difference between the potential of the surface and the interface would be lower (resulting in a lower core level shift), due to a shorter distance over which the electric field would be applied. Having the same number of vacancies exclusively at the surface would lead to twice the potential difference and a straight curve (constant electric field between the charged surface and the interface as in a plate capacitor).

Using the results from the calculation, an XPS spectrum can be created by using a weighted average of the single spectra from all layers: The Zr 3d spectrum of each layer is shifted according to the calculated electrostatic potential of this layer; the attenuations are simulated using the SESSA code [73]. Here, we have to exclude the bottommost Zr layer (“interface peak” in Figure 4.5), due to its different photoelectron energy [42] (originating from different screening in the vicinity of the metal substrate as compared to sites inside the insulator). Each layer’s peak width (FWHM) is set to 1.33 eV, which is the minimum value found in experiments (for monoclinic films). Figure 4.11b shows this synthetic spectrum together with its contributions. We find that the peak of the spectrum is shifted 1.2 eV – 0.2 eV less than the maximum potential difference chosen for this model. In addition, we notice a broadening of the peak; the FWHM increases from 1.33 to 1.49 eV.

A calculation of the extreme case of a potential difference of 1.8 eV yields a vacancy concentration of 1.66% with an even higher peak width of 1.59 eV. Both FWHM val-

ues, 1.49 and 1.59 eV, are higher than typically encountered in our measurements, where the upper end of the FWHM range measured for tetragonal films is 1.50 eV. A lower FWHM value can be reached by assuming the top layer to be fully oxidized, in agreement with DFT calculations on ZrO₂ clusters indicating a higher vacancy formation energy at the surface [150]. The potential is then almost equal for the two topmost Zr layers. For the potential differences of 1.4 eV and 1.8 eV, the FWHM is lowered to 1.43 eV and 1.50 eV, respectively, while the vacancy concentration in the remaining four layers increases to 2.0% (1.6% over all five layers) and 2.6% (2.1% over all five layers), respectively.

4.4.5 Discussion

The main reason for the XPS binding energy shifts in 5 ML-thick zirconia films is doping: Tetragonal zirconia films are inherently slightly reduced. Oxygen vacancies typically lead to n-doping, i.e. filled gap states; this shifts all energy levels down (towards higher E_B). For reducible (semiconducting) oxides, oxygen-vacancy states are close to the conduction band minimum. This is in contrast to zirconia: There, the oxygen vacancy states filled by two electrons (F-center, V_O^\times in Kröger-Vink notation) are only slightly above mid-gap [151]. This is not far from the Fermi level of the Rh substrate, which is also slightly above a mid-gap position as indicated by XPS measurements of the band gap in this chapter, and DFT calculations [41]. Thus, in zirconia, a filled vacancy state would not lead to a substantial shift of the bands. It has been noted, however, that in the presence of a nearby metal, the vacancies become positively charged $V_O^{\bullet\bullet}$; the electrons get transferred to the metal, leading to a substantial decrease of the V_O formation energy from ≈ 6 eV to ≈ 3 eV [152,153]. Then, the (unoccupied) vacancy state is at the bottom of the conduction band [148], and the positive charge causes downward band bending, similar to gap states in reducible oxides.

Band bending — as induced by electronic doping of the metallic substrate below the zirconia film — affects each layer of the film in varying strength; due to the positively charged V_O s distributed over the zirconia film, upper layers have a more positive potential (higher E_B). Such a layer-by-layer split of XPS peaks cannot be resolved directly with a lab-based XPS setup. Furthermore, the distribution of the V_O s will lead to variations of the electrostatic potential within the layers. However, the dependence of the Zr 3d_{5/2} binding energy on film thickness can be explained only

when taking the depth-dependent potential into account. When adding more material to a 4 ML film, as in Figure 4.7, additional layers are added to the side of the film with the more positive potential, i.e. the high- E_B side. The average E_B then shifts to higher values. For monoclinic zirconia, which is assumed to be stoichiometric (no oxygen vacancies inducing an electric field), no such thickness dependence is found. The (preparation) temperature dependence of the binding energy confirms the explanation by oxygen vacancies: Higher annealing temperatures lead to more V_O s (as long as no oxidation is possible, see below) and therefore to a larger total E_B .

The simple electrostatic band bending model presented in section 4.4.4 can be used to predict the average position of V_O s. The model, which assumes a homogeneous distribution of V_O s, leads to FWHM values that are too large. When shifting the V_O distribution towards the interface, i.e. a higher V_O density deeper in the film, the upper layers (with lower attenuation) will have more uniform binding energy values and the total FWHM will be reduced. (However, a higher number of V_O s would then be needed for the same total potential difference.) Therefore, it can be concluded that V_O s in zirconia films are preferentially located close to the interface. This is confirmed by FWHM variations in tetragonal films: With higher E_B , i.e. a higher concentration of V_O s — where the binding energy of the single layers is spread over a larger energy range — the FWHM is reduced. The opposite result would be expected for a constant V_O distribution. However, if the majority of V_O s is close to the interface, the FWHM could indeed be reduced by a increasing amount of V_O s.

The total E_B shift induced by oxygen vacancies is limited, as can be seen from the binding energies of a 50 ML-thick zirconia film (Figure 4.8). Although the film has a composition of $ZrO_{1.83}$ according to the XPS quantification, see section 4.4.1, the Zr 3d_{5/2} peak was found at 183.7 eV — only +0.3 eV above the maximum found for 5 ML-thick films. A simple electrostatic model as in section 4.4.4 would predict an absolutely unrealistic shift of the potential at the surface of ≈ 900 eV. It can therefore be assumed that at a certain point positive $V_O^{\bullet\bullet}$ become less stable than neutral F-centers V_O^\times . Two effects lead to such a limit: Firstly, electrostatic repulsion becomes dominant at high V_O concentrations; $ZrO_{1.83}$ corresponds to one V_O per three tetragonal unit cells. Secondly, the band bending has a natural limit when the zirconia conduction band reaches the Fermi energy and Zr states would become filled. However, before that, the vacancy states close to the conduction band minimum [151] become filled, and these shift down to an almost mid-gap energy. Comparing the formation of en-

ergy of a charged V_O in an unfavorable environment with a neutral V_O is not trivial, as distortions of the lattice have to be taken into account.

Full oxidation of tetragonal films is only possible via oxygen spill-over from a catalyst for oxygen dissociation, such as deposited catalytic metals or the Rh substrate. The latter is accessible in case of a monoclinic film or a broken tetragonal film. When annealing in oxygen, O_2 molecules dissociate at the metal and spill over to the oxide. V_O s are additionally stabilized below or near metal clusters [153, 154]. Thus, clusters help providing atomic oxygen and at the same time can attract oxygen vacancies to the surface. As a result of oxidation, the core levels shift to lower E_B , i.e. closer to the monoclinic levels. The minimum E_B difference found between a fully oxidized monoclinic and an oxidized tetragonal film was 0.3 eV, in contrast to a maximum difference of 1.8 eV. Oxidation makes tetragonal films very unstable; the transformation process to monoclinic zirconia starts already at 610 °C, much lower than for continuous tetragonal films, where the transformation begins only above 730 °C since oxygen cannot dissociate. As the tetragonal–monoclinic transformation goes hand in hand with the formation of holes in the film [24], and therefore the exposure of the bare Rh substrate enabling O_2 dissociation, the transformation would probably occur at even higher temperatures if the formation of holes could be suppressed.

Let us finally discuss the behaviour of the interface layer with its separate doublet in XPS: The peak area varies from preparation to preparation. It is therefore possible that only parts of the interface layer contribute to this peak. Also, the peak shifts away from the main peak with rising binding energy, i.e. with reduction level. It is likely that these changes result from a changing amount of oxygen vacancies at the interface – fitting to the result of V_O s being preferentially situated near the interface. DFT calculations show that Rh-Zr bonds lead to the different binding energy of the interface layer [42]. Therefore, a higher number of V_O s can lead to a strong bond between Rh and the Zr atoms surrounding the vacancy. For all Zr in the interface layer to be affected directly, at least 33% of the oxygen at the interface would need to be missing, as each interface-O has 3 Zr neighbours. This alone would mean that 3.3% of the total amount of oxygen in the film is missing – an unrealistic assumption, as this would mean that all V_O s are located in the first layer (the estimated total vacancy concentrations is $\lesssim 2\%$, and the XPS signal from the lowest layer is attenuated by $\approx 50\%$), which would result in all Zr layers having the same E_B . It is therefore not surprising that only parts of the interface layer are strongly bound to Rh. When

the film becomes more oxidized, the main peak shifts to lower E_B values, while the interface peak is affected less by Rh and shifts to higher E_B .

4.4.6 Conclusion

An XPS study of 5 ML-thick zirconia was conducted. A binding-energy difference of up to 1.8 eV between monoclinic and tetragonal films was found, which originates from the different reduction states of the two films. Tetragonal films are inherently slightly reduced. The resulting positively charged oxygen vacancies, which are preferentially located near the interface, bend the whole electronic structure, i.e. both, the O 1s and Zr 3d levels shift by equal amounts. Tetragonal films, which cover the whole Rh substrate, cannot be more oxidized due to the lack of a catalyst for O₂ dissociation. The surface offers no catalytic sites for O₂ from the gas phase to dissociate. The films only become more oxidized when an external catalyst is providing oxygen spill-over; this can be the Rh(111) substrate or Rh (or other catalytically active metals) deposited on top of the film. The substrate is accessible for O₂ in case of a broken film, which is always the case for monoclinic films. Therefore, monoclinic films are inherently more oxidized than tetragonal films, explaining the different binding energies measured in XPS.

4.5 Thin ZrO₂ Films on Pt(111) and Pt₃Zr(0001)

In addition to Rh(111), zirconia film growth was also investigated on two other substrates known from studies of ultrathin zirconia films: Pt(111) and Pt₃Zr(0001). Both substrates turned out to give lower quality films, i.e. films of lower ordering and smaller domain size.

4.5.1 Pt(111)

Zirconia films were deposited on clean Pt(111) in the same fashion as on Rh(111). According to XPS, no metallic Zr was dissolved in Pt before deposition. To test whether the film behaves similarly to that on Rh(111), it was annealed stepwise in $p_{\text{O}_2} = 5 \times 10^{-7}$ mbar at 540 °C, 650 °C, 800 °C, and then 880 °C. Figure 4.12 shows LEED measurements that confirm the tetragonal (2×1) structure at all temperatures. The

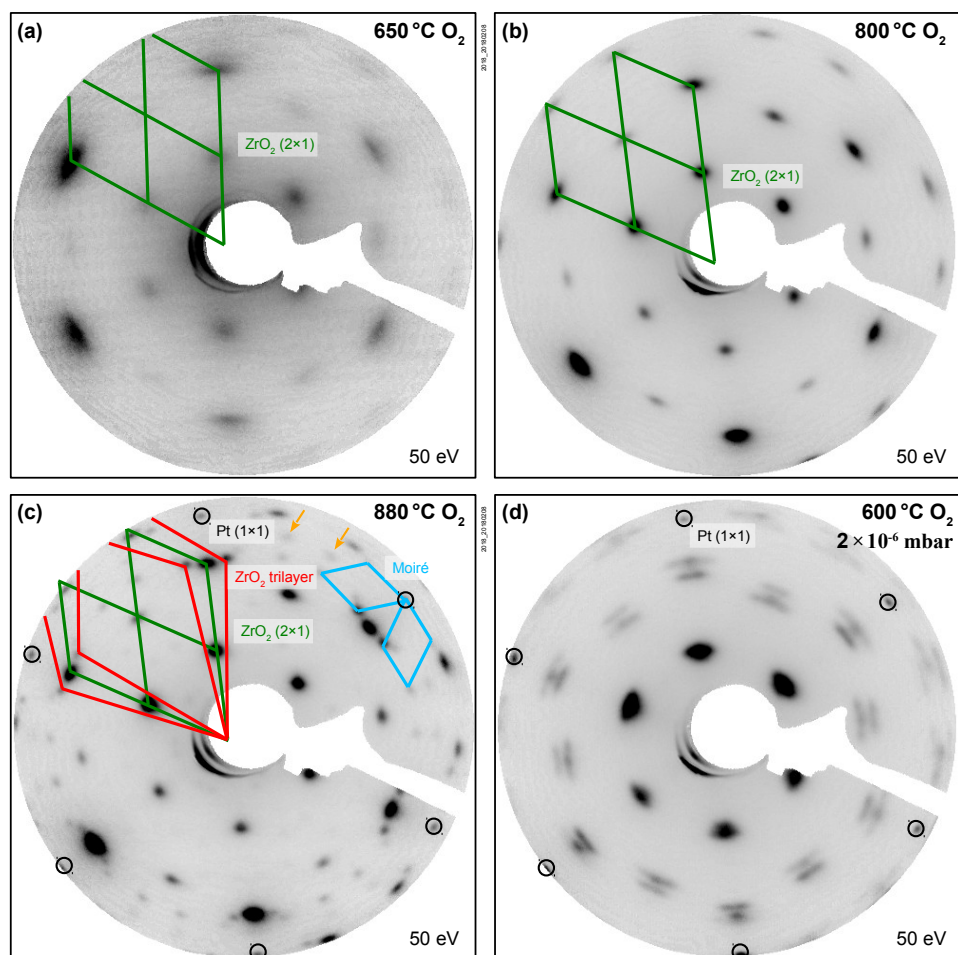


Figure 4.12: 5 ML-thick ZrO_2 on a Pt(111) single crystal grown by sputter-deposition, measured with LEED after annealing at (a) 650 °C, (b) 800 °C, and (c) 880 °C in O_2 . The film stays in its tetragonal (2×1) structure, but breaks at 880 °C. This leads to Pt spots appearing, as well as spots from an ultrathin zirconia layer. Weak spots that cannot be explained by the ultrathin film are marked with orange arrows. (d) After breaking of the film, annealing at 600 °C at higher p_{O_2} leads to the film structure transforming to monoclinic – see monoclinic films on Rh(111), Figure 4.4.

film broke at 880 °C, yet remained tetragonal. In addition, the signature of an ultrathin film appeared (as when oxidizing Pt₃Zr(0001), see Refs. 41, 42, and chapter 3), which is rotated $\pm 6^\circ$ w.r.t. the Pt substrate. Such an ultrathin film covers the holes of the broken film, and leads to additional moiré spots of this ($\sqrt{19} \times \sqrt{19}$) superstructure. Additional, weak spots just outside the moiré spots (marked by orange arrows) can not be explained by the ultrathin film and are of unknown origin. STM measurements confirm the creation of an ultrathin zirconia film in holes, see Figure 4.13. Only after an additional oxidation step at a higher p_{O_2} (2×10^{-6} mbar), monoclinic zirconia is formed, see Figure 4.12d. The increased stability of the tetragonal phase as compared with ZrO₂/Rh(111) (on Rh(111), the tetragonal-monoclinic transformation begins above 650 °C) was also confirmed by STM, see Figure 4.14. Panel (a) shows large tetragonal domains after annealing at 800 °C. On a smaller scale, see Figure 4.14b, two types of common defects can be discerned. The standard dark feature on a bright row (examples marked with circles) are single defects, and could be oxygen vacancies in the surface layer; these defects are also commonly found on tet-ZrO₂/Rh(111), see Figure 4.2. Adsorbates can however not be excluded at this point. Furthermore, dark features with three surrounding bright features on neighbouring rows can be found (example marked with a triangle). As these three features are in similar distance to each other, and no defect with only two bright features can be found, we suggest a subsurface oxygen vacancy as the reason for this phenomenon. This second type of defect was not found on ZrO₂/Rh(111).

5 ML-thick zirconia films were also analyzed by XPS (not shown); the ratio of Pt/Zr increases slightly at 800 °C, and significantly at 880 °C, while the Zr/O ratio stays constant within the typical measurement accuracy. This is expected from a film that starts to dewet from its substrate. (The ultrathin film appearing at 880 °C has a similar E_{B} as the interface layer of 5 ML-thick films, and can therefore not be discerned in XPS.) The binding energy of Zr 3d_{5/2} is 182.6 eV after annealing at 540 °C and shifts to 182.9 eV at 650 °C (the film becomes more reduced). At even higher annealing temperatures, the film becomes more oxidized; E_{B} shifts to 182.8 eV at 800 °C, and to 182.6 eV for 880 °C. After the transformation to m-ZrO₂, E_{B} shifts to 181.7 eV – a typical value for the oxidized monoclinic structure, see section 4.4.

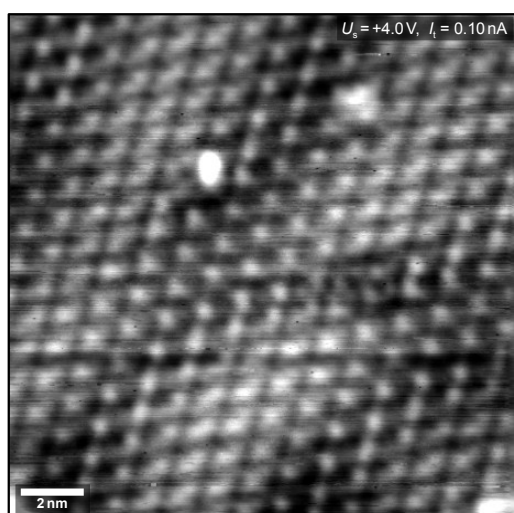


Figure 4.13: STM image of an ultrathin ZrO_2 layer on Pt(111) located in a hole of a 5 ML-thick ZrO_2 film. When annealing 5 ML ZrO_2 on Pt(111) at 880 °C in O_2 , the film breaks at 880 °C, which leads to the growth of the ultrathin ZrO_2 layer in the holes; the structure has a ≈ 1.2 nm periodicity, and is therefore an approximate $(\sqrt{19} \times \sqrt{19})$ moiré w.r.t. Pt(111), similar to ultrathin zirconia on Pt_3Zr [41].

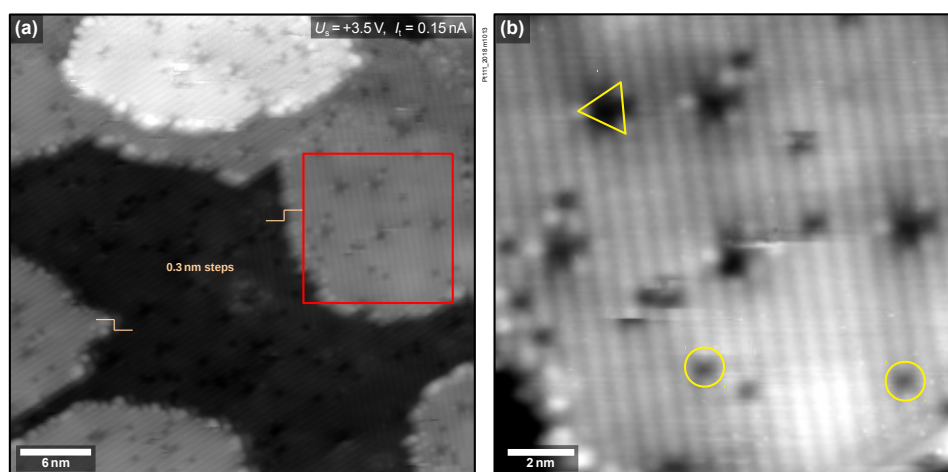


Figure 4.14: STM images of 5 ML-thick ZrO_2 on Pt(111), annealed at 800 °C in O_2 . **(a)** The film stays in its tetragonal (2×1) structure and forms large domains. **(b)** Enlarged area (marked in red in (a)) with two typical types of defects marked: Normal in-row defects (circled) and defects surrounded by triangularly aligned species (triangle).

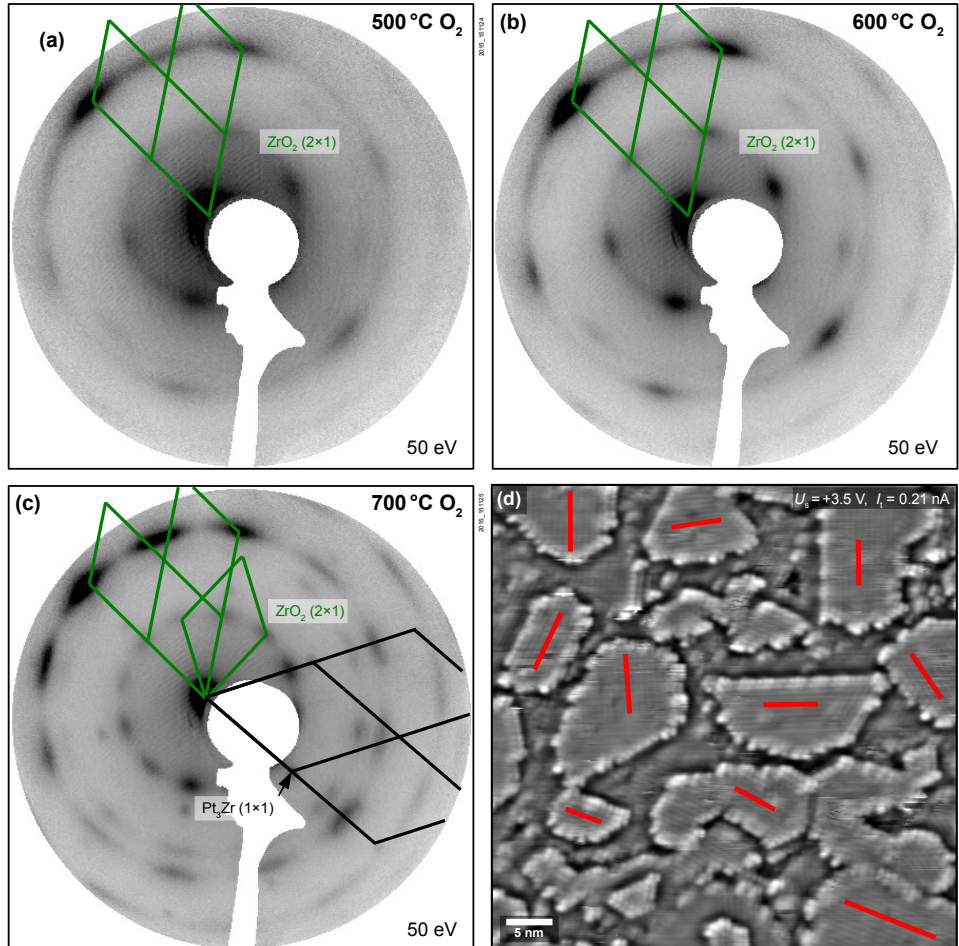


Figure 4.15: 5 ML ZrO_2 on $Pt_3Zr(0001)$ grown by sputter-deposition, measured with LEED after annealing at (a) 500 °C, (b) 600 °C, and (c) 700 °C in O_2 . While the structural order increases, even at 700 °C the zirconia domains are not well-aligned with the substrate. At 700 °C, the film breaks up, as $Pt_3Zr(1 \times 1)$ spots appear, plus higher order spots. (d) STM image taken after annealing to 600 °C (high-pass filtered). Every unique row orientation is marked with a red line.

4.5.2 Pt₃Zr(0001)

Pt₃Zr(0001) has a major advantage compared to Rh(111) and even more so when compared to Pt(111): Dissolution of Zr from a deposited film into the substrate is impossible, as the bulk is already saturated with Zr. However, one has to keep in mind that oxidation of uncovered areas would lead to additional ZrO₂ formation.

To investigate the growth and structure of sputter-deposited ZrO₂ films on Pt₃Zr(0001), a 5 ML-thick ZrO₂ film was deposited as on the other substrates and annealed consecutively at 500 °C, 600 °C, and 700 °C in 5×10^{-7} mbar O₂. (For ultrathin films grown by oxidation of Pt₃Zr, see Refs. 41, 42, 44, 45, and chapter 3.) Figures 4.15a–c show LEED images of each of the preparations. At low temperatures, the direction of the zirconia domains is only very weakly oriented along the Pt₃Zr axes; the resulting spots form a circle with weak maxima. This behaviour is not surprising as the unit cells of Pt₃Zr (0.56 nm) is far larger than that of ZrO₂. The closest nearly commensurate ratio, a 2:3 superstructure, still does not give a good coincidence (1.12 nm vs. 1.08 nm). The maxima become more distinct at 600 °C. Only after annealing at 700 °C, truly separated maxima appear. However, they are still smeared out, forming a broken ring. Maxima appear again in the direction of the Pt₃Zr-spots, and now additionally 30° rotated. Additionally, Pt₃Zr(0001)-(1 × 1) spots appear, so the films break up at $T = 700$ °C. STM images of the same preparations were taken, showing an increase in domain size with increasing annealing temperature. Figure 4.15d shows an STM image taken after annealing at 600 °C; rows originating from tetragonal zirconia are clearly visible. However, the different domains are seemingly randomly distributed, as expected from LEED; this can be seen by the red lines, where each marks a unique domain orientation. Additionally, very small, monoclinic domains can be made out already after annealing at 600 °C. The core levels of the films was analyzed after annealing at 500 °C and 600 °C, see Figure 4.16. The Zr 3d region, see Figure 4.16a, shows the Zr 3d_{5/2} peaks at 183.2 eV and 183.5 eV, respectively. The O 1s peaks are located at 531.0 and 531.3 eV, respectively. Compared to the E_B range of t-ZrO₂ on Rh(111) (182.6 – 183.4 eV), these are high values, pointing towards a high concentration of oxygen vacancies in the film. The additional peak at low E_B originates from Zr in the substrate. Interestingly, with a binding energy of 180.1 eV, it is shifted by +0.5 eV with respect to measurements of alloyed Zr in Pt₃Zr [42].

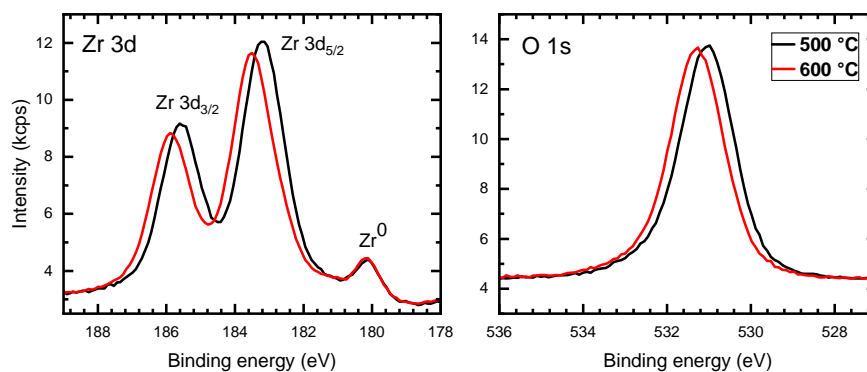


Figure 4.16: XPS on 5 ML ZrO₂ on a Pt₃Zr(0001) substrate, grown by sputter-deposition and annealed at 500 °C (black) and 600 °C (red). **(a)** The Zr 3d range consists of a major doublet from the film at 183.2 or 183.5 eV, respectively, and a substrate peak at 180.1 eV. The area in-between originates from an interface peak. **(b)** O1s spectrum.

4.5.3 Discussion

Both substrates, Pt(111) and Pt₃Zr(0001), give rise to less oriented ZrO₂ films as on Rh(111). This problem is more pronounced on Pt₃Zr, where domain orientations do not align with each other even at high annealing temperatures. On Pt on the other hand, STM measurements show large, well-ordered domains, yet LEED reveals that the structural order is still inferior to Rh(111). On Pt₃Zr, a further problem is unintentional growth of additional ZrO₂; it is possible to add zirconia to the deposited amount by oxidation of the substrate in holes in the film. The growth of ultrathin zirconia films in holes was also observed on Pt(111), where no Zr was dissolved in the bulk prior to deposition; the Zr bound in the ultrathin film must therefore originate from the 5 ML-thick film, which was reduced during annealing. This reduction is confirmed by rising E_B in XPS at lower annealing temperatures (before breaking of the film).

With the appearance of holes to the substrate, one would expect (from the results on Rh(111), see section 4.4) the thin-film Zr 3d and O 1s signals to shift strongly towards smaller binding energies. Although holes down to the substrate form (according to LEED and STM), the shift is only -0.3 eV. This is due to the substrate being covered by an ultrathin zirconia film, which blocks oxygen from accessing the dissociation catalyst Pt. Most likely, when annealing at higher $p_{O_2} = 2 \times 10^{-6}$ mbar, the ultrathin film is fully oxidized and removed. On the bare Pt(111) surface, oxygen dis-

sociation becomes possible and the tetragonal film – not stabilized by V_Os anymore – transforms to the thermodynamically stable monoclinic form.

In which case could these two substrates become interesting? Pt(111) features the possibility of annealing t-ZrO₂ at significantly higher temperatures than on Rh(111) without a tetragonal-monoclinic phase transformation; high-temperature studies of t-ZrO₂ become possible. Pt₃Zr(0001), on the other hand, is of interest for studies involving UHV annealing. The substrate cannot take up more Zr; thus, reduced Zr would stay in the zirconia film. Reduction of ZrO₂ is assisted by Zr dissolution in the substrate (gain in enthalpy); it is therefore expected that ZrO₂ reduction is generally harder on Pt₃Zr.

Chapter 5

SMSI of Zirconia on Rh(111) and Pt(111)

In this chapter, the wetting and dewetting of Rh(111) and Pt(111) by an ultrathin zirconia layer originating from zirconia islands is investigated. The behaviour is similar to the so-called Strong Metal-Support Interaction (SMSI) known from catalysis. The chapter is based on an upcoming article, Ref. [111](#). All measurements in this chapter were conducted in the RT-STM chamber, see chapter [2.1.1](#). The sample preparation, including sputter deposition of thin zirconia films onto Rh(111) and Pt(111), followed the same preparation methods as described in chapter [4.1](#).

5.1 Introduction

Already in the late 1970es, Tauster *et al.* reported a strong change in reactivity after annealing oxide-supported catalysts under reducing conditions [[155–157](#)]. This increase or decrease of reactivity, depending on the reaction, seemed to stem from an interaction between metal particles and their oxide support, hence the effect was named “strong metal-support interaction” (SMSI). The effect is reversible; the original state can be recovered by reoxidation. The SMSI effect was studied intensively, as the change in reactivities can be used for tuning the selectivity of oxide-supported catalysts towards the desired end product [[158](#)]. For the prototypical oxide support TiO_2 , it was shown later that the SMSI effect was due to a heavily-reduced oxide film ($\text{TiO}_{1.1}$) encapsulating Pt clusters [[159, 160](#)]. This explanation, which was first considered by Meriaudeau *et al.* [[161](#)], was also applied to many other combinations

of reducible oxides and metals, e.g. Pd/TiO₂ [162], Fe/TiO₂ [163], Pt/Fe₃O₄ [164], and Pt, Pd, Rh/CeO₂ [165]. This mechanism is very different from the original idea of a modification of the metal's electronic structure by the oxide support, which had led to the term "SMSI" [166]. Nevertheless, the name "SMSI" is still used for this phenomenon. Early SMSI studies of Ir on different oxide supports found that the tendency of the system to exhibit the SMSI effect depends on the reducibility of the support [156]. For materials commonly seen as hard to reduce or non-reducible, such as HfO₂ and ZrO₂, no effect was found that went beyond cluster agglomeration. This is in agreement with the explanation of the SMSI effect as covering the metal by a reduced oxide film (suboxide). It was later shown that SMSI can also be encountered for Rh/ZrO₂ [167], Pt/ZrO₂ [168–170], and Au/ZrO₂ [171]. In view of the fact that ZrO_{2-x} suboxides are unstable or at best marginally stable [5, 172], this questions the accepted mechanism of the metal being coated by a suboxide being responsible for the SMSI effect.

This work focusses on the so-called SMSI effect on ZrO₂. Inverse model systems of zirconia on Rh(111) or Pt(111) are used to show that reducing conditions indeed lead to the formation of ultrathin zirconia films covering the metal; the ultrathin films can be removed by oxidation.

5.2 Results

5.2.1 Zirconia on Rh(111)

The preparation of an inverse model system of zirconia on a metal starts with sputter-deposition of a closed zirconia film on a clean Rh(111) single crystal. Upon annealing in O₂ ($T > 750$ °C, usually $p_{\text{O}_2} = 5 \times 10^{-7}$ mbar), zirconia begins to dewet the surface, see Figure 5.1a, b. ZrO₂ migrates to the top of the film, increasing the total height of the film by one layer (≈ 0.3 nm).

To increase the exposed Rh surface, and thereby increase the potential area where the SMSI effect can be studied, only two monolayers (ML) of zirconia were deposited on the substrate. (A study of the surface of a mildly-annealed 2 ML-thick film can be found in chapter 4.2.1 and Ref. 24.) The sample was oxidized at a pressure of 5×10^{-7} mbar at 870 °C. During this annealing step, zirconia forms islands and reveals the substrate in-between the islands, see Figure 5.1d1. The substrate either shows

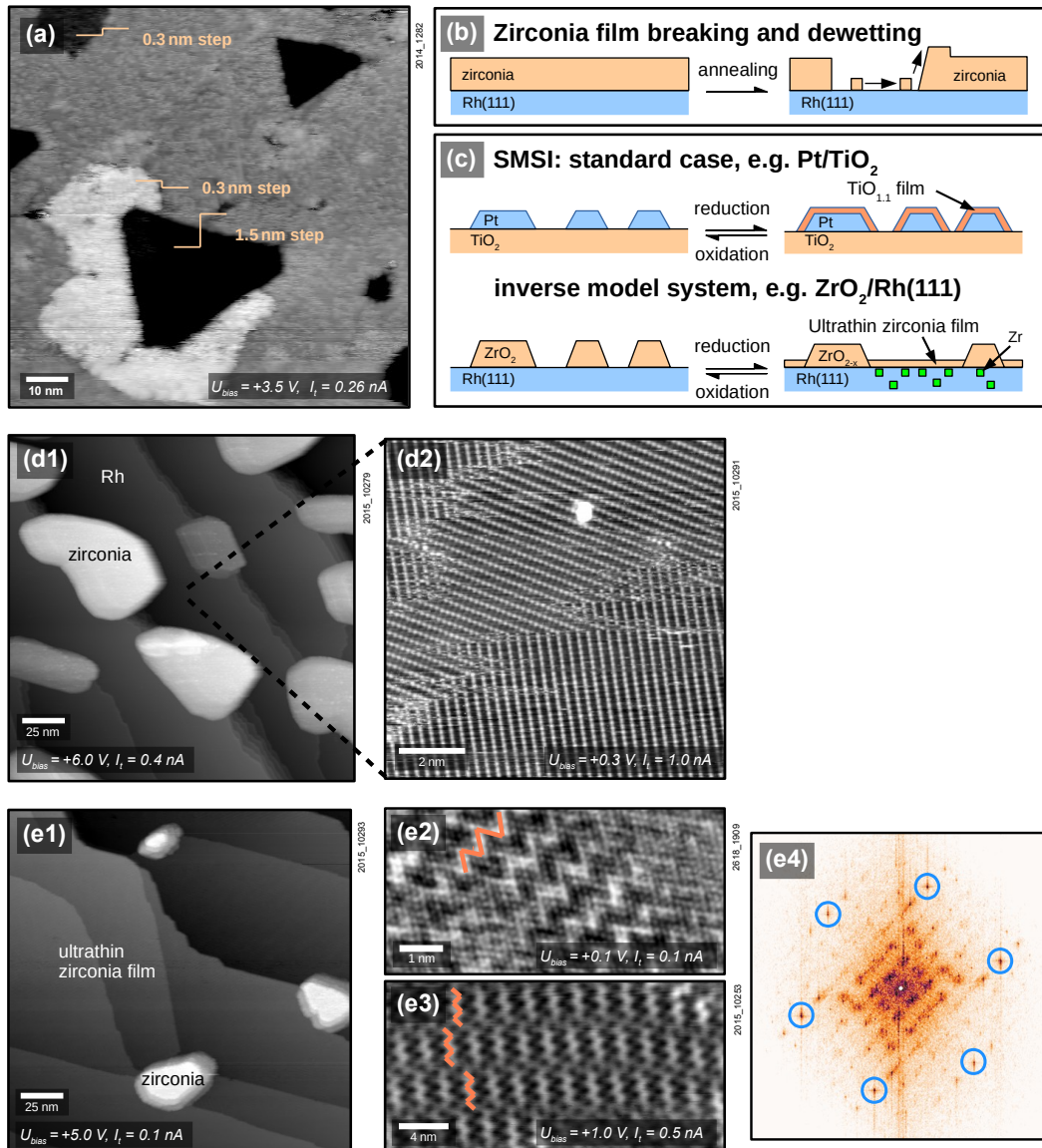


Figure 5.1: (a) STM image and (b) sketch showing dewetting of a 5 ML-thick ZrO₂ film on Rh(111) after annealing at 750 °C in O₂. Dewetting leads to holes down to the Rh substrate, and oxide creeping from the holes onto the film surface. (c) Sketch showing the standard SMSI mechanism leading to metal particles being overgrown by substoichiometric oxide thin films, as well as the mechanism on inverse model systems. (d1) 2 ML of zirconia/Rh(111) after annealing at 870 °C in O₂: Zirconia dewets the substrate and forms islands. (d2) : Rh(111)-(2 × 1)-O superstructure from cooling in oxygen. (e1) After annealing at 870 °C in UHV, the amount of zirconia contained in islands is reduced, and the surface is covered with an ultrathin zirconia film. (e2, e3) show the ultrathin film with the typical zigzag moiré-pattern (marked in orange) in a typical resolution (e3), and high resolution (e2). (e4) The FFT clearly shows a 0.35 nm periodicity (blue circles).

a Rh(111) (1×1) structure or a (2×1)-O superstructure, depending on the oxygen pressure during cooling, see below. The O superstructure can be seen in Figure 5.1d2. When exposing the sample to reducing conditions by annealing at 880 °C in UHV instead of oxygen, an ultrathin film is formed that covers the Rh surface completely, see Figures 5.1e2,e3. The total amount of zirconia in the islands decreases drastically. The remaining islands cover about 2% of the surface with an average height of about 5 ML, thus they accommodate only $\approx 5\%$ of the material deposited. The ultrathin film between the islands can be assumed to be one layer of $\text{ZrO}_2(111)$, the remaining Zr must be dissolved in the Rh substrate (see below). The process is reversible; the ultrathin zirconia film disappears upon annealing in oxygen and the islands grow in size. The total amount of zirconia on the sample decreases with each reduction-oxidation cycle, as some Zr is lost to the bulk, see below. For the deposition of 2 ML, 10% of the total Zr is lost after the first cycle. The reduction-oxidation cycle is depicted in Figure 5.1c, both for inverse model systems and for real catalysts.

A closer look on the ultrathin film reveals a hexagonal lattice with interatomic distances of 0.35 nm, with only slight distortions, as is typical for ultrathin zirconia films [41, 43], see the Fourier transform (FFT) in Figure 5.1e4. When comparing two domains rotated by a multiple of $\approx 60^\circ$, their lattices agree within 1%, demonstrating that the deviations from an exactly hexagonal structure are small. The lattice constant of 0.35 nm is also confirmed by LEED (not shown), when using a tetragonal zirconia film and the Rh(111) lattice as a references. STM images without atomic resolution mainly show a moiré pattern, typically with a zigzag appearance (Figure 5.1e2,e3).

This zigzag moiré pattern can be regular over long distances as in Figure 5.2a, or less prominent as in Figure 5.2b and c. The degree of long-range order correlates with the annealing temperature, annealing time and amount of deposited material; when the annealing temperature and/or time reaches the values necessary for a full coverage of the ultrathin film, the order of the zigzag moiré pattern decreases with further annealing. The moiré pattern ordered over large distances was never encountered for a fully closed film – closing a film requires higher temperatures if less material is available. The STM images of Figure 5.2a and b show two regions of the same preparation (1.2 ML zirconia, $T = 950^\circ\text{C}$, $t = 10$ min), yet the first image was taken at the border of the crystal where slightly less material was deposited. Therefore, the same T is sufficient in the middle of the crystal for a fully closed film with thin stripes of the zigzag structure, interrupted by stripes not showing the moiré. Few, elongated

zigzag patterns reach from one moiré stripe to the next, with no zigzag patterns in between; an example of an elongated zigzag pattern is marked in orange in the inset of Figure 5.1b. After annealing for another 10 min at 950 °C, parts of the film show no zigzag pattern at all, see left half of the detailed image in Figure 5.2c. In the overview image, only small patches of ordered zigzag patterns can be found. The preparation investigated by XPS (section 5.2.3, Figure 5.4) shows a similar pattern. Even when comparing areas with and without any zigzag structure, i.e. the left and right half of the detailed image in Figure 5.2c, the 0.35 nm zirconia lattice parameter varies by < 1%. The exact atomic structure however can not be explained as of yet, as the Rh spots cannot be clearly identified in the FFT; this would be required to explain such a complex moiré pattern. Furthermore, no spots of an ordered Rh-Zr alloy were found.

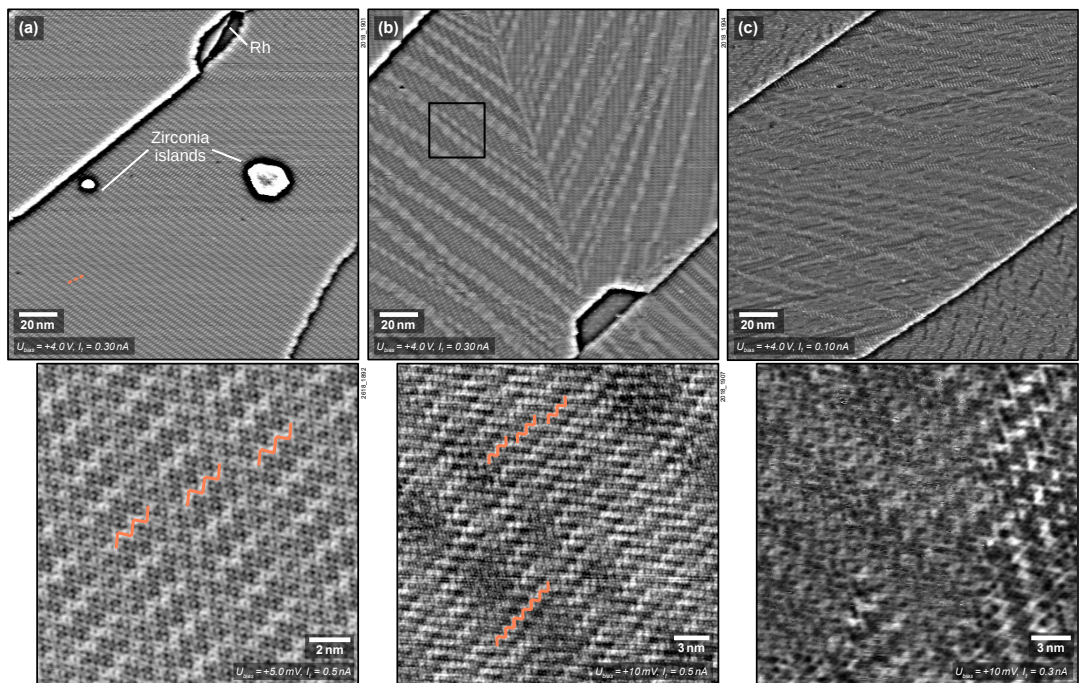


Figure 5.2: STM images of ultrathin zirconia films in different states of order. The insets show the structures at a smaller scale. **(a)** When the film is not fully closed, the film exhibits large domains with an ordered zigzag moiré structure (orange). **(b)** Fully closed films exhibit zigzag domains only in long stripes (imaged dark in the overview image, bright in the inset). **(c)** At higher T , the film shows large areas without zigzag moiré. Overview images are high-pass filtered.

On the Rh(111) surface between the multilayer ZrO_2 islands, a (2×1) -O superstructure can be formed. This depends on the oxygen pressure p_{O_2} (or chemical potential

$\mu_{1/2\text{O}_2}$) during cool-down after annealing the sample in O_2 [138, 145]. To test whether the disappearance of the ultrathin zirconia film upon annealing in oxygen is driven by oxygen adsorption on the Rh(111) surface, the same preparation was repeated with different p_{O_2} during cooling. Firstly, p_{O_2} was held at 5×10^{-7} mbar during cooling down to ≈ 300 °C. This resulted in the $(2 \times 1)\text{-O}$ superstructure in Figure 5.1d2. In a second experiment, the sample was cooled while keeping the chemical potential of oxygen constant at $\mu_{1/2\text{O}_2} = -2.3$ eV, where the coverage of oxygen on Rh(111) should be very low [138, 145]. For this purpose, p_{O_2} was adjusted to keep $\mu_{1/2\text{O}_2}$ constant from 870 °C to ≈ 730 °C, where a pressure of $p < 1 \times 10^{-9}$ mbar was reached, and no oxygen was supplied to the chamber anymore. At this pressure, the impingement rate is low enough to have no effect on the film formation. The resulting surface was similar to when cooling in O_2 , as zirconia islands still formed and the ultrathin film was removed. However, between the islands, the bare Rh(111) substrate was observed (not shown) instead of the $(2 \times 1)\text{-O}$ superstructure. Subsequent annealing in UHV led to the formation of an ultrathin zirconia film.

5.2.2 Zirconia on Pt(111)

As a second inverse model system, zirconia was studied on Pt(111). A zirconia film of ≈ 5 ML thickness was deposited. The sample was annealed at 640 °C for 10 min in UHV directly after sputter-deposition, leading to the formation of zirconia islands and an ultrathin zirconia film in between, see Figure 5.3a. The ultrathin zirconia film shows a Zr–Zr distance of 0.350 ± 0.003 nm, as also observed for $\text{Pt}_3\text{Zr}(0001)$ [41] and $\text{Pd}_3\text{Zr}(0001)$ [43]. The moiré pattern shown in the inset of Figure 5.3a exhibits the same $(\sqrt{19} \times \sqrt{19})$ superstructure (w.r.t. the substrate) as ultrathin films on $\text{Pt}_3\text{Zr}(0001)$ [41].

The creation of the ultrathin film can be reversed by annealing at 640 °C in 5×10^{-7} mbar O_2 for 10 min, see Figure 5.3b. The behavior on Pt(111) does however differ from that on Rh(111) after the oxidation. When annealing at 640 °C for 10 min in UHV again, no ultrathin film forms. Only when annealing at 750 °C in UHV for 10 min, $\approx 26\%$ of the Pt(111) surface are covered with an ultrathin zirconia film, while $\approx 34\%$ of the surface are still bare Pt, see Figure 5.3c. The same film was annealed in $p_{\text{O}_2} = 5 \times 10^{-7}$ mbar at 640 °C, followed by annealing in UHV at 860 °C; the surface remains covered by islands, yet the ultrathin film is not found, although increasing

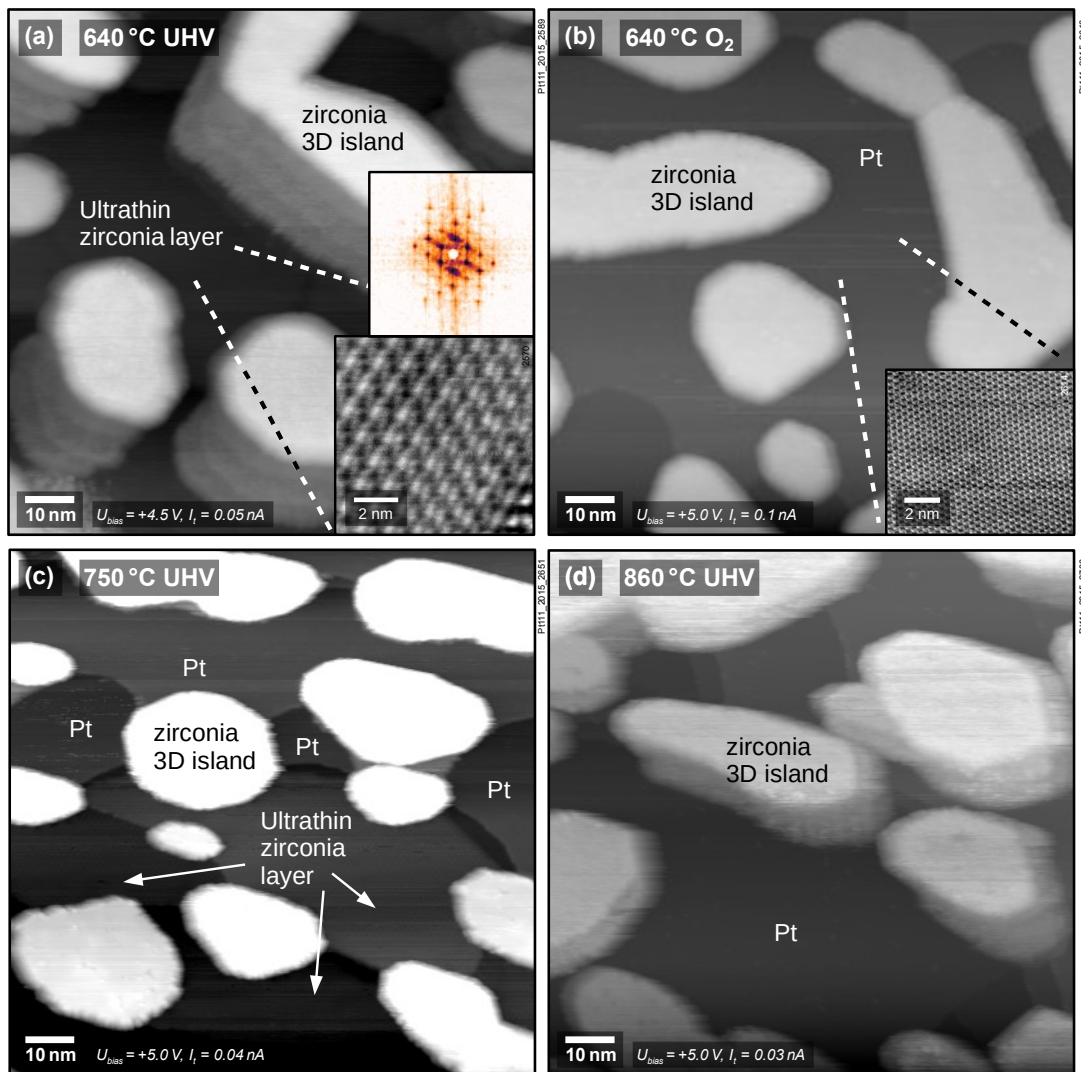


Figure 5.3: The SMSI effect of zirconia/Pt(111): **(a)** Annealing at 640 °C in UHV after deposition yields an ultrathin film between islands. The inset shows an STM image of the $(\sqrt{19} \times \sqrt{19})$ moiré pattern of the ultra thin film and its FFT. **(b)** The ultrathin film is completely removed by annealing at 640 °C in O₂; the inset shows the Pt(111) lattice. **(c)** A partial coverage can be formed again by annealing at 750 °C in UHV, **(d)** but is removed when annealing at 860 °C in UHV.

the temperature at constant (though negligible) O_2 pressure corresponds to more reducing conditions.

In a second preparation, an ultrathin film could also be produced by annealing 2 ML of ZrO_2 at $640^\circ C$ in 5×10^{-7} mbar O_2 for 10 min followed by 30 min of UHV annealing at the same temperature (not shown). This shows that the formation of ultrathin films on Pt(111) is strongly dependent on the preparation conditions and film thickness — in contrast to Rh(111). Additionally, the growth behaviour on Pt(111) is more dependent on the crystal's history, i.e. the amount of Zr dissolved in the bulk, see below. This makes reproducing STM images difficult. A set of STM images as in Figure 5.3 was only taken once, which explains the poor quality of some images (double tip in 5.3a and d).

5.2.3 Photoelectron Spectroscopy

2 ML of zirconia/Rh(111) were investigated using x-ray photoelectron spectroscopy (XPS) in both the reduced and the oxidized state, see Figure 5.4. The oxidized system ($T = 820^\circ C$, $p_{O_2} = 5 \times 10^{-7}$ mbar, $t_{\text{anneal}} = 10$ min) shows only one doublet in the Zr 3d region (binding energy E_B of Zr $3d_{5/2} = 182.3$ eV), which is close to fully oxidized tetragonal zirconia, see chapter 4.4 and [137]. This comes to no surprise as STM shows that all zirconia is contained in islands, see Figure 5.1d1, while the Rh(111) surface is exposed and acts as an oxygen dissociation catalyst (chapter 4.4 and [137]). On the other hand, three doublets are found for the reduced system ($T = 820^\circ C$, $t_{\text{anneal}} = 10$ min). The first can again be attributed to zirconia islands (183.4 eV), although the signal is shifted by 1.1 eV towards higher E_B , caused by reduction (n-type doping by oxygen vacancies; the Fermi level is closer to the conduction band, see chapter 4.4 and [137]). The FWHM of these doublet peaks increases from 1.47 eV to 1.84 eV; possibly due variations of the doping level (reduction) between different islands. The second doublet originates from ultrathin zirconia (180.5 eV), as previously observed on Pt_3Zr [42]. The third doublet (179.0 eV) is slightly shifted with respect to metallic Zr (178.9 eV [70]). This shift is typical when alloying occurs, in this case with the Rh substrate, but it is less than that in the Pt_3Zr intermetallic phase (179.6 eV [173]). The fact that ZrO_2 can be reduced to its metallic state on a metallic substrate was already shown for ZrO_2/Pd [48, 174]. The area ratio of the Zr 3d doublets strongly depends on the preparation.

The peak area of the tetragonal ZrO_2 islands depends on the amount of ZrO_2 deposited. The alloy peak area depends on the annealing conditions, i.e. how much zirconia was already fully reduced. It can be both higher and lower than in the measurement shown in Figure 5.4b; in the case of very little deposited ZrO_2 (e.g. 1.1 ML or 1.2 ML, as in section 5.2.4), the peak vanishes below the detection limit, which is ≈ 0.04 ML, or 1 Zr atom every 25 zirconia unit cells. For Pt, the peak for alloyed Zr was not resolved; however, as Zr alloyed with Pt is shifted significantly towards higher E_B (179.6 eV (+0.6 eV w.r.t. Zr alloyed with Rh) [42]), and therefore overlapping more with the ultrathin zirconia peak, only higher amounts (> 0.08 ML) could be detected. (Additionally, Pt data were taken with an older detector, see chapter 2.1.1.)

The O 1s region shows a single peak for both preparations, overlapping with the tail of the Rh $3p_{1/2}$ substrate peak ($E_B = 521.3$ eV), see Figure 5.4c, d. By subtracting a normalized Rh $3p_{1/2}$ peak measured on a clean Rh(111) surface, the O 1s peak can be extracted. This procedure is however not perfect, as it cannot be excluded that a small amount of O (below the detection limit due to overlapping peaks) was dissolved in clean Rh(111), leading to a slight underestimation of the amount of oxygen in the zirconia films. The O 1s peak of the oxidized preparation is found at 530.1 eV with a FWHM value of 1.58 eV, as for oxidized tetragonal zirconia in chapter 4.4. In the reduced preparation, a high-binding-energy shoulder appears, increasing the total FWHM to 1.83 eV. The peak maximum stays nearly constant at 530.2 eV. This is expected for a system consisting of an ultrathin zirconia film with a lower E_B (529.9 eV [42]) and reduced islands with a higher E_B (due to reduction/n-doping, the peak shifts to $E_B \approx 531.0$ eV, see chapter 4.4). The two shifts nearly average out; the resolution of our measurement setup is too poor to quantitatively deconvolute the two O 1s signals.

5.2.4 Stoichiometry of Ultrathin Zirconia

The area ratio of Zr 3d (excluding alloyed Zr) to O 1s can be used to calculate the stoichiometry of the ultrathin film. A closed, fully oxidized (using Rh clusters as catalyst, see Ref. 24) 5 ML-thick zirconia film was annealed at 610 °C (below the dewetting temperature) and is then used as a reference. The surface structure of this film is known [24]. To be able to compare the ultrathin film to the reference and to convert

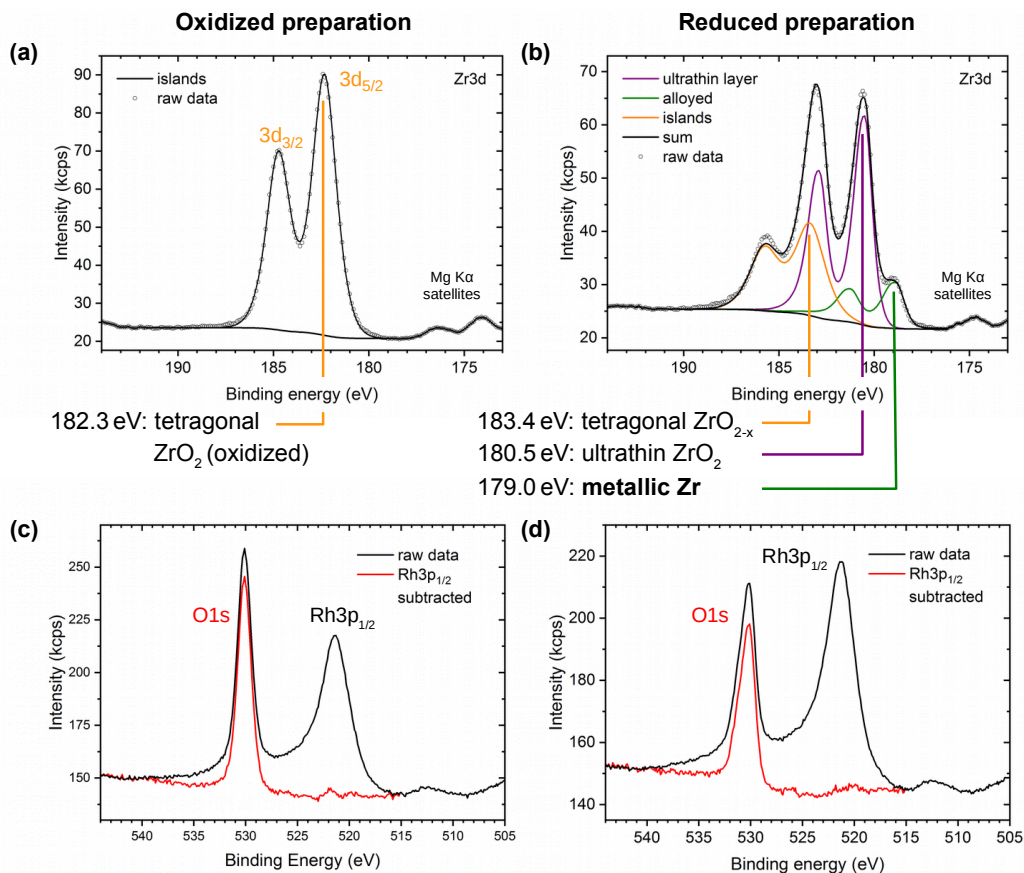


Figure 5.4: XPS of the oxidized (a,c) and reduced (b,d) preparation. (top) Zr 3d region. The oxidized preparation shows one doublet assigned to bulk-like ZrO_2 islands. The reduced preparation shows a shifted island doublet and two new doublets assigned to the ultrathin film and metallic Zr, respectively. (bottom) O 1s and Rh 3p region: For each, the raw data and the data after subtraction of the Rh 3p peak are shown.

the O:Zr ratio into a stoichiometry, we have simulated the XPS spectra of both systems using the SESSA code [73]. This approach leads to a number of uncertainties, which are discussed in detail below. The method yields a stoichiometry of $\text{ZrO}_{1.0^{+0.26}_{-0.12}}$ for the ultrathin film. For the zirconia islands of the oxidized preparation, the result was $\text{ZrO}_{1.94 \pm 0.14}$; the expected value of ZrO_2 lies within the range.

For determination of stoichiometries using XPS, a reference sample has to be used due to the unknown calibration function (sensitivity over electron energy) of the electron analyzer. Bulk zirconia cannot be used as a reference due to its insulating nature (charging), and possibly undetected hydroxylation, which would affect the O:Zr ratio. Although available as single crystal, the same problems affect YSZ, where yttria segregation [35] comes as a further complication. This leaves the possibility of using a well-determined 5-ML-thick zirconia film as a reference. Even then, problems remain. First and foremost, 1 ML-thick films cannot be compared directly with thicker films due to energy-dependent attenuation of photoelectrons. To account for that problem, we have simulated the XPS spectra of both systems using the SESSA code [73]. Secondly, the area fraction of ultrathin zirconia (excluding the 3D islands) can only be determined locally using STM; this value might vary from position to position (e.g., at step bunches, which are difficult to measure by STM). Thirdly, the ZrO_2 film used as standard is not perfectly stoichiometric. This problem is fortunately a minor one, since even slightly-reduced tetragonal and fully-oxidized monoclinic films show the same O:Zr ratio within the error bars, see chapter 4.4, so the tetragonal films used here do not significantly deviate from ZrO_2 . Finally, photoelectron diffraction (mainly forward focussing [173]) may be different between ultrathin zirconia and ZrO_2 islands; this is not taken into account by the simulation. To estimate the extent of forward focussing effects on the O:Zr ratio, XPS was measured under varying emission angle (0° , 15° , 35° , 55° off-normal). The lowest O:Zr ratio was measured for 15° (the standard angle); the other angles led to a maximum increase of $\Delta(\text{O:Zr}) = 0.18$. Finally, the accuracy of the method suffers from the unknown amount of O dissolved in the Rh substrate. All the possible errors were estimated and included in the error bars above.

Another method to gain information on the stoichiometry is the direct comparison of the O 1s intensity of an ultrathin zirconia film and an O-Rh-O trilayer [175], both prepared on the same Rh(111) single crystal. The O-Rh-O trilayer was prepared by annealing Rh(111) at $T = 410^\circ\text{C}$ for 10 min in $p_{\text{O}_2} = 1 \times 10^{-4}$ mbar (using

Substrate	Growth	Method	Reference (material)	Source	O:Zr ultrathin film	Assumptions
Rh(111)	SMSI	XPS	RhO ₂	Chpt. 5	≈ ZrO _{1.5}	Islands: ZrO ₂
Rh(111)	SMSI	XPS	5 ML ZrO ₂	Chpt. 5	ZrO _{1.0^{+0.26}_{-0.12}}	Islands: ZrO ₂ [*]
Pt ₃ Zr(0001)	Alloy	XPS	1 ML water	Chpt. 3	ZrO _{1.4}	Islands: ZrO ₂
Pt ₃ Zr(0001)	Alloy	AES	RhO ₂	[41]	ZrO _{1.62}	No islands
Pt ₃ Zr(0001)	Alloy	synchrotron-based XPS	–	[42]	ZrO _{1.82}	Islands: ZrO _{1.82}
Pd ₃ Zr(0001)	Alloy	AES	RhO ₂	[43]	ZrO _{2.19}	No islands

Table 5.1: Stoichiometries of ultrathin zirconia films with different preparation methods and substrates. (*) The possibility of reduced islands is included in the error bars.

an oxygen doser similar to a shower head; chamber pressure was 5×10^{-6} mbar). In this pressure regime, the preparation is self-limiting and forms no islands. Two ultrathin zirconia films were prepared with only 1.2 ML and 1.1 ML of zirconia, respectively, to minimize the amount of remaining islands. The zirconia films were annealed in oxygen for 10 min at $T = 550$ °C and 670 °C, respectively, to gain fully oxidized islands, then reduced for 20 min at $T = 950$ °C and 70 min at $T = 860$ °C, respectively, in UHV. To compensate for possible variations of the x-ray intensity, the x-ray-induced sample current was measured at the sample holder before inserting the sample; the results were normalized by this value. By this direct comparison method, inaccuracies induced by simulations and reference films can be avoided. However, it has to be assumed that no oxygen was dissolved in the Rh substrate; especially for the RhO₂ film, this might not be true, and would lead to an underestimation of the zirconia oxygen content. Furthermore, the area of uncovered substrate must be estimated from (local) STM images. The resulting O1s intensity ratios between the zirconia-covered surface and the RhO₂ film are 0.62 for the 1.2 ML and 0.50 for the 1.1 ML zirconia deposition. A ratio of 0.75 is expected for a fully oxidized trilayer of ZrO₂ due to the larger lattice constant of zirconia (0.35 nm compared to 0.302 nm for O-Rh-O [175]). The resulting stoichiometries are therefore ZrO_{1.7} and ZrO_{1.4}, respectively. Comparing the photoelectron-induced O_{KLL} Auger peaks yields ZrO_{1.6} and ZrO_{1.5}, respectively. This method has, on the one hand, a higher inaccuracy due to a very different background for ultrathin RhO₂ and zirconia. On the other hand, Auger peaks have a higher surface sensitivity, i.e. are less sensitive to O dissolved in

the Rh bulk.

The XPS measurements indicating a substoichiometric ultrathin film also imply that other ultrathin zirconia films are substoichiometric, regardless of whether they were obtained by oxidation of alloys, see chapter 3 and [41, 43–45], or deposition of Zr and oxidation [38]. Comparison of the Auger signals between the ultrathin zirconia films and the RhO₂ trilayer leads to compositions of ZrO_{1.62} and ZrO_{2.19} for the ultrathin oxides on Pt₃Zr [41] and Pd₃Zr [43], respectively; the latter value is rather inaccurate due to O dissolved in the Pd₃Zr bulk. A synchrotron-based XPS study [42] has found ZrO_{1.82} for both the ultrathin oxide and 3D oxide islands on Pt₃Zr. As it is unlikely that the 3D islands are strongly non-stoichiometric, the ultrathin film most likely contain less O. All stoichiometry measurements are summarized in Table 5.1. It should however be noted that not all ultrathin zirconia films necessarily have the same stoichiometry.

5.2.5 Diffusion of Alloyed Zr in Rh and Pt

The diffusion of alloyed Zr was investigated by XPS for Rh(111) and Pt(111), see Figure 5.5. The diffusion of Zr into Rh and Pt was measured by depositing 0.48 ML of metallic Zr on each surface. The samples were annealed in UHV in 110 °C steps for 10 min each. Due to the high reactivity of Zr, part of the deposited Zr is in oxidized form (possibly due to adsorption of residual-gas species), but this signal disappeared after annealing to 640 °C on Rh and 420 °C on Pt. On Pt(111), Zr disappears into the bulk at much lower temperatures than on Rh(111), indicating that the diffusion of Zr is faster in Pt than in Rh. Zr dissolution happens at a lower temperature in Pt due to the more negative dissolution enthalpy (−4.4 to −4.9 eV vs. −3.3 eV for Zr in Pt and Rh, respectively [139, 140]). Also, the formation energy of Pt₃Zr (−128 kJ g^{−1} atom^{−1} [176], an Engel-Brewer alloy [177]) is lower than for Rh₃Zr (−72 kJ g^{−1} atom^{−1} [178]). The lattice constant of Rh is smaller than for Pt (0.2687 nm vs. 0.2775 nm, respectively), which makes dissolution of the large Zr atoms less favorable. Furthermore, Rh has a higher melting point than Pt (1964 °C vs. 1768 °C, respectively). Thus, diffusion in Rh tends to be slower than in Pt.

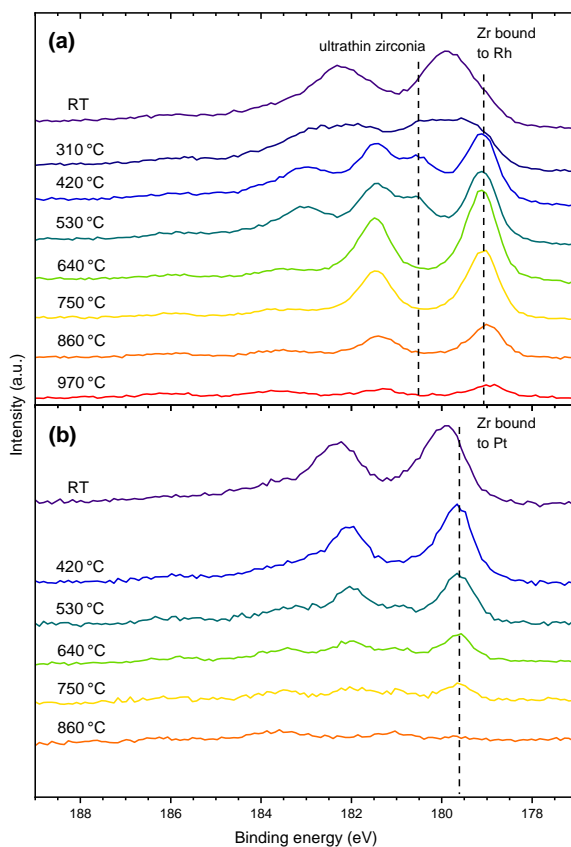


Figure 5.5: XPS of diffusion of 0.48 ML Zr into (a) Rh(111) and (b) Pt(111). After deposition, small amounts of oxidized Zr are present, but vanish soon. Metallic Zr disappears faster into the Pt bulk compared with Rh. All spectra are normalized to the background on the low-binding-energy side.

5.2.6 Transfer through Air

The ultrathin zirconia film can be easily repared, even when transferred between vacuum chambers through air (≈ 3 h). Directly after transfer, a large C 1s peak is visible, see Figure 5.6. The Zr 3d region showed Zr 3d_{5/2} peaks at 181.4 and 179.0 eV. The low E_B peak originates from metallic Zr alloyed with Rh, see above. 181.4 eV most likely originates from 3D zirconia islands, see chapter 4.4, shifted from usual values of m-ZrO₂ (181.6 eV) to lower E_B due to carbon contaminations. After annealing at 790 °C for 20 min in UHV, no measurable C contaminations were found in XPS, and no obvious contaminations were found in STM (not shown). The ultrathin film was recovered; Zr 3d appears at the usual 180.6 eV.

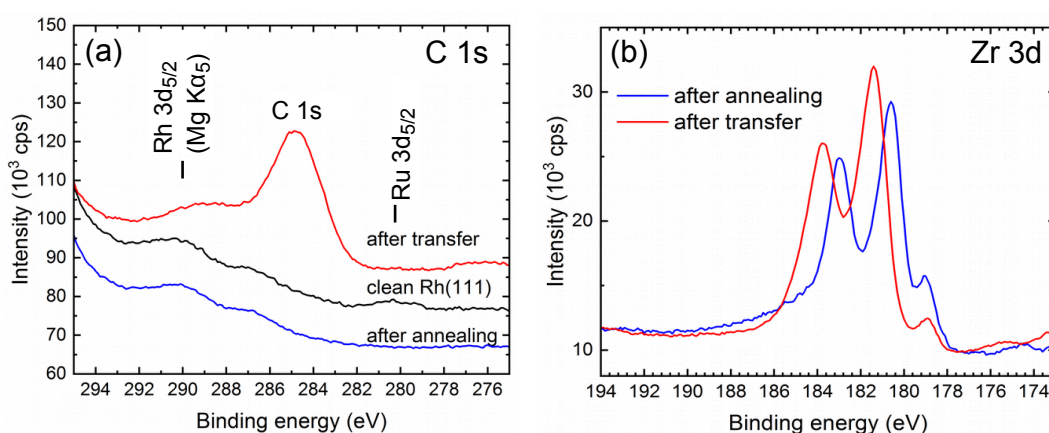


Figure 5.6: XPS measurements of ultrathin zirconia after transferring the sample from one vacuum chamber to another. **(a)** The C 1s region shows a large peak after transfer, which is completely removed by annealing at 790 °C for 20 min in UHV. **(b)** Zr 3d peaks shift by -0.8 eV after annealing; before transfer, zirconia was present in bulk form (181.4 eV). After annealing, an ultrathin film forms again (180.6 eV). All spectra are normalized at low E_B . C 1s was measured with a pass energy of 50 eV for higher count rates.

5.3 Discussion

The current work clearly demonstrates that metal–ZrO₂ systems show a similar type of so-called SMSI effects as observed for reducible oxides such as the prototypical system Pt/TiO₂ [155, 159, 160]. Upon reduction, the metal gets covered by an ultrathin oxide film, which is substoichiometric (\approx ZrO_{1.5}), though probably to a lesser

degree than for e.g. TiO_2 , where the film exhibits a $\text{TiO}_{1.1}$ stoichiometry. The ultrathin zirconia film has essentially the same lattice constant as the respective films on Pt_3Zr [41] and Pd_3Zr [43], so it is likely that it has the same base structure, an O–Zr–O trilayer. Density functional theory (DFT) calculations show that oxygen vacancies can form much more easily in such a metal-supported ultrathin zirconia film than in the bulk; for oxygen at the interface the vacancy formation energy is about half the bulk value [116]. The reason is that Zr in the ultrathin film can remain in its $4+$ state upon formation of an oxygen vacancy; the electrons are transferred to the metal. In addition, if an interface oxygen gets removed, a strong Zr–metal bond can form [179]. In contrast to oxides of polyvalent metals, reduction of the ultrathin zirconia films will always require transferring two electrons per missing oxygen atom to the metal to circumvent the formation of Zr^{3+} , thus the non-stoichiometry will be limited by the electrostatic field introduced with the charge transfer.

The calculated vacancy formation energy of 2.92 eV at the interface of the ultrathin film [116] roughly agrees with the experimental conditions for forming a complete layer of ultrathin zirconia on Rh; a chemical potential of $\mu_{1/2\text{O}_2} = -2.92$ eV corresponds to an O_2 pressure of 4×10^{-12} mbar at $T = 870$ °C. It should be noted, however, that the formation of ultrathin zirconia films starts already at lower temperatures (observed for 640 °C on Pt); thus, it could be facilitated by factors other than just reduction. In this respect, it is noteworthy that the formation of an ultrathin zirconia film often coincides with the observation of alloying, i.e. Zr dissolution in the metal.

The absence of an ultrathin zirconia film after annealing $\text{ZrO}_2/\text{Pt}(111)$ at high temperatures combined with remaining ZrO_2 islands indicates that not only reduction governs the growth of ultrathin zirconia. If that was the case, all ZrO_2 islands would be transformed first to ultrathin zirconia (which spreads out over the remaining surface) and then be fully reduced to metallic Zr upon annealing at more and more reducing conditions. Before the ultrathin film vanishes, all material contained in islands would be consumed. To explain why this is not observed experimentally on Pt(111), two hypotheses are proposed:

In the first hypothesis, ultrathin zirconia films require Zr dissolved in the metal substrate; strong bonds between the Zr in the uppermost metal layer and the oxygen of the ultrathin zirconia film help to stabilize the ultrathin zirconia – an alloying-supported SMSI effect. This stabilization mechanism was also suggested for zirconia films on Pd_3Zr (0001) [43]. It has been proposed previously that the so-called SMSI

effect may be related to alloying [180]; here, a reason for why this might happen is given. On Pt at high temperatures, the concentration of Zr dissolved in Pt is lower than in Rh due to easier diffusion into the bulk, see Figure 5.5. As a result, the strong Zr-O bonds cannot be formed, and the ultrathin film becomes energetically unfavorable. What speaks against this hypothesis? For zirconia preparations with 1.1 ML and 1.2 ML (chapter 5.2.4), the XPS signal for alloyed Zr was found to be below the detection limit, which is in this case 0.04 ML. The resulting upper limit of one additional bond per 25 Zr atoms in the ultrathin zirconia film would give little energy gain. However, without the additional influence of alloyed Zr, reduction of zirconia at temperatures as low as 640 °C is difficult to explain.

The second, competing hypothesis is based on different diffusion rates of ultrathin zirconia along the surface and Zr into the substrate. For Rh, diffusion into the bulk is slow, so the ultrathin film can form upon reduction, even at high temperatures. For Pt, this is only possible at low temperatures. The two diffusion processes would therefore have a different temperature dependence. In this hypothesis, Zr dissolved in the substrate is “passive” – no stabilizing bonds to Zr in the substrate are required for the ultrathin film. Both hypotheses include the formation of ultrathin films and alloyed Zr. An experimental proof for one or the other is difficult, as the ultrathin films cannot be prepared in the absence of any (fully reduced) Zr alloyed with the substrate. DFT calculations might give additional insights.

Similar to the reducible oxides, the “SMSI” effect is reversible also for metal–ZrO₂ systems. We can exclude competition between the ultrathin zirconia and oxygen adsorption on the metal as a driving force for disappearance of the ultrathin zirconia, as demonstrated by cooling at conditions where adsorbed O on Rh should be unstable. Rather, the effect of oxidizing conditions must be seen in (1) the ultrathin suboxide becoming unfavorable with respect to fully-oxidized ZrO₂, and (2), in case of hypothesis number one, oxidation of Zr in the uppermost Rh (or Pt) layer, so the stabilization by these Zr atoms disappears. For our inverse catalysts, this reversibility is limited by Zr disappearing into the bulk, especially in case of the Pt support, where Zr diffuses quickly. This would not happen for “real” catalysts, i.e., metal nanoparticles supported by zirconia, where no semi-infinite metal reservoir is present. On the other hand, Zr dissolution in metal nanoparticles may lead to an increased lattice constant, which is not observed in our case (no indications of subsurface misfit dislocations). Since the metal will be covered by the ultrathin zirconia in this state,

a modification of the metal lattice constant will not modify the surface chemistry, however. Under oxidizing conditions, at sufficiently high temperatures, dissolved Zr will diffuse, eventually reach the surface and there be caught by oxygen and get incorporated in the fully-oxidized (bulk-like) ZrO_2 again.

Assuming that alloying is required for the stabilization of the ultrathin zirconia film (following the first hypothesis), the SMSI effect should occur only on metals where Zr-metal alloys can form. Alloying requires a high enthalpy of solution ΔH of Zr in the metal, otherwise Zr will be more stable in oxidized form even under reducing conditions. Calculations of ΔH [140] show that Ir should behave similar to Rh, and Pd similar to Pt. The formation of ultrathin zirconia layers on Pd is shown in chapter 6.

5.4 Summary

We have demonstrated the so-called SMSI effect for zirconia on metal substrates (Rh and Pt). When annealed under reducing conditions, the substrate between 3D zirconia islands is covered by a sub-stoichiometric, ultrathin zirconia film similar to the zirconia films previously obtained by oxidation of zirconium alloys. When annealing in oxygen, all Zr becomes fully oxidized and the ultrathin film disappears. Two hypotheses that explain the influence of Zr diffusion in the Pt or Rh substrate on the film growth were presented. Easier reduction of an oxide in contact to a metal solves the long standing problem of the SMSI effect observed for oxides that are usually non-reducible.

Chapter 6

Chemical Vapor Deposition of Zirconia

This chapter shows the growth of ultrathin zirconia films on Pd(111) using chemical vapor deposition (CVD) of Zirconium (IV) Tert-Butoxide (ZTB); these films were found in a study aiming to investigate an inverse model Pd/Zr catalyst. The results on fully reduced Zr are published in an article [48], and this chapter is meant as an addendum. Parts of this chapter are based on said article.

6.1 Sample Preparation

Measurements were conducted in the RT-STM chamber, see chapter 2.1.1. A Pd(111) single crystal (from MaTeck, Germany) was used and prepared by sputter/anneal cycles (2 keV Ar⁺ ions, $\approx 2 \mu\text{A}/\text{cm}^2$ current density; 10 min at $T \approx 650 \text{ }^\circ\text{C}$). ZTB (Zirconium (IV) tert-butoxide, $\text{Zr}(\text{O}-t-\text{C}_4\text{H}_9)_4$, for the structure see Figure 6.1, from Sigma Aldrich, purity: 99.999%) was dosed via a leak valve. The vapor pressure of ZTB at room temperature is $\approx 8 \text{ mbar}$ [181]. Similar to the typical approach for water, ZTB (a liquid) was filled into a steel cylinder and connected to the leak valve. However, ZTB has to be handled under Ar atmosphere, as it immediately forms white powder when in contact to air moisture. Freeze-pump-thaw cycles were performed by LN₂ cooling (freezing point of ZTB is 269 K). During deposition, the Pd(111) temperature was held at 450 °C. ZTB then decomposed at the surface, leaving ZrO₂ behind [182]. Pressures between $5 \times 10^{-8} \text{ mbar}$ and $5 \times 10^{-6} \text{ mbar}$ were used; to calculate the dosage, uncorrected ion gauge measurements in Langmuir ($1 \text{ L} = 1 \times$

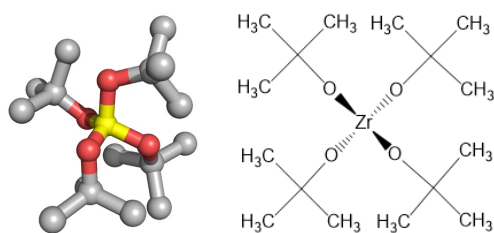


Figure 6.1: (left) 3D model, and (right) Natta projection of ZTB (Zirconium (IV) tert-butoxide). Taken from [183].

10^{-6} mbar torr·s) were used.

6.2 Results and Discussion

1000 L of ZTB were dosed on a cleaned Pd(111) single crystal surface. After post-annealing at ≈ 450 °C in UHV, an ultrathin film formed, covering small parts of the Pd surface. XPS showed [48] that 26% of the Zr 3d signal originating from deposited Zr that was fully reduced and alloyed with the Pd substrate ($E_B = 179.6$ eV), as on Pt_3Zr [42, 45]. Another 27% of the Zr signal originated from bulk-like ZrO_2 islands ($E_B = 183.1 - 182.3$ eV), and the remaining 47% in the form of ultrathin films ($E_B = 180.9$ eV). No remaining C from the precursor was detected in the C 1s region. Zr in the substrate possibly stabilizes the formation of ultrathin films on the surface via Zr-O bonds, see chapter 5. Figure 6.2a shows an atomically resolved STM image of an area covered by the ultrathin film. In the FFT, see inset, Pd(111) and ZrO_2 spots can be located; the average unit cell parameter of ZrO_2 is 0.351 nm – a value which is in line with previously reported ultrathin films on Pd_3Zr [43], Pt_3Zr , see chapter 3 and [41], and Rh(111), see chapter 5 and [111]. The film is however slightly distorted, deviating from the tetragonal structure by 2.6%.

When annealing at $T = 450$ °C for 50 min in UHV after deposition of 500 L ZTB, only fully reduced Zr is left on the surface. As discussed in chapters 5 and 4.4, the reduction of zirconia is enhanced by zirconia-metal interfaces as well as the availability of a large bulk volume for Zr dissolution (energy gain via a rise in entropy). As the dissolution of Zr in Pd is similarly favorable as for Pt [140], it is not surprising that reduction is easily possible. Before dissolving in the bulk, Zr is found in the second layer, below a top layer of pure Pd [48]. Figure 6.2b shows an STM image of

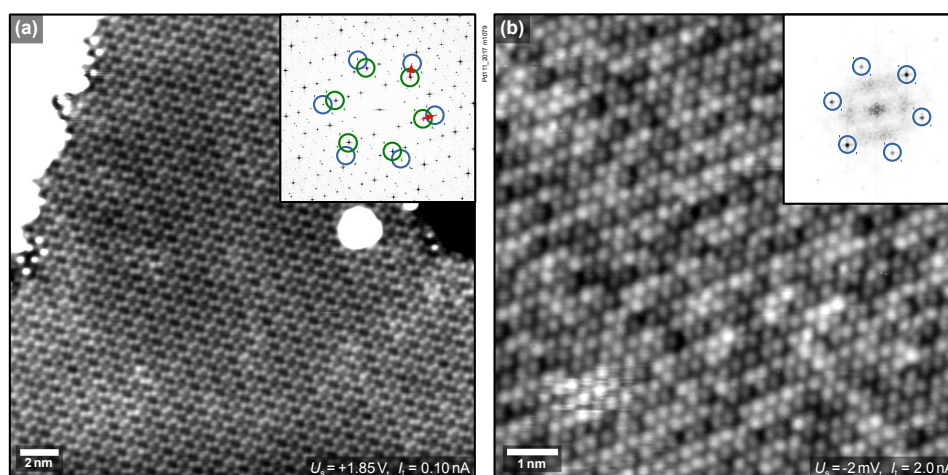


Figure 6.2: STM images of ZTB deposited on Pd(111). The insets show the FFT. **(a)** Ultrathin zirconia film patches can be found after annealing at 450 °C for 10 min. 1000 L ZTB were deposited. The FFT shows Pd(111) spots (blue), ZrO_2 spots (green) and the resulting moiré vectors (red). **(b)** When annealing at 450 °C for 50 min after depositing 500 L ZTB, metallic Zr is formed. In the FFT, the inner Pd(111) spots are marked in blue, and a ring originating from amorphous-like order of dissolved Zr can be seen.

such a structure. In the FFT (inset), the Pd spots are clearly visible, yet Zr gives rise to a smaller ring in the FFT; this is a clear sign of amorphous-like ordering, which is rare in surfaces and only has few known examples, such as bilayers of SiO_2 [184] or GeO_2 [185] on Ru(0001).

Chapter 7

Oxidation of Zr(0001)

In this chapter, an attempt to grow zirconium oxide structures by oxidizing a Zr(0001) single crystal is documented. The work was inspired by the PhD thesis of Wen Ma from the Yildiz group at the Massachusetts Institute of Technology [186], where such a growth behaviour was reported. The reported structures could however not be created reproducibly, and are probably related to Ni impurities in the crystal and carbon contamination.

7.1 Previous Results

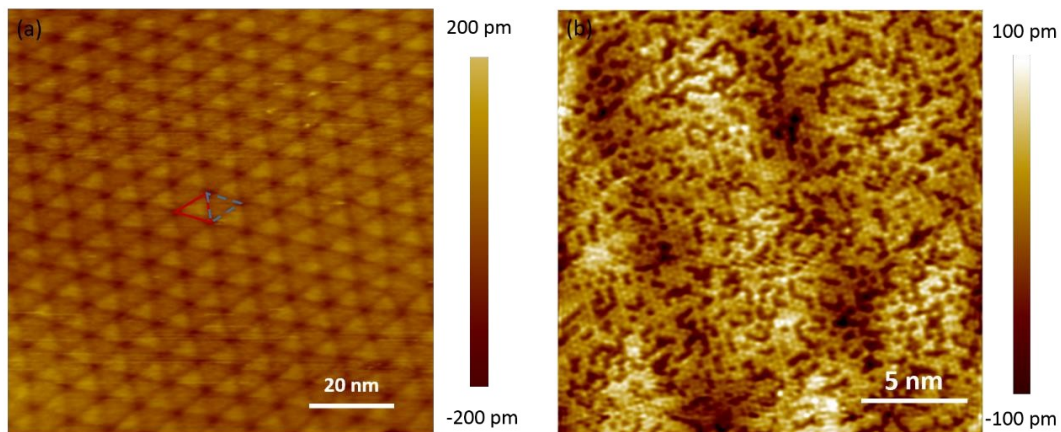


Figure 7.1: Triangular moiré structure on Zr(0001) as found by Wen Ma, after 1 min $p_{O_2} = 2.6 \times 10^{-8}$ mbar and annealing at 530 °C for 4 h: (a) overview STM image (b) atomically resolved STM image showing a high number of dark features assigned to oxygen vacancies. Figure taken from [186].

The surface oxidation of Zr(0001) was studied by Wen Ma in his PhD thesis [186],

resulting in the discovery of two structures: After dosing 2.6×10^{-8} mbar of oxygen for 1 min and annealing in UHV at 530°C for 4 h, a triangular moiré structure formed. With further dosing and UHV annealing, more and more of this structure was replaced by what was designated as a second layer of zirconia forming a row structure. Figure 7.1 shows an overview of the triangular moiré structure and the atomically-resolved, hexagonal surface lattice. This structure has a lattice parameter of 0.331 nm and forms a moiré structure with an 8.8 nm repeat unit together with the Zr(0001) lattice below. The model proposed for the structure was an ultrathin zirconia (111) trilayer on the metallic substrate, as on e.g. Pt₃Zr [41]. The dark spots visible in 7.1b were interpreted as oxygen vacancies (45% coverage), and a stoichiometry of ZrO_{1.1} was followed. This large oxygen deficiency is used to explain the large difference between the lattice parameter found for zirconia on Zr(0001) and bulk zirconia (0.36 nm [24]) or other ultrathin zirconia films (0.35 nm [41, 43]). From the STM images shown in [186], an V_O concentration of $\approx 20 - 30\%$ appears to be more realistic; the stoichiometry of ZrO_{1.1} seems to be based on the assumption that the same amount of V_Os is found in the O-layer close to the substrate. No further studies were conducted to corroborate the assignment of the dark spots to oxygen vacancies. Thus, contaminations can not be ruled out as a reason for the dark species.

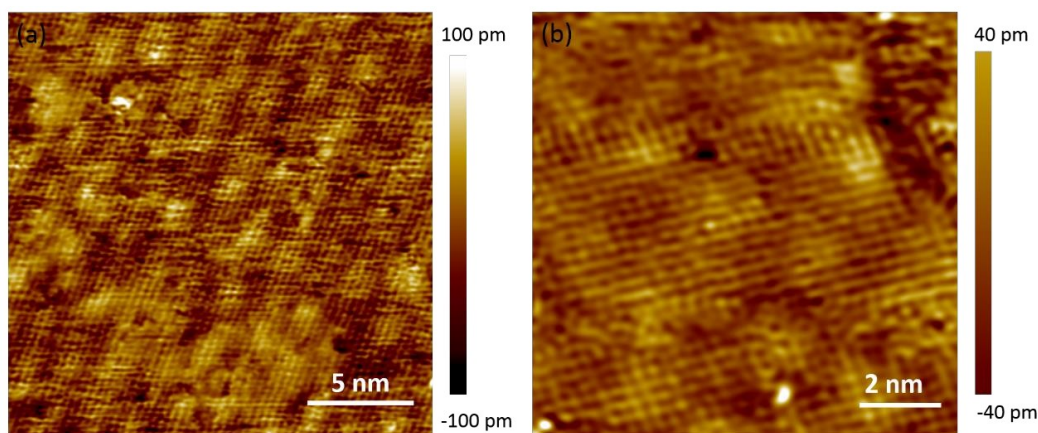


Figure 7.2: Square structure on Zr(0001) as found by Wen Ma: **(a)** The large-scale STM image shows the typical appearance as rows. **(b)** On a smaller scale, the lattice can be resolved (best visible in the lower third of the image). Figure taken from [186].

When dosing oxygen after formation of the triangular structure, a second structure forms, see Figure 7.2. This structure shows rows with a periodicity of 2.2 nm; on an atomic scale, Wen Ma found a square lattice with a lattice constant of 0.36 nm in the

FFT. This was attributed to a $\text{ZrO}_2(100)$ bilayer as a second layer on top of the first zirconia trilayer.

Both structures found by Wen Ma are astonishing. Firstly, it is surprising that an ultrathin film similar to a layer of $\text{ZrO}_2(111)$ was found with a lattice constant of 0.33 nm — much closer to the 0.3232 nm of metallic $\text{Zr}(0001)$ [187] than to the 0.36 nm of zirconia. As discussed in chapter 1.2, cubic and tetragonal zirconia with a lattice parameter around 0.36 nm are not stable at room temperature or without oxygen vacancies. Ultrathin films as on $\text{Pt}_3\text{Zr}(0001)$ (see chapter 3) or $\text{Rh}(111)$ (see chapter 5) can only contract to 0.35 nm due to oxygen being able to buckle out of plane to keep a high O-O distance. These films contain about 25–30% oxygen vacancies, see chapter 5.2.4 and 3.4.3 — compared to 45% suggested by Wen Ma. Secondly, the growth of a square structure on top of a hexagonal structure is unusual. Especially a bilayer structure would come as a surprise, as zirconia in the (100) direction is polar with a $\text{Zr-O}_2\text{-Zr-O}_2$ stacking (see figure 1.1); such a Tasker type 3 structure is typically considered unstable if no compensation mechanism is present [188, 189]. The following studies were conducted to reproduce the zirconia structures on $\text{Zr}(0001)$ and confirm the proposed models.

7.2 Sample Preparation

All measurements in this chapter were conducted in the RT-STM chamber, see chapter 2.1.1. For all studies on $\text{Zr}(0001)$, a single crystal ($10 \times 5 \times 2$ mm, from Princeton Scientific Corp.) was used. It was kindly lent to us by Bilge Yildiz and was the same crystal that was used in the original studies by Wen Ma. As metallic Zr has a phase transition from a close-packed hexagonal to body-centered cubic lattice at ≈ 870 °C [190], annealing was limited to temperatures below the transformation temperature to avoid risking the destruction of the single crystal. Real temperatures in the RT-STM chamber are typically higher than the temperatures shown by the thermocouple, so with $T < 700$ °C a safe distance was kept to this transition temperature. A range of parameters was applied during sputter and anneal cycles: The sample was sputtered with 2 keV Ar^+ ions for typically 30 min, at temperatures between room temperature and 600 °C. Afterwards, the sample was annealed at 600 °C to 640 °C for 30 min to 3 h. To grow zirconia films, oxygen was dosed at $p_{\text{O}_2} = 1 \times 10^{-9}$ mbar and 1×10^{-8} mbar for 30 s to 20 min. Post-annealing was done in UHV at up to 580 °C

for 30 min to 4 h. Temperatures given here are estimated as being 10% higher than the thermocouple temperatures; no calibration with a disappearing filament pyrometer was possible due to the rather low temperatures. (Our disappearing filament pyrometer gives reasonable accuracy above ≈ 800 °C.)

7.3 Results

7.3.1 Initial Reproducibility

Both structures found by Wen Ma [186] could be found during our studies, yet not reproducibly. The triangular structure could only be reproduced once after removing species adsorbed since the last cleaning cycle five days prior with a single sputter/anneal cycle (22 cycles in total since introducing the crystal into the chamber) directly followed by dosing oxygen for 1 min at $p_{O_2} = 3 \times 10^{-8}$ mbar at RT and 4.5 h of annealing at 530 °C in UHV. The STM image, see Figure 7.3, was taken on the following day. The triangular structure appears to be decorated with bright species, which were aligned with the underlying lattice an FFT of these species gives a lattice parameter of 331 ± 1 pm (as found by Wen Ma), which also coincides with the lattice parameter from the analysis of the moiré structure. We therefore conclude that this is the same film as found in previous studies. XPS taken on the same surface showed signals of C, O, Co, and Ni, see section 7.3.3.

In another preparation, the “square” (or “row”) structure was found after dosing $p_{O_2} = 5 \times 10^{-8}$ mbar for 5 min and annealing at 580 °C for 30 min, see Figure 7.4a. The area covered by this structure was larger than 200×200 nm². However, taking STM images in a different region of the crystal showed an area with nearly no coverage of the “square” structure. Therefore, contrary to Ref. 186, the structure is a local phenomenon and not directly linked to higher oxygen doses. Again, the structures measured by Wen Ma [186] can be confirmed: The structure consists of rows with a periodicity of 2.20 nm. On the atomic scale, the lattice was found to be slightly rectangular; in the FFT, see Figure 7.4b, the lattice constant of this structure can be determined as ≈ 0.351 nm on average (using 323.2 pm for Zr [187] as a ruler) – slightly smaller than the 0.359 nm reported by Wen Ma. The measured value is the average of two directions; a systematic difference between the two directions was found, so the structure is slightly rectangular by about one percent. Figure 7.4a shows

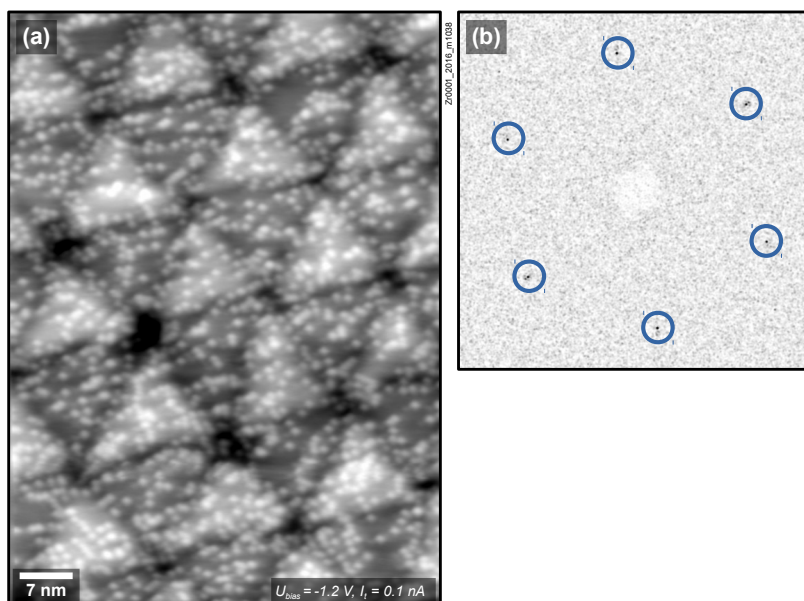


Figure 7.3: (a) STM image of the triangular moiré structure on Zr(0001). Apart from the moiré, bright species of unknown origin can be seen. (b) FFT of the locations of the bright species shows the underlying atomic structure with a lattice parameter of 331 ± 1 pm.

a large amount of species adsorbed on the rectangular grid, which amount to 0.2–0.3 ML.

A large area covered by the “square” structure as discussed above was only found once; the typical appearance was on step edges as shown in 7.4c. On the terraces, patches of the O-(2 × 2) structure (see below) can be found. In between, the bare Zr(0001) is found with a few adsorbates. The structure on step edges was found both after O₂ dosing followed by UHV annealing and directly after sputter/anneal cycles, i.e. on a cleaned surface. The growth behaviour of the “square” structure on top of the triangular structure described by Wen Ma [186] was not observed during any of our measurements.

7.3.2 Oxygen Dosing on Clean Surface

After prolonged cleaning, i.e. ≈ 50 cleaning cycles with varying temperatures during sputtering and annealing, none of the structures reported by Wen Ma [186] were encountered anymore. Directly after dosing 18 L of oxygen at RT, only clusters could be found on the surface with STM, see Figure 7.5a. In XPS, three Zr 3d doublets were

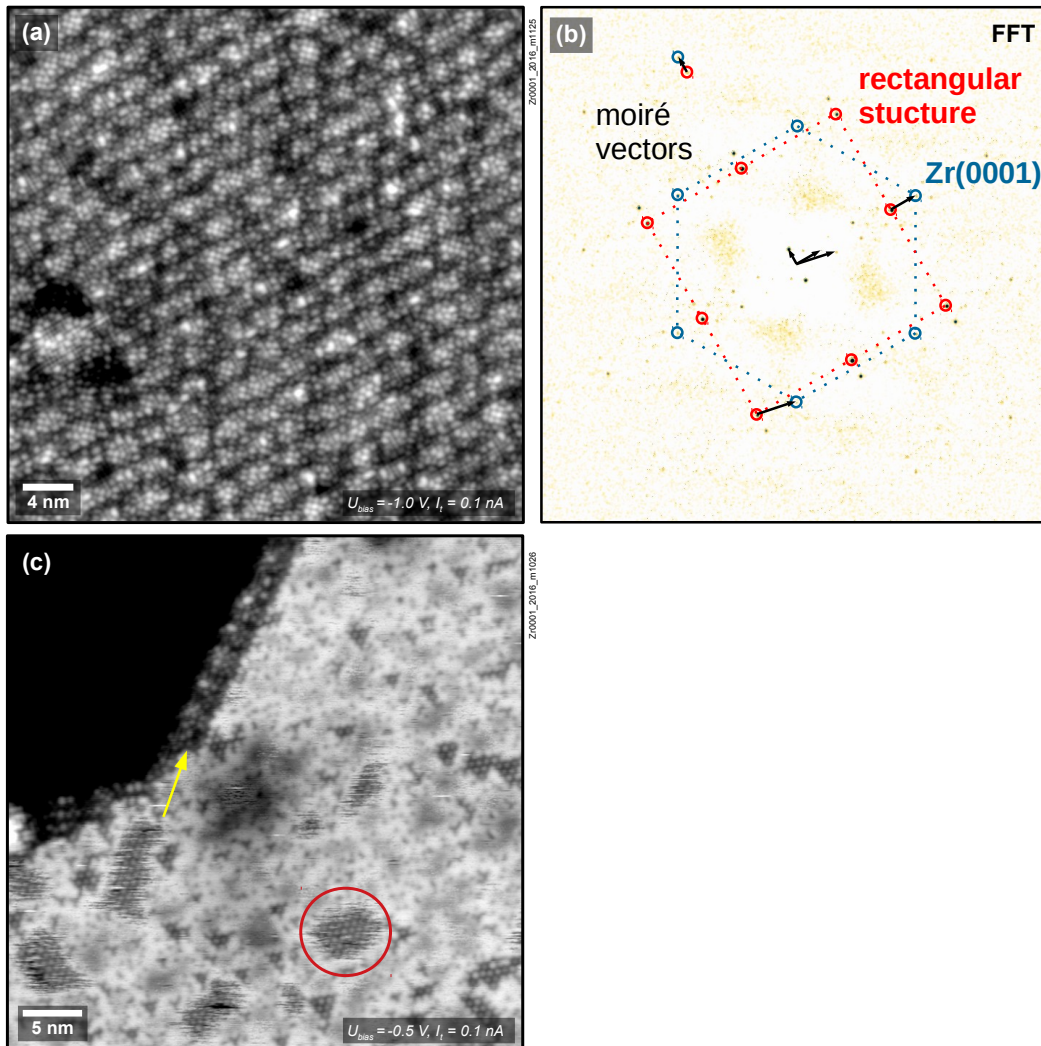


Figure 7.4: STM images of the rectangular (“square”) structure on Zr(0001): **(a)** Large-area image of the structure (found in an area $> 200 \times 200 \text{ nm}^2$ only once). **(b)** FFT of (a), showing the rectangular lattice of the overlayer structure, the underlying Zr(0001) structure and the resulting moiré vectors (black) leading to the row-like appearance. **(c)** Typically, the rectangular structure appears at step edges only (yellow arrow). On the flat terraces, patches of a mobile O-(2×2) structure can be found (red circle). The remaining surface is bare Zr(0001) with few adsorbates.

found, originating from

- metallic Zr: $E_{\text{B}}(\text{Zr } 3d_{5/2}) = 178.9 \text{ eV}$,
- bulk ZrO_2 : $E_{\text{B}}(\text{Zr } 3d_{5/2}) = 182.6 \text{ eV}$, as in chapter 4.4 and [137]), and
- ultrathin or interface zirconia: $E_{\text{B}}(\text{Zr } 3d_{5/2}) = 180.3 \text{ eV}$ [42].

The O 1s signal was formed by overlapping peaks from both oxide species and was located at $E_{\text{B}} = 531.1 \text{ eV}$. The single peaks cannot be resolved with the lab-based XPS setup used here. However, upon annealing in UHV, the O 1s signal vanished quickly, see Figure 7.6. There, 10 L of O_2 were dosed and annealed stepwise for 5 min each. Already after annealing at 110°C , no bulk ZrO_2 signal could be found in the Zr 3d region. However, two separate peaks remained in the O 1s region; compared to the clean surface, the Zr 3d doublet appeared shifted to a higher E_{B} by 50 meV. This is most likely due to a remaining Zr 3d doublet with a E_{B} similar to that of ultrathin or interface zirconia; in this case, it is most likely linked to the O-(2×2) structure described below. No further change was found until 420°C , pointing towards a metastable structure between these two temperatures. Already at 520°C – the temperatures used for the creation of the triangular structure – no O_2 was left on the surface, and Zr 3d was only showing metallic Zr.

The only ordered structure found on the thoroughly cleaned crystal was a (2×2) structure on flat terraces, covering varying areas of the surface, see Figure 7.7. It is difficult to predict the O-(2×2) coverage, as even after several sputter/anneal cycles a nearly full coverage can be present without dosing oxygen, e.g. as in Figure 7.7a. After annealing this sample at 530°C , the coverage was reduced from 70% to 35%. In XPS, two peaks appear. While the high- E_{B} (531.8 eV) peak is reduced by 25% by the annealing, the low- E_{B} peak (530.6 eV) is reduced by 2/3. It can therefore be assigned to the (2×2) superstructure found in STM. The origin of the high- E_{B} peak remains unclear – O dissolved in Zr would be an obvious candidate. Furthermore, mobile OH species could not be resolved by STM and would be a further, yet unlikely, option, as OH is expected to desorb below 300 C on Zr(0001) [191].

7.3.3 Cleanliness

Impurities could play a significant role in the creation of superstructures on Zr(0001). Indeed in AES measurements, several elements apart from Zr and O were found: Ni,

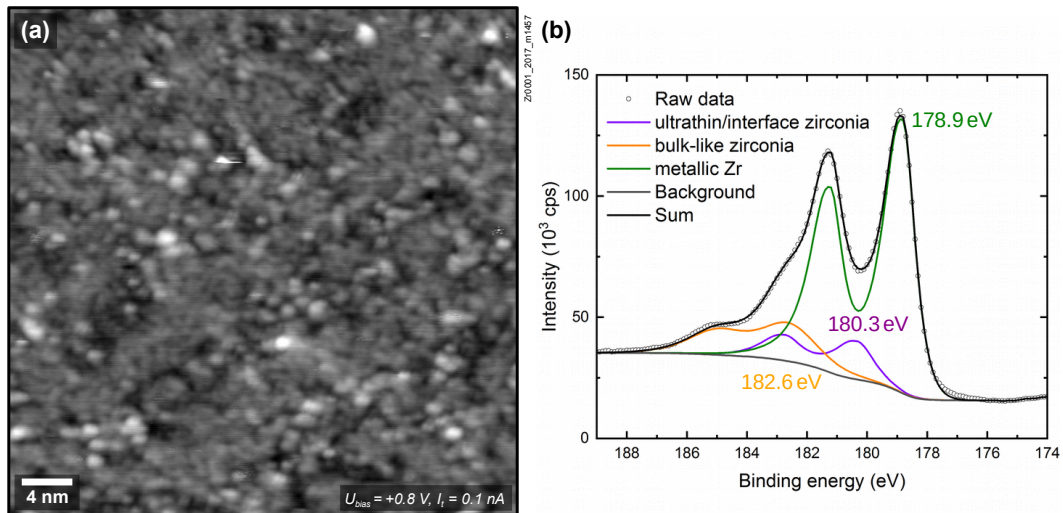


Figure 7.5: Dosing 18 L of oxygen at room temperature leads to disordered structures on the surface (before annealing). **(a)** STM image of the surface showing clusters. **(b)** XPS of the Zr 3d region fitted with a bulk-like zirconia peak originating from clusters and a peak typically assigned to ultrathin films or interface oxides.

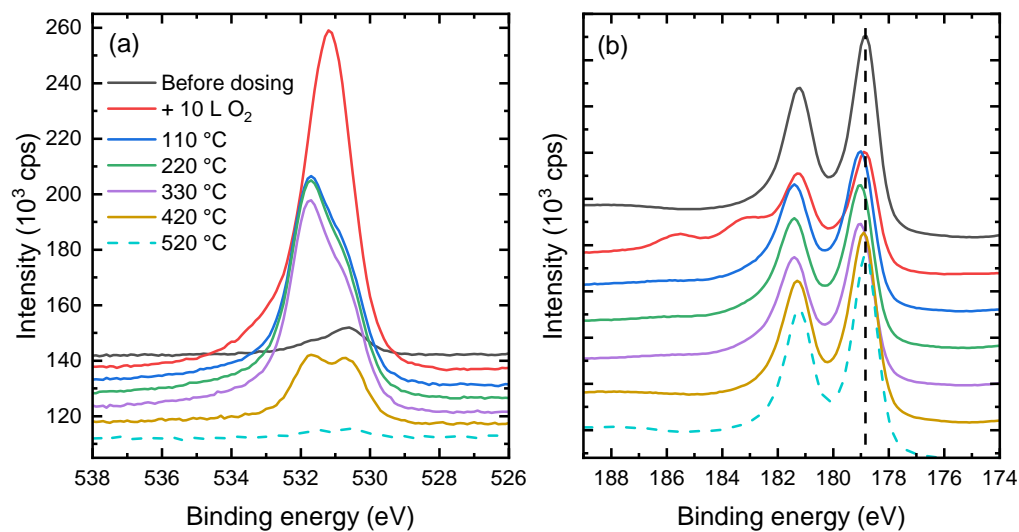


Figure 7.6: XPS data show that upon annealing stepwise for 5 min each, 10 L of oxygen dosed at RT diffuse in the bulk. **(a)** The O 1s region shows that one peak is found after dosing at RT, which splits into two upon annealing. Between 330 and 420 °C, these peaks also start to vanish. **(b)** Zr 3d shows that ZrO₂ clusters vanish already when annealing at 110 °C. All spectra are normalized to the low-energy side of the 520 °C curve, and shifted upwards linearly for the sake of clarity.

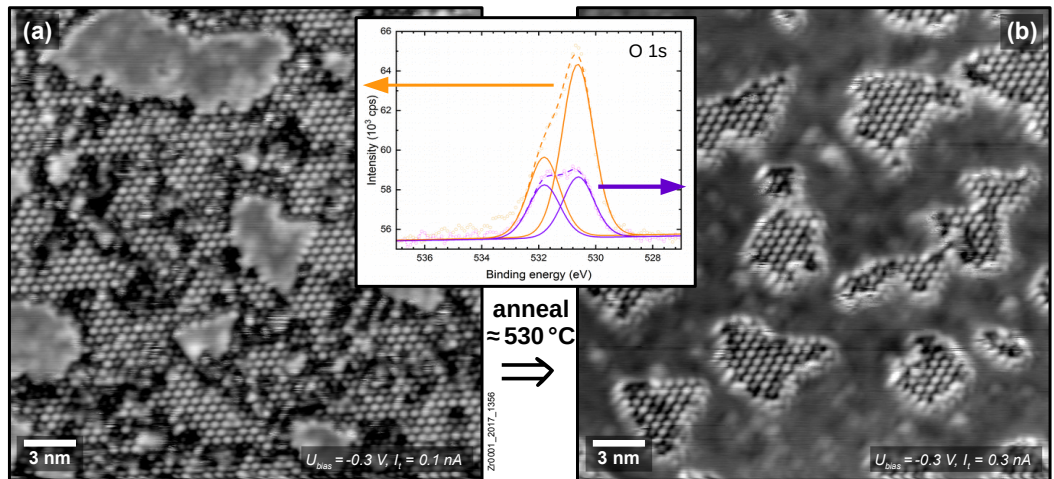


Figure 7.7: STM images with different amounts of O-(2×2) coverage **(a)** after 5 sputtering (30 min, 110 °C) and anneal (550 °C, 3 h) cycles, and **(b)** after annealing to 530 °C. In the middle, XPS spectra are shown in orange and violet, respectively. The low- E_B peak falls with the O-(2 × 2) coverage.

Co, and carbon were the main constituents. (A small peak at 690 eV fits praseodymium, which is however an unlikely impurity.) The intensity of these peaks varied from preparation to preparation, see the green and red curves in Figure 7.8, with no clear, recognizable pattern. This might also be related to local variations of the impurity density, as AES measures only in a small spot ($<1 \text{ mm}^2$).

XPS, which averages over the whole crystal, was measured after dosing O_2 for 1 min at $p_{\text{O}_2} = 3 \times 10^{-8}$ mbar at RT and 4.5 h UHV annealing, after the STM measurements shown in Figure 7.3. There, Co was not detected. This could mean that Co was a local contamination and not enough material is present for a measurable signal in XPS. As AES was measured near the border of the crystal (due to experimental limitations), STM however in the center, Co is most likely not related to the STM structures in question. F can only be measured by XPS, as it desorbs immediately under electron bombardment. C and Ni remain as major contaminations. (A small Ta signal originates from the sample clips.)

7.4 Discussion

The dissolution of oxygen or zirconium oxide into Zr is described in literature. According to the phase diagram, almost 30% oxygen is soluble in the Zr bulk [192].

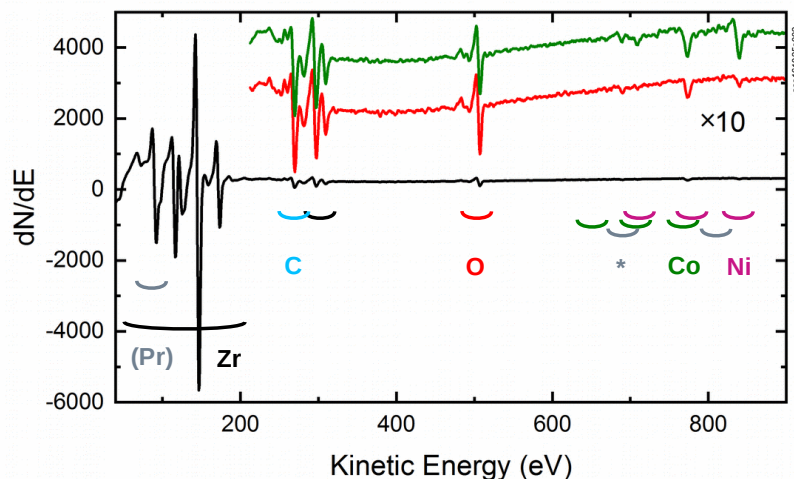


Figure 7.8: AES spectra of Zr(0001): The spectrum shown in black and red ($\times 10$) was taken after sputtering at 400°C and annealing at 640°C for 3 h, before dosing oxygen for the preparation that showed the triangular structure in Figure 7.3. The green spectrum ($\times 10$) was taken after one additional sputter/anneal cycle after STM (same parameters except $T_{\text{sputter}} = 275^\circ\text{C}$, $t_{\text{anneal}} = 1\text{ h}$). Except for the expected Zr, the spectra show clear peaks for C and O, as well as peaks that can be assigned to Co and Ni. One additional peak (marked by an asterisk) at 690 eV would fit Pr, which is however an unlikely impurity. The low-energy Pr peak (91 eV) is too close to a Zr peak at 96 eV to discern whether it is present. Element names are given at the position of the strongest peak of this element.

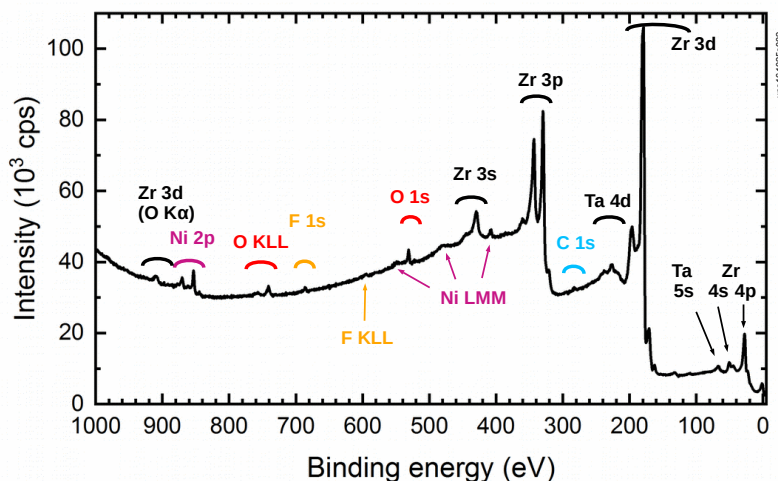


Figure 7.9: XPS measurement of Zr(0001) after dosing O_2 ($p = 3 \times 10^{-8}$ mbar, 1 min) and annealing 4.5 h in UHV. Apart from Zr and O, several other elements are detected: Ni, C, and F. The Ta peak results from sample clips.

The enthalpy of O₂ dissolution in Zr (−1200 to −1300 kJ/mol [193]) is larger than the enthalpy of ZrO₂ formation (−1097 kJ/mol [194]), with dissolution being favoured additionally by the gain in entropy. Dissolution is also not kinetically hindered at the annealing temperatures used in the experiments; already at 500 °C, dissolution happens with > 2 Å/min and 100 Å/min at 600 °C [195]. The amount of oxygen in the bulk therefore rises over time and oxygen cannot be depleted by sputtering and annealing. Kinetics explain why Zr is known for its corrosion resistance in reactor applications, which comes from the formation of zirconia on the surface, although dissolution is thermodynamically favored. This effect happens at ≈ 300 °C where dissolution is still kinetically hindered. The study of Zr corrosion is a field in its own right [196].

The favored oxygen dissolution, combined with features of the two structures reported by Wen Ma [186], which are unlikely for zirconia structures (e.g. the small lattice parameter, low reproducibility, structures found only locally), open the question whether the triangular and the “square” structures found in STM are truly zirconia-based.

Two non-oxide candidates were found that fit to the unit cell parameters observed by STM and are based on the two most common contaminations: nickel and carbon. Carbon is a common impurity on Zr, as CO dissociates easily on Zr [197]. Zirconium carbide (ZrC_{1-x}) exhibits the NaCl structure [198] with a lattice parameter of 469.8 pm. The (111) plane would therefore have a smaller lattice parameter by a factor of $\sqrt{2}$: 332.2 pm. This gives a close fit to the lattice constant of the triangular structure: 331 ± 1 pm. Additionally, in contrast to oxygen, carbon is nearly non-soluble in Zr [199], leading to the enthalpy of C dissolution (−164 kJ/mol [200]) being higher than the enthalpy of ZrC formation (−197 kJ/mol [194]).

A rectangular layer on a hexagonal structure is a combination that is typically not very favorable. This can be compensated by a very stable film. Carbon forms a $c(2 \times 2)$ reconstruction with distortions on a nickel substrate, the so-called Ni₂C “clock reconstruction” [201,202] with a lattice parameter of 352 pm, fitting the lattice parameter measured for the Zr(0001)-based “square” structure (351 pm). This reconstruction is known for its stability, as it does not only form on Ni(100) [201,202], but also on Ni(111) [203,204], where the surface layer is transformed from a hexagonal to a rectangular structure. The “square” structure could therefore be explained by a Ni₂C film. Such an impurity-based structure could explain why it was found in one

place on the crystal, while not being found at all in another.

Let us finally discuss the single ad-species found on both the triangular and the “square” structures. These could be explained by other contaminants that were found in XPS and AES. Fluorine would be a prime candidate for such single protrusions.

Chapter 8

Conclusion and Outlook

The reader will already have noticed that many effects described in this thesis are discussed and explained in terms of oxygen vacancies (V_{O}). This is a usual approach when studying oxides. For zirconia, however, V_{O} are no obvious candidates, as it is often considered hard to reduce. Any model of zirconia involving V_{O} therefore has to include an explanation of why V_{O} can form in the first place.

5 ML-thick zirconia films on Rh(111) were found to be stable in the tetragonal phase until annealing above 730 °C, the onset of the transformation to the monoclinic phase. This is contrary to the bulk behaviour, where the monoclinic phase is the only stable phase at room temperature, and tetragonal zirconia is stable only from 1205 °C on. For 5 ML-thick films, only slight substoichiometries were found, yet with substantial influence. While monoclinic films are (close to) fully oxidized, tetragonal films contain up to $\approx 2\%$ oxygen vacancies; these lead to a shift of the electronic states of up to 1.8 eV towards higher binding energies. Additionally, V_{O} are the major factor in the stabilization of the tetragonal structure, similar to zirconia in powder form [26]. Therefore, the transformation from tetragonal to monoclinic films needs oxidation; this can be achieved either by annealing at temperatures sufficient for dewetting of the film, i.e. revealing of the Rh substrate, or by deposition of a catalytically active metal on top of the film. The thorough research on thin zirconia films presented here opens the possibility of adding another complexity level, e.g. by adding a third element, such as yttrium, for the study of yttria-stabilized zirconia.

The adsorption and desorption behaviour on ultrathin films on $\text{Pt}_3\text{Zr}(0001)$ was studied for water, methanol, CO_2 , CO, O_2 , and Kr. The water study showed combined (weakly bound) molecular and (strongly bound) dissociative adsorption, yet also revealed the zirconia film to be substoichiometric, $\approx \text{ZrO}_{1.40}$. This did however

not have significant influence on the adsorption behaviour, suggesting a preferred oxygen vacancy location in the lower oxygen layer, at the interface to the substrate.

A similar tendency was found for 5 ML-thick films, where V_{O} s were located preferentially near the interface, which could be extracted from an XPS study. A direct and clear observation of V_{O} s via STM would be a future goal, as would be the observation of V_{O} filling. An explanation for the existence of vacancies is given by DFT [116, 153, 154], where the V_{O} energy of formation is drastically reduced for thin films due to the underlying metal substrate; the two electrons from the V_{O} are transferred to the metallic bulk. For V_{O} s directly at the interface, substrate atoms can rearrange and partly compensate for the missing oxygen atom.

The strong metal-support interaction (SMSI) chapter shows that substoichiometric films alone cannot explain every phenomenon. There, ultrathin zirconia formed on the bare Rh(111) and Pt(111) substrate between islands upon reduction and could be removed by oxidation. This showed that the SMSI effect does also occur for zirconia. Ultrathin films showed a similar stoichiometry as on Pt_3Zr , $\approx \text{ZrO}_{1.5}$.

At last, two further possible growth methods are discussed in this thesis: Oxidation of Zr(0001) turned out not to be useable, as oxygen quickly diffuses into the bulk at temperatures as low as 500 °C. Previously reported structures were most likely carbon-based (which does not diffuse into the Zr bulk) in combination with Ni impurities.

The growth of zirconia by chemical vapor deposition is offering the potential of a simple way of zirconia deposition without the use of a sputter source or evaporator. However, the growth of ordered films thicker than one monolayer has yet to be shown.

Appendix A

Thermocouple Temperatures

T_{real} in °C	T_{TC} in °C for the crystal		
	Rh(111)c	Pt(111), Rh(111)	Pt ₃ Zr(0001)
300		310	
390	410		
400		430	
500	550**	540**	500
550	610	600	
570	630		
600	670	650	600
650	730		
680	770		
700		770	700
715	810		
725	820*	800	
750	860		
765	870		
800	920/950*	880*	
850			880*
900		970	

Table A.1: Thermocouple temperatures T_{TC} in the RT-STM chamber vs. temperatures estimated from disappearing filament pyrometer measurements. When two temperatures are given, two different measurements gave slightly different results. The temperatures that were measured with the disappearing filament pyrometer are marked with “*”. For calculating lower temperatures, one temperature has to be assumed, which is marked with “**”.

Appendix B

Raw Data Locations

Figure	Measurement		
	Date	File number or name	Part of group name
2.5a-c	26.4.2017	20170425_sputtersource_cleanZrmetal	clean Rh(111)c, 2 cycles, ... +2ML of Zr metal
2.5d,e	13.9.2017	20170913 ... (monoclinic)+Rh	Rh(111)c clean?, Rh(111)c 5ML ZrO2 RT
3.3	7.7.2016	923, 946-958	
3.4	18.7.2016	XPS_D2O4L	
3.6a	27.7.2016	1037-1044,1046,1053,1054	
3.6b	27.7.2016	1036,1057,1060	
3.11	29.7.2016	1066,1067,1069-1073	
3.12	1.8.2016	xps_methanol	
3.13	6.7.2016	937,938,940-944	
3.14 3.15	19.7.2016	977-982,984	
3.16	27.7.2016	1035,1055,1061	
3.17	22.7.2016	1006,1008-1014	
4.5a,b	23.1.2018	20180117 ... variation_2ndtry	...150V/100V ... + 600C O2
4.5c,d	5.6.2018	20180604 ... (monoclinic)+1ML Ni	annealed at 715 C in O2

Table B.1: Raw data file names, sorted by Figure number, part 1

Figure	Measurement		
	Date	File number or name	Part of group name
4.5inset	26.11.2018	20181126_50ML_tetragonal_for_LT	5 ML, 20 ML
4.6	18.9.2017	20170918 ... thickfilms_ZrO2	500C, 550C, 600C
4.7a 4 ML	3.11.2015	xps151103s004	
4.7a 5 ML	15.10.2015	xps151030s003	
4.7a 7.5 ML	15.10.2015	xps151022s002	
4.7b 4 ML	30.5.2018	20180529 ... 0.5 ML Ni	annealed at 680 C in O2
4.7b 5 ML	as Figure 4.5c		
4.7b 7 ML	9.8.2018	20180809_thickfilms_ZrO2	annealing in O2 at 750 C
4.8 5 ML	as Figure 4.5c		
4.8 50 ML	27.11.2018	20181126_50ML_tetragonal_for_LT	600C in O2 100min
4.10 tet ×3	20.2.2018	20180219 ... variation_3rd	570C O2, + 0.016 ML Rh, + annealed 550C O2
4.10 mon	as Figure 4.5c		
4.16 500 °C	25.11.2015	xps151125s003	
4.16 600 °C	27.11.2015	xps151127s003,5	
5.4a,c	21.4.2017	20170418_ZrO2_SMSI_check	+720C 10min O2
5.4b,d	21.4.2017	20170418_ZrO2_SMSI_check	+720C 10min UHV
5.5a	22.12.2015	xps151222s003,5,7	
	23.12.2015	xps151223s003,5,6,11,13	
5.5b	14.01.2016	xps160114s011	
	15.01.2016	xps160115s001,5,8,12,15	
5.6	4.12.2018	20181204 ... transferedfromLT	
5.6clean	6.11.2018	20181031 ... RhO2_ZrO2	20181106-Rh(111)
7.5	10.3.2017	20170302 Zr0001 O2 dosing 3	10/03/2017 Dosing 18L O2 at RT
7.6	14.12.2016	20161214 ... O2 dosing 2nd try	
7.7	8.3.2017	20170302 Zr0001 O2 dosing 3	Tann=500C, Tsput=100C + ann. (Tc=480C, t=30min)
7.8	25.10.2016	aes161025s002	
	24.10.2016	aes161024s002	

Table B.2: Raw data file names, sorted by Figure number, part 2

Bibliography

- [1] Jiang H., Gomez-Abal R.I., Rinke P. and Scheffler M., *Electronic Band Structure of Zirconia and Hafnia Polymorphs from the GW Perspective*: Physical Review B, 81(8):085119 (2010), doi:[10.1103/PhysRevB.81.085119](https://doi.org/10.1103/PhysRevB.81.085119)
- [2] Ganduglia-Pirovano M.V., Hofmann A. and Sauer J., *Oxygen Vacancies in Transition Metal and Rare Earth Oxides: Current State of Understanding and Remaining Challenges*: Surface Science Reports, 62(6):219–270 (2007), doi:[10.1016/j.surfrep.2007.03.002](https://doi.org/10.1016/j.surfrep.2007.03.002)
- [3] Nielsen R.H. and Wilfing G., *Zirconium and Zirconium Compounds*: In *Ullmann's Encyclopedia of Industrial Chemistry*, Wiley-VCH Verlag GmbH & Co. KGaA, Weinheim, Germany (2000), doi:[10.1002/14356007.a28_543.pub2](https://doi.org/10.1002/14356007.a28_543.pub2)
- [4] Kisi E.H. and Howard C.J., *Crystal Structures of Zirconia Phases and Their Inter-Relation*: Key Engineering Materials, 153:1–36 (1998), doi:[10.4028/www.scientific.net/KEM.153-154.1](https://doi.org/10.4028/www.scientific.net/KEM.153-154.1)
- [5] Abriata J.P., Garcés J. and Versaci R., *The O-Zr (Oxygen-Zirconium) System*: Bulletin of Alloy Phase Diagrams, 7(2):116–124 (1986), doi:[10.1007/BF02881546](https://doi.org/10.1007/BF02881546)
- [6] Hannink R.H.J., Kelly P.M. and Muddle B.C., *Transformation Toughening in Zirconia-Containing Ceramics*: Journal of the American Ceramic Society, 83(3):461–487 (2000), doi:[10.1111/j.1151-2916.2000.tb01221.x](https://doi.org/10.1111/j.1151-2916.2000.tb01221.x)
- [7] Garvie R.C., Hannink R.H. and Pascoe R.T., *Ceramic Steel?*: Nature, 258(5537):703–704 (1975), doi:[10.1038/258703a0](https://doi.org/10.1038/258703a0)
- [8] Yamaguchi T., Nakano Y. and Tanabe K., *Infrared Study of Surface Hydroxyl Groups on Zirconium Oxide*: Bulletin of the Chemical Society of Japan, 51(9):2482–2487 (1978), doi:[10.1246/bcsj.51.2482](https://doi.org/10.1246/bcsj.51.2482)
- [9] Tanabe K., *Surface and catalytic properties of ZrO₂*: Mater. Chem. Phys., 13(3):347–364 (1985), doi:[10.1016/0254-0584\(85\)90064-1](https://doi.org/10.1016/0254-0584(85)90064-1)
- [10] Garvie R.C., *The Occurrence of Metastable Tetragonal Zirconia as a Crystal-lite Size Effect*: The Journal of Physical Chemistry, 69(4):1238–1243 (1965), doi:[10.1021/j100888a024](https://doi.org/10.1021/j100888a024)
- [11] Padture N.P., Gell M. and Jordan E.H., *Thermal Barrier Coatings for Gas-Turbine Engine Applications*: Science, 296(5566):280–284 (2002), doi:[10.1126/science.1068609](https://doi.org/10.1126/science.1068609)

- [12] Manicone P.F., Rossi Iommetti P. and Raffaelli L., *An Overview of Zirconia Ceramics: Basic Properties and Clinical Applications*: Journal of Dentistry, 35(11):819–826 (2007), doi:[10.1016/j.jdent.2007.07.008](https://doi.org/10.1016/j.jdent.2007.07.008)
- [13] Hisbergues M., Vendeville S. and Vendeville P., *Zirconia: Established facts and perspectives for a biomaterial in dental implantology*: J. Biomed. Mater. Res. B, 88B(2):519–529 (2009), doi:[10.1002/jbm.b.31147](https://doi.org/10.1002/jbm.b.31147)
- [14] Wenckus J.F., *Mass Production of Refractory Oxide Crystals: Cubic Zirconia*: Journal of Crystal Growth, 128(1):13–14 (1993), doi:[10.1016/0022-0248\(93\)90289-9](https://doi.org/10.1016/0022-0248(93)90289-9)
- [15] Choi J.H., Mao Y. and Chang J.P., *Development of Hafnium Based High-k Materials—A Review*: Materials Science and Engineering: R: Reports, 72(6):97–136 (2011), doi:[10.1016/j.mser.2010.12.001](https://doi.org/10.1016/j.mser.2010.12.001)
- [16] McIntosh S. and Gorte R.J., *Direct Hydrocarbon Solid Oxide Fuel Cells*: Chem. Rev., 104(10):4845–4866 (2004), doi:[10.1021/cr020725g](https://doi.org/10.1021/cr020725g)
- [17] Liu Y., Parisi J., Sun X. and Lei Y., *Solid-state gas sensors for high temperature applications – a review*: J. Mater. Chem. A, 2(26):9919–9943 (2014), doi:[10.1039/C3TA15008A](https://doi.org/10.1039/C3TA15008A)
- [18] Ober J.A., *Mineral Commodity Summaries 2018*: USGS Unnumbered Series, U.S. Geological Survey, Reston, VA (2018)
- [19] *Mineral Commodity Summaries 1998*: USGS Unnumbered Series, U.S. Geological Survey (1998)
- [20] Terblanche S.P., *Thermal-Expansion Coefficients of Yttria-Stabilized Cubic Zirconias*: Journal of Applied Crystallography, 22(3):283–284 (1989), doi:[10.1107/S0021889888013937](https://doi.org/10.1107/S0021889888013937)
- [21] Strickler D.W. and Carlson W.G., *Electrical Conductivity in the ZrO₂-Rich Region of Several M₂O₃–ZrO₂ Systems*: Journal of the American Ceramic Society, 48(6):286–289 (1965), doi:[10.1111/j.1151-2916.1965.tb14742.x](https://doi.org/10.1111/j.1151-2916.1965.tb14742.x)
- [22] Igawa N. and Ishii Y., *Crystal Structure of Metastable Tetragonal Zirconia up to 1473 K*: Journal of the American Ceramic Society, 84(5):1169–1171 (2001), doi:[10.1111/j.1151-2916.2001.tb00808.x](https://doi.org/10.1111/j.1151-2916.2001.tb00808.x)
- [23] Howard C.J., Hill R.J. and Reichert B.E., *Structures of ZrO₂ Polymorphs at Room Temperature by High-Resolution Neutron Powder Diffraction*: Acta Crystallographica Section B Structural Science, 44(2):116–120 (1988), doi:[10.1107/S0108768187010279](https://doi.org/10.1107/S0108768187010279)

- [24] Lackner P., Zou Z., Mayr S., Choi J.I.J., Diebold U. and Schmid M., *Surface Structures of ZrO₂ Films on Rh(111): From Two Layers to Bulk Termination*: Surface Science, 679:180–187 (2019), doi:[10.1016/j.susc.2018.09.004](https://doi.org/10.1016/j.susc.2018.09.004)
- [25] Hillert M. and Sakuma T., *Thermodynamic Modeling of the c → t Transformation in ZrO₂ Alloys*: Acta Metallurgica et Materialia, 39(6):1111–1115 (1991), doi:[10.1016/0956-7151\(91\)90198-A](https://doi.org/10.1016/0956-7151(91)90198-A)
- [26] Shukla S. and Seal S., *Mechanisms of Room Temperature Metastable Tetragonal Phase Stabilisation in Zirconia*: International Materials Reviews, 50(1) (2005), doi:[10.1179/174328005X14267](https://doi.org/10.1179/174328005X14267)
- [27] Raza M., Cornil D., Cornil J., Lucas S., Snyders R. and Konstantinidis S., *Oxygen Vacancy Stabilized Zirconia (OVSZ); a Joint Experimental and Theoretical Study*: Scripta Materialia, 124:26–29 (2016), doi:[10.1016/j.scriptamat.2016.06.025](https://doi.org/10.1016/j.scriptamat.2016.06.025)
- [28] Scott H.G., *Phase Relationships in the Zirconia-Yttria System*: Journal of Materials Science, 10(9):1527–1535 (1975), doi:[10.1007/BF01031853](https://doi.org/10.1007/BF01031853)
- [29] Christensen A. and Carter E.A., *First-principles study of the surfaces of zirconia*: Phys. Rev. B, 58(12):8050–8064 (1998), doi:[10.1103/PhysRevB.58.8050](https://doi.org/10.1103/PhysRevB.58.8050)
- [30] Leger J.M., Tomaszewski P.E., Atouf A. and Pereira A.S., *Pressure-Induced Structural Phase Transitions in Zirconia under High Pressure*: Physical Review B, 47(21):14075–14083 (1993), doi:[10.1103/PhysRevB.47.14075](https://doi.org/10.1103/PhysRevB.47.14075)
- [31] Müller J., Böske T.S., Schröder U., Mueller S., Bräuhäus D., Böttger U., Frey L. and Mikolajick T., *Ferroelectricity in Simple Binary ZrO₂ and HfO₂*: Nano Letters, 12(8):4318–4323 (2012), doi:[10.1021/nl302049k](https://doi.org/10.1021/nl302049k)
- [32] Materlik R., Künneth C. and Kersch A., *The Origin of Ferroelectricity in Hf_{1-x}Zr_xO₂: A Computational Investigation and a Surface Energy Model*: Journal of Applied Physics, 117(13):134109 (2015), doi:[10.1063/1.4916707](https://doi.org/10.1063/1.4916707)
- [33] Ohtaka O., Yamanaka T., Kume S., Hara N., Asano H. and Izumi F., *Structural Analysis of Orthorhombic ZrO₂ by High Resolution Neutron Powder Diffraction*: Proceedings of the Japan Academy, 66:193–196 (1990)
- [34] Morrow S.L., Luttrell T., Carter A. and Batzill M., *High Temperature Scanning Tunneling Microscopy of Purely Ion Conducting Yttria Stabilized Zirconia (YSZ)*: Surface Science, 603(13):L78–L81 (2009), doi:[10.1016/j.susc.2009.04.009](https://doi.org/10.1016/j.susc.2009.04.009)
- [35] Majumdar D. and Chatterjee D., *X-ray Photoelectron Spectroscopic Studies on Yttria, Zirconia, and Yttria-stabilized Zirconia*: Journal of Applied Physics, 70(2):988–992 (1991), doi:[10.1063/1.349611](https://doi.org/10.1063/1.349611)

- [36] Meinel K., Schindler K.M. and Neddermeyer H., *Growth, Structure and Annealing Behaviour of Epitaxial ZrO₂ Films on Pt(111)*: Surface Science, 532-535:420-424 (2003), doi:[10.1016/S0039-6028\(03\)00187-0](https://doi.org/10.1016/S0039-6028(03)00187-0)
- [37] Meinel K., Eichler A., Schindler K.M. and Neddermeyer H., *STM, LEED, and DFT characterization of epitaxial ZrO₂ films on Pt(111)*: Surf. Sci., 562(1-3):204-218 (2004), doi:[10.1016/j.susc.2004.06.035](https://doi.org/10.1016/j.susc.2004.06.035)
- [38] Meinel K., Eichler A., Förster S., Schindler K.M., Neddermeyer H. and Widdra W., *Surface and interface structures of epitaxial ZrO₂ films on Pt(111): Experiment and density-functional theory calculations*: Phys. Rev. B, 74(23):235444 (2006), doi:[10.1103/PhysRevB.74.235444](https://doi.org/10.1103/PhysRevB.74.235444)
- [39] Maurice V., Salmeron M. and Somorjai G., *The epitaxial growth of zirconium oxide thin films on Pt(111) single crystal surfaces*: Surf. Sci., 237(1-3):116-126 (1990), doi:[10.1016/0039-6028\(90\)90524-C](https://doi.org/10.1016/0039-6028(90)90524-C)
- [40] Gao Y., Zhang L., Pan Y., Wang G., Xu Y., Zhang W. and Zhu J., *Epitaxial Growth of Ultrathin ZrO₂(111) Films on Pt(111)*: Chinese Science Bulletin, 56(6):502-507 (2011), doi:[10.1007/s11434-010-4309-7](https://doi.org/10.1007/s11434-010-4309-7)
- [41] Antlanger M., Mayr-Schmölzer W., Pavelec J., Mittendorfer F., Redinger J., Varga P., Diebold U. and Schmid M., *Pt₃Zr(0001): A substrate for growing well-ordered ultrathin zirconia films by oxidation*: Phys. Rev. B, 86(3):035451 (2012), doi:[10.1103/PhysRevB.86.035451](https://doi.org/10.1103/PhysRevB.86.035451)
- [42] Li H., Choi J.I.J., Mayr-Schmölzer W., Weilach C., Rameshan C., Mittendorfer F., Redinger J., Schmid M. and Rupprechter G., *Growth of an ultrathin zirconia film on Pt₃Zr examined by high-resolution X-ray photoelectron spectroscopy, temperature-programmed desorption, scanning tunneling microscopy, and density functional theory*: J. Phys. Chem. C, 119(5):2462-2470 (2015), doi:[10.1021/jp5100846](https://doi.org/10.1021/jp5100846)
- [43] Choi J.I.J., Mayr-Schmölzer W., Mittendorfer F., Redinger J., Diebold U. and Schmid M., *The growth of ultra-thin zirconia films on Pd₃Zr(0001)*: J. Phys.: Condens. Matter, 26(22):225003 (2014), doi:[10.1088/0953-8984/26/22/225003](https://doi.org/10.1088/0953-8984/26/22/225003)
- [44] Choi J.I.J., Mayr-Schmölzer W., Valenti I., Luches P., Mittendorfer F., Redinger J., Diebold U. and Schmid M., *Metal adatoms and clusters on ultrathin zirconia films*: J. Phys. Chem. C, 120(18):9920-9932 (2016), doi:[10.1021/acs.jpcc.6b03061](https://doi.org/10.1021/acs.jpcc.6b03061)
- [45] Lackner P., Hulva J., Köck E.M., Mayr-Schmölzer W., Choi J.I.J., Penner S., Diebold U., Mittendorfer F., Redinger J., Klötzer B., Parkinson G.S. and Schmid M., *Water adsorption at zirconia: from the ZrO₂(111)/Pt₃Zr(0001) model system to powder samples*: Journal of Materials Chemistry A, 6(36):17587-17601 (2018), doi:[10.1039/C8TA04137G](https://doi.org/10.1039/C8TA04137G)

- [46] Chang J.P., Lin Y.S., Berger S., Kepten A., Bloom R. and Levy S., *Ultrathin Zirconium Oxide Films as Alternative Gate Dielectrics*: Journal of Vacuum Science & Technology B: Microelectronics and Nanometer Structures Processing, Measurement, and Phenomena, 19(6):2137–2143 (2001), doi:[10.1116/1.1415513](https://doi.org/10.1116/1.1415513)
- [47] Mayr L., Shi X.R., Köpfle N., A. Milligan C., Y. Zemlyanov D., Knop-Gericke A., Hävecker M., Klötzer B. and Penner S., *Chemical Vapor Deposition-Prepared Sub-Nanometer Zr Clusters on Pd Surfaces: Promotion of Methane Dry Reforming*: Physical Chemistry Chemical Physics, 18(46):31586–31599 (2016), doi:[10.1039/C6CP07197J](https://doi.org/10.1039/C6CP07197J)
- [48] Köpfle N., Mayr L., Lackner P., Schmid M., Schmidmair D., Götsch T., Penner S. and Klötzer B., *Zirconium-Palladium Interactions during Dry Reforming of Methane*: ECS Transactions, 78(1):2419–2430 (2017), doi:[10.1149/07801.2419ecst](https://doi.org/10.1149/07801.2419ecst)
- [49] Mayr L., Shi X., Köpfle N., Klötzer B., Zemlyanov D.Y. and Penner S., *Tuning of the Copper–Zirconia Phase Boundary for Selectivity Control of Methanol Conversion*: Journal of Catalysis, 339:111–122 (2016), doi:[10.1016/j.jcat.2016.03.029](https://doi.org/10.1016/j.jcat.2016.03.029)
- [50] Lackner P., Choi J.I.J., Diebold U. and Schmid M., *Construction and evaluation of an ultrahigh-vacuum-compatible sputter deposition source*: Rev. Sci. Instrum., 88(10):103904 (2017), doi:[10.1063/1.4998700](https://doi.org/10.1063/1.4998700)
- [51] Pavelec J., Hulva J., Halwidl D., Bliem R., Gamba O., Jakub Z., Brunbauer F., Schmid M., Diebold U. and Parkinson G.S., *A multi-technique study of CO₂ adsorption on Fe₃O₄ magnetite*: J. Chem. Phys., 146(1):014701 (2017), doi:[10.1063/1.4973241](https://doi.org/10.1063/1.4973241)
- [52] Michely T., Kalff M. and Comsa G., *The effect of deposition method on growth morphology - Comparison of molecular beam epitaxy, ion beam assisted deposition and sputter deposition*: Mat. Res. Soc. Symp. Proc., 528:179 (1998), doi:[10.1557/PROC-528-179](https://doi.org/10.1557/PROC-528-179)
- [53] Mayr L., Köpfle N., Auer A., Klötzer B. and Penner S., *An (ultra) high-vacuum compatible sputter source for oxide thin film growth*: Rev. Sci. Instrum., 84(9):094103 (2013), doi:[10.1063/1.4821148](https://doi.org/10.1063/1.4821148)
- [54] Götsch T., Wallisch W., Stöger-Pollach M., Klötzer B. and Penner S., *From zirconia to yttria: Sampling the YSZ phase diagram using sputter-deposited thin films*: AIP Advances, 6(2):025119 (2016), doi:[10.1063/1.4942818](https://doi.org/10.1063/1.4942818)
- [55] Schwebel C., Meyer F., Gautherin G. and Pellet C., *Growth of silicon homoepitaxial thin films by ultrahigh vacuum ion beam sputter deposition*: Journal of Vacuum Science & Technology B: Microelectronics Processing and Phenomena, 4(5):1153–1158 (1986), doi:[10.1116/1.583475](https://doi.org/10.1116/1.583475)

- [56] Lee N.E., Xue G. and Greene J., *Epitaxial Si(001) grown at 80–750 °C by ion-beam sputter deposition: Crystal growth, doping, and electronic properties*: Journal of Applied Physics, 80(2):769–780 (1996), doi:[10.1063/1.362885](https://doi.org/10.1063/1.362885)
- [57] Klötzer B. and Penner S.: private communication
- [58] Bischler U. and Bertel E., *Simple source of atomic hydrogen for ultrahigh vacuum applications*: J. Vac. Sci. Technol. A, 11(2):458–460 (1993), doi:[10.1116/1.578754](https://doi.org/10.1116/1.578754)
- [59] Eibl C., Lackner G. and Winkler A., *Quantitative characterization of a highly effective atomic hydrogen doser*: J. Vac. Sci. Technol. A, 16(5):2979–2989 (1998), doi:[10.1116/1.581449](https://doi.org/10.1116/1.581449)
- [60] Matsunami N., Yamamura Y., Itikawa Y., Itoh N., Kazumata Y., Miyagawa S., Morita K., Shimizu R. and Tawara H., *Energy Dependence of the Yields of Ion-Induced Sputtering of Monatomic Solids*: Technical Report IPPJ-AM-32, Institute of Plasma Physics, Nagoya University, Japan (1983)
- [61] Jordan R.G., Begley A.M., Barrett S.D., Durham P.J. and Temmerman W.M., *Experimental and theoretical spectra from the 4p core levels of yttrium*: Sol. State Commun., 76(5):579–581 (1990), doi:[10.1016/0038-1098\(90\)90092-P](https://doi.org/10.1016/0038-1098(90)90092-P)
- [62] Methfessel M., Hennig D. and Scheffler M., *Ab-initio calculations of the initial- and final-state effects on the surface core-level shift of transition metals*: Surf. Sci., 287:785–788 (1993), doi:[10.1016/0039-6028\(93\)91072-W](https://doi.org/10.1016/0039-6028(93)91072-W)
- [63] Harper J.M.E., Cuomo J.J., Gambino R.J. and Kaufman H.R., *Modification of thin film properties by ion bombardment during deposition*: Nucl. Instrum. Meth. B, 7–8:886–892 (1985), doi:[10.1016/0168-583X\(85\)90489-6](https://doi.org/10.1016/0168-583X(85)90489-6)
- [64] Schmid M., Lenauer C., Buchsbaum A., Wimmer F., Rauchbauer G., Scheiber P., Betz G. and Varga P., *High island densities in pulsed laser deposition: Causes and implications*: Phys. Rev. Lett., 103(7):076101 (2009), doi:[10.1103/PhysRevLett.103.076101](https://doi.org/10.1103/PhysRevLett.103.076101)
- [65] Lin Y. and Joy D.C., *A new examination of secondary electron yield data*: Surf. Interface Anal., 37(11):895–900 (2005), doi:[10.1002/sia.2107](https://doi.org/10.1002/sia.2107)
- [66] Benes E., Gröschl M., Burger W. and Schmid M., *Sensors based on piezoelectric resonators*: Sensor. Actuator. A, 48(1):1–21 (1995), doi:[10.1016/0924-4247\(95\)00846-2](https://doi.org/10.1016/0924-4247(95)00846-2)
- [67] Hayderer G., Schmid M., Varga P., Winter H. and Aumayr F., *A highly sensitive quartz-crystal microbalance for sputtering investigations in slow ion-surface collisions*: Rev. Sci. Instrum., 70(9):3696–3700 (1999), doi:[10.1063/1.1149979](https://doi.org/10.1063/1.1149979)

- [68] Binnig G., Rohrer H., Gerber C. and Weibel E., *Surface Studies by Scanning Tunneling Microscopy*: Physical Review Letters, 49(1):57 (1982), doi:[10.1103/PhysRevLett.49.57](https://doi.org/10.1103/PhysRevLett.49.57)
- [69] Schmid M.: IAP, TU Wien
- [70] Moulder J.F., Stickle W.F., Sobol P.E. and Bomben K.D., *Handbook of X-Ray Photoelectron Spectroscopy*: Perkin-Elmer Corporation, Physical Electronics Division (1992), ISBN 0-9627026-2-5
- [71] Doniach S. and Sunjic M., *Many-Electron Singularity in X-Ray Photoemission and X-Ray Line Spectra from Metals*: Journal of Physics C: Solid State Physics, 3:285–291 (1970), doi:[10.1088/0022-3719/3/2/010](https://doi.org/10.1088/0022-3719/3/2/010)
- [72] Scofield J.H., *Theoretical Photoionization Cross Sections from 1 to 1500 keV*: Technical Report UCRL-51326, California Univ., Lawrence Livermore Lab., United States (1973), doi:[10.2172/4545040](https://doi.org/10.2172/4545040)
- [73] Smekal W., Werner W.S.M. and Powell C.J., *Simulation of electron spectra for surface analysis (SESSA): a novel software tool for quantitative Auger-electron spectroscopy and X-ray photoelectron spectroscopy*: Surf. Interface Anal., 37(11):1059–1067 (2005), doi:[10.1002/sia.2097](https://doi.org/10.1002/sia.2097)
- [74] Bott M., Hohage M., Michely T. and Comsa G., *Pt(111) Reconstruction Induced by Enhanced Pt Gas-Phase Chemical Potential*: Physical Review Letters, 70(10):1489–1492 (1993), doi:[10.1103/PhysRevLett.70.1489](https://doi.org/10.1103/PhysRevLett.70.1489)
- [75] Hecht E.S., Gupta G.K., Zhu H., Dean A.M., Kee R.J., Maier L. and Deutschmann O., *Methane reforming kinetics within a Ni-YSZ SOFC anode support*: Appl. Catal. A, 295(1):40–51 (2005), doi:[10.1016/j.apcata.2005.08.003](https://doi.org/10.1016/j.apcata.2005.08.003)
- [76] Henderson M.A., *The interaction of water with solid surfaces: fundamental aspects revisited*: Surf. Sci. Rep., 46(1-8):1–308 (2002), doi:[10.1016/S0167-5729\(01\)00020-6](https://doi.org/10.1016/S0167-5729(01)00020-6)
- [77] Thiel P.A. and Madey T.E., *The interaction of water with solid surfaces: Fundamental aspects*: Surf. Sci. Rep., 7(6-8):211–385 (1987), doi:[10.1016/0167-5729\(87\)90001-X](https://doi.org/10.1016/0167-5729(87)90001-X)
- [78] Mu R., Zhao Z.j., Dohnálek Z. and Gong J., *Structural motifs of water on metal oxide surfaces*: Chem. Soc. Rev., 46(7):1785–1806 (2017), doi:[10.1039/C6CS00864J](https://doi.org/10.1039/C6CS00864J)
- [79] Campbell C.T. and Sellers J.R.V., *Enthalpies and entropies of adsorption on well-defined oxide surfaces: Experimental measurements*: Chem. Rev., 113(6):4106–4135 (2013), doi:[10.1021/cr300329s](https://doi.org/10.1021/cr300329s)

- [80] Herman G.S., Dohnálek Z., Ruzycki N. and Diebold U., *Experimental investigation of the interaction of water and methanol with anatase-TiO₂(101)*: J. Phys. Chem. B, 107(12):2788–2795 (2003), doi:[10.1021/jp0275544](https://doi.org/10.1021/jp0275544)
- [81] Stirniman M.J., Huang C., Smith R.S., Joyce S.A. and Kay B.D., *The adsorption and desorption of water on single crystal MgO(100): The role of surface defects*: J. Chem. Phys., 105(3):1295–1298 (1996), doi:[10.1063/1.471993](https://doi.org/10.1063/1.471993)
- [82] Zhang Z., Bondarchuk O., Kay B.D., White J.M. and Dohnálek Z., *Imaging water dissociation on TiO₂(110): Evidence for inequivalent geminate OH groups*: J. Phys. Chem. B, 110(43):21840–21845 (2006), doi:[10.1021/jp063619h](https://doi.org/10.1021/jp063619h)
- [83] Schaub R., Thostrup P., Lopez N., Lægsgaard E., Stensgaard I., Nørskov J.K. and Besenbacher F., *Oxygen vacancies as active sites for water dissociation on rutile TiO₂(110)*: Phys. Rev. Lett., 87(26):266104 (2001), doi:[10.1103/PhysRevLett.87.266104](https://doi.org/10.1103/PhysRevLett.87.266104)
- [84] Henderson M.A., *Structural sensitivity in the dissociation of water on TiO₂ single-crystal surfaces*: Langmuir, 12(21):5093–5098 (1996), doi:[10.1021/la960360t](https://doi.org/10.1021/la960360t)
- [85] Henderson M.A. and Chambers S.A., *HREELS, TPD and XPS study of the interaction of water with the α -Cr₂O₃(001) surface*: Surf. Sci., 449(1–3):135–150 (2000), doi:[10.1016/S0039-6028\(99\)01246-7](https://doi.org/10.1016/S0039-6028(99)01246-7)
- [86] Henderson M.A., Joyce S.A. and Rustad J.R., *Interaction of water with the (1 × 1) and (2 × 1) surfaces of α -Fe₂O₃(012)*: Surf. Sci., 417(1):66–81 (1998), doi:[10.1016/S0039-6028\(98\)00662-1](https://doi.org/10.1016/S0039-6028(98)00662-1)
- [87] Hu X.L., Carrasco J., Klimeš J. and Michaelides A., *Trends in water monomer adsorption and dissociation on flat insulating surfaces*: Phys. Chem. Chem. Phys., 13(27):12447 (2011), doi:[10.1039/c1cp20846b](https://doi.org/10.1039/c1cp20846b)
- [88] Halwidl D., Mayr-Schmölzer W., Fobes D., Peng J., Mao Z., Schmid M., Mitendorf F., Redinger J. and Diebold U., *Ordered hydroxyls on Ca₃Ru₂O₇(001)*: Nat. Commun., 8:23 (2017)
- [89] Lobo A. and Conrad H., *Interaction of H₂O with the RuO₂(110) surface studied by HREELS and TDS*: Surf. Sci., 523(3):279–286 (2003), doi:[10.1016/S0039-6028\(02\)02459-7](https://doi.org/10.1016/S0039-6028(02)02459-7)
- [90] Kan H.H., Colmyer R.J., Asthagiri A. and Weaver J.F., *Adsorption of water on a PdO (101) thin film: Evidence of an adsorbed HO–H₂O complex*: J. Phys. Chem. C, 113(4):1495–1506 (2009), doi:[10.1021/jp808008k](https://doi.org/10.1021/jp808008k)
- [91] Meier M., Hulva J., Jakub Z., Pavelec J., Setvín M., Bliem R., Schmid M., Diebold U., Franchini C. and Parkinson G.S., *Water agglomerates on Fe₃O₄ (001)*: Proc. Natl. Acad. Sci. U.S.A., page 201801661 (2018), doi:[10.1073/pnas.1801661115](https://doi.org/10.1073/pnas.1801661115)

- [92] Ushakov S.V. and Navrotsky A., *Direct measurements of water adsorption enthalpy on hafnia and zirconia*: Appl. Phys. Lett., 87(16):164103 (2005), doi:[10.1063/1.2108113](https://doi.org/10.1063/1.2108113)
- [93] Radha A.V., Bomati-Miguel O., Ushakov S.V., Navrotsky A. and Tartaj P., *Surface enthalpy, enthalpy of water adsorption, and phase stability in nano-crystalline monoclinic zirconia*: J. Am. Ceram. Soc., 92(1):133–140 (2009), doi:[10.1111/j.1551-2916.2008.02796.x](https://doi.org/10.1111/j.1551-2916.2008.02796.x)
- [94] Orlando T.M., Aleksandrov A.B. and Herring J., *Electron-stimulated desorption of H^+ , H_2^+ , OH^+ , and $H^+(H_2O)_n$ from water-covered zirconia surfaces*: J. Phys. Chem. B, 107(35):9370–9376 (2003), doi:[10.1021/jp030117k](https://doi.org/10.1021/jp030117k)
- [95] Köck E.M., Kogler M., Klötzer B., Noisternig M.F. and Penner S., *Structural and Electrochemical Properties of Physisorbed and Chemisorbed Water Layers on the Ceramic Oxides Y_2O_3 , YSZ, and ZrO_2* : ACS Appl. Mater. Interfaces, 8(25):16428–16443 (2016), doi:[10.1021/acsami.6b03566](https://doi.org/10.1021/acsami.6b03566)
- [96] Kogler M., Köck E.M., Bielz T., Pfaller K., Klötzer B., Schmidmair D., Perfler L. and Penner S., *Hydrogen surface reactions and adsorption studied on Y_2O_3 , YSZ, and ZrO_2* : J. Phys. Chem. C, 118(16):8435–8444 (2014), doi:[10.1021/jp5008472](https://doi.org/10.1021/jp5008472)
- [97] Köck E.M., Kogler M., Bielz T., Klötzer B. and Penner S., *In situ FT-IR spectroscopic study of CO_2 and CO adsorption on Y_2O_3 , ZrO_2 , and yttria-stabilized ZrO_2* : J. Phys. Chem. C, 117(34):17666–17673 (2013), doi:[10.1021/jp405625x](https://doi.org/10.1021/jp405625x)
- [98] Maurice V., Takeuchi K., Salmeron M. and Somorjai G.A., *The bonding of diethyl ether, ethanol and their fluorinated analogs to zirconium oxide thin films*: Surf. Sci., 250(1):99–111 (1991), doi:[10.1016/0039-6028\(91\)90713-3](https://doi.org/10.1016/0039-6028(91)90713-3)
- [99] Takeuchi K., Perry S.S., Salmeron M. and Somorjai G.A., *The bonding properties of hydrogenated and fluorinated molecules to zirconium oxide thin films: influence of surface defects and water coadsorption*: Surf. Sci., 323(1):30–38 (1995), doi:[10.1016/0039-6028\(94\)00621-0](https://doi.org/10.1016/0039-6028(94)00621-0)
- [100] de Jong A.M. and Niemantsverdriet J.W., *Thermal desorption analysis: Comparative test of ten commonly applied procedures*: Surf. Sci., 233(3):355–365 (1990), doi:[10.1016/0039-6028\(90\)90649-S](https://doi.org/10.1016/0039-6028(90)90649-S)
- [101] Habenschaden E. and Küppers J., *Evaluation of flash desorption spectra*: Surf. Sci., 138(1):L147–L150 (1984), doi:[10.1016/0039-6028\(84\)90488-6](https://doi.org/10.1016/0039-6028(84)90488-6)
- [102] Chaix L., van den Bergh H. and Rossi M.J., *Real-time kinetic measurements of the condensation and evaporation of D_2O molecules on ice at $140 K < T < 220 K$* : J. Phys. Chem. A, 102(50):10300–10309 (1998), doi:[10.1021/jp983050n](https://doi.org/10.1021/jp983050n)

- [103] Dohnálek Z., Kimmel G.A., Joyce S.A., Ayotte P., Smith R.S. and Kay B.D., *Physisorption of CO on the MgO(100) surface*: J. Phys. Chem. B, 105(18):3747–3751 (2001), doi:[10.1021/jp003174b](https://doi.org/10.1021/jp003174b)
- [104] Setvín M., Buchholz M., Hou W., Zhang C., Stöger B., Hulva J., Simschitz T., Shi X., Pavelec J., Parkinson G.S., Xu M., Wang Y., Schmid M., Wöll C., Selloni A. and Diebold U., *A multitechnique study of CO adsorption on the TiO₂ anatase (101) Surface*: J. Phys. Chem. C, 119(36):21044–21052 (2015), doi:[10.1021/acs.jpcc.5b07999](https://doi.org/10.1021/acs.jpcc.5b07999)
- [105] Tait S.L., Dohnálek Z., Campbell C.T. and Kay B.D., *n-alkanes on MgO(100). I. Coverage-dependent desorption kinetics of n-butane*: J. Chem. Phys., 122(16):164707 (2005), doi:[10.1063/1.1883629](https://doi.org/10.1063/1.1883629)
- [106] Halwidl D., Stöger B., Mayr-Schmölzer W., Pavelec J., Fobes D., Peng J., Mao Z., Parkinson G.S., Schmid M., Mittendorfer F., Redinger J. and Diebold U., *Adsorption of water at the SrO surface of ruthenates*: Nat. Mater., 15(4):450–455 (2016), doi:[10.1038/nmat4512](https://doi.org/10.1038/nmat4512)
- [107] Coustet V. and Jupille J., *Hydroxyl groups on oxide surfaces*: Nouv. Cim. D, 19(11):1657–1664 (1997), doi:[10.1007/BF03185360](https://doi.org/10.1007/BF03185360)
- [108] Wagner M., Lackner P., Seiler S., Brunsch A., Bliem R., Gerhold S., Wang Z., Osiecki J., Schulte K., Boatner L.A., Schmid M., Meyer B. and Diebold U., *Resolving the structure of a well-ordered hydroxyl overlayer on In₂O₃(111): Nanomanipulation and theory*: ACS Nano, 11(11):11531–11541 (2017), doi:[10.1021/acsnano.7b06387](https://doi.org/10.1021/acsnano.7b06387)
- [109] Kerber S.J., Bruckner J.J., Wozniak K., Seal S., Hardcastle S. and Barr T.L., *The nature of hydrogen in x-ray photoelectron spectroscopy: General patterns from hydroxides to hydrogen bonding*: J. Vacuum Sci. Techn. A, 14(3):1314–1320 (1996), doi:[10.1116/1.579947](https://doi.org/10.1116/1.579947)
- [110] Choi J.I.J., *Studies of Zirconia Surfaces on the Atomic Scale*: Ph.D. thesis, Institute of Applied Physics, TU Wien (2016)
- [111] Lackner P., Choi J.I.J., Diebold U. and Schmid M.: to be published
- [112] Kimmel G.A., Persson M., Dohnálek Z. and Kay B.D., *Temperature independent physisorption kinetics and adsorbate layer compression for Ar adsorbed on Pt(111)*: J. Chem. Phys., 119(13):6776–6783 (2003), doi:[10.1063/1.1604111](https://doi.org/10.1063/1.1604111)
- [113] Hulva J., Jakub Z., Novotny Z., Johansson N., Knudsen J., Schnadt J., Schmid M., Diebold U. and Parkinson G.S., *Adsorption of CO on the Fe₃O₄(001) surface*: J. Phys. Chem. B, 122(2):721–729 (2018), doi:[10.1021/acs.jpcc.7b06349](https://doi.org/10.1021/acs.jpcc.7b06349)

- [114] Henderson M.A., *Evidence for bicarbonate formation on vacuum annealed TiO₂ (110) resulting from a precursor-mediated interaction between CO₂ and H₂O*: Surface Science, 400(1):203–219 (1998), doi:[10.1016/S0039-6028\(97\)00863-7](https://doi.org/10.1016/S0039-6028(97)00863-7)
- [115] Li H., Rameshan C., Bukhtiyarov A.V., Prosvirin I.P., Bukhtiyarov V.I. and Rupprechter G., *CO₂ Activation on Ultrathin ZrO₂ Film by H₂O Co-Adsorption: In Situ NAP-XPS and IRAS Studies*: Surface Science (2018), doi:[10.1016/j.susc.2018.08.028](https://doi.org/10.1016/j.susc.2018.08.028)
- [116] Puigdollers A.R. and Pacchioni G., *Reducibility of ZrO₂/Pt₃Zr and ZrO₂/Pt 2D films compared to bulk zirconia: a DFT+U study of oxygen removal and H₂ adsorption*: Nanoscale, 9(20):6866–6876 (2017), doi:[10.1039/C7NR01904A](https://doi.org/10.1039/C7NR01904A)
- [117] Tennyson J., Bernath P.F., Brown L.R., Campargue A., Császár A.G., Daumont L., Gamache R.R., Hodges J.T., Naumenko O.V., Polyansky O.L. and et al., *IUPAC critical evaluation of the rotational–vibrational spectra of water vapor, Part III: Energy levels and transition wavenumbers for H₂¹⁶O*: J. Quant. Spectrosc. Radiat. Transfer, 117:29–58 (2013), doi:[10.1016/j.jqsrt.2012.10.002](https://doi.org/10.1016/j.jqsrt.2012.10.002)
- [118] Korhonen S.T., Calatayud M. and Krause A.O.I., *Stability of Hydroxylated (̄111) and (̄101) surfaces of monoclinic zirconia: A combined study by DFT and infrared spectroscopy*: J. Phys. Chem. C, 112(16):6469–6476 (2008), doi:[10.1021/jp8008546](https://doi.org/10.1021/jp8008546)
- [119] Piskorz W., Gryboś J., Zasada F., Cristol S., Paul J.F., Adamski A. and Sojka Z., *Periodic DFT and atomistic thermodynamic modeling of the surface hydration equilibria and morphology of monoclinic ZrO₂ nanocrystals*: J. Phys. Chem. C, 115(49):24274–24286 (2011), doi:[10.1021/jp2086335](https://doi.org/10.1021/jp2086335)
- [120] Klimeš J., Bowler D. and Michaelides A., *Van der Waals density functionals applied to solids*: Phys. Rev. B, 83(19):1–13 (2011), doi:[10.1103/PhysRevB.83.195131](https://doi.org/10.1103/PhysRevB.83.195131)
- [121] Klimeš J., Bowler D.R. and Michaelides A., *Chemical accuracy for the van der Waals density functional*: J. Phys. Condens. Matter, 22(2):022201 (2010), doi:[10.1088/0953-8984/22/2/022201](https://doi.org/10.1088/0953-8984/22/2/022201)
- [122] Whalley E., *The difference in the intermolecular forces of H₂O and D₂O*: Trans. Faraday Soc., 53:1578–1585 (1957), doi:[10.1039/TF9575301578](https://doi.org/10.1039/TF9575301578)
- [123] Setvín M., Wagner M., Schmid M., Parkinson G.S. and Diebold U., *Surface point defects on bulk oxides: atomically-resolved scanning probe microscopy*: Chem. Soc. Rev., 46(7):1772–1784 (2017), doi:[10.1039/C7CS00076F](https://doi.org/10.1039/C7CS00076F)
- [124] Dewhurst J.K. and Lowther J.E., *Relative stability, structure, and elastic properties of several phases of pure zirconia*: Phys. Rev. B, 57(2):741–747 (1998), doi:[10.1103/PhysRevB.57.741](https://doi.org/10.1103/PhysRevB.57.741)

- [125] Tzvetkov G., Zubavichus Y., Koller G., Schmidt T., Heske C., Umbach E., Grunze M., Ramsey M. and Netzer F., *Growth of H₂O layers on an ultra-thin Al₂O₃ film: from monomeric species to ice*: Surf. Sci., 543(1–3):131–140 (2003), doi:[10.1016/S0039-6028\(03\)01029-X](https://doi.org/10.1016/S0039-6028(03)01029-X)
- [126] Yi C.W. and Szanyi J., *D₂O adsorption on an ultrathin alumina film on NiAl(110)*: J. Phys. Chem. C, 111(47):17597–17602 (2007), doi:[10.1021/jp074459s](https://doi.org/10.1021/jp074459s)
- [127] Daschbach J.L., Dohnálek Z., Liu S.R., Smith R.S. and Kay B.D., *Water adsorption, desorption, and clustering on FeO(111)*: J. Phys. Chem. B, 109(20):10362–10370 (2005), doi:[10.1021/jp058013s](https://doi.org/10.1021/jp058013s)
- [128] Kresse G., Schmid M., Napetschnig E., Shishkin M., Köhler L. and Varga P., *Structure of the ultrathin aluminum oxide film on NiAl(110)*: Science, 308(5727):1440–1442 (2005), doi:[10.1126/science.1107783](https://doi.org/10.1126/science.1107783)
- [129] Mullins D.R., *The surface chemistry of cerium oxide*: Surf. Sci. Rep., 70(1):42–85 (2015), doi:[10.1016/j.surfrep.2014.12.001](https://doi.org/10.1016/j.surfrep.2014.12.001)
- [130] Pacchioni G., Giordano L. and Baistrocchi M., *Charging of metal atoms on ultrathin MgO/Mo(100) films*: Phys. Rev. Lett., 94(22):226104 (2005), doi:[10.1103/PhysRevLett.94.226104](https://doi.org/10.1103/PhysRevLett.94.226104)
- [131] Sterrer M., Risse T., Heyde M., Rust H.P. and Freund H.J., *Crossover from three-dimensional to two-dimensional geometries of Au nanostructures on thin MgO(001) films: A confirmation of theoretical predictions*: Phys. Rev. Lett., 98(20):206103–4 (2007), doi:[10.1103/PhysRevLett.98.206103](https://doi.org/10.1103/PhysRevLett.98.206103)
- [132] Gamba O., Hulva J., Pavelec J., Bliem R., Schmid M., Diebold U. and Parkinson G.S., *The Role of Surface Defects in the Adsorption of Methanol on Fe₃O₄(001)*: Topics in Catalysis, 60(6):420–430 (2017), doi:[10.1007/s11244-016-0713-9](https://doi.org/10.1007/s11244-016-0713-9)
- [133] Peng X.D. and Barteau M.A., *Acid-Base Properties of Model Magnesium Oxide Surfaces*: Langmuir, 7(7):1426–1431 (1991), doi:[10.1021/la00055a023](https://doi.org/10.1021/la00055a023)
- [134] Blatnik M., Drechsel C., Tsud N., Surnev S. and Netzer F.P., *Decomposition of Methanol on Mixed CuO–CuWO₄ Surfaces*: The Journal of Physical Chemistry B, 122(2):679–687 (2018), doi:[10.1021/acs.jpcc.7b06233](https://doi.org/10.1021/acs.jpcc.7b06233)
- [135] Matolín V., Libra J., Škoda M., Tsud N., Prince K.C. and Skála T., *Methanol Adsorption on a CeO₂(111)/Cu(111) Thin Film Model Catalyst*: Surface Science, 603(8):1087–1092 (2009), doi:[10.1016/j.susc.2009.02.010](https://doi.org/10.1016/j.susc.2009.02.010)
- [136] Schlichting H. and Menzel D., *Techniques for Attainment, Control, and Calibration of Cryogenic Temperatures at Small Single-Crystal Samples under Ultrahigh Vacuum*: Review of Scientific Instruments, 64(7):2013 (1993), doi:[10.1063/1.1143992](https://doi.org/10.1063/1.1143992)

- [137] Lackner P., Zou Z., Mayr S., Diebold U. and Schmid M.: to be published
- [138] Ganduglia-Pirovano M.V. and Scheffler M., *Structural and Electronic Properties of Chemisorbed Oxygen on Rh(111)*: Physical Review B, 59(23):15533 (1999), doi:[10.1103/PhysRevB.59.15533](https://doi.org/10.1103/PhysRevB.59.15533)
- [139] Gao Y., Guo C., Li C. and Du Z., *Thermodynamic Modeling of the Pt–Zr System*: International Journal of Materials Research (formerly Zeitschrift fuer Metallkunde), 101(7):819–826 (2010), doi:[10.3139/146.110351](https://doi.org/10.3139/146.110351)
- [140] Niessen A.K. and Miedema A.R., *The Enthalpy Effect on Forming Diluted Solid Solutions of Two 4d and 5d Transition Metals*: Berichte der Bunsengesellschaft für physikalische Chemie, 87(9):717–725 (1983), doi:[10.1002/bbpc.19830870903](https://doi.org/10.1002/bbpc.19830870903)
- [141] Müller J., Böske T.S., Schröder U., Reinicke M., Oberbeck L., Zhou D., Weinreich W., Kücher P., Lemberger M. and Frey L., *Improved Manufacturability of ZrO₂ MIM Capacitors by Process Stabilizing HfO₂ Addition*: Microelectronic Engineering, 86(7):1818–1821 (2009), doi:[10.1016/j.mee.2009.03.076](https://doi.org/10.1016/j.mee.2009.03.076)
- [142] Ebert Ph., *Nano-Scale Properties of Defects in Compound Semiconductor Surfaces*: Surface Science Reports, 33(4–8):121–303 (1999), doi:[10.1016/S0167-5729\(98\)00011-9](https://doi.org/10.1016/S0167-5729(98)00011-9)
- [143] Guo X., Sigle W., Fleig J. and Maier J., *Role of Space Charge in the Grain Boundary Blocking Effect in Doped Zirconia*: Solid State Ionics, 154–155:555–561 (2002), doi:[10.1016/S0167-2738\(02\)00491-5](https://doi.org/10.1016/S0167-2738(02)00491-5)
- [144] Yamamoto O., *Solid Oxide Fuel Cells: Fundamental Aspects and Prospects*: Electrochimica Acta, 45(15-16):2423–2435 (2000), doi:[10.1016/S0013-4686\(00\)00330-3](https://doi.org/10.1016/S0013-4686(00)00330-3)
- [145] Köhler L., Kresse G., Schmid M., Lundgren E., Gustafson J., Mikkelsen A., Borg M., Yuhara J., Andersen J.N., Marsman M. and Varga P., *High-Coverage Oxygen Structures on Rh(111): Adsorbate Repulsion and Site Preference Is Not Enough*: Physical Review Letters, 93(26):266103 (2004), doi:[10.1103/PhysRevLett.93.266103](https://doi.org/10.1103/PhysRevLett.93.266103)
- [146] Králik B., Chang E.K. and Louie S.G., *Structural Properties and Quasiparticle Band Structure of Zirconia*: Physical Review B, 57(12):7027–7036 (1998), doi:[10.1103/PhysRevB.57.7027](https://doi.org/10.1103/PhysRevB.57.7027)
- [147] French R.H., Glass S.J., Ohuchi F.S., Xu Y.N. and Ching W.Y., *Experimental and Theoretical Determination of the Electronic Structure and Optical Properties of Three Phases of ZrO₂*: Physical Review B, 49(8):5133–5142 (1994), doi:[10.1103/PhysRevB.49.5133](https://doi.org/10.1103/PhysRevB.49.5133)

- [148] Matsushima T., *Dissociation of Oxygen Admolecules on Rh(111), Pt(111) and Pd(111) Surfaces at Low Temperatures*: Surface Science, 157(2):297–318 (1985), doi:[10.1016/0039-6028\(85\)90674-0](https://doi.org/10.1016/0039-6028(85)90674-0)
- [149] Harrop P.J. and Wanklyn J.N., *The Dielectric Constant of Zirconia*: British Journal of Applied Physics, 18(6):739 (1967), doi:[10.1088/0508-3443/18/6/305](https://doi.org/10.1088/0508-3443/18/6/305)
- [150] Ruiz Puigdollers A., Illas F. and Pacchioni G., *ZrO₂ Nanoparticles: A Density Functional Theory Study of Structure, Properties and Reactivity*: Rendiconti Lincei, 28(1):19–27 (2017), doi:[10.1007/s12210-016-0591-x](https://doi.org/10.1007/s12210-016-0591-x)
- [151] Gionco C., Paganini M.C., Giamello E., Burgess R., Di Valentin C. and Pacchioni G., *Paramagnetic Defects in Polycrystalline Zirconia: An EPR and DFT Study*: Chemistry of Materials, 25(11):2243–2253 (2013), doi:[10.1021/cm400728j](https://doi.org/10.1021/cm400728j)
- [152] Puigdollers A.R. and Pacchioni G., *CO Oxidation on Au Nanoparticles Supported on ZrO₂: Role of Metal/Oxide Interface and Oxide Reducibility*: ChemCatChem, 9(6):1119–1127 (2017), doi:[10.1002/cctc.201601486](https://doi.org/10.1002/cctc.201601486)
- [153] Schlexer P., Ruiz Puigdollers A. and Pacchioni G., *Role of Metal/Oxide Interfaces in Enhancing the Local Oxide Reducibility*: Topics in Catalysis (2018), doi:[10.1007/s11244-018-1056-5](https://doi.org/10.1007/s11244-018-1056-5)
- [154] Ruiz Puigdollers A., Schlexer P., Tosoni S. and Pacchioni G., *Increasing Oxide Reducibility: The Role of Metal/Oxide Interfaces in the Formation of Oxygen Vacancies*: ACS Catalysis, 7(10):6493–6513 (2017), doi:[10.1021/acscatal.7b01913](https://doi.org/10.1021/acscatal.7b01913)
- [155] Tauster S.J., Fung S.C., Baker R.T.K. and Horsley J.A., *Strong Interactions in Supported-Metal Catalysts*: Science, 211(4487):1121–1125 (1981), doi:[10.1126/science.211.4487.1121](https://doi.org/10.1126/science.211.4487.1121)
- [156] Tauster S.J. and Fung S.C., *Strong Metal-Support Interactions: Occurrence among the Binary Oxides of Groups IIA–VB*: Journal of Catalysis, 55(1):29–35 (1978), doi:[10.1016/0021-9517\(78\)90182-3](https://doi.org/10.1016/0021-9517(78)90182-3)
- [157] Tauster S.J., Fung S.C. and Garten R.L., *Strong Metal-Support Interactions. Group 8 Noble Metals Supported on Titanium Dioxide*: Journal of the American Chemical Society, 100(1):170–175 (1978), doi:[10.1021/ja00469a029](https://doi.org/10.1021/ja00469a029)
- [158] Diebold U., *The Surface Science of Titanium Dioxide*: Surface Science Reports, 48(5-8):53–229 (2003), doi:[10.1016/S0167-5729\(02\)00100-0](https://doi.org/10.1016/S0167-5729(02)00100-0)
- [159] Datye A.K., Kalakkad D.S., Yao M.H. and Smith D.J., *Comparison of Metal-Support Interactions in Pt/TiO₂ and Pt/CeO₂*: Journal of Catalysis, 155(1):148–153 (1995), doi:[10.1006/jcat.1995.1196](https://doi.org/10.1006/jcat.1995.1196)

- [160] Dulub O., Hebenstreit W. and Diebold U., *Imaging Cluster Surfaces with Atomic Resolution: The Strong Metal-Support Interaction State of Pt Supported on TiO₂(110)*: Physical Review Letters, 84(16):3646–3649 (2000), doi:[10.1103/PhysRevLett.84.3646](https://doi.org/10.1103/PhysRevLett.84.3646)
- [161] Meriaudeau P., Dutel J.F., Dufaux M. and Naccache C., *Further Investigation on Metal-Support Interaction: TiO₂, CeO₂, SiO₂ Supported Platinum Catalysts*: In B. Imelik, C. Naccache, G. Coudurier, H. Praliaud, P. Meriaudeau, P. Gallezot, G.A. Martin and J.C. Vedrine, editors, *Studies in Surface Science and Catalysis*, volume 11 of *Metal-Support and Metal-Additive Effects in Catalysis*, pages 95–104, Elsevier (1982), doi:[10.1016/S0167-2991\(09\)61381-1](https://doi.org/10.1016/S0167-2991(09)61381-1)
- [162] Bennett R.A., Pang C.L., Perkins N., Smith R.D., Morrall P., Kvon R.I. and Bowker M., *Surface Structures in the SMSI State; Pd on (1 × 2) Reconstructed TiO₂(110)*: The Journal of Physical Chemistry B, 106(18):4688–4696 (2002), doi:[10.1021/jp0138328](https://doi.org/10.1021/jp0138328)
- [163] Pan J.M. and Madey T.E., *The Encapsulation of Fe on TiO₂(110)*: Catalysis Letters, 20(3-4):269–274 (1993), doi:[10.1007/BF00769299](https://doi.org/10.1007/BF00769299)
- [164] Qin Z.H., Lewandowski M., Sun Y.N., Shaikhutdinov S. and Freund H.J., *Encapsulation of Pt Nanoparticles as a Result of Strong Metal-Support Interaction with Fe₃O₄ (111)*: The Journal of Physical Chemistry C, 112(27):10209–10213 (2008), doi:[10.1021/jp801756q](https://doi.org/10.1021/jp801756q)
- [165] Bernal S., Calvino J.J., Cauqui M.A., Gatica J.M., Larese C., Pérez Omil J.A. and Pintado J.M., *Some Recent Results on Metal/Support Interaction Effects in NM/CeO₂ (NM: Noble Metal) Catalysts*: Catalysis Today, 50(2):175–206 (1999), doi:[10.1016/S0920-5861\(98\)00503-3](https://doi.org/10.1016/S0920-5861(98)00503-3)
- [166] Haller G.L. and Resasco D.E., *Metal-Support Interaction: Group VIII Metals and Reducible Oxides*: In D.D. Eley, H. Pines and P.B. Weisz, editors, *Advances in Catalysis*, volume 36, pages 173–235, Academic Press (1989), doi:[10.1016/S0360-0564\(08\)60018-8](https://doi.org/10.1016/S0360-0564(08)60018-8)
- [167] Dall’Agnol C., Gervasini A., Morazzoni F., Pinna F., Strukul G. and Zanderighi L., *Hydrogenation of Carbon Monoxide: Evidence of a Strong Metal-Support Interaction in RhZrO₂ Catalysts*: Journal of Catalysis, 96(1):106–114 (1985), doi:[10.1016/0021-9517\(85\)90364-1](https://doi.org/10.1016/0021-9517(85)90364-1)
- [168] Hoang D.L. and Lieske H., *Effect of Hydrogen Treatments on ZrO₂ and Pt/ZrO₂ Catalysts*: Catalysis Letters, 27(1-2):33–42 (1994), doi:[10.1007/BF00806975](https://doi.org/10.1007/BF00806975)
- [169] Hoang D.L., Berndt H. and Lieske H., *Hydrogen Spillover Phenomena on Pt/ZrO₂*: Catalysis Letters, 31(2-3):165–172 (1995), doi:[10.1007/BF00808830](https://doi.org/10.1007/BF00808830)

- [170] Bitter J.H., Seshan K. and Lercher J.A., *The State of Zirconia Supported Platinum Catalysts for CO₂/CH₄ Reforming*: Journal of Catalysis, 171(1):279–286 (1997), doi:[10.1006/jcat.1997.1792](https://doi.org/10.1006/jcat.1997.1792)
- [171] Widmann D., Liu Y., Schüth F. and Behm R.J., *Support Effects in the Au-Catalyzed CO Oxidation – Correlation between Activity, Oxygen Storage Capacity, and Support Reducibility*: Journal of Catalysis, 276(2):292–305 (2010), doi:[10.1016/j.jcat.2010.09.023](https://doi.org/10.1016/j.jcat.2010.09.023)
- [172] Xue K.H., Blaise P., Fonseca L.R.C. and Nishi Y., *Prediction of Semimetallic Tetragonal Hf₂O₃ and Zr₂O₃ from First Principles*: Physical Review Letters, 110(6):065502 (2013), doi:[10.1103/PhysRevLett.110.065502](https://doi.org/10.1103/PhysRevLett.110.065502)
- [173] Li H. and Tong S.Y., *Forward-Focusing and Shadowing Effects in Solids*: Surface Science, 281(3):L347–L352 (1993), doi:[10.1016/0039-6028\(93\)90634-V](https://doi.org/10.1016/0039-6028(93)90634-V)
- [174] Guo Q. and Joyner R.W., *An X-Ray Photoelectron Spectroscopy Study of the Stability of ZrO₂ Films on Pd(110)*: Applied Surface Science, 144–145:375–379 (1999), doi:[10.1016/S0169-4332\(98\)00827-7](https://doi.org/10.1016/S0169-4332(98)00827-7)
- [175] Gustafson J., Mikkelsen A., Borg M., Lundgren E., Köhler L., Kresse G., Schmid M., Varga P., Yuhara J., Torrelles X., Quirós C. and Andersen J.N., *Self-Limited Growth of a Thin Oxide Layer on Rh(111)*: Physical Review Letters, 92(12):126102 (2004), doi:[10.1103/PhysRevLett.92.126102](https://doi.org/10.1103/PhysRevLett.92.126102)
- [176] Srikrishnan V. and Ficalora P., *Measurement of the Enthalpies of Formation of ZrPt₃ and HfPt₃ by Fluorine Bomb Calorimetry*: Metallurgical and Materials Transactions B, 5(6):1471–1475 (1974), doi:[10.1007/BF02646634](https://doi.org/10.1007/BF02646634)
- [177] Brewer L., *A Most Striking Confirmation of the Engel Metallic Correlation*: Acta Metallurgica, 15(3):553–556 (1967), doi:[10.1016/0001-6160\(67\)90088-0](https://doi.org/10.1016/0001-6160(67)90088-0)
- [178] Predel B., *Rh-Zr (Rhodium-Zirconium): Datasheet from Landolt-Börnstein - Group IV Physical Chemistry · Volume 5f*: doi:[10.1007/10551312.2631](https://doi.org/10.1007/10551312.2631)
- [179] Wang H. and Carter E.A., *Metal-Metal Bonding in Engel-Brewer Intermetallics: "Anomalous" Charge Transfer in Zirconium-Platinum (ZrPt₃)*: Journal of the American Chemical Society, 115(6):2357–2362 (1993), doi:[10.1021/ja00059a034](https://doi.org/10.1021/ja00059a034)
- [180] Cairns J.A., Baglin J.E.E., Clark G.J. and Ziegler J.F., *Strong Metal-Support Interactions for Pt and Rh on Al₂O₃ and TiO₂: Application of Nuclear Backscattering Spectrometry*: Journal of Catalysis, 83(2):301–314 (1983), doi:[10.1016/0021-9517\(83\)90056-8](https://doi.org/10.1016/0021-9517(83)90056-8)
- [181] Bradley D.C. and Swanwick J.D., *Vapour Pressures of Metal Alkoxides. Part II. Zirconium Tetra-Tert.-Butoxide and -Amyloxide*: Journal of the Chemical Society (Resumed), 0(0):748–752 (1959), doi:[10.1039/JR9590000748](https://doi.org/10.1039/JR9590000748)

- [182] Mayr L., Shi X.R., Köpfle N., A. Milligan C., Y. Zemlyanov D., Knop-Gericke A., Hävecker M., Klötzer B. and Penner S., *Chemical Vapor Deposition-Prepared Sub-Nanometer Zr Clusters on Pd Surfaces: Promotion of Methane Dry Reforming*: *Physical Chemistry Chemical Physics*, 18(46):31586–31599 (2016), doi:[10.1039/C6CP07197J](https://doi.org/10.1039/C6CP07197J)
- [183] Mayr L., *Catalytic synergisms at (bi)metallic and oxidic surfaces and interfaces in SOFC-relevant reforming processes*: Ph.D. thesis, Institute of Physical Chemistry, University Innsbruck (2016)
- [184] Lichtenstein L., Büchner C., Yang B., Shaikhutdinov S., Heyde M., Sierka M., Włodarczyk R., Sauer J. and Freund H.J., *The Atomic Structure of a Metal-Supported Vitreous Thin Silica Film*: *Angewandte Chemie International Edition*, 51(2):404–407 (2012), doi:[10.1002/anie.201107097](https://doi.org/10.1002/anie.201107097)
- [185] Lewandowski A.L., Schlexer P., Tosoni S., Gura L., Marschalik P., Büchner C., Burrall H., Burson K.M., Schneider W.D., Pacchioni G. and Heyde M., *Determination of Silica and Germania Film Network Structures on Ru(0001) at the Atomic Scale*: *The Journal of Physical Chemistry C* (2018), doi:[10.1021/acs.jpcc.8b07110](https://doi.org/10.1021/acs.jpcc.8b07110)
- [186] Ma W., *Initial Oxidation of Zirconium: Chemistry, Atomic Structure, Transport and Growth Kinetics*: Ph.D. thesis, Department of Nuclear Science and Engineering, Massachusetts Institute of Technology (2016)
- [187] Olinger B. and Jamieson J.C., *Zirconium: Phases and Compressibility to 120 Kilobars*: *High Temperatures-High Pressures*, 5:123–131 (1973)
- [188] Tasker P.W., *The Stability of Ionic Crystal Surfaces*: *Journal of Physics C: Solid State Physics*, 12(22):4977–4984 (1979), doi:[10.1088/0022-3719/12/22/036](https://doi.org/10.1088/0022-3719/12/22/036)
- [189] Noguera C., *Polar Oxide Surfaces*: *Journal of Physics: Condensed Matter*, 12(31):R367 (2000), doi:[10.1088/0953-8984/12/31/201](https://doi.org/10.1088/0953-8984/12/31/201)
- [190] Skinner G.B. and Johnston H.L., *Thermal Expansion of Zirconium between 298°K and 1600°K*: *The Journal of Chemical Physics*, 21(8):1383–1384 (1953), doi:[10.1063/1.1699227](https://doi.org/10.1063/1.1699227)
- [191] Kang Y.C. and Ramsier R.D., *Kinetic Effects of Subsurface Species on Zr(0001) Surface Chemistry*: *Surface Science*, 519(3):229–236 (2002), doi:[10.1016/S0039-6028\(02\)02210-0](https://doi.org/10.1016/S0039-6028(02)02210-0)
- [192] Predel B., *O-Zr (Oxygen-Zirconium): Datasheet from Landolt-Börnstein - Group IV Physical Chemistry · Volume 5I*: doi:[10.1007/10542753_2335](https://doi.org/10.1007/10542753_2335)
- [193] Boureau G. and Gerdanian P., *High Temperature Thermodynamics of Solutions of Oxygen in Zirconium and Hafnium*: *Journal of Physics and Chemistry of Solids*, 45(2):141–145 (1984), doi:[10.1016/0022-3697\(84\)90112-4](https://doi.org/10.1016/0022-3697(84)90112-4)

- [194] Chase M.W., *NIST-JANAF Thermochemical Tables*: Number 9 in Journal of Physical and Chemical Reference Data Monograph, American Chemical Society ; American Institute of Physics for the National Institute of Standards and Technology, [Washington, D.C.; Woodbury, N.Y. (1998)
- [195] Doerffler W.W., *The Dissolution and Diffusion of Oxygen in Zirconium*: Technical Report AECL-2268, Atomic Energy of Canada Ltd., Chalk River, Ontario (Canada) (1965)
- [196] Cox B., *Some Thoughts on the Mechanisms of In-Reactor Corrosion of Zirconium Alloys*: Journal of Nuclear Materials, 336(2):331–368 (2005), doi:[10.1016/j.jnucmat.2004.09.029](https://doi.org/10.1016/j.jnucmat.2004.09.029)
- [197] Andreoni W. and Varma C.M., *Binding and Dissociation of CO on Transition-Metal Surfaces*: Physical Review B, 23(2):437–444 (1981), doi:[10.1103/PhysRevB.23.437](https://doi.org/10.1103/PhysRevB.23.437)
- [198] Dash R.K., Yushin G. and Gogotsi Y., *Synthesis, Structure and Porosity Analysis of Microporous and Mesoporous Carbon Derived from Zirconium Carbide*: Microporous and Mesoporous Materials, 86(1–3):50–57 (2005), doi:[10.1016/j.micromeso.2005.05.047](https://doi.org/10.1016/j.micromeso.2005.05.047)
- [199] Predel B., *C-Zr (Carbon-Zirconium): Datasheet from Landolt-Börnstein - Group IV Physical Chemistry · Volume 12B*: doi:[10.1007/978-3-540-44756-6_106](https://doi.org/10.1007/978-3-540-44756-6_106)
- [200] Xu Y., Roques J., Domain C. and Simoni E., *Carbon Diffusion in Bulk HCP Zirconium: A Multi-Scale Approach*: Journal of Nuclear Materials, 473:61–67 (2016), doi:[10.1016/j.jnucmat.2016.02.010](https://doi.org/10.1016/j.jnucmat.2016.02.010)
- [201] Onuferko J.H., Woodruff D.P. and Holland B.W., *LEED Structure Analysis of the Ni{100} (2 × 2)C (P4g) Structure; A Case of Adsorbate-Induced Substrate Distortion*: Surface Science, 87(2):357–374 (1979), doi:[10.1016/0039-6028\(79\)90535-1](https://doi.org/10.1016/0039-6028(79)90535-1)
- [202] Klink C., Olesen L., Besenbacher F., Stensgaard I., Laegsgaard E. and Lang N., *Interaction of C with Ni(100): Atom-Resolved Studies of the “Clock” Reconstruction*: Physical Review Letters, 71(26):4350–4353 (1993), doi:[10.1103/PhysRevLett.71.4350](https://doi.org/10.1103/PhysRevLett.71.4350)
- [203] Vang R.T., Honkala K., Dahl S., Vestergaard E.K., Schnadt J., Lægsgaard E., Clausen B.S., Nørskov J.K. and Besenbacher F., *Ethylene Dissociation on Flat and Stepped Ni(111): A Combined STM and DFT Study*: Surface Science, 600(1):66–77 (2006), doi:[10.1016/j.susc.2005.10.006](https://doi.org/10.1016/j.susc.2005.10.006)
- [204] Klink C., Stensgaard I., Besenbacher F. and Lægsgaard E., *An STM Study of Carbon-Induced Structures on Ni(111): Evidence for a Carbide-Phase Clock Reconstruction*: Surface Science, 342(1):250–260 (1995), doi:[10.1016/0039-6028\(95\)00697-4](https://doi.org/10.1016/0039-6028(95)00697-4)

Personal information

Surname, First name	Lackner, Peter
Titles	Bachelor of Science Master of Science (Diplomingenieur)
Email address:	lackner@iap.tuwien.ac.at
Nationality	Austrian
Date of birth	28 of June, 1989

Education

July 2015 – April 2019	Doctoral programme in Engineering Sciences: Technical Physics At the TU Wien, Institute of Applied Physics <ul style="list-style-type: none">• Topic of Thesis: Surface Science Studies on Zirconia Thin-Film Model Systems• Supervisors: Prof. Michael Schmid, Prof. Ulrike Diebold
January 2013 – June 2015	Technical Physics, Master's Program At the TU Wien <ul style="list-style-type: none">• Graduated with distinction• Merit-based scholarship (Dec 2014) awarded by the University• Erasmus exchange semester at KTH Stockholm from August 2013 until January 2014 with specialisation on astroparticle physics and space plasma physics• 1st project work on “Size distribution of FeNiB nanoparticles” in Vienna (Prof. Reissner) and at the University of Zagreb (One month stay, Assistant Prof. Pajić)• 2nd project work on “Finding a surface model for the magnetite (110) surface” (Prof. Diebold)• Master's thesis on the In₂O₃(111) surface (Prof. Diebold) including measurements at the MAX-lab Synchrotron in Lund, Sweden
October 2009 – January 2013	Technical Physics, Bachelor's Program At the TU Wien <ul style="list-style-type: none">• Graduated with distinction• Bachelor's thesis on “Material identification using Mößbauer spectroscopy and reconstruction of a Mößbauer system” (German) (Prof. Reissner)
September 2003 – June 2008	Studied Electronics , focusing on Technical Informatics At the Technical High School Hollabrunn (Höhere Technische Lehranstalt (HTL) Hollabrunn)

List of publications

As first author	<i>Surface structures of ZrO₂ films on Rh(111): From two layers to bulk termination</i> P. Lackner, Z. Zou, S. Mayr, <i>et al.</i> Surface Science 679 , 180 (2019). <i>Water adsorption at zirconia: from the ZrO₂(111)/Pt₃Zr(0001) model system to powder samples</i> P. Lackner, J. Hulva, E.-M. Köck, <i>et al.</i> J. Mater. Chem. A 6 , 17587 (2018). <i>Construction and evaluation of an ultrahigh-vacuum-compatible sputter deposition source</i> P. Lackner, J. I. J. Choi, U. Diebold, and M. Schmid, Rev. Sci. Instrum. 88 , 103904 (2017).
-----------------	---

	<p><i>Size distribution of FeNiB nanoparticles</i> P. Lackner, D. Pajic, M. Reissner et al., EPJ Web. Conf. 75, 05008 (2014)</p>
As coauthor	<p><i>Resolving the Structure of a Well-Ordered Hydroxyl Overlayer on In₂O₃(111): Nanomanipulation and Theory</i> M. Wagner, P. Lackner, S. Seiler, et al. ACS Nano 11, 11531 (2017).</p> <p><i>Zirconium-Palladium Interactions during Dry Reforming of Methane</i> N. Köpfle, L. Mayr, P. Lackner, et al. ECS Trans. 78, 2419 (2017).</p> <p><i>Well-Ordered In Adatoms at the In₂O₃ (111) Surface Created by Fe Deposition</i> M. Wagner, P. Lackner, S. Seiler, et al. Phys. Rev. Lett. 117, 206101 (2016).</p> <p><i>Fe₃O₄(110)–(1×3) revisited: Periodic (111) nanofacets</i> G. S. Parkinson, P. Lackner, O. Gamba et al. Surf. Sci. 649, 120 (2016)</p>
Conference visits including talks	<p>Workshop „Functional Oxide Surfaces & Interfaces“ (2016, 2017, 2018, 2019) VI San Luis, Santa Fe Argentina (2018) DPG – German Physical Society Spring Meeting (2016, 2017, 2018) ECOSS – European Conference on Surface Science (2017, 2018) International Symposium „Functional Oxide Surfaces & Interfaces“ (2017) Austrian Physical Society Meeting (2016)</p>
Conference visits including posters	<p>Symposium on Surface Science (2017) MBE Workshop Vienna (2017) FOXSI International Symposium (2016, 2017)</p>

Supervised Student Work

Master's Thesis	<p><i>Studies of Few-Monolayer Zirconia Films and Metal Nucleation on Zirconia Surfaces</i> By Sabrina Mayr</p>
Project Work	<p><i>Alignment of a new hemispherical analyzer and preliminary studies on Zr(0001)</i> By Sabrina Mayr</p>
Project Work	<p><i>Surface Analysis of Ultrathin Zirconia Films on Zirconium (0001)</i> By Katharina Newrkla</p>
Bachelor's Thesis	<p><i>H₂O and CO₂ on a Zirconia Trilayer on Pt₃Zr(0001)</i> By Matthias Maurer</p>
Project Work	<p><i>Structure and annealing behaviour of sputter-deposited ZrO₂ films on Rh(111) and Pt₃Zr(0001)</i> By Dorota Kowalczyk</p>